Chirality, symmetry-breaking, and chemical substitution in multiferroics

A Dissertation Presented for the

Doctor of Philosophy

Degree

The University of Tennessee, Knoxville

Kiman Park

August 2023

Acknowledgements

First and foremost I wish to thank my advisor, Professor Janice L. Musfeldt, for introducing me to the world of solid-state physics and spectroscopy. Even though we had arguments, you never stopped encouraging and leading me to do better. I will always be grateful.

I am grateful to Professors David Mandrus, Konstantinos Vogiatzis, and Bhavya Sharma for serving on my committee, as well as for all of their interest and advice.

I wish to acknowledge all the members of our research group: Ken O'Neal, Michael Yokosuk, Amanda Clune, Kendall Hughey, Nathan Harms, Kevin Smith, Sabine Neal, and Avery Blockmon for their help, encouragement, and collaboration. I am grateful to all the faculty and staff of the Chemistry Department who shared their knowledge with me and helped in a variety of ways during my graduate program.

I would like to thank Gheorghe L. Pascut, Heung-Sik Kim, Sungkyun Choi, Jinwoong Kim, Bin Gao, Xianghan Xu, Ghanashyam Khanal, Jaewook Kim, Valery Kiryukhin, Alexander P. Litvinchuk, Kristijan Haule, Mykhaylo Ozerov, Matthias J. Gutmann, Junjie Yang, Sang-Wook Cheong, David Vanderbilt, John Singleton, Mateusz Goryca, Scott A. Crooker, Vivien Zapf, Minseong Lee, Stephen McGill, and Jun Hee Lee for their collaboration and inspiring conversations during these years. For some, they took their valuable time to teach me step-by-step, which helped me immensely during this journey. I couldn't have done this without them.

Finally, I wish to thank my family for always believing in and supporting me. I

could not have finished my degree without your guidance, patience, and understanding. I will also thank my partner-in-crime, Abby Carpenter, for supporting me and releasing the pressure of graduate school.

Abstract

Multiferroic materials attract significant attention due to their potential utility in a broad range of device applications. The inclusion of heavy metal centers in these materials enhances their magnetoelectric properties, yielding fascinating physical phenomena such as the Dzyaloshinskii–Moriya interaction, nonreciprocal directional dichroism, enhancement of spin-phonon coupling, and spin-orbit-entangled ground states. This dissertation provides a comprehensive survey of magnetoelectric multiferroics containing heavy metal centers and explores spectroscopic techniques under extreme conditions. A microscopic examination of phase transitions, symmetry-breaking, and structure-property relationships enhances the fundamental understanding of coupling mechanisms.

In $A_2Mo_3O_8$ (A = Fe, Zn, Ni, and Mn), we use optical spectroscopy to analyze the electronic properties and compare our findings with first principles electronic structure calculations. We find that Fe^{2+} ions in the A site create a many-body effect from a valence band due to screening of the local moment – similar to a Zhang-Rice singlet. These findings advance the understanding of unusual hybridization with orbital occupation and the structure-property relationships in various metal-substituted systems.

In a chiral, polar magnet, Ni_3TeO_6, we explore toroidal geometry to complete the set of configurations and develop structure-property relations by combining magneto-optical spectroscopy and first-principles calculations. The formation of Ni toroidal

moments is responsible for the largest effects near 1.1 eV - a tendency that is captured by our microscopic model and computational implementation. Furthermore, we demonstrate deterministic control of nonreciprocal directional dichroism in Ni_3TeO_6 across the entire telecom wavelength range. This discovery will accelerate the development of photonics applications that take advantage of unusual symmetry characteristics.

In $Co_4B_2O_9$ (B = Nb, Ta), we combine variable temperature infrared spectroscopy, lattice dynamics calculations, and several different models of spin-phonon coupling to reveal the mechanism of magnetoelectricity. We reveal a spin-phonon coupling in Co^{2+} shearing mode near 150 cm^{-1} with coupling constants of 3.4 and 3.4 cm^{-1} for $Co_4Nb_2O_9$ and the Ta analog, respectively. These coupling constants derive from interlayer exchange interactions, which contain competing antiferromagnetic and ferromagnetic contributions. Comparison to other contemporary oxides shows that spin-phonon coupling in this family of materials is among the strongest ever reported, suggesting an origin for magnetoelectric coupling.

Table of Contents

1 Introduction **1**

1.1 Spectroscopic methods for complex oxides 7

1.2 Main findings of this work 20

1.2.1 Band-Mott mixing hybridizes the gap in $Fe_2Mo_3O_8$ 20

1.2.2 Nonreciprocal directional dichroism at telecom wavelengths . . 23

1.2.3 Spin-phonon interactions, frustration, and magnetoelectric coupling in $Co_4Nb_2O_9$ and the Ta analog 24

1.2.4 Spin-lattice coupling in $MnPS_3$ and giant magnetic circular dichroic signal in $CrPS_4$ 24

1.3 Outline 25

2 Literature survey **26**

2.1 Multiferroic materials 26

2.2 Magnetoelectric coupling 29

2.3 Magnetoelectric coupling mechanisms 34

2.4 Nonreciprocal directional dichroism 42

2.5 Spin-phonon coupling 49

2.6 Magnetism in a honeycomb lattice 57

2.7 Two-dimensional transition metal chalcogenides 66

2.8 Materials of interest 73

2.8.1 $Fe_2Mo_3O_8$ and its analogs . . . 73
2.8.2 Ni_3TeO_6 . . . 75
2.8.3 $Co_4B_2O_9$ (B = Nb, Ta) . . . 78
2.8.4 $MnPS_3$ and $CrPS_4$ . . . 80

3 Spectroscopic methods **83**

3.1 Optical theory . . . 83
3.1.1 Maxwell's Equations . . . 84
3.1.2 Beer's law . . . 87
3.1.3 Kramers-Kronig analysis and sum rules . . . 89
3.1.4 Drude and Lorentz models . . . 91
3.1.5 Band gap analyses . . . 95
3.1.6 Polarization and crystal anisotropy . . . 101
3.1.7 Magnetic circular dichroism . . . 104
3.2 Spectrometers . . . 109
3.2.1 Fourier transform infrared spectroscopy . . . 110
3.2.2 Bruker IFS 113v Fourier transform infrared spectrometer . . . 112
3.2.3 Bruker Equinox 55 Fourier Transform Infrared spectrometer with Bruker IR Scope II . . . 115
3.2.4 Perkin Elmer λ-1050 grating spectrometer . . . 119
3.3 Spectroscopy under extreme conditions . . . 122
3.3.1 Variable temperature spectroscopy . . . 123
3.3.2 High magnetic field spectroscopy . . . 125
3.3.3 Magnetic circular dichroism setup at the National High Magnetic Field Laboratory . . . 129
3.4 Project-specific details: Sample growth, measurements, and complementary calculations . . . 131

3.4.1 Band-Mott mixing hybridizes the gap in $Fe_2Mo_3O_8$ 131
3.4.1.1 Single crystals growth 131
3.4.1.2 Optical measurements 131
3.4.1.3 Complementary electronic structures calculations . . 132
3.4.2 Nonreciprocal directional dichroism at telecom wavelengths . . 132
3.4.2.1 Crystal growth and orientation 132
3.4.2.2 Optical spectroscopy 133
3.4.2.3 Magneto-optical spectroscopy 133
3.4.2.4 Modeling the optical diode effect 136
3.4.3 Spin-phonon interactions, frustration, and magnetoelectric coupling in $Co_4Nb_2O_9$ and the Ta analog 137
3.4.3.1 Single crystals growth 137
3.4.3.2 Reflectance spectroscopy and Kramers-Kronig analysis 137
3.4.3.3 Lattice dynamics calculations 137
3.4.4 Spin-lattice coupling in $MnPS_3$ and giant magnetic circular dichroic signal in $CrPS_4$ 138
3.4.4.1 Crystal Growth 138
3.4.4.2 Optical spectroscopy 138
3.4.4.3 Magnetic circular dichroism spectroscopy 139

4 Band-Mott mixing hybridizes the gap in $Fe_2Mo_3O_8$ 141

4.1 Optical response of $Fe_2Mo_3O_8$ and the A-substituted analogs (A = Zn, Mn, Ni) 142
4.2 Strong hybridization, resonance, and interaction with the Mo trimer . 147
4.3 Structure-property relations in the metal-substituted analogs 154

5 Nonreciprocal directional dichroism at telecom wavelengths 158

5.1 Crystal structure, properties, and symmetry analysis 158

5.2 Nonreciprocal effect in different measurement configurations 161

5.3 Field dependence of the dichroic contrast in the toroidal geometry . . 162

5.4 Nonreciprocal directional dichroism at telecom wavelengths 168

5.5 Structure-property relations for photonics applications 170

6 Spin-phonon interactions, frustration, and magnetoelectric coupling in $Co_4Nb_2O_9$ and the Ta analog 171

6.1 Vibrational properties of B-site substituted materials 171

6.2 Spin-phonon coupling in $Co_4B_2O_9$ (B = Nb, Ta) 173

6.3 Structure-property relations in this family of materials 177

6.4 Revealing the origin of magnetoelectric coupling 181

7 Summary and Outlook 182

Bibliography 185

Vita 223

List of Tables

1.1 Differences of transition metals and heavy metals. 3

1.2 Scientific problems and important findings in this dissertation 21

2.1 Spatial-inversion and time-reversal symmetry in ferroics. 28

3.1 Relationships between the various response functions $\epsilon(\omega)$, $\sigma(\omega)$, and $N(\omega)$ 88

3.2 Conditions for differently polarized light 103

3.3 Bruker IFS 113v operating parameters 116

3.4 Operating parameters of Bruker IRscope II 117

3.5 λ-1050 operating parameters 121

6.1 Spin-phonon coupling in $Co_4Nb_2O_9$ and $Co_4Ta_2O_9$ compared with that in a number of representative $3d$, $4d$, $5d$, and mixed oxides. An asterisk (*) indicates where information was available for us to estimate values. 178

List of Figures

1.1 (a,b) Crystal structure of $Cu_3Nb_2O_8$ in b-axis and a-axis views are displayed, respectively. (c) Magnetic vectors imposed on the crystal structure are shown to demonstrate the spin rotations. (d) A diagram of the polarization that is perpendicular to the plane of the spin rotation is shown [35]. 6

1.2 (a) The crystal structure of $Sr_2CoSi_2O_7$ is displayed. The κ and $-\kappa$ represent the rotation of the tetrahedron where the chirality arises. (b) Absorption spectra as a function of the magnetic field are displayed with different polarization. Nonreciprocal directional dichroism is observed by the difference in the intensity of peaks, which is achieved by changing the light propagation k [39]. 8

1.3 (a) Colossal magnetoresistance in the perovskite manganite. The upper panel schematically represents the magnetic-field-induced melting of the charge–orbital ordered state as the microscopic origin of colossal magnetoresistance [40, 41]. (b) Electric-double-layer gating-induced insulator–metal transition in VO_2 thin film. The upper panel shows the concurrent switching of the near-infrared photo-absorption spectrum, representing radiation device functionality [41–43]. (c) Photo-melting of the charge-orbital ordered state in manganite [41, 44]. . . 9

1.4 (a) Energy-dispersive X-ray spectrum of $Cr_{1/3}TaS_2$ is shown to verify the chemical composition. The inset is the picture of the crystal [45]. (b) Magnetic phase diagrams are shown here with magnetization and magnetoresistance measurements [45]. (c) The magnetic phase diagram of Cu_2OSeO_3 is shown here with magnetization measurements on the top left. SkX, C, H, FM, and P represent the skyrmion lattice, conical, helical, ferromagnetic, and paramagnetic states, respectively. To the top right, the magnetic resonance spectra ΔL_{11} at 25 K is corresponding to the magnetization [46]. The bottom two plots are also from the magnetic resonance spectra with the combination of theoretical calculations [46]. 10

1.5 Schematic showing optical processes in solids, with an indication of the frequencies where these processes typically may be studied [55]. . 12

1.6 Raman spectra are displayed as a function of temperature. (a) stacked spectra are shown to reveal new phonon peaks across the charge-density-wave transition. (b) Peaks are tracked as a function of temperature and phonon assignments. (c) Raman spectra of 2H-NbS_2 at 300 and 4 K with peak assignments for comparison [60]. 14

1.7 (a) Crystal structure of $Y_2Ir_2O_7$ is shown. (b) susceptibility as a function of temperature is displayed. The T_N is at 170 K. (c) $\sigma_1(\omega)$ spectra are shown, which are fitted using the Fano-Lorentz model to get infrared-active phonons. Phonon frequencies of Ph4, Ph5, and Ph6 have shifted abruptly across the T_N, signaling for spin-phonon coupling. (d) Phonon frequencies and full-width half maximums of Ph4, Ph5, and Ph6 as a function of temperature are displayed to quantify spin-phonon coupling for each phonon mode [63]. 15

1.8 (a) and (b) Absorbance and refractive index spectra with different polarization at around 12 and 14 K are shown. (c) Absorbance spectra as a function of temperature are displayed. The emergence of the peak below the T_N proves that this peak is a magnetic excitation. (d) Transmittance and absorption spectra as a function of the magnetic field at 4 K are displayed. The open circles and solid lines represent the light propagation direction. The difference in intensity between the open circle and the solid line is due to nonreciprocal directional dichroism. (f) absorption difference spectra as a function of temperature are shown. Nonreciprocal directional dichroism persists above the magnetic transition temperature [64]. 16

1.9 Two models to calculate local d-to-d excitations. (a,b) Tanabe-Sugano diagram is used to assign octahedrally coordinated Ni^{2+} excitations [68] in Ni_3TeO_6. (c,d) The Point-Charge model is used to assign excitations of octahedral and tetrahedral Fe^{2+} environment [29] in $Fe_2Mo_3O_8$. Parameters are Dq, A_2, A_4, λ, ρ, and H_m, which $\sim$ 303, -33.3, -339, 117, 1.1, and 18.2 cm^{-1} for the tetrahedral site and -685, -596, -332, -117, 1.1, and 13.6 cm^{-1} for the octahedral site were used [29]. 18

1.10 (a) Tanabe-Sugano diagram of Ni^{2+} ion in the NiO is shown with parameters. (b) Crystal field of Ni^{2+} is calculated using Point-Charge model with spin-orbit coupling (λ) and molecular field (n) [69]. . . . 19

1.11 (a) $\Delta\alpha$(E,H) of $BiFeO_3$ for different magnetic fields at 4 K. Schematic illustration of exciton and magnon sidebands [70]. (b) $\Delta\alpha$ spectra of α-Fe_2O_3 at 4.2 K for the α-polarization and B $\parallel$ [111] at selected magnetic fields: 5, 10, 15, 35 T [71]. 22

2.1 A diagram of spin, orbital, charge, and lattice degrees of freedom. They can couple with each other to form various couplings [75]. . . 27

2.2 A diagram showing the cross-coupling of "ferroic". E, electric field, is controlling the polarization. H, magnetic field, is controlling the magnetism. σ, mechanical stress, is controlling the ϵ, which is a strain. The diagram shows how couplings can affect, for example, polarization with the magnetic field, magnetism with the electric field, strain with the magnetic field, and so on [1]. 30

2.3 An example of magnetoelectric coupling is shown. (a) $Fe_2Mo_3O_8$ and Ni_3TeO_6 display changes in the magnetism as a function of the electric field [28]. (b,c) A diagram of the experimental setup and the images of propagation of the domain [76]. 31

2.4 A diagram of multiferroic materials represented in a tree. Starting with conventional ferroelectric d^0 materials and d^n magnetism, different kinds of multiferroics are organized by various multiferroic mechanisms and mixing of metal centers [75]. 33

2.5 The crystal structure of $BiFeO_3$ and $TbMnO_3$ are displayed. (a) The crystal structure of $BiFeO_3$ with a-axis view and c-axis view is presented. The space group is $R3c$ (No. 161) [83]. (b) The crystal structure of $TbMnO_3$ is shown here with a-axis view and c-axis view. The space group is $Pnma$ (No. 62) [84]. 35

2.6 Various mechanisms for multiferroicity are shown. (a-c) The lone-pair mechanism, geometric ferroelectricity, and charge-ordering are Type-I multiferroic mechanisms, in which structural distortion occurs independently from magnetic ordering. (d) The spin-driven mechanism supports Type-II multiferroics. By the inverse Dzyaloshinskii-Moriya interaction, exchange striction, and spin-dependent $p-d$ hybridization, magnetism affects structural distortion, creating electric polarization for ferroelectricity [85]. 36

2.7 (a,b) Crystal structure of BaMiF$_4$ (M = Co, Ni, Zn, Mg) where the rotation/tilting creates a noncentrosymmetric structure in panel (a), whereas no distortion maintains the centrosymmetric structure [86]. (c-e) Crystal structure of $YMnO_3$ and electron density distribution maps above and below the Curie temperature [87]. Lu1-O3 bonding can be observed below the T_C. 38

2.8 (a) A crystal structure of $LuFe_2O_4$ is displayed. It has a space group of C2/m. Alternating Fe^{2+} and Fe^{3+} local sites can be observed. (b) A distinct local environment of Fe^{2+} and Fe^{3+} [90]. 40

2.9 A diagram is displayed to show the symmetry requirement for nonreciprocal directional dichroism. (a) Only inversion symmetry is broken. (b) Mirror symmetry is remained unbroken. (c) All of symmetries are broken. Thus, nonreciprocal directional dichroism can be observed. 44

2.10 Nonreciprocal effect of different materials in the terahertz infrared region. The materials shown are $BiFeO_3$ (a) [109], $CaBaCo_4O_7$ (b) [110], $FeZnMo_3O_8$ (c) [64], and $Ba_2CoGe_2O_7$ (d) [111]. 47

2.11 Nonreciprocal effect in the optical region is shown with (a) $GaFeO_3$ [112] and (b) CuB_2O_4 [113] 48

2.12 (a) Absorption spectra of $Pb(TiO)Cu_4(PO_4)_4$ at 4.2, 8, and 290 K. (b) Distorted CuO_5 square pyramid. The purple arrow represents the magnetic moment vector. (c) Absorption spectra with different polarization. (d) Absorption difference spectra from different polarization. (e) Microscopy images using polarization. (f) The images are subtracted to show the difference, just like absorption difference [119]. 50

2.13 (a) Temperature dependence of each phonon mode in $Y_2Ru_2O_7$. (b) Phonon frequency (ω), damping constant (Γ), strength (S), and broad response ($1/q$) as a function of temperature. The deviation from the predicted behavior from the normal thermal effect indicates spin-phonon coupling [133]. 54

2.14 Phonon displacement pattern of $Cd_2Os_2O_7$ is shown on the top. The parameters (ω = phonon frequency, Γ = damping constant, Ω = phonon plasma frequency) for phonon modes as a function of temperature are displayed [136]. 56

2.15 (a) A 1-dimensional ferromagnetic structure with $J > 0$. (b) antiferromagnetic structure with $J < 0$. 59

2.16 A schematic of superexchange between metal ions through a ligand. If the angle is 180°, antiferromagnetic interaction is favored. If the angle is 90°, ferromagnetic interaction is favored. 60

2.17 (a) A schematic of a honeycomb lattice with one type of atom is displayed. (b) A schematic of a honeycomb lattice with two distinct types of atoms is displayed. (c) A triangular interaction that leads to frustration. (d) One of the ways is to relieve the magnetic frustration, which leads to a noncollinear magnetic structure. 62

2.18 (a,b) A schematic of honeycomb bilayer structure and magnetic interactions in $Bi_3Mn_4O_{12}(NO_3)$ is displayed. (c) Calculated neutron scattering spectra with linear spin wave theory is displayed here. The magnetic field (10 T) is included perpendicular to the spin directions [145]. 63

2.19 (a,b) Hybridization and hopping of 'flux-pair', respectively. (c) continuous topological phase transition is shown. The $h < h_c$ is topologically trivial, but the $h > h_c$ includes six merons [164]. 65

2.20 (a) A crystal structure of Na_2IrO_3, zig-zag magnetic structure, and evidence of the anisotropic bonds in RIXS measurement are displayed [165, 166]. (b) A crystal structure of α-$RuCl_3$, a picture of physical crystal, and neutron scattering measurement are shown [167, 168]. (c) A crystal structure of $Na_2Co_2TeO_6$ and two phase diagrams as a function of temperature and magnetic field are shown [169, 170, 173]. . . 67

2.21 (a) Images of exfoliated MoS_2 flakes on Si substrate is displayed. The exfoliation was performed down to 1 layer. (b) Reflection and photoluminescence spectra of MoS_2 layers are shown. The absorption is at 1.85 and 1.98 eV [182]. 69

2.22 (a) A schematic of the CrI_3 crystal structure with magnetic ordering is shown. (b) A schematic of a CrI_3 dual-gated device is displayed. (c) the image of the dual-gated device is shown. (d) The reflectance magneto-circular dichroism (RMCD) signal as a function of the magnetic field is displayed for CrI_3. It starts as an antiferromagnetic state and transitions to a ferromagnetic state at around 0.75 T [202]. (e) Magnetoresistance signal as a function of the magnetic field and the angle is shown for $Cr_2Ge_2Te_6$. (f) A saturated field as a function of the angle γ in degrees is shown [203]. 71

2.23 (a) Antiferromagnetic structure of $MnPS_3$. (b) Magnetization and magnetic susceptibility as a function of the magnetic field. (c) Resistance of a six-layer $MnPS_3$ device measured with 1.6 V (red) and 1.8 V (blue) applied bias. (d) Tunneling current density j at T = 1.5 K as a function of bias for different thicknesses of $MnPS_3$. (e) In the Fowler-Nordheim tunneling regime at high bias, $\ln(\frac{j}{V^2}$ is proportional to $\frac{N}{V}$. (f) The linear tunneling conductance decreases exponentially with $MnPS_3$ thickness. (g) the coefficient α decreases linearly with d [209]. (h) Pressure-induced color change of $MnPS_3$. (i) Absorption spectra and Tauc's plot as a function of pressure is displayed with band gap vs. pressure plot. (j) A schematic of pressure transitions [210]. . . 72

2.24 (a) Crystal structure of $Fe_2Mo_3O_8$. (b) A top view of the Fe-O layer, where the honeycomb lattice can be seen. The line represents the largest Fe-Fe exchange interaction J. (c) A schematic of antiferromagnetic (AFM) state and ferrimagnetic (FRM) state is displayed for $Fe_2Mo_3O_8$. (d) The change in polarization is along the c-axis due to the oxygen shift. (e) Magnetic susceptibility reveals $T_N \approx 61$ K. (f) Heat capacity also displays a phase transition at around 61 K with a picture of the crystal in the inset [28]. 74

2.25 (a) A phase diagram of Ni_3TeO_6 is shown as a function of temperature and magnetic field. The T_N is at 53 K where the antiferromagnetic (AFM) ground state is displayed. At around 9 T, the spin-flop transition is observed and the metamagnetic state is achieved at above 50 T. The saturation field is extrapolated to be above 100 T. [250]. . . . 76

2.26 (a) The basic building block of Ni_3TeO_6 is displayed, which corresponds to one-third of one unit cell. We denoted the shortest bonds in red and blue triangles as bold lines. (b) Two different ferri-chiral states are shown as red and blue colors. (c) An optical microscope image of a 100 μm-thick single crystal of Ni_3TeO_6 is shown with the scale bar equals 1 mm. (d-j) The chiral domains of a Ni_3TeO_6 crystal are visible in transmission polarized optical microscope images are shown. Blue and red bars represent the angles of a polarizer and an analyzer, respectively [248]. (k) Magnetic structure and magnetic phase transitions are shown [252]. (l) Polished single crystal of Ni_3TeO_6 is shown, which has only one chiral domain [250]. (m) Spectroscopic properties of Ni_3TeO_6 as a function of the magnetic field. [68]. 77

2.27 (a) A crystal structure of $Co_4Nb_2O_9$. (b) Magnetic structure in a honeycomb lattice in $Co_4Nb_2O_9$. (c,d,e) susceptibility, permittivity, and strain measurements reveal a magnetic ordering transition at around 27 K. (f) permittivity as a function of the magnetic field. Spin-flop transitions are revealed and anisotropic behavior is displayed as the directions of the magnetic field change [263]. 79

2.28 (a) The crystal structure of $MnPS_3$ in the a-axis view is displayed. The sheet thickness and size of the van der Waals gap are indicated as 3.22 and 3.27 $\mathring{A}$. (b) the c-axis view shows a clear hexagonal structure in the ab-plane. (c) The crystal structure of $CrPS_4$ with the sheet thickness of 3.69 $\mathring{A}$ and van der Waals gap of 2.46 $\mathring{A}$. (d) Unlike $MnPS_3$, $CrPS_4$ has a rectangular structure. (e) The experimental diagram is shown, displaying two light propagation, k, to differentiate the unpolarized and circularly-polarized measurements for optical spectroscopy and magnetic circular dichroism. H is the magnetic field. The bottom slab is the sample as indicated with the crystal structure. 81

3.1 (a) Reflectance spectra of Fe_xTaS_2 is displayed with x = 0, 1/3, and 1/4. (b) σ_1 is shown by using Kramer-Kronig analysis on the reflectance data. (c) Using TaS_2 as a reference to isolate Fe layer conductivity [302]. 96

3.2 Energy diagram of the band gap defined by the energy difference between the top of the valence band to the bottom of the conduction band. 97

3.3 Examples of the extraction of band gaps in Si, Ge, ZnO, and TiO_2 using Tauc plot. A linear region in the graph is extrapolated linearly to obtain the gap energy. 98

3.4 Band gap energies as a function of temperature for $Fe_2Mo_3O_8$ and its analogs are shown using Varshini's model. (a) The abrupt change across the T_N signifies spin-charge coupling in the system. (b-e) Normal temperature trends are shown [314]. 100
3.5 Schematic diagram of the representation of the linear, circular, and elliptical polarization. (a) Linear polarization can be achieved by using a linear polarizer. (b,c) For circular and elliptical polarization, a quarter wave plate is used with a linear polarizer. 102
3.6 (a) Generic model of excitation with a selection of RCP and LCP for atomic/molecular transitions (b) Diagram of MCD response shows the derivative-like A-term response function and show the expected shape for B and C term response functions. (c) An example of a peak in the absorption spectrum and MCD spectrum. MCD exhibits a derivative feature as shown in Eqn. 3.48. 106
3.7 Schematic view of the density of states for (a) a non-magnetic and (b) a magnetic semiconductor [316]. 107
3.8 Schematic view of a Michelson interferometer in a Fourier transform infrared spectrometer setup. 111
3.9 Typical interferogram is displayed here. (a,b) The intensity is measured as a function of a temporal delay (T) and (c,d) as a function of frequency [323]. 113
3.10 Schematic view of the Bruker IFS 113v FTIR spectrometer. 114

3.11 Optical path diagram of Bruker IRscope II. 1,16: a visible light source; 2,19: visible light aperture; 3,22: motorized switch mirror; 4,18: optional iris or knife edge aperture; 5,9,10,17: beam splitter changer; 6: objective lens; 7: Sample; 8: iris or knife edge aperture which defines the area of the sample analyzed; 12: binocular eyepiece; 13: two position detector selection mirror; 14: mirror routing to detector; 15: detector; 20: condenser; 21: IR beam (from spectrometer); 23,24: camera port; 25,26,27: polarizers. 118

3.12 Optical layout of Perkin-Elmer λ-1050. 120

3.13 Set-up of LT-3-110 Heli-Tran liquid transfer line and cryostat 124

3.14 (a) A schematic energy scale of various magnets (superconducting, resistive, hybrid, and pulsed magnets) at National High Magnetic Field Laboratory. (b) Magnetic field profile of the short pulsed magnet at National High Magnetic Field Laboratory-Los Alamos National Laboratory. We note that split helix magnet is resistive, but only goes up to 25 T. 126

3.15 A Voigt geometry sample holder, made of nonmagnetic PEEK (polyetheretherketone) material. It consists of three pieces: a mountable sample slide, a prism holder to reflect the light onto the sample and back into the detector, and a piece to hold everything together and attach at the end of the magneto-optics probe. (a)-(d) shows the process of mounting the sample to attaching it to the probe for the Voigt geometry. 128

3.16 (a) Detailed structure of the 25 T split helix magnet in the NHMFL. Images are available at: https://nationalmaglab.org/about/around-the-lab/meet-the-magnets/meet-the-split-helix-magnet. (b) Sample mounting probe of the magnetic circular dichroism experiment. (c) MCD experimental setup at the NHMFL. 130

3.17 The image shows polished Ni_3TeO_6 crystal with single domain in *ab*-plane (a) and *c*-axis (b) [250]. 134

3.18 Schematics display three geometries in Ni_3TeO_6 to observe nonreciprocal directional dichroism. (a) Magnetochiral geometry consists of light propagation (k) parallel to chirality (**C**) and magnetic moment (**M**). (b) Transverse magnetochiral geometry has k parallel to **M**, but **C** is perpendicular. (c) Toroidal geometry (**T**) is composed of electric polarization (**P**) perpendicular to **M**. The light propagation direction is orthogonal to both. 135

4.1 (a) Crystal structure of the $A_2Mo_3O_8$ compounds where A = Mn, Fe, Co, Ni, Zn. A(T) and A(O) represent ions in trigonally-distorted tetrahedral and octahedral environments, respectively. (b) Schematic view of the Mo trimer. (c-e) Absorption spectra of $Zn_2Mo_3O_8$, $FeZnMo_3O_8$, and $Fe_2Mo_3O_8$ measured at room temperature. (f) A Tauc plot reveals the direct band gap of $Zn_2Mo_3O_8$ and the Fe substituted analogs. (g) Band gap schematic showing the impact of two different types of T and O-site substitution. The upper and lower trend lines correspond to the $(Fe,Zn)_2Mo_3O_8$ series and the $A_2Mo_3O_8$ (A = Fe, Mn, Ni) materials, respectively. (h,i) Calculated optical conductivity of the $A_2Mo_3O_8$ materials. 143

4.2 (a, d) Tauc plot of $(\alpha \cdot E)^2$ vs. energy for $Fe_2Mo_3O_8$ and a plot of band gap vs. temperature with a fit to the Varshni model. (b, e) Close-up view of the Fe^{2+} d-to-d on-site excitation on the tetrahedral site showing the fine structure that develops due to spin-orbit coupling below the 61 K magnetic ordering transition. (c, f) Close-up view of the Fe^{2+} d-to-d on-site excitation on the octahedral site and oscillator strength vs. temperature along with a fit to a modified vibronic coupling model [353–355]. 144

4.3 (a,b) Absorption spectra of $Ni_2Mo_3O_8$ and $Mn_2Mo_3O_8$ single crystals in the ab-plane at room temperature. (c) A Tauc plot is used to extract the direct band gap of these materials. 146

4.4 The density of states (DOS) for $A_2Mo_3O_8$ (A = Fe and Zn): (a) total DOS; (b-g) atom- and orbital-projected DOS. The (T) and (O) symbols refer to trigonally-distorted tetrahedral and octahedral environments. The vertical solid lines are placed at zero chemical potential. The schematic insets of gray tetrahedra/octahedra are guides to the eye pointing the reader to the electronic states of the transition metal ions in the corresponding environment. (h, i) Orbital projected spectral functions for $Fe_2Mo_3O_8$ and $FeZnMo_3O_8$ (blue - $e(1)$ tetrahedra; green - a_1 and $e(2)$ octahedra; red - a_1, $e(2)$ tetrahedra and $e(1)$ octahedra). 148

4.5 Atom- and orbital-projected density of states (DOS) together with a schematic view of the orbital occupation and character for $A_2Mo_3O_8$ (A = Mn, Fe, Co, and Zn). Each panel shows a schematic view of the orbital occupation (left side) and DOS (right side). Panels (a, c, e, g) refer to ions in trigonally-distorted tetrahedral environments (A(T)), whereas panels (b, d, f, h) refer to ions in trigonally-distorted octahedral environments (A(O)). 150

4.6 Diagram of d-orbital splitting from free ion states to octahedral + tetrahedral symmetries to C_{3v} local symmetry for the distorted octahedral and tetrahedral sites in $Fe_2Mo_3O_8$. States of e and a_1 symmetry are revealed in both the trigonally-distorted octahedra and tetrahedra. For clarity, we label the degenerate $d_{x^2-y^2}$ and d_{xy} set of orbitals as $e(1)$ whereas the doubly degenerate d_{xz} and d_{yz} set are labeled as $e(2)$. The d_{z^2} orbital always transforms as a_1. Note that the order of the e symmetry orbitals is swapped on the distorted octahedral and tetrahedral sites, and the a_1 symmetry orbital is always associated with the $e(2)$ pair. 151

4.7 Atom projected density of states for $Fe_2Mo_3O_8$, computed using the self-consistent hybridization (red curve labeled "hybridization-ON") and the manually reduced hybridization in the energy region of the Kondo-like peak (green curve labeled "hybridization-OFF"), as explained in the text. Panels (a), (b), and (c) show the atom projected density of states for Fe d, Mo d, and one of the inequivalent O p atoms in the unit cell. 152

4.8 Temperature-dependent atom projected density of states for $Fe_2Mo_3O_8$. Panels (a), (b), and (c) show the atom projected density of states for Fe d, Mo d, and one of the inequivalent O p atoms in the unit cell. . 153

4.9 Density of states for the materials of interest in this work. Panels (a) and (e) show the density of states per unit cell. Panels (b-d) and (f-h) show the density of states per A, Mo, and O atoms. Only $Fe_2Mo_3O_8$ has a strong, sharp resonance near the Fermi energy. 155

5.1 **Illustrating symmetry considerations for nonreciprocity in Ni_3TeO_6.** (a) Full field absorption difference spectra of Ni_3TeO_6 as a function of energy for the (+**k**, +**H**) and (+**k**, -**H**) configurations in the toroidal measurement geometry. For illustration purposes, we employ **H** = 60 T. Nonreciprocal directional dichroism is shown in green. Here, $\Delta\alpha_{NDD}$(+**k**, ±**H**) = $\Delta\alpha$(+**k**, +**H**) - $\Delta\alpha$(+**k**, -**H**). Experimentally, it is common to reverse the magnetic field direction as we have done here. Nonreciprocity can also be defined in terms of counter-propagating beams, $\Delta\alpha_{NDD}$(±**k**, +**H**), as shown in Fig. 2. (b) Full-field absorption difference spectra in the (+**k**, +**H**) and (-**k**, -**H**) configurations. Notice that they are the same. α_{NDD}(±**k**, ±**H**) = $\Delta\alpha$(+**k**, +**H**) - $\Delta\alpha$(-**k**, -**H**) (also shown in green) vanishes when both light propagation and magnetic field direction are switched simultaneously. The absolute absorption spectrum is shown at the bottom of each panel to provide context. Note that we used cubic term symbols here ($^3A_{2g}$, $^3T_{2g}$, ^1E_g, $^3T_{1g}$, $^1T_{2g}$) to denote Ni^{2+} atomic multiplets because the deviation from cubic symmetry by trigonal distortion at the Ni sites is small (≈0.1 eV in terms of crystal fields). 159

5.2 **Nonreciprocity of Ni_3TeO_6 in the three different measurement configurations.** Summary of the three different measurement configurations of interest in this work: (a) toroidal ($\mathbf{k} \perp \mathbf{H} \perp$ polarization, (b) magnetochiral ($\mathbf{k} \parallel \mathbf{H} \parallel$ chirality), and (c) transverse magnetochiral ($\mathbf{k} \parallel \mathbf{H} \perp$ chirality). Nonreciprocal directional dichroism spectra of Ni_3TeO_6 at 60 T in the toroidal (d), magnetochiral (e), and transverse magnetochiral (f) configurations, respectively. These spectra were measured in the Voigt (d) and Faraday (e, f) geometries. The nonreciprocal responses in panels (b, c) are reproduced from Ref. 250. The linear absorption spectrum of Ni_3TeO_6 at 4.2 K is shown below each nonreciprocal panel for comparison. The polarization directions and on-site Ni d-to-d excitations are labeled. 160

5.3 **Nonreciprocity in the toroidal geometry.** (a) Nonreciprocal directional dichroism of Ni_3TeO_6 in the toroidal configuration measured between 0 and 60 T at 4.0 K. The inset is the integration of the indicated feature in the dashed box over an appropriate energy window. No hysteresis is observed. (b) Simulated nonreciprocal directional dichroism of Ni_3TeO_6 in the toroidal configuration. The inset shows a comparison of the calculated and measured results at 60 T. The intensity is normalized to the maximum of $\Delta\alpha_{NDD}$. (c) Close-up view of $\Delta\alpha_{\mathrm{NDD}}$ at 3.1 and 60 T compared with the linear absorption spectrum. (d) Close-up view of $\Delta\alpha_{\mathrm{NDD}}$ as a function of field between 0 and 60 T. The complete list of magnetic fields in panels (a) and (d) is: 0, 3.1, 5.5, 7.2, 10.7, 13.8, 15.8, 17.9, 20.3, 23.1, 26.1, 29.6, 33.3, 37.5, 42.1, 47.0, 52.1, 57.1, 60.2 T. 163

5.4 (a,c,e,g) Full-field absorption difference spectra as a function of energy for several different configurations as indicated. (b,d,f,h) Nonreciprocal directional dichroism is shown in green for four different configurations: $\Delta\alpha_{NDD}(+\mathbf{k}, \pm\mathbf{H})$, $\Delta\alpha_{NDD}(\pm\mathbf{k}, +\mathbf{H})$, $\Delta\alpha_{NDD}(-\mathbf{k}, \pm\mathbf{H})$, and $\Delta\alpha_{NDD}(\pm\mathbf{k}, -\mathrm{H})$, where for instance $\Delta\alpha_{NDD}(\pm\mathbf{k}, +\mathbf{H}) = \Delta\alpha(+\mathbf{k}, +\mathbf{H}) - \Delta\alpha(-\mathbf{k}, +\mathbf{H})$. These curves employ $\mathbf{H} = 60$ T. The absolute absorption spectrum is included to provide context. 165

5.5 (a,c) Full-field absorption difference spectra in various configurations. Notice that they are the same. (b,d) α_{NDD} (shown in green) vanishes when both light propagation and magnetic field direction are switched simultaneously. This is because time-reversal symmetry is not broken when the direction of both $\mathbf{k}$ and $\mathbf{H}$ are changed together. A magnetic field of 60 T was employed here. The absolute absorption spectrum is shown at the bottom of each panel to provide context. 166

5.6 **Nonreciprocity at telecom wavelengths.** Close-up view of the nonreciprocal directional dichroism in Ni_3TeO_6 on a percentage basis as a function of wavelength in the toroidal configuration at 4.0 K. $\Delta\alpha_{\mathrm{NDD}}$ is shown at 3.1 and 60 T. The absolute absorption spectrum is included for comparison. Various commercial telecom windows are summarized on the upper axes. The U-band (1625-1675 nm) is not shown. 169

6.1 (a, b) Crystal structure of $Co_4Nb_2O_9$ with c-axis and ab-plane views [256, 260, 268]. Blue, red, and green represent Co, O, and Nb/Ta centers, respectively. The octahedra are drawn only for the magnetic ions. (c) A simplified view of the planar Co^{2+} layer (blue) reveals a honeycomb-like structure. Only the Co^{2+} ion is shown. (d) This schematic illustrates both the planar (blue) and buckled (cyan) layers. There are two relevant interlayer interactions, which are shown with different colors (λ_2 and λ_3). Again, only the Co^2 ions are displayed here. (e) Calculated phonon frequencies are summarized for the E_u and A_{2u} modes. (f) Polarized infrared absorption spectra of $Co_4Nb_2O_9$ at room temperature. The response of $Co_4Ta_2O_9$ is similar and shown in the Supplementary information. The mode assignments are identical. 172

6.2 (a, b) Absorption spectrum of $Co_4Nb_2O_9$ as a function of temperature and peak position vs. temperature for the E_u symmetry shearing mode near 150 cm^{-1}. (c, d) Similar results for $Co_4Ta_2O_9$. The spectra in (a, c) are shifted for clarity, and the blue dashed lines in (b, d) are a simulated phonon response as discussed in the text. T_N is indicated by vertical gray lines. Phonon softening across T_N is readily apparent. (e) Calculated displacement pattern of the E_u symmetry phonon viewed along different directions. The shaded slabs in the top image indicate how the planar and buckled layers move against each other in a shearing motion. 174

Chapter 1

Introduction

Multiferroics are multi-functional materials that exhibit multiple ferroic orders simultaneously [1]. A ferroic order is a spontaneous alignment of electric polarization, magnetic moment, or strain, and toroidal moment. When two or more of these ferroic orders coexist and are coupled with each other, multiferroicity is achieved, which can be categorized by the space-inversion and time-reversal symmetries. Magnetoelectric multiferroics, therefore, break both space-inversion and time-reversal symmetries with the coexistence of ferroelectricity and magnetism. These broken symmetries play an important role in determining properties. Magnetoelectric multiferroics can be categorized into Type-I and Type-II by the mechanisms of ferroic ordering surrounding ferroelectricity and magnetism. Type-I systems host separate origins for ferroelectric and magnetic orderings whereas Type-II materials display magnetism-induced ferroelectricity. The former exhibit higher ordering temperature whereas the latter displays stronger magnetoelectric coupling strength.

Magnetoelectric multiferroics and the cross-coupling of electronic and magnetic properties are the main subjects of this dissertation. $BiFeO_3$ is a well-known room-temperature multiferroic, which displays magnetoelectric coupling with ferroelectricity of $\sim$100 $\mu C/cm^2$ along [111] and hosts both photovoltaic and photo-capacitance

applications [2–4]. As a Type-I multiferroic, the magnetoelectric coupling is weak due to the fact that the electric and magnetic ordering temperatures are different [5]. Type-II multiferroics like $MnWO_4$, $CoCr_2O_4$, $LiCu_2O_2$ have stronger magnetoelectric couplings, but low ordering temperatures [6–8]. In a search for a stronger magnetoelectric coupling, heavy metal centers are highly sought after due to stronger spin-orbit coupling, which enhances the multiferroicity [9,10]. In general, the energy of spin-orbit coupling is described as

$$E_{so} = \frac{Z^4}{2(137)^2 n^3} \frac{j(j+1) - l(l+1)}{s(s+1)2l(l+1/2)(l+1)}. \tag{1.1}$$

Here, Z is the atomic number, n, j, l, and s, are quantum numbers. Notice that $E \sim Z^4$. The heavier element introduces larger spin-orbit coupling. This leads to important consequences in quantum materials, such as the spin-orbit-entangled ground state of $J_{eff} = 1/2$ found in iridates [11]. Mixed metal systems can incorporate transition metals and heavy metals as well. Thus, the best qualities of both $3d$ transition metals and heavy metal centers are combined. Furthermore, mixed metal oxides with 3-, 4-, and $5d$ centers offer a perfect platform to perform structure-property relation analysis. As summarized in Table 1.1, $3d$-containing materials are well-known for strong electron correlations, narrow bandwidths, site- and orbital-selective states, and robust magnetism whereas 4- and $5d$ systems are recognized for a strong spin–orbit coupling, increased hybridization, extended orbitals, and a tendency toward dimerization [12–16]. The tendencies of $3d$-containing vs $4d/5d$-containing materials are tabulated in Table 1.1. Examples include interpenetrating sublattices with independent spin dynamics and ground states in Sr_2CoOsO_6 [17,18], self-healing photoelectrode materials like $CuRhO_2$ [19], the covalency-driven collapse of spin-orbit coupling in $Ba_5CuIr_3O_{12}$ [20], an ultra-high coercive field in Sr_3NiIrO_6 [21,22], spinels such as $CdCr_2O_4$ for unraveling trends in frustrated and two-sublattice magnetism

Table 1.1: Differences of transition metals and heavy metals.

	3d center	**4d/5d center**
Orbital character	Localized	Diffused
Electron-electron correlation	Strong $U = 5$ - 8 eV	Weak $U \approx 0.5$ eV
Spin-orbit coupling	Weak $\lambda \approx 0.02$ eV	Strong $\lambda \approx 0.5$ eV
Magnetism	Robust	Fragile
Tendency towards dimerization	No	Yes
Tendency towards band inversion	No	Yes

with spin-phonon coupling [23–25], surprising spin entropy effects across the magnetic quantum phase transition in $CoNb_2O_6$ [26], Sm_2CoIrO_6 with enhanced spin-phonon-electronic coupling [27]. Combining these qualities in mixed metal materials lead to a variety of unexpected properties.

We can tune the properties of quantum materials by chemical substitution and use structure-property relationships to examine how the interactions of spin, orbital, charge, and lattice degrees of freedom are affected. These substitutions can lead to changes in hybridization, magnetic properties, and optical properties. Furthermore, chemical substitution can affect the way in which different ferroic order parameters interact with each other. For instance, the substitution of one element for another can introduce different quantum states (L and S) which can affect the magnetic, electric, and optical properties of the material. As an example, the $A_2Mo_3O_8$ (A = Mn, Fe, Co, Ni, and Zn) system is a family of complex oxides that host strong magnetoelectric coupling and various magnetic structures [28–30]. Here, there are two A-sites that metal ions can occupy, an octahedral and a tetrahedral environment. By controlling the substitution of A-site with different transition metals, the magnetic structure can be controlled [31].

To recapitulate, one of the key concepts in multiferroics is symmetry. There are several symmetries to discuss, which are rotational, mirror, space-inversion, and time-reversal symmetries. Rotational symmetry is described by C_n, where the object rotates on an axis that returns back to the original geometry. Mirror symmetry is a translation through the plane whereas space-inversion is a translation, going through a point. Time-reversal symmetry is reversing time ($t \rightarrow -t$), and it is incorporated into materials by magnetism or magnetic field. Using group theory, the properties of materials can be explained and predicted. Taking an example that will be of interest in this work, $Co_2B_4O_9$ (B = Nb, Ta) has a non-polar trigonal space group

of $P\bar{3}c1$. Experimental values of ferroelectricity and the magnetoelectric mechanism are explained by analyzing the C_3 local symmetry of magnetic Co^{2+} ion sites [32]. One of the interesting symmetries is chirality, which refers to the property of an object or a system that is not superimposable onto its mirror image, i.e. broken mirror planes. In chemistry, chirality has important implications. For example, thalidomide is a medication for a number of diseases. The desired medication effect is exhibited by the (R)-enantiomer, whereas the (S)-enantiomer possesses toxicity, causing birth defects [33]. In multiferroic materials, chirality can arise due to the arrangement of atoms within the crystal lattice. Chiral multiferroics are of great interest because they exhibit strong magnetoelectric coupling, which means that their magnetic and electric properties are strongly linked [9, 34–36]. Chirality also affects the way in which domains of different ferroic order parameters interact with each other, which can have implications for the properties and behavior of multiferroics. Chirality also impacts the magnetic structure. Dzyaloshinskii–Moriya interaction (antisymmetric exchange interaction) can induce a noncollinear magnetic system including helical spin structure, skyrmion, spin spirals, and canted spins [37]. Figure 1.1 displays an example of the magnetic chirality in $Cu_3Nb_2O_8$ [35]. In the paramagnetic state (above the magnetic ordering temperature, T_N), the crystal structure is centrosymmetric with a space group of $P\bar{1}$. Below the Néel temperature, a coplanar helicoidal magnetic structure is observed. This chirality in the magnetism leads to the development of polarization perpendicular to the plane of spin rotations, thus achieving magnetoelectric coupling.

Symmetries and properties can be controlled by external stimuli. In multiferroic materials, symmetry-breaking can cause the coupling of electric and magnetic properties. For example, a magnetic field can induce an electric polarization in a material that is normally not ferroelectric, or an electric field can induce a magnetic

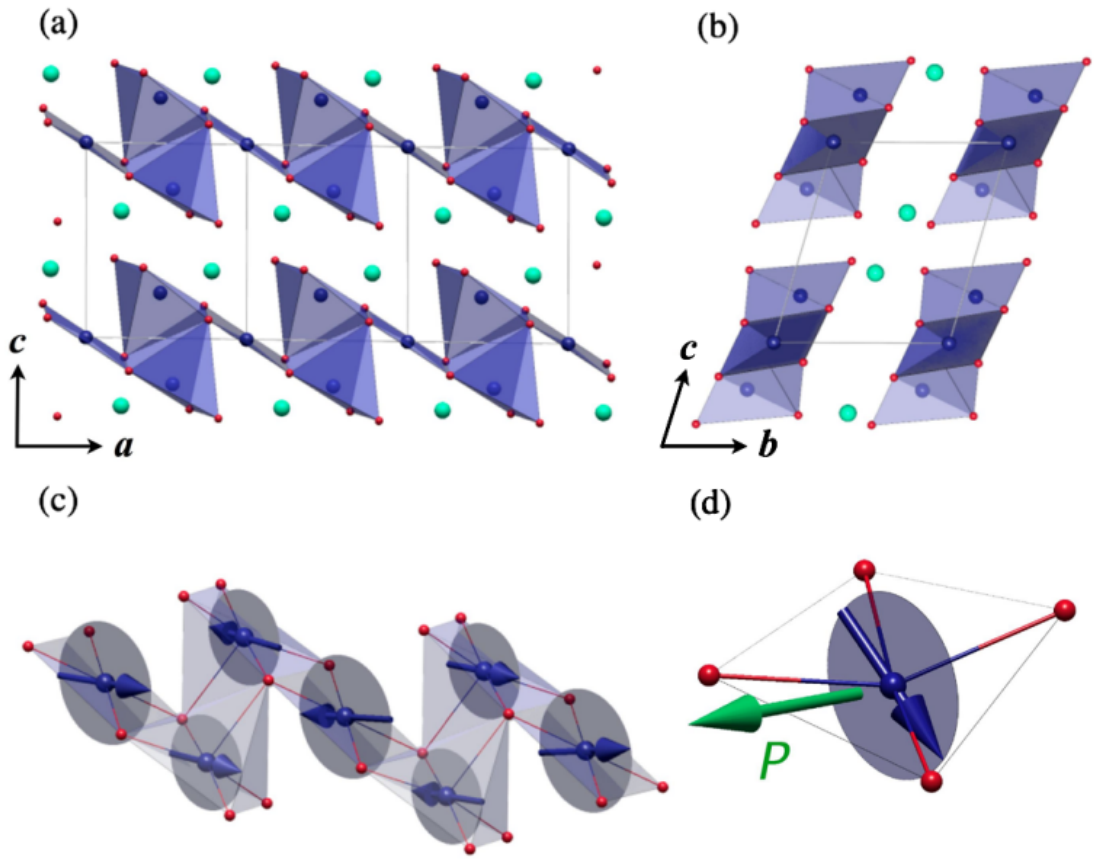


Figure 1.1: (a,b) Crystal structure of $Cu_3Nb_2O_8$ in b-axis and a-axis views are displayed, respectively. (c) Magnetic vectors imposed on the crystal structure are shown to demonstrate the spin rotations. (d) A diagram of the polarization that is perpendicular to the plane of the spin rotation is shown [35].

moment in a material that is normally not ferromagnetic. The low symmetry due to chirality can lead to interesting physics such as phase transitions, magneto-optical activities, second harmonic generation, photogalvanic effects, and Hall-effect transport properties [38]. One example is nonreciprocal directional dichroism. It is one-way transparency that emerges from symmetry-breaking. An example of nonreciprocal directional dichroism in $Sr_2CoSi_2O_7$ is shown in Fig. 1.2 [39].

Overall, chirality, symmetry-breaking, and chemical substitution can all play important roles in the behavior of multiferroic materials, affecting the way in which different ferroic order parameters interact with each other and the properties and behavior. Understanding these effects is important for the design and development of systems with bespoke properties for a range of applications.

1.1 Spectroscopic methods for complex oxides

Many multiferroics are complex oxides. They exhibit various quantum phase transitions when tuned by external stimuli such as applied magnetic/electric field, pressure, light, and chemical substitution [Fig. 1.3] [47]. Unlike traditional transitions, thermal fluctuation should be minimized to reveal the quantum phases, in which the ideal temperature is at zero. Then, the external parameter is used as a tuning parameter, 'g', to drive the quantum transitions. Quantum transitions result from the competing ground states due to quantum fluctuations in complex oxides. Quantum phases in complex materials often host an incredible variety of physical phenomena, such as insulator-to-metal transitions, colossal magnetoresistance, and high-temperature superconductivity [48–50]. Multiferroicity is among them. Examples include the chiral magnetic structure of $Cr_{1/3}TaS_2$ [Fig. 1.4(a,b)] [45, 51] and magnetic skyrmion and topological solitons in Cu_2OSeO_3 [Fig. 1.4(c)] [46, 52, 53]. As shown in Fig. 1.4, $Cr_{1/3}TaS_2$ hosts a complicated phase diagram with chiral

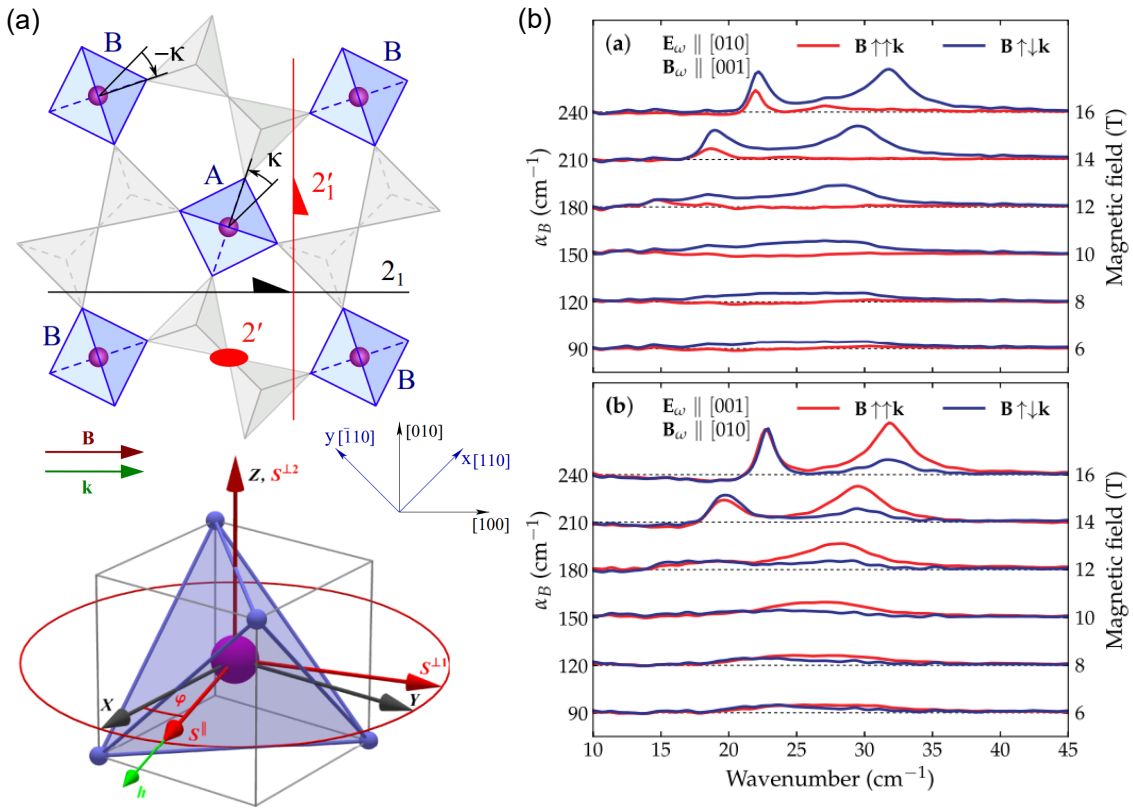


Figure 1.2: (a) The crystal structure of $Sr_2CoSi_2O_7$ is displayed. The κ and $-\kappa$ represent the rotation of the tetrahedron where the chirality arises. (b) Absorption spectra as a function of the magnetic field are displayed with different polarization. Nonreciprocal directional dichroism is observed by the difference in the intensity of peaks, which is achieved by changing the light propagation k [39].

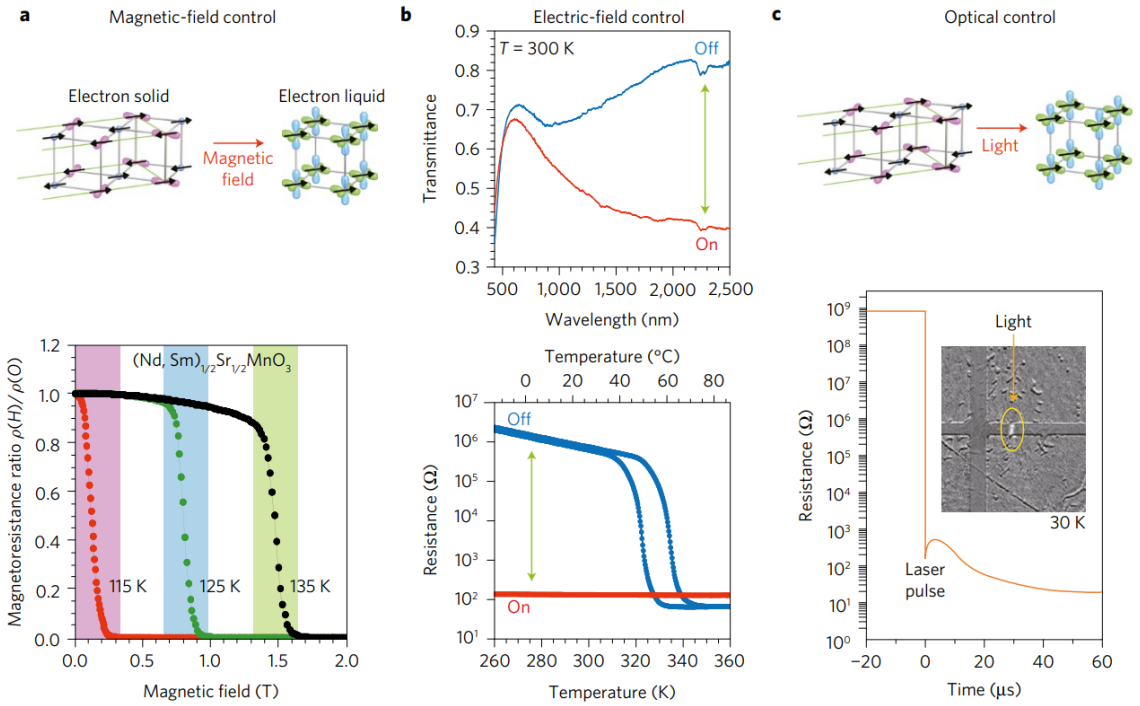


Figure 1.3: (a) Colossal magnetoresistance in the perovskite manganite. The upper panel schematically represents the magnetic-field-induced melting of the charge–orbital ordered state as the microscopic origin of colossal magnetoresistance [40, 41]. (b) Electric-double-layer gating-induced insulator–metal transition in VO_2 thin film. The upper panel shows the concurrent switching of the near-infrared photo-absorption spectrum, representing radiation device functionality [41–43]. (c) Photo-melting of the charge-orbital ordered state in manganite [41, 44].

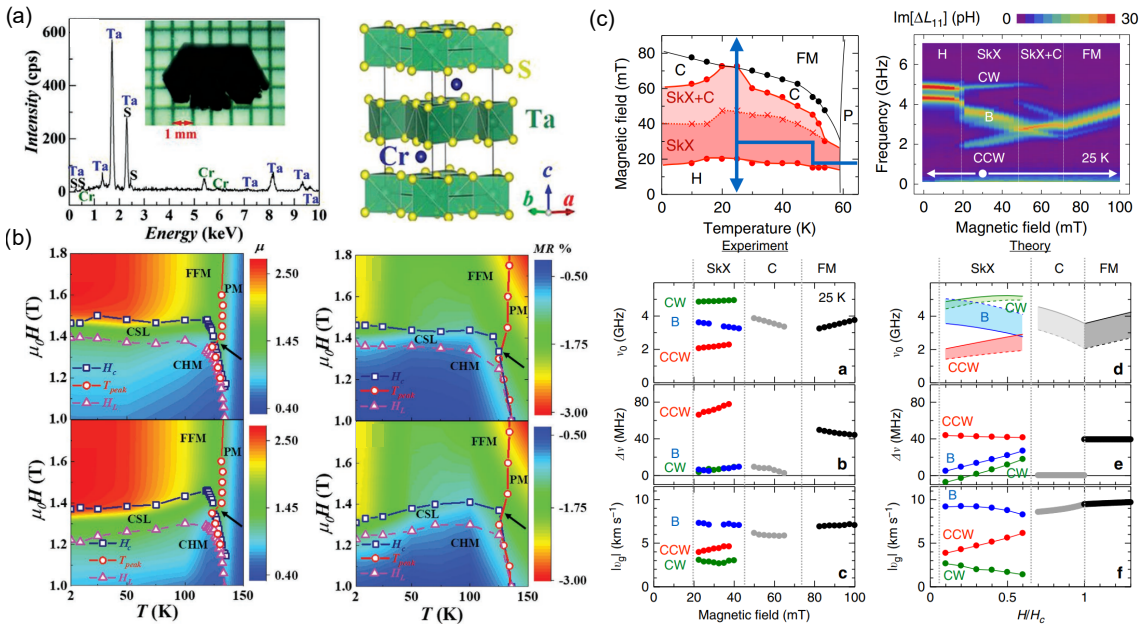


Figure 1.4: (a) Energy-dispersive X-ray spectrum of $Cr_{1/3}TaS_2$ is shown to verify the chemical composition. The inset is the picture of the crystal [45]. (b) Magnetic phase diagrams are shown here with magnetization and magnetoresistance measurements [45]. (c) The magnetic phase diagram of Cu_2OSeO_3 is shown here with magnetization measurements on the top left. SkX, C, H, FM, and P represent the skyrmion lattice, conical, helical, ferromagnetic, and paramagnetic states, respectively. To the top right, the magnetic resonance spectra ΔL_{11} at 25 K is corresponding to the magnetization [46]. The bottom two plots are also from the magnetic resonance spectra with the combination of theoretical calculations [46].

helimagnet, fully polarized, and soliton phases. Figure 1.4(c) summarizes the magnetic phase diagram of Cu_2OSeO_3, another example of a chiral multiferroic. The space group of Cu_2OSeO_3 is $P2_13$. Similar to $Cr_{1/3}TaS_2$, Cu_2OSeO_3 also exhibits complex magnetic phases. It has a Néel temperature of $\sim$ 58 K with a helical magnetic structure. With the application of a magnetic field, skyrmion, conical, and ferromagnetic phases are observed [46, 54]. Furthermore, the room-temperature skyrmion phase can be achieved with pressure [53]. Clearly, complex oxide materials host a variety of competing and tunable ground states and phase transitions. The ability to probe the interplay of spin, orbital, charge, and lattice degrees of freedom, and to drive these quantum phases with external stimuli is absolutely essential to explore quantum phases and properties of complex oxides.

Optical spectroscopy is a microscopic technique. Hence, these techniques are highly suitable to dive deeper into underlying physics, unlike bulk measurements for conductivity, heat capacity, magnetization, and resistance. Our primary interest is in far-infrared to ultraviolet regions since the energy range of elementary excitations, such as phonon, crystal field, and charge transfer appear in those regions [Fig. 1.5].

In the low-frequency range, infrared spectroscopy can provide measurements of vibrational modes (phonons), Drude response, low-lying electronic excitations, and magnetic excitations (magnons). These features play a major role in many material properties including magnetic anisotropy [56], thermal, and electrical conductivities [57]. Also, Raman spectroscopy provides complementary techniques to infrared-active phonons and reveals magnetic excitations as well. Using a group theory and symmetry analysis, phonon behavior can be used to probe the local structure and symmetry [58]. Because phonons are the fundamental excitations of the lattice, splitting or disappearance of phonon peaks can reveal structural phase transition or distortion. One example is the onset of ferroelectric transition, which can be

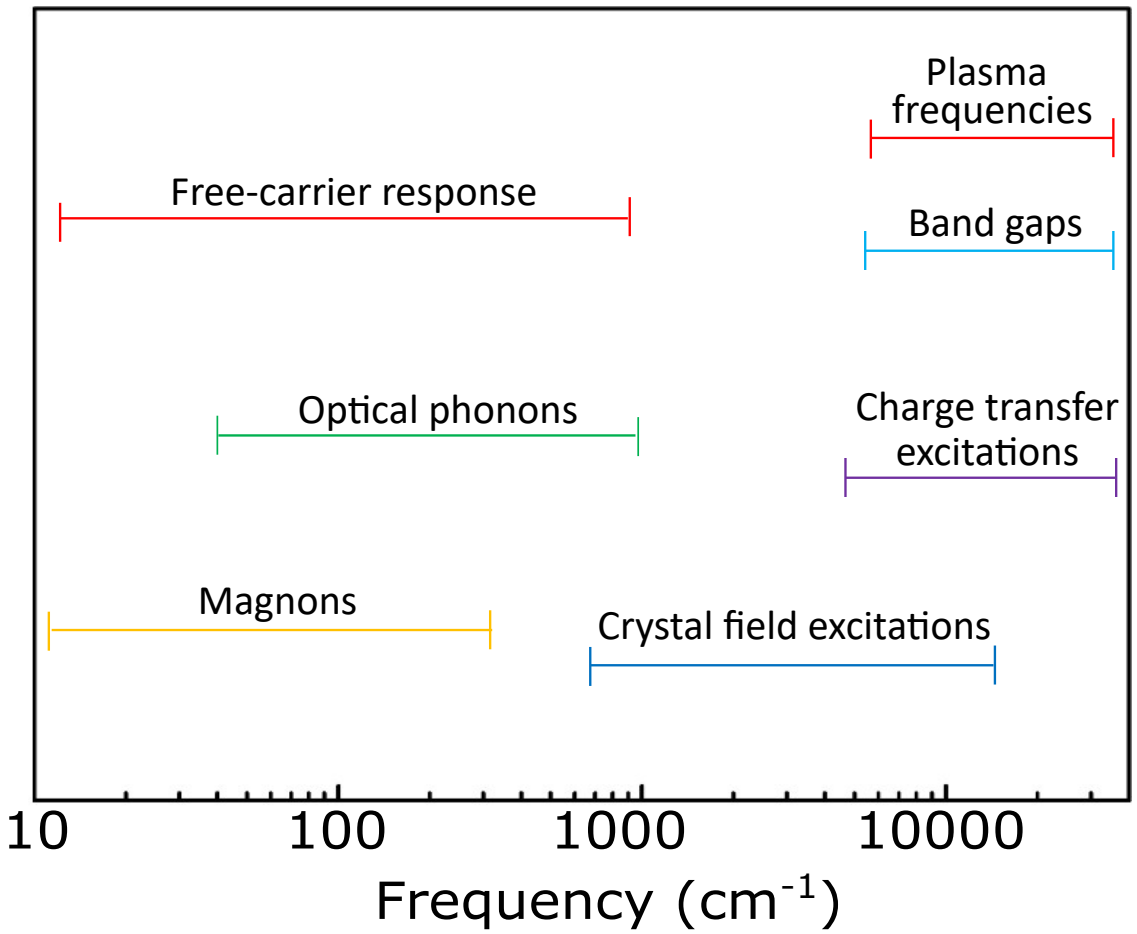


Figure 1.5: Schematic showing optical processes in solids, with an indication of the frequencies where these processes typically may be studied [55].

observed by tracking the soft mode (or modes), revealing the displacive nature or order-disorder of a ferroelectric phase transition [59]. Another example is the charge density wave transitions, which must be accompanied by structural distortion. Figure 1.6 displays Raman spectra of 2H-TaS_2 as a function of temperature [60]. New phonon structures can be observed across the transition temperature at 100 K, which is associated with the charge density wave transition [Fig. 1.6 (a,b)]. Moreover, lattice can couple with magnetism. For example, the lattice can be sensitive to any number of spin transitions, such as a spin-flop transition, Néel transition, or spins aligning towards the fully saturated magnetic state [61, 62]. Figure 1.7 shows an example of spin-phonon coupling in pyrochlore $Y_2Ir_2O_7$. Figure 1.7(c) displays three phonon modes as a function of temperature. As the temperature decreases across the Néel temperature, those three phonon frequencies soften abruptly, signifying spin-phonon coupling [Fig. 1.7(d)]. The softening of the phonon frequency is related to the weakening of the bond strength and a wider bond angle. The O-Ir-O bond angle is also examined as a function of isotropic exchange and antisymmetric exchange interactions, which concludes that spin-phonon coupling is mediated by the Dzyaloshinskii-Moriya interaction. This is the first report of spin-phonon coupling mediated by the Dzyaloshinskii-Moriya interaction [63]. Lastly, an example of low-lying magnetic excitation in $FeZnMo_3O_8$ is shown in Fig. 1.8. The excitation is observed in the terahertz range [Fig. 1.8(a,b,c)]. The emergence of the peak below the Néel temperature indicates that this is a magnetic excitation. Furthermore, this excitation is used to explore the nonreciprocal directional dichroism effect. By applying the magnetic field and switching the light propagation direction, the intensity of the magnetic excitation is different [Fig. 1.8(d,e,f)]. At 8 T, one-way transparency is almost achieved [64].

In the higher frequency range, local and charge-transfer excitations dominate the

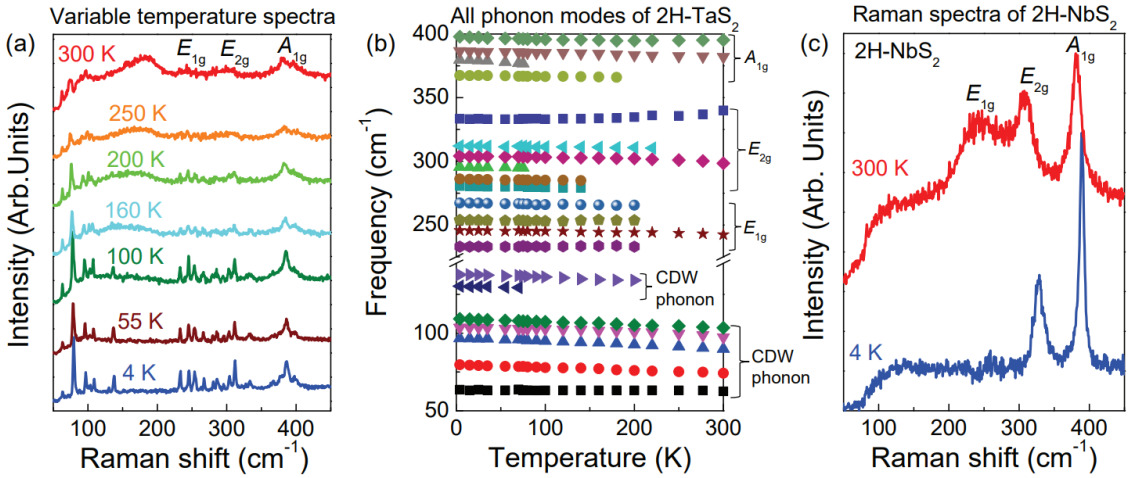


Figure 1.6: Raman spectra are displayed as a function of temperature. (a) stacked spectra are shown to reveal new phonon peaks across the charge-density-wave transition. (b) Peaks are tracked as a function of temperature and phonon assignments. (c) Raman spectra of 2H-NbS_2 at 300 and 4 K with peak assignments for comparison [60].

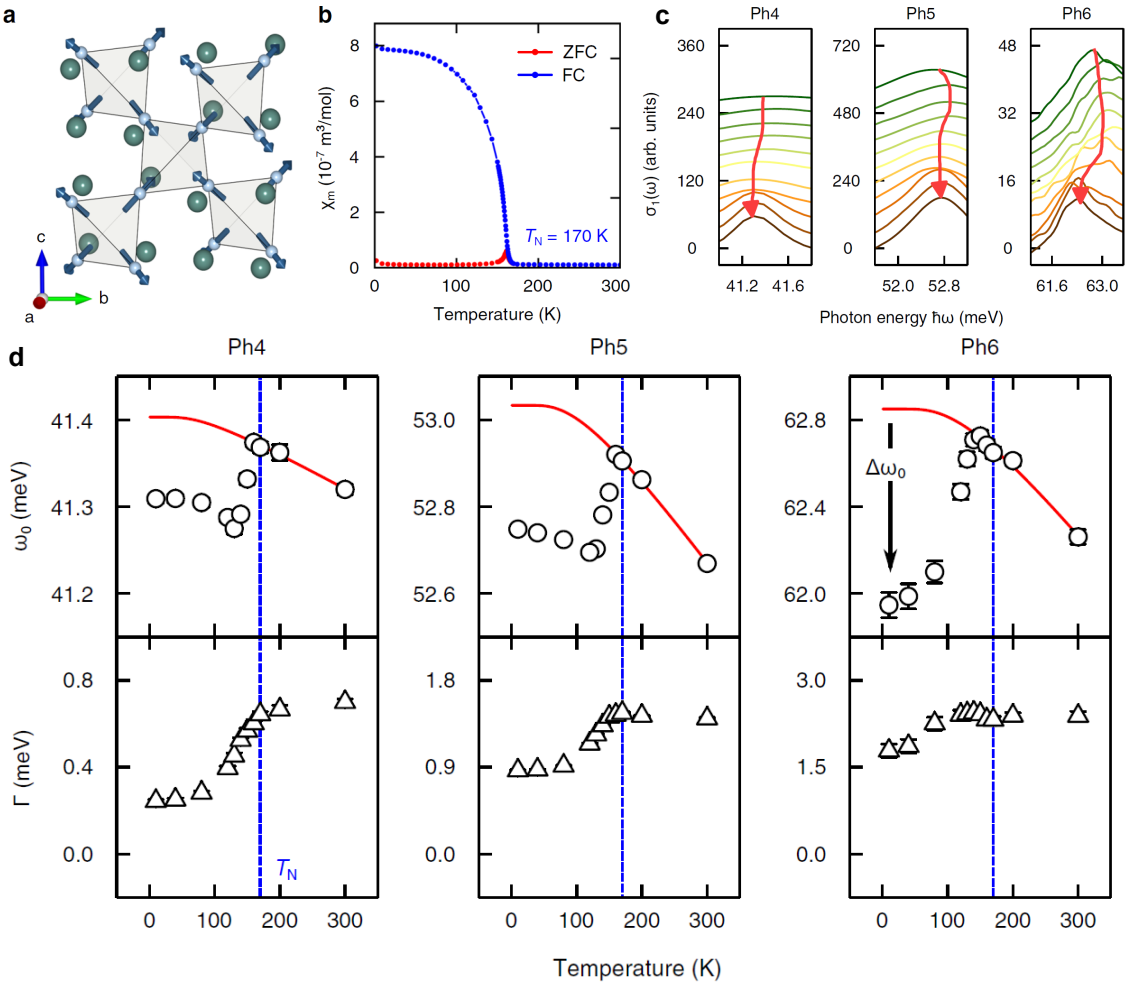


Figure 1.7: (a) Crystal structure of $Y_2Ir_2O_7$ is shown. (b) susceptibility as a function of temperature is displayed. The T_N is at 170 K. (c) $\sigma_1(\omega)$ spectra are shown, which are fitted using the Fano-Lorentz model to get infrared-active phonons. Phonon frequencies of Ph4, Ph5, and Ph6 have shifted abruptly across the T_N, signaling for spin-phonon coupling. (d) Phonon frequencies and full-width half maximums of Ph4, Ph5, and Ph6 as a function of temperature are displayed to quantify spin-phonon coupling for each phonon mode [63].

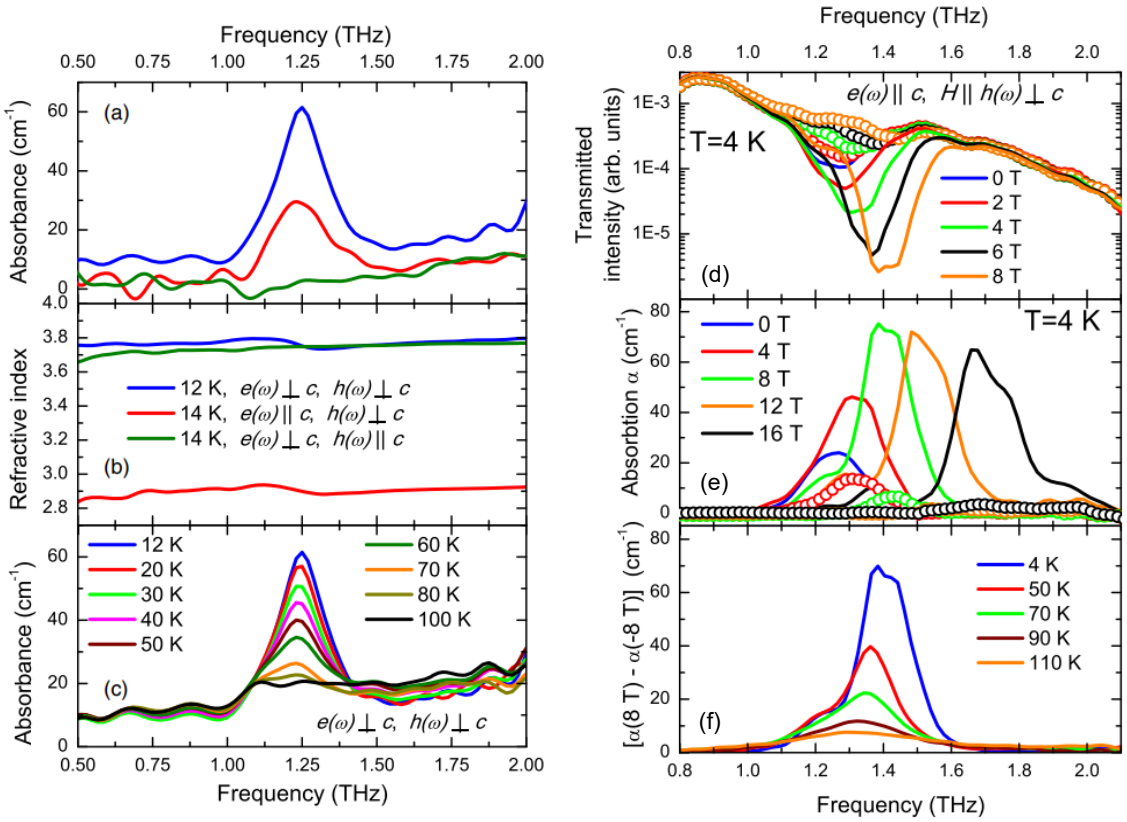


Figure 1.8: (a) and (b) Absorbance and refractive index spectra with different polarization at around 12 and 14 K are shown. (c) Absorbance spectra as a function of temperature are displayed. The emergence of the peak below the T_{N} proves that this peak is a magnetic excitation. (d) Transmittance and absorption spectra as a function of the magnetic field at 4 K are displayed. The open circles and solid lines represent the light propagation direction. The difference in intensity between the open circle and the solid line is due to nonreciprocal directional dichroism. (f) absorption difference spectra as a function of temperature are shown. Nonreciprocal directional dichroism persists above the magnetic transition temperature [64].

absorption spectrum. For complex oxides, oxygen is a strong-field ligand with a -2 charge. A Tanabe-Sugano diagram can be utilized to assign d-to-d excitations using ligand field strength (Dq or Δ) and Racah parameters (A, B, and C). We also have to consider the number of electrons in the d-shell, the low/high ligand field, which will determine term symbols for excitations, high- or low-spin states, the ratio of excitations, and peak splittings. The point charge model is another semi-empirical approach [65, 66]. By fitting this semi-empirical model to the experimental data, both electronic and magnetic properties can be simulated [67]. Furthermore, these on-site excitations have a spin selection rule and LaPort selection rule, where $\Delta s = 0$ and $\Delta l = 1$, respectively. These rules can be broken by several ways including broken space-inversion symmetry, spin-orbit coupling, vibronic coupling, and orbital hybridization. Figure 1.9 presents examples of two models to assign local d-to-d excitations of Ni_3TeO_6 and $Fe_2Mo_3O_8$. As another example, Ni_3TeO_6 assigns on-site d-to-d excitation using the Tanabe-Sugano diagram [Fig. 1.9(a,b)]. The Dq (Δ) and B parameters were both 0.11 eV [68]. On the other hand, assignments of local excitations in $Fe_2Mo_3O_8$ are more challenging due to the combination of the tetrahedral sites [Fig. 1.9(c)] and octahedral sites [Fig. 1.9(d)]. They are determined by the point charge model. Figure 1.10 provides an example of how these two models can be compared [69]. Using the Tanabe-Sugano diagram, the crystal field of octahedrally coordinated Ni^{2+} ion in NiO is characterized with $Dq = 0.11$ eV and $B = 0.13$ eV. Using the Point-Charge model, crystal field parameters are also derived and calculated, which results in $B_4 = 0.0018$, $B_2 = 0.0043$, λ = -0.041, and n_{dd} = -0.012 eV. The B_4 parameter is the primary octahedral/tetrahedral parameter, which is related to Dq by $10Dq \approx 600 \cdot B_4$ [69]. B_2 is the trigonal distortion parameter and n is the molecular field parameter (due to magnetic ordering). Another common electronic excitation is the band gap, which is an excitation from the valence to the conduction

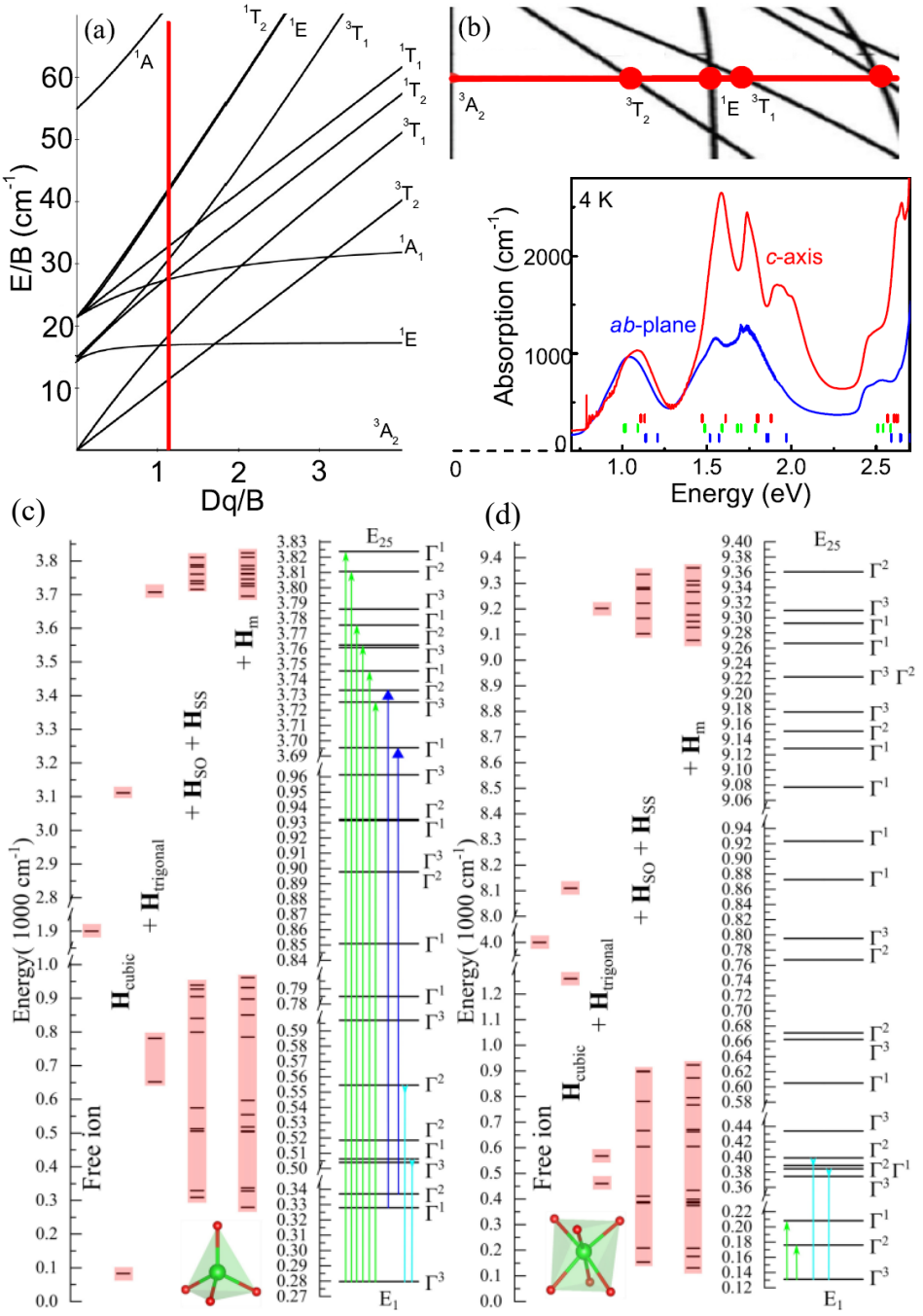


Figure 1.9: Two models to calculate local d-to-d excitations. (a,b) Tanabe-Sugano diagram is used to assign octahedrally coordinated Ni^{2+} excitations [68] in Ni_3TeO_6. (c,d) The Point-Charge model is used to assign excitations of octahedral and tetrahedral Fe^{2+} environment [29] in $Fe_2Mo_3O_8$. Parameters are Dq, A_2, A_4, λ, ρ, and H_m, which $\sim$ 303, -33.3, -339, 117, 1.1, and 18.2 cm^{-1} for the tetrahedral site and -685, -596, -332, -117, 1.1, and 13.6 cm^{-1} for the octahedral site were used [29].

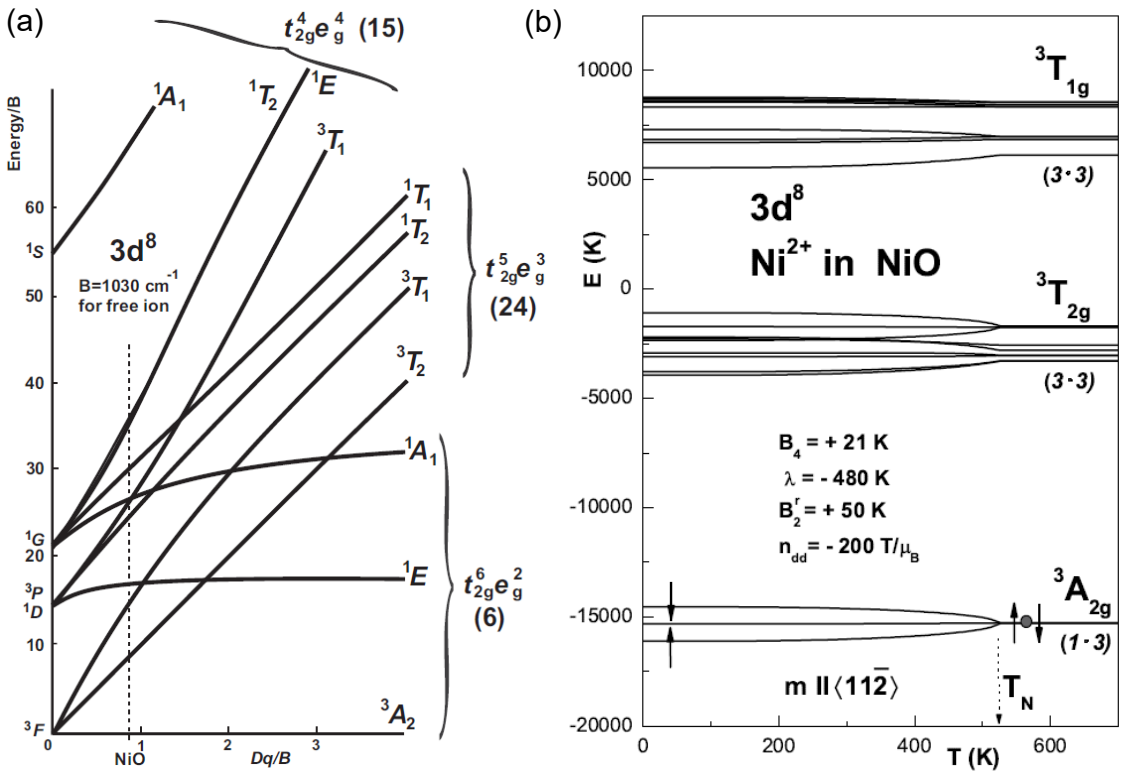


Figure 1.10: (a) Tanabe-Sugano diagram of Ni^{2+} ion in the NiO is shown with parameters. (b) Crystal field of Ni^{2+} is calculated using Point-Charge model with spin-orbit coupling (λ) and molecular field (n) [69].

band. This type of excitation is often charge transfer in nature. Microscopically, it is a transition between a fully occupied oxygen $2p$ orbital to a vacant metal $3d$ orbital in these materials. First-principles calculations, such as density of states provide insight into the electronic structure of material including band symmetry and band hybridization. These calculations are used to compare with experimental results [70, 71]. Furthermore, there are collective excitations such as excitons and magnon sidebands. They can also be revealed by optical spectroscopy. Exictons and magnon sidebands are typically observed on the leading edge of an electronic transition. The exchange coupling induces these excitations and is sensitive to changes in magnetism, resulting in useful probes for magnetic ordering transitions [71–74]. Figure 1.11 displays the magnetic field dependence of both excitons and magnons in $BiFeO_3$ and α-Fe_2O_3 [70, 71].

In this dissertation, we will explore the spectroscopic response of several quantum materials of contemporary interest under magnetic field. To focus our efforts, we concentrate on bimetallic oxides with both $3d$ and heavy metal centers. The main findings are summarized below [Table 1.2].

1.2 Main findings of this work

1.2.1 Band-Mott mixing hybridizes the gap in $Fe_2Mo_3O_8$

We combined optical spectroscopy and first principles electronic structure calculations to reveal the charge gap in the polar magnet $Fe_2Mo_3O_8$. Iron occupation on the octahedral site draws the gap strongly downward compared to the Zn parent compound, and subsequent occupation of the tetrahedral site creates a narrow resonance near the Fermi energy that draws the gap downward even further. This resonance is a many-body effect that emanates from a flat valence band in a Mott-like state due

Table 1.2: Scientific problems and important findings in this dissertation

Model Compound	Scientific Problem	Our Findings
$A_2Mo_3O_8$ (A = Fe, FeZn, Zn, Mn, Ni)	• Reveal the on-site d-to-d excitations and charge gap energies • Investigate structure-property relations of charge excitation	• Local d-to-d excitations assignments of Fe^{2+} octahedral and tetrahedral site as well as the charge transfer energies are determined • The lowering of band gap energies with Fe substitution and hybridization • Spin-charge coupling • Many-body resonance emanating from a Mott-like state, which is similar to Zhang-Rice singlet, is revealed in the tetrahedral Fe^{2+} ion
Ni_3TeO_6	• Investigate the nonreciprocal directional dichroism in the toroidal configuration • Reveal structure-property relations in nonreciprocity	• 1 eV d-to-d excitation exhibits toroidal characteristics whereas higher on-site local excitations indicate strong chiral characteristics • Antisymmetric behavior of phonon sidebands with respect to the directions of the light propagation or magnetic field in the toroidal geometry • Nonreciprocal directional dichroism spectra in the entire telecom wavelength range, where toroidal geometry displays the largest effect at almost 50 percent
$Co_4B_2O_9$ (B = Nb, Ta)	• Investigate the behavior of phonon across the T_N • Quantify spin-phonon coupling • Examine symmetry relations • Uncovering the origin of magnetoelectricity	• Spin-phonon coupling across T_N with the large coupling constants • Only inter-plane magnetic interactions in spin-phonon coupling • Competition between the ferromagnetic and antiferromagnetic exchange interaction • Spin-phonon coupling driving the magnetodielectric and magnetoelectric coupling
$MnPS_3$ and $CrPS_4$	• Revisit the temperature dependence of optical properties • Investigate magnetic properties using magnetic circular dichroism	• Spin-charge coupling in $MnPS_3$ • Huge magnetic circular dichroic signal in $CrPS_4$

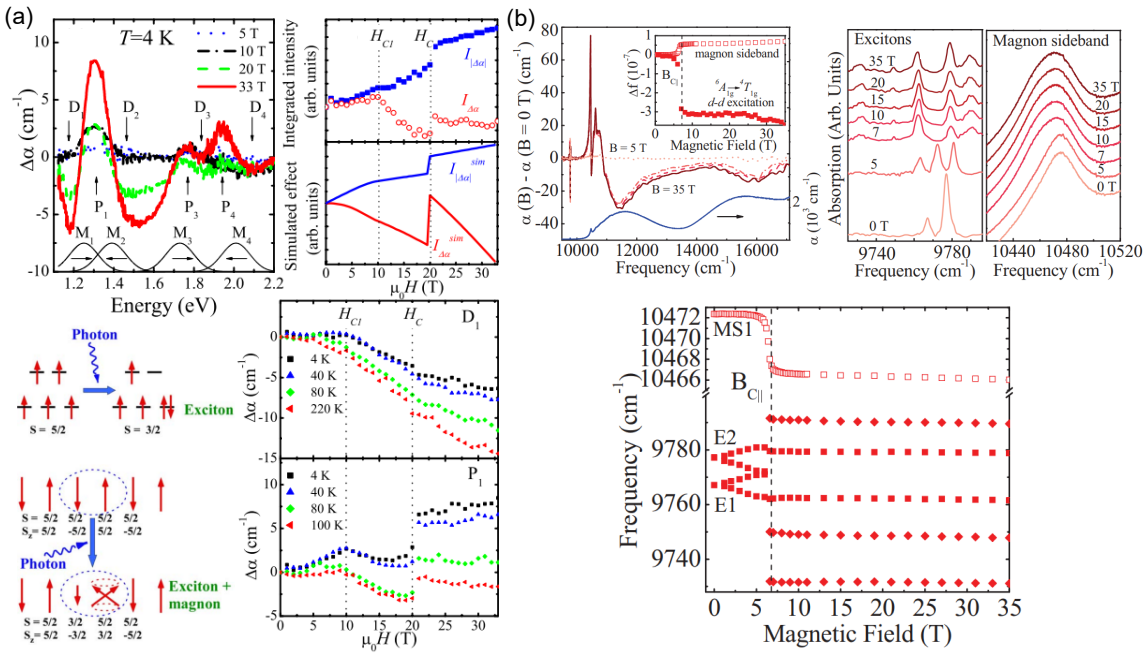


Figure 1.11: (a) $\Delta\alpha$(E,H) of $BiFeO_3$ for different magnetic fields at 4 K. Schematic illustration of exciton and magnon sidebands [70]. (b) $\Delta\alpha$ spectra of α-Fe_2O_3 at 4.2 K for the α-polarization and B $\parallel$ [111] at selected magnetic fields: 5, 10, 15, 35 T [71].

to screening of the local moment - similar to expectations for a Zhang-Rice singlet, except that here, it appears in a semi-conductor. We discuss the unusual hybridization in terms of orbital occupation and character as well as the structure-property relationships that can be unveiled in various metal-substituted systems (Ni, Mn, Co, Zn).

1.2.2 Nonreciprocal directional dichroism at telecom wavelengths

Magnetoelectrics with ultra-low symmetry and spin-orbit coupling are well known to display a number of remarkable properties including nonreciprocal directional dichroism. As a polar and chiral magnet, Ni_3TeO_6 is predicted to host this effect in three fundamentally different configurations, although only two have been experimentally verified. Inspired by the opportunity to unravel the structure-property relations of such a unique light-matter interaction, we combined magneto-optical spectroscopy and first-principles calculations to reveal nonreciprocity in the toroidal geometry and compared our findings with the chiral configurations. We find that formation of Ni toroidal moments is responsible for the largest effects near 1.1 eV - a tendency that is captured by our microscopic model and computational implementation. At the same time, we demonstrate deterministic control of nonreciprocal directional dichroism in Ni_3TeO_6 across the entire telecom wavelength range. This discovery will accelerate the development of photonics applications that take advantage of unusual symmetry characteristics.

1.2.3 Spin-phonon interactions, frustration, and magnetoelectric coupling in $Co_4Nb_2O_9$ and the Ta analog

In order to explore the consequences of spin-orbit coupling on spin-phonon interactions in a set of chemically-similar mixed metal oxides, we measured the infrared vibrational properties of $Co_4B_2O_9$ (B = Nb, Ta) as a function of temperature and compared our findings with lattice dynamics calculations and several different models of spin-phonon coupling. Frequency vs. temperature trends for the Co^{2+} shearing mode near 150 cm^{-1} reveal significant shifts across the magnetic ordering temperature that are especially large in relative terms. Bringing these results together and accounting for noncollinearity, we obtain spin-phonon coupling constants of -3.4 and -4.3 cm^{-1} for $Co_4Nb_2O_9$ and the Ta analog, respectively. Analysis reveals that these coupling constants derive from interlayer (rather than intralayer) exchange interactions and that the interlayer interactions contain competing antiferromagnetic and ferromagnetic contributions. At the same time, beyond-Heisenberg terms are minimized due to fortuitous symmetry considerations, different than most other 4*d*- and 5*d*-containing oxides. Comparison with other contemporary oxides shows that spin-phonon coupling in this family of materials is among the strongest ever reported, suggesting an origin for magnetoelectric coupling.

1.2.4 Spin-lattice coupling in $MnPS_3$ and giant magnetic circular dichroic signal in $CrPS_4$

In order to explore the optical properties of $MnPS_3$ and $CrPS_4$ as a function of temperature and magnetic field, we combined optical spectroscopy, magnetic circular dichroism spectroscopy, and magnetic field in order to understand the local and charge excitations and reveal the microscopic mechanism in the magnetic properties.

We reveal spin-charge coupling in $MnPS_3$, which is observed in both local d-to-d excitations and the band gap across the T_N. Furthermore, we reveal a giant magnetic circular dichroic signal in $CrPS_4$ that is on the orders of magnitude higher than $MnPS_3$. Through the energy cut of $\Delta\alpha(E,H)$ as a function of the magnetic field, the spin-flop transition is observed for both compounds with magnetic field $\perp$ ab-plane. $MnPS_3$ does not saturate even at 65 T. However, $CrPS_4$ displays a linear increase above the supposed saturation field, which is another magnetic phase.

1.3 Outline

The remainder of the dissertation is organized as follows: Chapter 2 presents a literature survey of multiferroics materials, magnetoelectric coupling, magnetoelectric coupling mechanisms, nonreciprocal directional dichroism, spin-phonon coupling, magnetism and honeycomb lattice, two-dimensional transitional chalcogenides, and materials of interest. Chapter 3 discusses our experimental and theoretical methods. Chapter 4 presents our spectroscopic findings of $Fe_2Mo_3O_8$ and its analogs including electronic excitations, Mott vs. band characters, and many-body resonance. Chapter 5 gives the details of nonreciprocal directional dichroism measurements and the findings of Ni_3TeO_6 including toroidal nonreciprocity, chiral vs. polar character, and the control of nonreciprocity in the telecom wavelength range. Chapter 6 discusses spin-phonon coupling, impacts of symmetry in the spin hamiltonian and spin-phonon coupling, and the origin of magnetoelectricity in $Co_4Nb_2O_7$ and the Ta analog. Chapter 7 discusses the optical properties of $MnPS_3$ and $CrPS_4$ as a function of temperature and magnetic field and the findings of spin-charge coupling in $MnPS_3$, a giant magnetic circular dichroic signal in $CrPS_4$, and a new magnetic phase in $CrPS_4$. Chapter 8 summarizes my work.

Chapter 2

Literature survey

2.1 Multiferroic materials

Multiferroic materials often display unusual phase diagrams. This is due to the cross-coupling of ferroic orders arising from spin, orbital, charge, and lattice degrees of freedom [Fig. 2.1] [75]. There are a total of four primary ferroic orders: ferroelectric, ferromagnetic, ferroelastic, and ferrotoroidic orders. These properties have structural, charge, and/or magnetic components that can be described by space-inversion and/or time-reversal symmetries. Table. 2.1 summarizes four ferroic orders in terms of space-inversion and time-reversal symmetries. Ferroelectric materials exhibit spontaneous electric polarization (**P**). By applying an external electric field (**E**), the direction of the electric polarization can be switched. Ferroelectricity can be described by broken space-inversion symmetry. On the other hand, ferromagnetic materials break time-reversal symmetry, which allows spontaneous magnetization (**M**) to form. The direction of the magnetic moment can be switched by the external magnetic field (**H**). Ferroelastic and ferrotoroidic materials can also be expressed by space-inversion and time-reversal symmetries. Ferroelastic materials display spontaneous strain (σ), which does not break space-inversion or time-reversal symmetries.

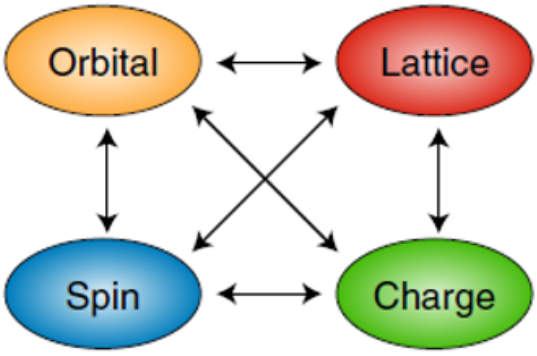


Figure 2.1: A diagram of spin, orbital, charge, and lattice degrees of freedom. They can couple with each other to form various couplings [75].

Table 2.1: Spatial-inversion and time-reversal symmetry in ferroics.

Ferroic orders	**Space-inversion symmetry**	**Time-reversal symmetry**
Ferromagnetism	Intact	Broken
Ferroelectricity	Broken	Intact
Ferroelasticity	Intact	Intact
Ferrotoroidicity	Broken	Broken

On the other hand, Ferrotoroidicity breaks both, exhibiting a complicated spontaneous magnetic vortex and generating a toroidal moment.

When two or more ferroic orders are present in a material, multiferroicity is achieved [Fig. 2.2] [1]. For example, the coupling of ferroelectric and ferromagnetic orders induces magnetoelectricity. This has interesting consequences for the physical properties because the orders couple with one another. Commonly, the magnetic moment can be controlled by only the external magnetic field. However, magnetoelectric materials allow the external magnetic field to manipulate the electric polarization as well. Furthermore, the external electric field can switch both electric polarization and magnetization, enabling multi-functionalities. Of course, there are other multiferroic coupling terms including piezoelectricity (lattice strain + electric polarization) and piezomagnetism (lattice strain + magnetism). However, we are most interested in magnetoelectric multiferroics in the form of complex oxides.

2.2 Magnetoelectric coupling

Briefly, we discussed the symmetry and physical example of magnetoelectric coupling and the consequence of the cross-coupling of polarization and magnetism.

We can also mathematically explain the cross-coupling using Landau's equation of the free energy of the system [77]:

$$-F(E,H) = \frac{1}{2}\epsilon_0\epsilon_{ij}E_iE_j + \frac{1}{2}\mu_0\mu_{ij}H_iH_j + \alpha_{ij}E_iH_j + \frac{\beta_{ijk}}{2}E_iH_jH_k + \frac{\gamma_{ijk}}{2}H_iE_jE_k + \cdots \tag{2.1}$$

where, P_i^s = - $\frac{\partial F}{\partial E_i}$, M_i^s = - $\frac{\partial F}{\partial H_i}$, and $\alpha_{ij} = \frac{\partial P_i}{\partial H_j} = \frac{1}{\mu_0}\frac{\partial M_i}{\partial E_j}$, P_i^s and M_i^s are the static electric polarization and magnetization, and α_{ij} is the linear magneto-electric coupling coefficient. Figure 2.3(a) displays an example of magnetoelectric materials ($Fe_2Mo_3O_8$ and Ni_3TeO_6) exhibiting changes in the magnetism as a function of the

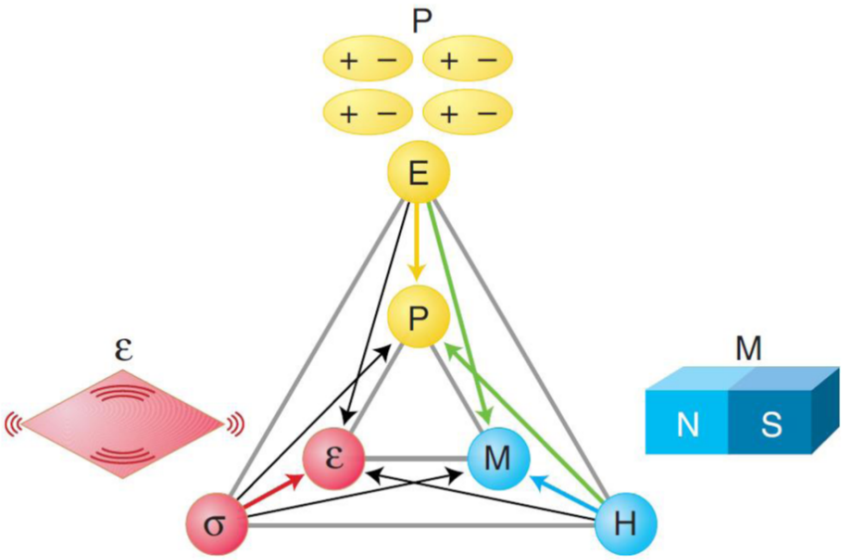


Figure 2.2: A diagram showing the cross-coupling of "ferroic". E, electric field, is controlling the polarization. H, magnetic field, is controlling the magnetism. σ, mechanical stress, is controlling the ϵ, which is a strain. The diagram shows how couplings can affect, for example, polarization with the magnetic field, magnetism with the electric field, strain with the magnetic field, and so on [1].

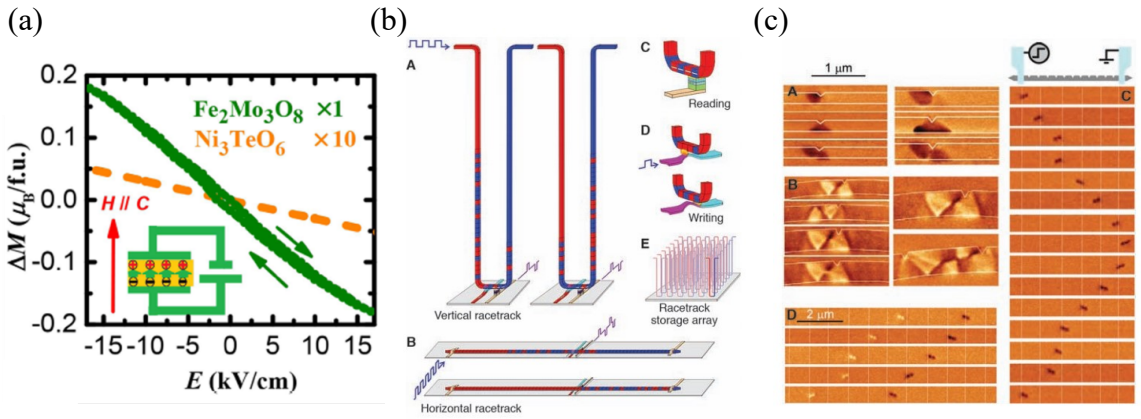


Figure 2.3: An example of magnetoelectric coupling is shown. (a) $Fe_2Mo_3O_8$ and Ni_3TeO_6 display changes in the magnetism as a function of the electric field [28]. (b,c) A diagram of the experimental setup and the images of propagation of the domain [76].

electric field. Furthermore, an example of how these materials can be used for memory device applications is shown in Fig. 2.3(b,c). However, magnetoelectric materials are extremely rare in nature [78]. Usually, ferroelectricity and ferromagnetism are mutually exclusive [79, 80]. Ferroelectricity tends to be observed in insulators and requires empty d orbital in general whereas ferromagnetism tends to be found in metals and requires unpaired d electrons. However, ferrimagnetism and antiferromagnetism can be found in insulators. The microscopic reason for this behavior is the competition between the hybridization and the Coulomb interaction. We can understand microscopically by the occupancy of d-orbital electrons. For d^0 non-magnetic metal centers, the energy of covalent or ionic bonding is higher than the Coulomb interaction between electrons since there are no electrons in the d-orbital, leading to a high hybridization between the metal center and the oxygen. This breaks centrosymmetry as the metal center shifts away from the center, inducing electric polarization. This can typically extend to d^1 metals as well. When the d-orbital starts to fill partially, the Coulomb interaction starts to dominate over the hybridization, keeping the centrosymmetric position without forming an electric polarization. However, this framework breaks down as d^n metal center sits on the asymmetric double potential well created by the chemistry or the crystal structure. Therefore, a number of other strategies have been devised. Figure 2.4 summarizes several different ferroelectric materials depending on their mechanisms for creating ferroelectricity [75].

Multiferroics can be described into two types depending on the ferroelectric and magnetic ordering transition temperature. Type-I corresponds to materials with separate transition temperatures whereas Type-II multiferroics have the same transition temperature. The reason for mismatched temperatures is the different mechanisms responsible for ferroelectricity and magnetic ordering. Type-II multiferroics have magnetic ordering breaking inversion symmetry to induce ferroelectricity, leading

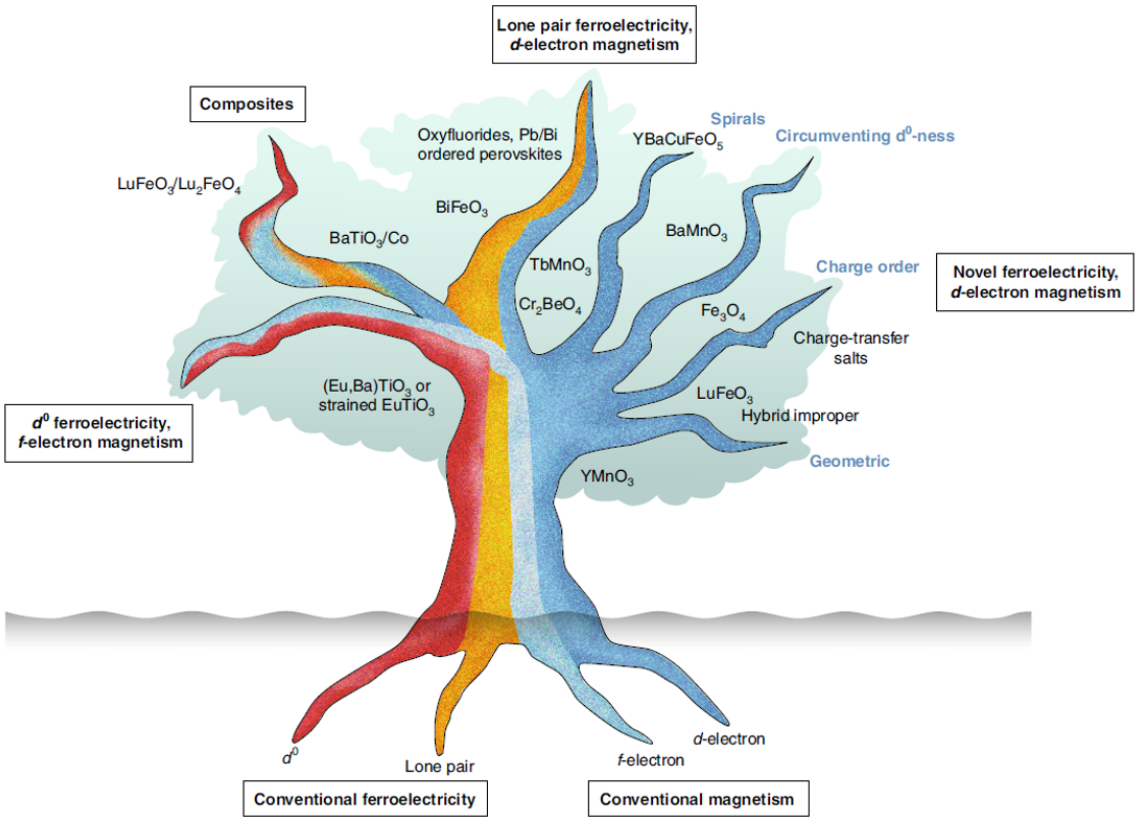


Figure 2.4: A diagram of multiferroic materials represented in a tree. Starting with conventional ferroelectric d^0 materials and d^n magnetism, different kinds of multiferroics are organized by various multiferroic mechanisms and mixing of metal centers [75].

to the same transition temperature. $BiFeO_3$ is an example of Type-I multiferroics - the most famous multiferroic material [81, 82]. It has the perovskite structure where non-magnetic Bi occupies the A-site and magnetic Fe sits on the B-site [Fig. 2.5(a)]. The Bi atoms hybridize with oxygen atoms and move off-center to break the space-inversion symmetry, inducing ferroelectricity. On the other site, magnetic Fe has a partially filled d-orbital, providing magnetism. The Fe atoms exhibit antiferromagnetic ordering below the magnetic Curie temperature. Here, the magnetic ordering transition does not occur concurrently with ferroelectricity, which is the reason for the classification of Type-I multiferroics. An example of Type-II multiferroics is $TbMnO_3$ - another famous multiferroic material [Fig. 2.5(b)]. In contrast to $BiFeO_3$, the structural phase transition and the magnetic ordering transition temperatures are concurrent for $TbMnO_3$. There are advantages and disadvantages to both types. Type-I usually provides high ordering temperature (room temperature or higher) whereas Type-II does not. However, Type-II multiferroics exhibit stronger magnetoelectric coupling since Type-I has different mechanisms for ferroelectricity and magnetic ordering, leading to weaker coupling strength. The goal is to develop multiferroic materials with high transition temperatures with strong magnetoelectric coupling strength, which is the most challenging part since magnetoelectric materials are already so rare in nature.

2.3 Magnetoelectric coupling mechanisms

There are various mechanisms that support magnetoelectric coupling including electronic lone pairs, geometric filling, charge-ordering, and spin-driven mechanisms as shown in Fig. 2.6. The first three cases fall under Type-I since they are independent of magnetism, whereas the spin-driven mechanism induces electric polarization, leading to the same ferroelectric and magnetic transitions. The latter supports Type-

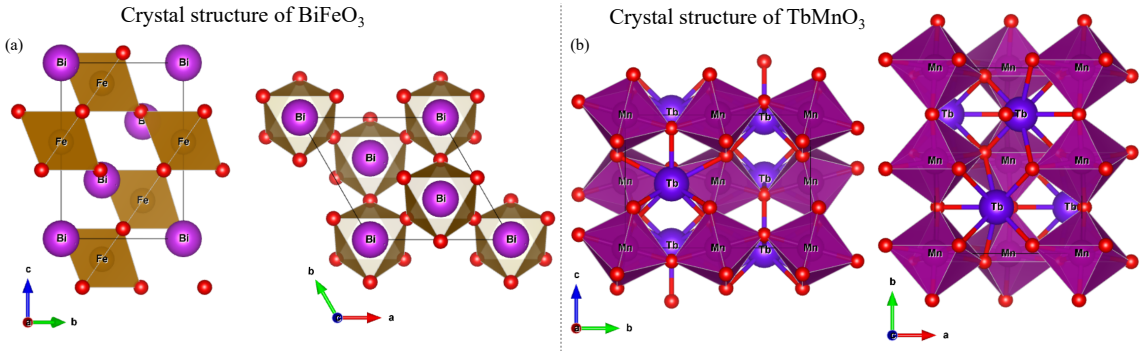


Figure 2.5: The crystal structure of $BiFeO_3$ and $TbMnO_3$ are displayed. (a) The crystal structure of $BiFeO_3$ with a-axis view and c-axis view is presented. The space group is $R3c$ (No. 161) [83]. (b) The crystal structure of $TbMnO_3$ is shown here with a-axis view and c-axis view. The space group is $Pnma$ (No. 62) [84].

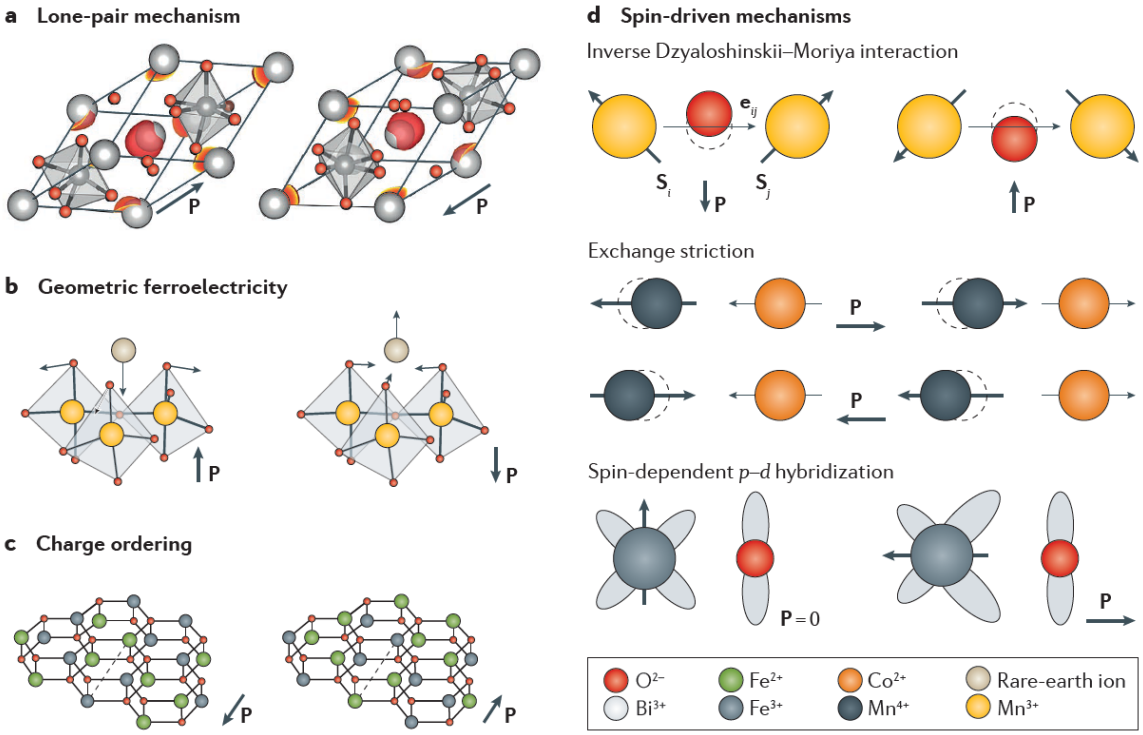


Figure 2.6: Various mechanisms for multiferroicity are shown. (a-c) The lone-pair mechanism, geometric ferroelectricity, and charge-ordering are Type-I multiferroic mechanisms, in which structural distortion occurs independently from magnetic ordering. (d) The spin-driven mechanism supports Type-II multiferroics. By the inverse Dzyaloshinskii-Moriya interaction, exchange striction, and spin-dependent $p-d$ hybridization, magnetism affects structural distortion, creating electric polarization for ferroelectricity [85].

II multiferroics. We will discuss each mechanism in detail.

Lone-pair ferroelectricity is the spatial asymmetry due to the anisotropic distribution of unbonded valence electrons [Fig. 2.6(a)] [85]. $BiFeO_3$ is the most famous example of this mechanism. The large polarization arises from a pair of Bi^{3+} valence electrons in the $6s$ orbital. They create a local dipole without getting involved in the *sp* hybridization. The spontaneous polarization of $\approx 100 \mu C/cm^2$ emerge below T_C = 1,103 K [82]. The Néel temperature is at 643 K, where the antiferromagnetic structure is observed. Surprisingly, $BiFeO_3$ is the only room-temperature multiferroic among the lone-pair systems. Again, we can see that the ferroelectric transition is independent of the magnetic ordering transition. Hence, the magnetoelectric coupling in $BiFeO_3$ is rather weak.

The space-filling effects and geometric constraints are the cause of the geometric ferroelectricity by creating structural instabilities in materials [Fig. 2.6(b)] [85]. In other words, the arrangement of atoms in a given space drives the ionic shifts, creating polarization due to steric effects rather than the bonding chemistry. This can result in the formation of geometric ferroelectricity. Usually, the small non-magnetic cation in the *A*-site allows for the rotation or tilt of the polyhedra centered with the *B*-site cation, accompanying the distortion of the *A*-site and generating polarization. This can be important because the rotation or tilt of the polyhedra can induce a canted magnetic structure, offering a coupling between polarization and magnetism. Furthermore, ferroelectric materials can be identified as a proper or improper type depending on whether the spontaneous polarization is a primary order parameter or a secondary effect, respectively. $BaNiF_4$ provides an example of proper ferroelectricity [Fig. 2.7(a,b)]. The softening of a polar phonon mode causes the rotation of fluorine octahedron, leading to the polar displacement of the Ba cations [86, 88]. Since the distortion is polar in nature, this material represents a confirmed example of

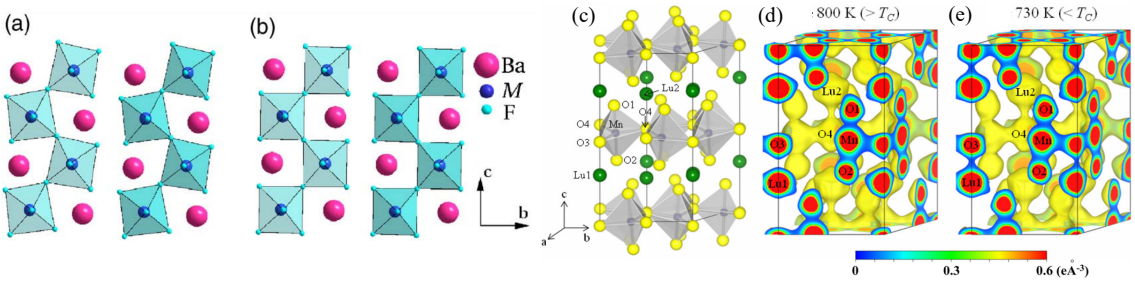


Figure 2.7: (a,b) Crystal structure of BaMiF$_4$ (M = Co, Ni, Zn, Mg) where the rotation/tilting creates a noncentrosymmetric structure in panel (a), whereas no distortion maintains the centrosymmetric structure [86]. (c-e) Crystal structure of $YMnO_3$ and electron density distribution maps above and below the Curie temperature [87]. Lu1-O3 bonding can be observed below the T_C.

proper geometric ferroelectrics. An example of improper ferroelectricity is h-RMnO$_3$ (R = Sc, Y, In, or Dy-Lu) [Fig. 2.7(c-e)]. The ferroelectricity emerges at above 1,200 K, with a polarization of 5.6 μC/cm^2. The ferroelectricity comes from a coupling between an unstable zone-boundary mode with a stable zone-center mode [89]. The polar distortion does not directly cause ferroelectricity, which is why it is a secondary effect.

Charge-ordering is another mechanism supporting ferroelectricity. The non-uniform distribution of valence electrons around the metal center in the crystal lattice forms a periodic superstructure [Fig. 2.6(c)] [85]. $LuFe_2O_4$ is the most famous and studied charge-ordering ferroelectric material. There are Fe double layers hosting alternatively ordered Fe^{2+} and Fe^{3+} sites [Fig. 2.8] [90]. The unequal distribution of charge inside the Fe bilayers induces an internal electric polarization. However, there are some studies questioning the ferroelectricity in $LuFe_2O_4$ [90, 91]. A recent development confirms that non-polar crystal structure through a combination of magnetic circular dichroism spectroscopy and first-principles calculations [92]. Fortunately, there is some progress in multiferroics with charge-ordering with a polar charge-ordered state below 100 K in the ferrimagnetic magnetite, Fe_3O_4 [75, 93].

Lastly, spin-driven mechanisms are more complicated and perhaps the most interesting of all. Magnetic ordering can also break the space-inversion symmetry and induce a ferroelectric state due to the interaction of spins and charges [85]. Since ferroelectricity is a secondary effect of magnetic ordering, multiferroics with this mechanism are improper ferroelectrics. There are three main types of spin-driven mechanisms [Fig. 2.6(d)]. The first type is the inverse Dzyaloshinskii-Moriya interaction. Typically, the Dzyaloshinskii-Moriya interaction promotes an antisymmetric magnetic interaction by the noncentrosymmetric environment whereas the inverse Dzyaloshinskii-Moriya interaction has the canted spin structure, driving non-

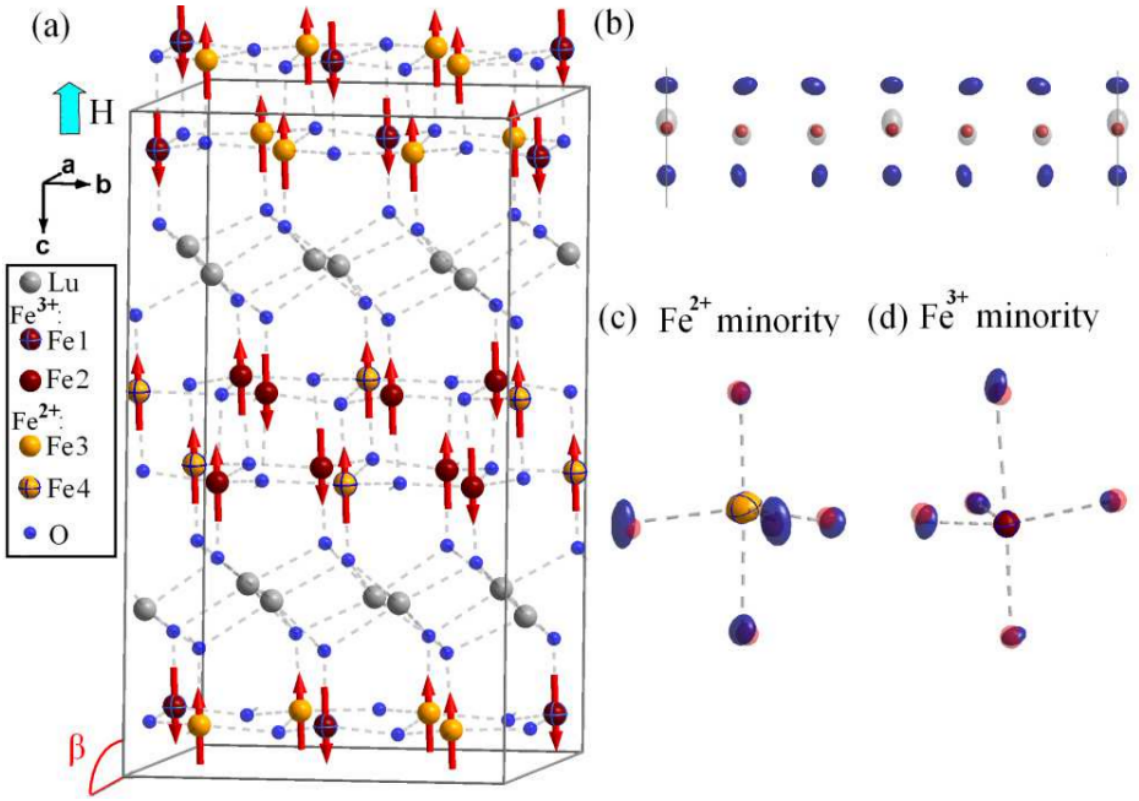


Figure 2.8: (a) A crystal structure of $LuFe_2O_4$ is displayed. It has a space group of C2/m. Alternating Fe^{2+} and Fe^{3+} local sites can be observed. (b) A distinct local environment of Fe^{2+} and Fe^{3+} [90].

centrosymmetric displacement of charges by minimizing the lattice energy. This can be expressed by the antisymmetric exchange interaction of neighboring spins as $S_i \times S_j$. This can cause electric polarization. This type of mechanism was first found in Cr_2BeO_4 and $CaMn_7O_{12}$ [36, 94]. As discussed in the Introduction, $Cu_3Nb_2O_8$ also falls under this category [95]. As a reminder, $Cu_3Nb_2O_8$ has a chiral magnetic structure that induces polarization perpendicular to the plane of the spin rotations as shown in Fig. 1.1(d). The second type is the exchange striction, which is similar to the inverse Dzyaloshinskii-Moriya interaction. However, the exchange striction describes a collinear spin structure, which induces a ferroelectric polarization by optimizing the spin product as $S_i \cdot S_j$ [Fig. 2.6(d)] [85]. Typically, this interaction is stronger than the antisymmetric exchange interaction ($|S_i \cdot S_j| > |S_i \times S_j|$), leading to an order of magnitude larger electric polarization. One example is o-$TbMnO_3$, where the polarization amplitude dramatically increases during the magnetic transition from a canted magnetic state to a collinear antiferromagnetic state under pressure [96]. Lastly, the spin-dependent *p-d* hybridization mechanism is unlike both mentioned above. Rather than spin-spin correlation, the hybridization mechanism with a single spin is responsible for the modulation of charges. Local polar bond e_{ij} arise from the connection between spin site i and the ligand site j by the spin-orbit coupling [85, 97]. Examples include $Ba_2CoGe_2O_7$ and CuMnO_2 (M = Fe or Cr) [98, 99]. In rare cases, two mechanisms exist in the same material [100].

Overall, spin-driven multiferroics usually display stronger magnetoelectric coupling, which can lead to potential device applications. In fact, it is thought that the Type-II mechanism may be the only way to get full coupling. However, the main challenge of obtaining a high magnetic ordering transition temperature complicates the development of applications for common usage that requires room temperature. On the other hand, Type-I multiferroics display a larger electric polarization with

phase transitions at or above room temperature. Yet, a different challenge is presented by the weaker magnetoelectric coupling, preventing progress in a contrasting way.

One way forward is integrating $4d$- and $5d$ heavy metal centers. They offer stronger spin-orbit coupling, which is one of the crucial ingredients in magnetoelectricity [9]. As mentioned in the Introduction section, heavy metals typically have diffuse orbital characteristics, which typically have metallic behavior. However, it is not always true due to dimerization. The first example is Sr_2CrOsO_6, which is a ferrimagnetic insulator with magnetic ordering temperature above room temperature [101, 102]. Furthermore, spin-phonon coupling is a well-known mechanism that is closely associated with multiferroicity. By incorporating heavy metals, giant spin-phonon coupling is observed such as $SrMnO_3$ (T_N = 233 K and $\Delta\omega$ = 25 cm^{-1}) [103], $NaOsO_3$ (magnetic metal-insulator transition = 410 K and $\Delta\omega$ = 40 cm^{-1}) [104], Ba_2FeReO_6 (T_C = 305 K and $\Delta\omega$ = ∼30 cm^{-1}) [105], and Sr_2CrReO_6 (T_C = ∼600–635 K and $\Delta\omega$ = ∼30 cm^{-1}) [105]. These examples display high transition temperatures and the largest frequency shifts ever exhibited. Multiferroics with the integration of heavy metals show extremely promising directions to investigate.

2.4 Nonreciprocal directional dichroism

Magnetoelectric coupling gives rise to exotic physics, complicated phase diagrams, and practical applications, but it can extend further with certain additonal broken symmetries - toward a unique property called nonreciprocal directional dichroism. The fundamental description of nonreciprocity is 'one-way transparency'. Also, this is known as the "optical diode effect". As one measures an absorption in one direction of the light propagation direction, the absorption in the opposite direction is not the same [106]. To gain a simple picture of what is required to achieve this effect, we

can think about symmetry. Nonreciprocity occurs when all of the symmetries are broken. This includes rotational, mirror, inversion, and time-reversal symmetries. Figure 2.9 provides examples to illustrate how nonreciprocal directional dichroism emerges. Specifically, we have a light propagation direction ($\pm k$). First, let us consider a material that has electric polarization (P) in c-axis, which is perpendicular to k [Fig. 2.9(a)]. When the light propagation direction is in the opposite direction ($-k$), inversion symmetry is broken. In other words, the configuration of k and $-k$ in Fig. 2.9(a) cannot be related by applying inversion symmetry. However, mirror, rotational, and time-reversal symmetries can be applied to relate those two configurations. Therefore, nonreciprocal directional dichroism cannot be observed. Next, we apply the magnetic field to induce a net magnetic moment (M) parallel to k [Fig. 2.9(b)]. Then, rotational, inversion, and time-reversal symmetries are broken. Yet, mirror symmetry is unbroken, unable to observe a nonreciprocal effect. Now, we apply the magnetic field perpendicular to P, which induces toroidal moment ($T = P \times M$). Moreover, we apply the magnetic field so that M is not only perpendicular to P but also k [Fig. 2.9(c)]. This configuration breaks all of the symmetries (mirror, rotational, inversion, and time-reversal) with $-k$. Now nonreciprocal directional dichroism can be observed. This geometry is called toroidal configuration. There are other configurations, which relate to chiral structures. Magnetochiral configuration has k parallel to M and chiral axis. Transverse magnetochiral configuration is similar except the chiral axis is perpendicular to k and M. We note that $k \parallel H$ is a Faraday geometry, and $k \perp H$ is a Voigt geometry.

To discuss nonreciprocal directional dichroism from a spectroscopic perspective, we have to describe the response function (χ^{me} and χ^{em}) since magnetoelectric multiferroics have a coupling between the electric and magnetic states, resulting in an optical magnetoelectric effect. The electric and magnetic components of light induce

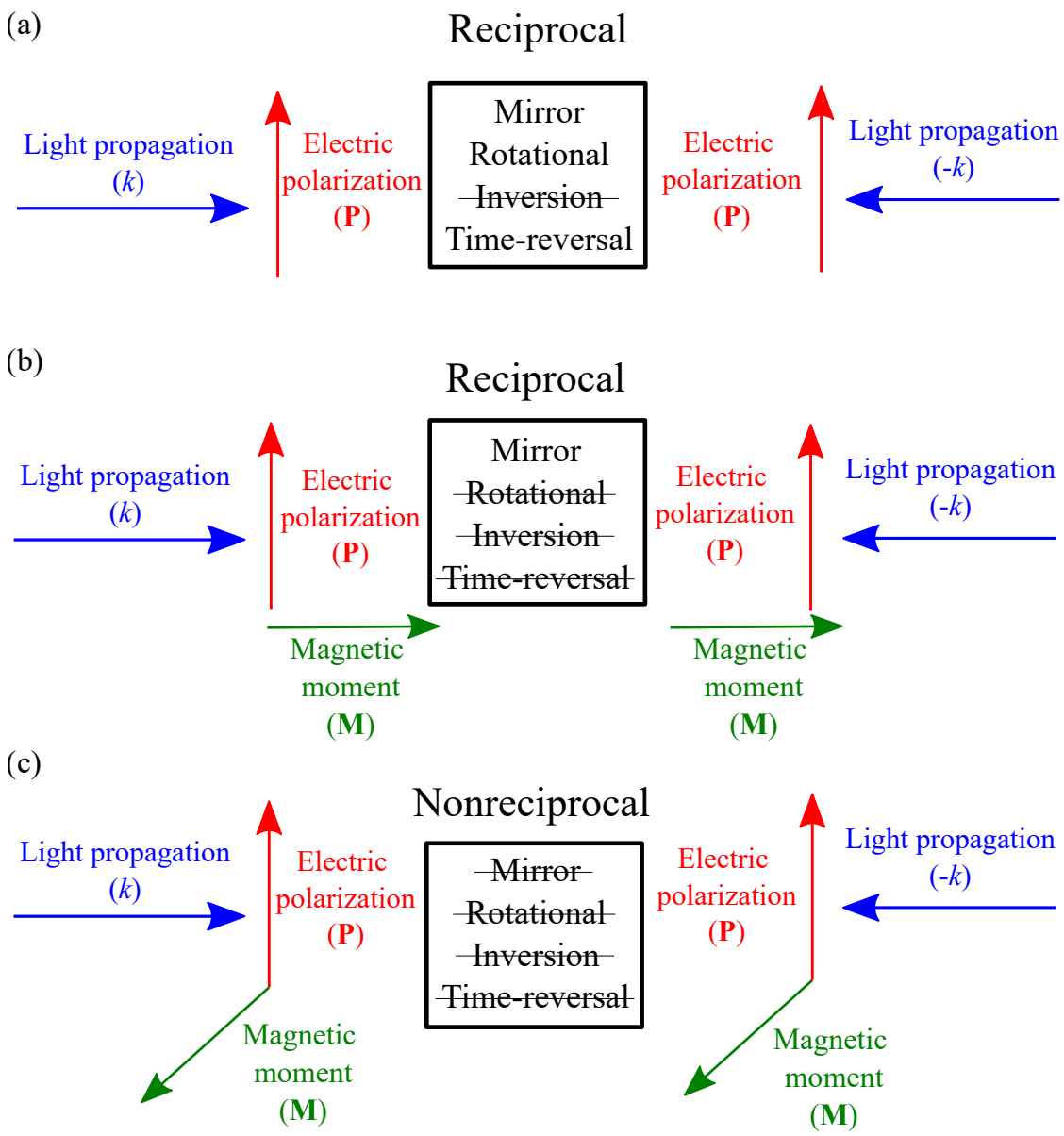


Figure 2.9: A diagram is displayed to show the symmetry requirement for nonreciprocal directional dichroism. (a) Only inversion symmetry is broken. (b) Mirror symmetry is remained unbroken. (c) All of symmetries are broken. Thus, nonreciprocal directional dichroism can be observed.

the oscillating magnetization (M^{ω}) and polarization (P^{ω}), respectively. The tensors for oscillating magnetization and polarization become:

$$\begin{aligned} M^{\omega} &= [\hat{\mu}(\omega) - 1]H^{\omega} + \sqrt{\epsilon_0 \mu_0}\chi^{me}(\omega)E^{\omega} \\ P^{\omega} &= \epsilon_0[\hat{\epsilon}(\omega) - 1]E^{\omega} + \sqrt{\epsilon_0 \mu_0}\chi^{em}(\omega)H^{\omega}. \end{aligned} \tag{2.2}$$

The refractive index for a given polarization is solved by the Maxwell equation with these generalized forms:

$$N_{ij}^{\pm} \approx \sqrt{\epsilon_{ii}(\omega)\mu_{jj}(\omega)} \pm \frac{1}{2}[\chi_{ji}^{me}(\omega) + \chi_{ij}^{em}(\omega)]. \tag{2.3}$$

Here, the $\pm$ signs represent wavevectors in the $\pm k$ directions [107].

The optical magnetoelectric effect is observed by transitions where both the electric and magnetic dipoles moments generated by an absorbed phonon with energy $\hbar\omega$ are finite:

$$\begin{aligned} \chi_{ji}^{me}(\omega) = \frac{2}{V\hbar}\sqrt{\frac{\mu_0}{\epsilon_0}}\sum_n [&\frac{\omega_{n0}\Re\{<0|m_j|n><n|p_i|0>\}}{\omega_{n0}^2 - \omega^2 - 2i\omega\delta_n} \\ &+ \frac{i\omega\Im\{<0|m_j|n><n|p_i|0>\}}{\omega_{n0}^2 - \omega^2 - 2i\omega\delta_n}] \\ &\triangleq \chi_{ji}^{'}(\omega) + \chi_{ji}^{''}(\omega). \end{aligned} \tag{2.4}$$

For the nonreciprocal effect to occur, both the electric and magnetic dipole matrix elements have to be non-zero and the excitation can be determined to be magnetoelectric. Hence, spin-orbit coupling in these materials is a necessary ingredient. Without it, the real part of the coupling of M and P matrix elements equals zero, at least in the linear-response regime. When the strength of this effect is strong, a material can either be fully absorbing or fully transparent. The magnetoelectric

ratio is defined as:

$$\gamma_{i,j} \equiv \frac{< n|m_j|0 >}{< n|p_i|0 >}. \tag{2.5}$$

When the magnetoelectric ratio is one, the material can be fully one-way transparent [107].

Experimentally, we have to take a few steps to calculate the nonreciprocal directional dichroism absorption spectra (α_{NDD}). First, we calculate the absorption difference as $\Delta\alpha_{+k,+H}(E) = \alpha_{+k}(E, +H)$ - $\alpha_{+k}(E, 0\ \mathrm{T})$ in the $+k$ and $+H$ direction. Next, we reverse the light propagation direction to $-k$ and do the same operation, which is $\Delta\alpha_{-k,+H}(E) = \alpha_{-k}(E, +H)$ - $\alpha_{-k}(E, 0\ \mathrm{T})$. Finally, we subtract the absorption differences to extract the nonreciprocal directional dichroism spectra as $\Delta\alpha_{NDD}(E) = \Delta\alpha_{+k,+H}(E)$ - $\Delta\alpha_{-k,+H}(E)$. Furthermore, we do not have to reverse the k direction. We can reverse the magnetic field direction to have $\Delta\alpha_{NDD}(E)$ $= \Delta\alpha_{+k,+H}(E)$ - $\Delta\alpha_{+k,-H}(E)$. The symmetry stays the same as reversing k direction [108]. This offers a more consistent and experimentally accessible method to achieve $\Delta\alpha_{NDD}$ since the magnetic field is easier to switch in the opposite direction [108].

Most nonreciprocal directional dichroism effects are observed in the terahertz regions because magnetoelectric excitations tend to arise in low energy regions, similar to electromagnons. Several examples are shown in Fig. 2.10 including $BiFeO_3$, $CaBaCo_4O_7$, $FeZnMo_3$, and $Ba_2CoGe_2O_7$ [64, 109–111]. There are a few examples in higher energy regions. The strength of spin-orbit coupling plays an important role since the purely electronic component needs to mix with the magnetic component. Two examples of the nonreciprocal effect in d-to-d excitations are $GaFeO_3$ and CuB_2O_4, shown in Fig. 2.11(a,b), respectively [112, 113]. These compounds have excitations that are magnetoelectric because they have strong spin-orbit coupling, which mixes the magnetic and electric dipole matrix elements. With the combination

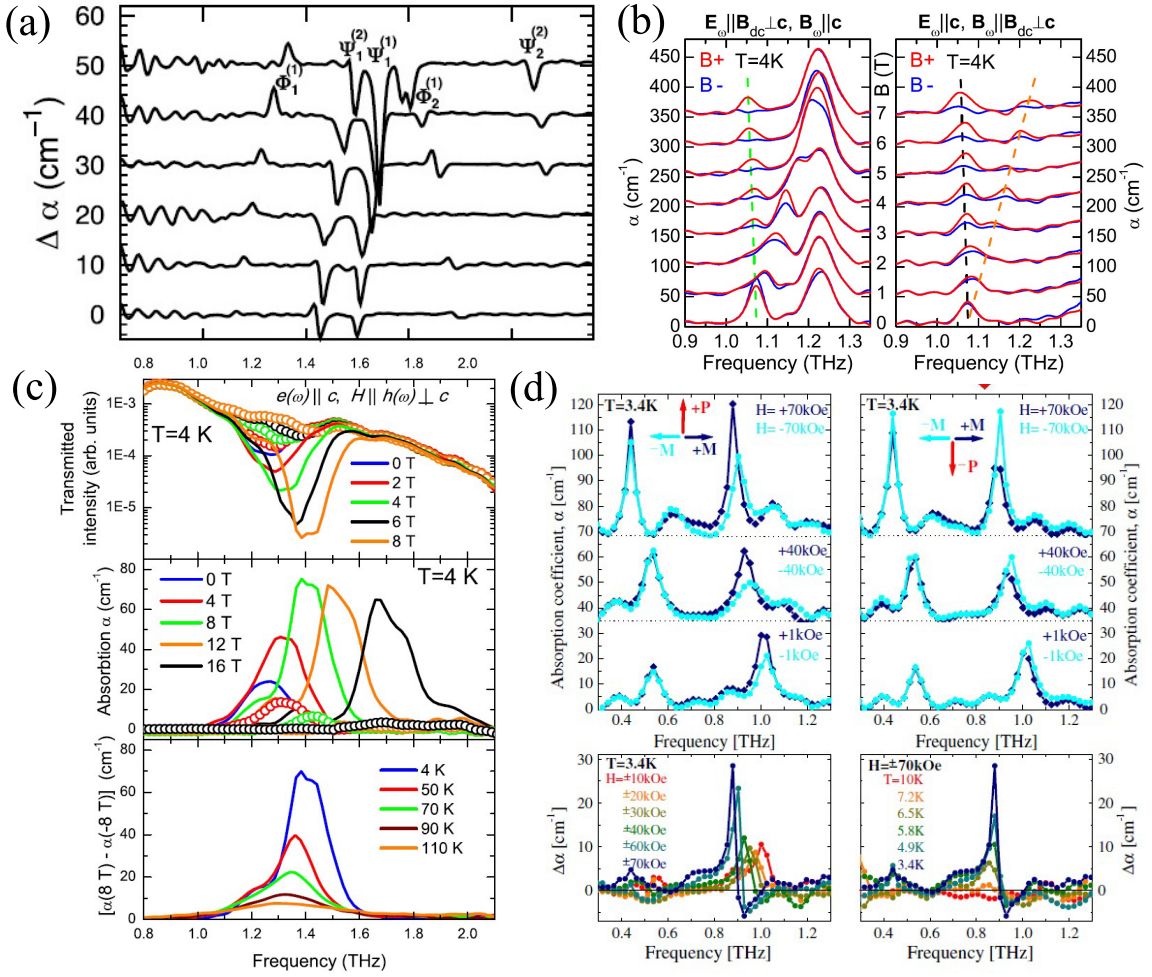


Figure 2.10: Nonreciprocal effect of different materials in the terahertz infrared region. The materials shown are $BiFeO_3$ (a) [109], $CaBaCo_4O_7$ (b) [110], $FeZnMo_3O_8$ (c) [64], and $Ba_2CoGe_2O_7$ (d) [111].

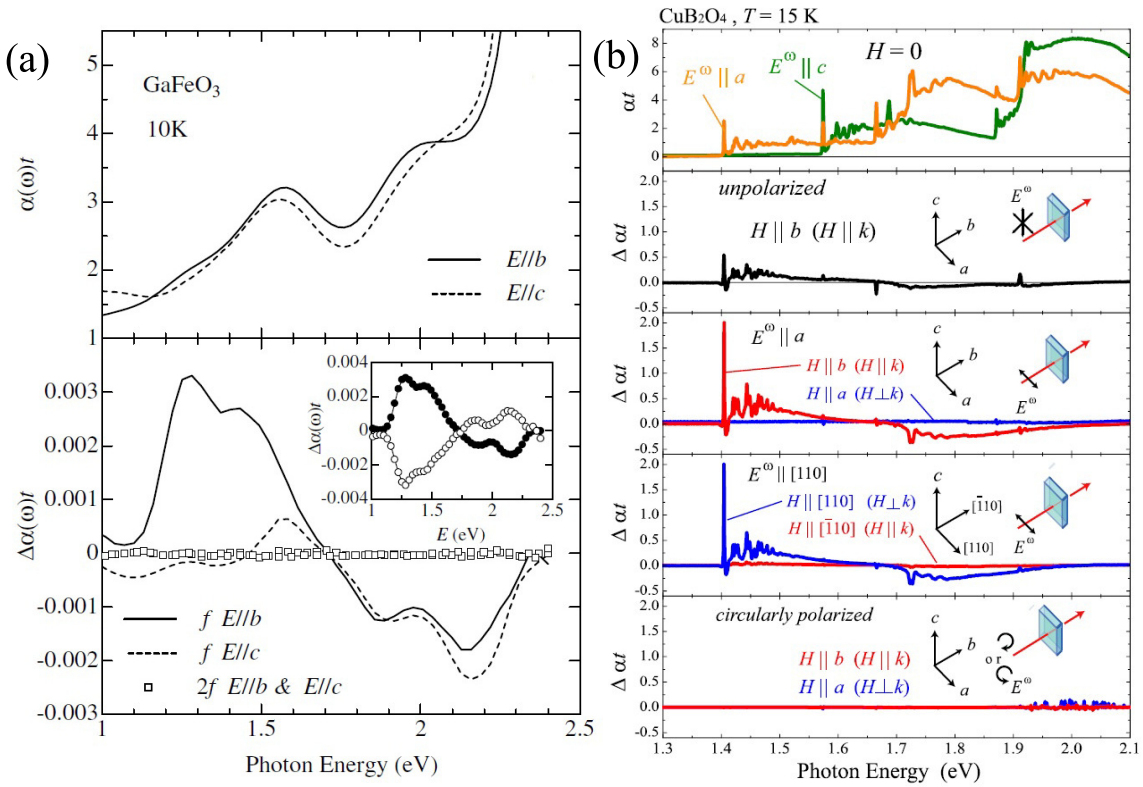


Figure 2.11: Nonreciprocal effect in the optical region is shown with (a) $GaFeO_3$ [112] and (b) CuB_2O_4 [113]

of low crystallographic and magnetic symmetry, these excitations display nonreciprocal directional dichroism.

The use of the nonreciprocal effect can be extended to the identification of antiferromagnetic domains. Typically, imaging and identifying antiferromagnetic domains are challenging due to the fact that there is no net magnetization. There are tools such as magnetic X-ray circular/linear dichroism spectroscopy with photoemission electron microscopy [114], scanning magnetic X-ray diffraction [115,116], and coherent X-ray techniques [117,118]. A recent study of nonreciprocal directional dichroism in $Pb(TiO)Cu_4(PO_4)_4$ demonstrated that imaging of antiferromagnetic domains is possible using the linear polarization microscopy in the transmittance geometry [119] in the visible range [Fig. 2.12]. This could also extend further to molecular chemistry and biology since chirality is found everywhere from DNA to pharmaceutical drugs.

2.5 Spin-phonon coupling

One of the fundamental ways for multiferroics to exhibit cross-coupling is by spin-phonon coupling. As mentioned in the Introduction, spin can couple with the lattice. Then, magnetostriction emerges, which gives rise to magnetoelastic and magnetodielectric coupling. Furthermore, magnetoelectric multiferroics also have spin-phonon coupling that can induce structure distortions and polarization. This effect has been known to occur [120], but there is a lot of renewed interest in spin-phonon coupling in multiferroics due to the spintronic applications with the thermal Hall effect [121] and quantum computing with spin relaxation information [122–126]. Furthermore, the rise of mixed metal oxides has given new mechanisms [63] and enhanced of spin-phonon coupling [104]. It is therefore of great interest to reexamine this process in mixed metal systems containing heavy metal centers.

We first have to understand the vibrational spectra of a material, which we can

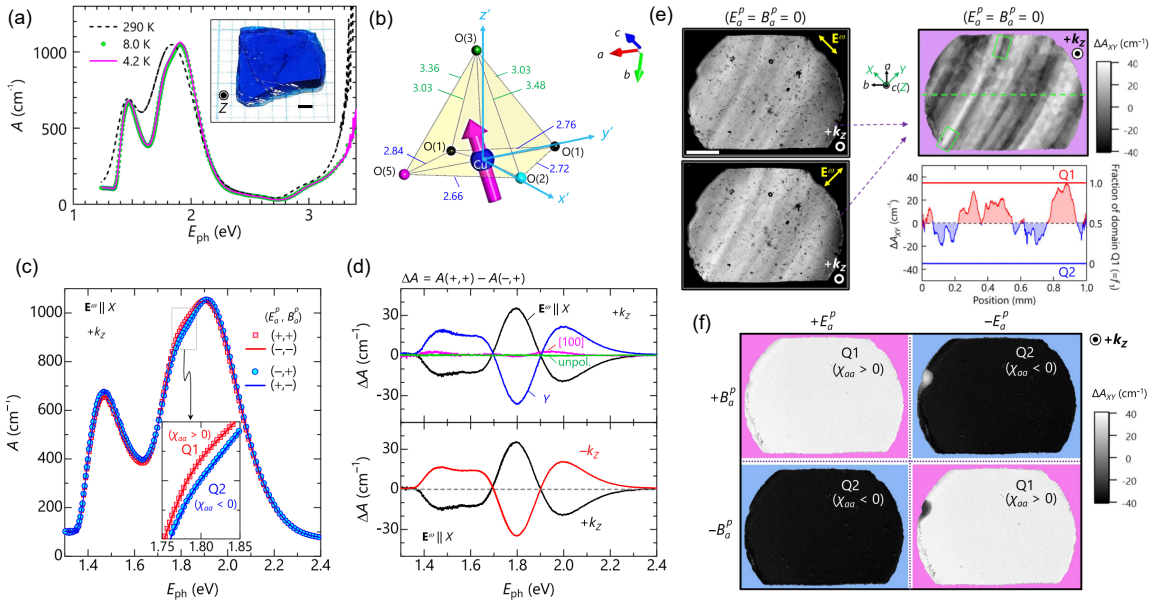


Figure 2.12: (a) Absorption spectra of $Pb(TiO)Cu_4(PO_4)_4$ at 4.2, 8, and 290 K. (b) Distorted CuO_5 square pyramid. The purple arrow represents the magnetic moment vector. (c) Absorption spectra with different polarization. (d) Absorption difference spectra from different polarization. (e) Microscopy images using polarization. (f) The images are subtracted to show the difference, just like absorption difference [119].

use as a harmonic oscillator for a simple model. From a macroscopic perspective, a simple Hooke's law is used for both a single mass system and a diatomic system. By treating this problem quantum mechanically, the Schrödinger equation can be written as [127]:

$$-\frac{\hbar^2}{2\mu}\frac{\partial^2\psi}{\partial x^2} + V(x)\psi(x) = E\psi(x). \tag{2.6}$$

Here, μ is the reduced mass, $\hbar = h/2\pi$, and the potential energy of the vibration is $V(x) = \frac{1}{2}kx^2$. k is the force constant and x is the displacement from the equilibrium position $(r_i - r_j)$. Solving Eqn. 2.6 for quantized energy values yields:

$$E_\omega = h\omega(n + \frac{1}{2}), n = 0, 1, 2... \tag{2.7}$$

with

$$\omega = \frac{1}{2\pi}\sqrt{\frac{k}{\mu}}, \tag{2.8}$$

where ω is the frequency of the vibration and n is the vibrational quantum number.

In a crystal, the periodic arrangement of atoms makes vibrational properties slightly different. The movements of an atom affect all neighboring atoms, which leads to collective excitations called phonons. Furthermore, the lattice vibrations have dispersion relations. Infrared spectroscopy probes the gamma point, $k = 0$, with high resolution. The inelastic neutron scattering technique can measure k-space but has poor resolution compared to infrared spectroscopy. The crystal is 3D with N number of atoms, which contains $3N$ optical and 3 acoustic branches. Optical branches describe the vibrations of atoms whereas acoustic branches are translation modes of atoms. Using group theory, a number of modes can be predicted along with displacement patterns. Assignments of modes to the experimental spectra can be made by measuring different crystal axes with linearly polarized light. A comparison between the experiment and theory is also critical to examine as well. Moreover,

displacement patterns can provide information about individual atoms' directions and contributions of specific vibrational modes.

Returning back to the model, there are many contributions to the potential including anharmonicity contribution, electron-phonon interaction, and spin-phonon coupling [128, 129]. In magnetic materials, a phonon can couple to the spin degrees of freedom, and the frequency of the mode is renormalized proportionally to the nearest-neighbor spin-spin correlation function [128, 130–132]. We consider the potential with harmonic oscillator and the spin-phonon coupling since complex oxides are typically insulators or semiconductors where the electron-phonon interaction is negligible [129].

$$V(x)\psi(x) = \frac{1}{2}kx^2 + \sum_{ij} J_{ij}(x)\langle S_i \cdot S_j \rangle. \tag{2.9}$$

By taking a second derivative, we can extract the k as [133]:

$$\frac{\partial^2 U}{\partial x^2} \approx k + \sum_{ij} \frac{\partial^2 J_{ij}}{\partial x^2}\langle S_i \cdot S_j \rangle. \tag{2.10}$$

In such cases, the frequency is expressed as [134]:

$$\omega = \omega_o + \lambda\langle S_i \cdot S_j \rangle. \tag{2.11}$$

Here, ω_o is the unperturbed phonon frequency, ω is the renormalized phonon frequency due to spin-phonon interactions, $\langle S_i \cdot S_j \rangle$ is the spin-spin correlation function, and λ is the spin-phonon coupling constant.

Experimentally, the phonon frequency as a function of temperature would follow an anharmonic behavior until the Néel temperature. The anharmoic behavior is

defined as [129, 133, 135]:

$$\omega_{anh}(T) = \omega_h + A(1 + \frac{2}{e^{\frac{\hbar\omega_O}{2k_BT}} - 1}). \tag{2.12}$$

Here, ω_h is the harmonic frequency of the optical mode, A is the anharmonic coefficient, $\hbar$ is the reduced Planck constant, k_B is the Boltzmann constant, and T is the temperature. Across T_{N}, The frequency deviates abruptly or splits. The phonon frequency can either harden (increase in frequency) or soften (decrease in frequency). For the former case, it indicates a shorter bond length, a wider bond angle, and a stronger bond strength. For the latter case, the opposite is suggested. Moreover, phonon splitting is an indication of a structural distortion or a phase transition. The example is shown by the temperature dependence of infrared-active phonon modes in pyrochlore $Y_2Ru_2O_7$ [Fig. 2.13] [133]. The pyrochlore structure of $Y_2Ru_2O_7$ is a geometrically frustrated structure, which is relieved by the lowering of its energy by spin-phonon coupling. This is indicated by the softening of the phonon across the T_{N}.

We can also consider spin-phonon coupling with more complexity by expressing the general spin Hamiltonian:

$$\hat{\mathcal{H}}_{spin} = \sum_{i,j}[J_{ij}\langle S_i \cdot S_j\rangle + DM_{ij}\langle S_i \times S_j\rangle + S_i \cdot \Gamma_{ij} \cdot S_j] + A\sum_i (n_i \cdot S_i)^2. \tag{2.13}$$

Here, J_{ij} is the isotropic exchange interaction, DM_{ij} is the Dzyaloshinskii–Moriya interaction, and Γ_{ij} is the anisotropic exchange interaction. A and n are the single-ion anisotropic interaction coefficient and vectors. The interaction between spins is influenced by the Coulomb interaction between adjacent electrons, which in turn is greatly influenced by the positions of neighboring ions. When these ions are displaced, the spin interaction changes, causing the phonon frequencies to be adjusted

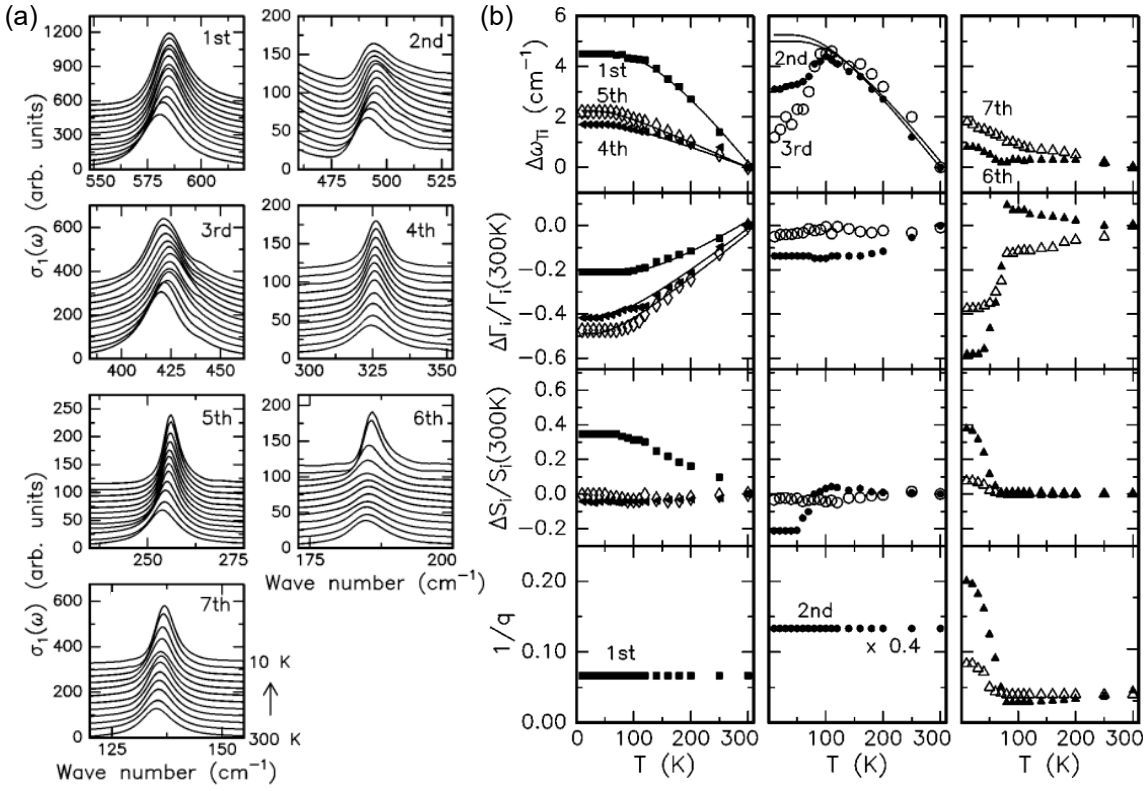


Figure 2.13: (a) Temperature dependence of each phonon mode in $Y_2Ru_2O_7$. (b) Phonon frequency (ω), damping constant (Γ), strength (S), and broad response ($1/q$) as a function of temperature. The deviation from the predicted behavior from the normal thermal effect indicates spin-phonon coupling [133].

or "renormalized". Simply, we ignore all of the terms except the symmetric exchange interaction, J_{ij}, so we can express the force constant ($k_{n,m}$) as:

$$k_{n,m} = \frac{\partial^2 \hat{\mathcal{H}}_{spin}}{\partial u_m \partial u_n} = \frac{\partial^2 J_{ij}}{\partial u_m \partial u_n}\langle S_i \cdot S_j \rangle + \frac{\partial^2 DM}{\partial u_m \partial u_n}\langle S_i \times S_j \rangle + \frac{\partial^2 A}{\partial u_m \partial u_n}(n^2 S_i^2) \\ = \lambda_J \langle S_i \cdot S_j \rangle + \lambda_{DM} \langle S_i \times S_j \rangle + \lambda_A (n^2 S_i^2). \tag{2.14}$$

Here, the $u_{n,m}$'s are the displacements. Typically, a $3d$ transition metal has dominant symmetric exchange interaction J_{ij}, which has a collinear spin structure. When 4- and $5d$ heavy metals are introduced, spin-orbit increases, leading to the Dzyaloshinskii–Moriya interaction and noncollinear spin structure. An example of spin-phonon coupling mediated by the Dzyaloshinskii–Moriya interaction in $Y_2Ir_2O_7$ is already given in the Introduction [Fig. 1.7]. An example of spin-phonon coupling mediated by single-ion anisotropy term is given by $Cd_2Os_2O_7$ in Fig. 2.14 [136].

Moreover, spin-phonon coupling can affect the phonon lifetime. The full width at half maximum of a phonon (Γ) is related to the phonon lifetime as:

$$\tau = \frac{\hbar}{\Gamma}. \tag{2.15}$$

Here, τ is the phonon lifetime, Γ is the full width at half maximum, and $\hbar$ is the reduced Planck's constant [137]. The phonon lifetime is determined by a combination of many different processes including three-phonon Umklapp, boundary, mass-difference, electron-phonon scattering, and spin-phonon scattering. By summing inverse lifetimes for each process, we can express $1/\tau$ as:

$$\frac{1}{\tau} = \frac{1}{\tau_u} + \frac{1}{\tau_b} + \frac{1}{\tau_m} + \frac{1}{\tau_{e-ph}} + \frac{1}{\tau_{s-ph}}, \tag{2.16}$$

where τ_u is Umklapp, τ_b is boundary, τ_m is mass-difference, τ_{e-ph} is the electron-

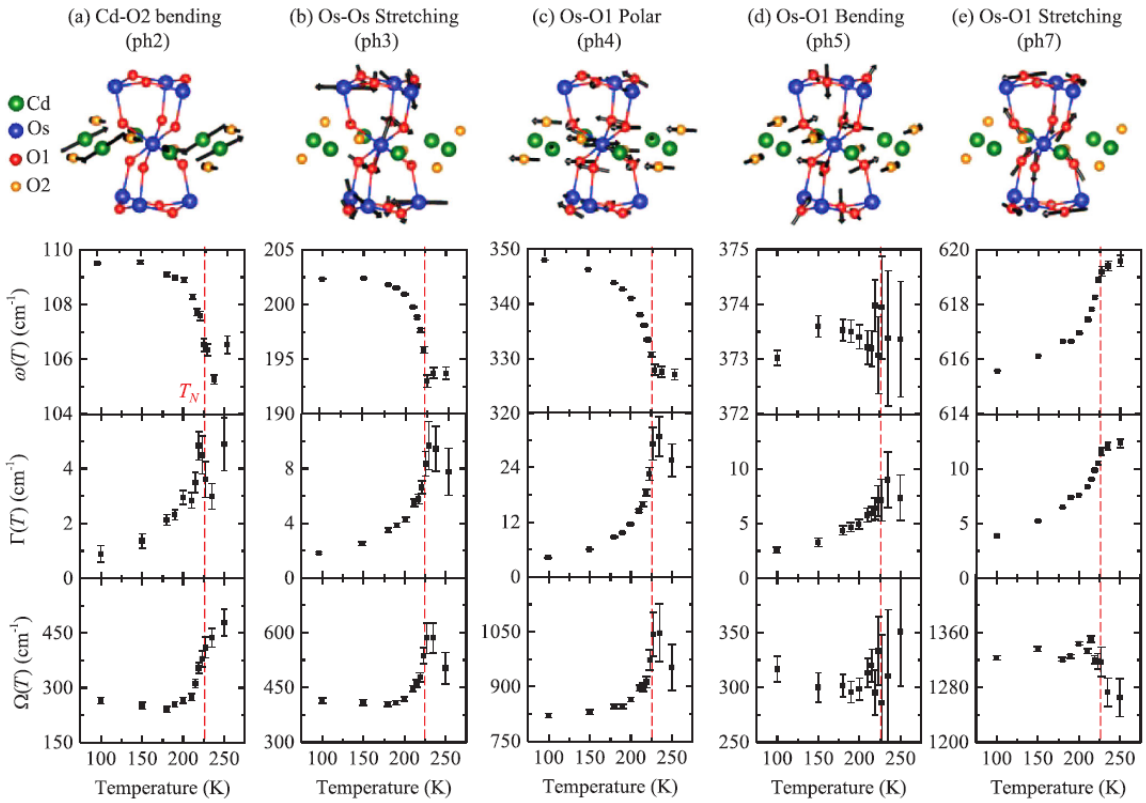


Figure 2.14: Phonon displacement pattern of $Cd_2Os_2O_7$ is shown on the top. The parameters (ω = phonon frequency, Γ = damping constant, Ω = phonon plasma frequency) for phonon modes as a function of temperature are displayed [136].

phonon scattering, τ_{s-ph} is the spin-phonon scattering [138]. Typically, the phonon lifetime will increase as the temperature decreases. Just like the phonon frequencies, the line widths will also behave anharmonically as [133]:

$$\Gamma_{anh}(T) = \Gamma_h + B(1 + \frac{2}{e^{\frac{\hbar\omega_o}{2k_BT}} - 1}). \tag{2.17}$$

Here, Γ_h is the harmonic contribution of line width, B is the anharmonic coefficient, $\hbar$ is the reduced Planck constant, k_B is the Boltzmann constant, and T is the variable temperature. However, different contributions of scattering will decrease the lifetime, which is important for spintronic applications [122–126].

2.6 Magnetism in a honeycomb lattice

To fundamentally lay the groundwork in magnetism, we discuss more in detail about different magnetic models we can use to describe frustration in magnetic interactions. The simplest magnetic model is the Ising model, an isotropic interaction between nearest-neighbor spins [139]. The spin is described in only two directions as only 'up' and 'down':

$$\hat{\mathcal{H}} = -J \sum_{ij} \sigma_i \sigma_j \quad \text{with} \quad \sigma_{i,j} = 1 \text{ or -1}. \tag{2.18}$$

Here, the $\sigma_{i,j}$ is the spin configuration of a discrete value of 1 and -1. The Heisenberg model is the same, except that spin configuration is in classical vectors as a continuous symmetry that can point in any direction [140]:

$$\hat{\mathcal{H}} = -J \sum_{ij} \hat{S}_i \cdot \hat{S}_j \tag{2.19}$$

Here, the $S_{i,j}$ are the spin operators. As you can see, the Heisenberg model has rotational symmetry with the spin operators. Both models have J as the symmetric interaction energy. If $J > 0$, the ferromagnetic interaction is favored [Fig. 2.15(a)]. For $J < 0$, the antiferromagnetic interaction is favored [Fig. 2.15(b)]. If $J = 0$, the spin is not interacting. The difference in treatment on the spin description has consequences in phase transitions, statistical mechanics, and physical properties with Mermin–Wagner theorem, which states that continuous symmetries cannot be spontaneously broken at finite temperature in systems of dimensions $d \leq 2$ [141]. Furthermore, there are other types of models that are derived from the Heisenberg model, such as the XXY model, the Kitaev model, the J_1-J_2 model, the $t - J$ model, and so forth.

In complex oxides, the direct exchange interaction does not occur often. Metal ions 'talk' through a ligand (oxygens in complex oxides). This is called superexchange interaction as shown in Fig. 2.16. In this type of exchange, there is a parameter called the hopping integral t, which is related to J by:

$$J \sim -\frac{t^2}{U} \tag{2.20}$$

and U is the Coulomb energy [142].

The Goodenough-Kanamori-Anderson rules are the general rules associated with this hopping parameter t and the geometry of the superexchange interaction [143]. These rules cover the tendencies toward a type of magnetic order. For example, antiferromagnetism is favored when electron transfers between overlapping orbitals that are half-filled. Ferromagnetism will occur for the electron transfer from a half-filled to an empty orbital and from a filled to a half-filled orbital. Here, a specific orbital involved in the exchange is critical. If the same orbital is involved, the antiferromagnetic state is favored, and ferromagnetism is preferred if the orbitals

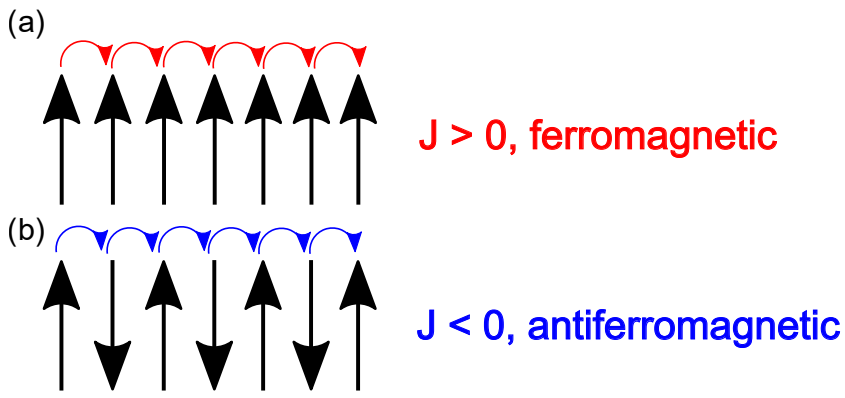


Figure 2.15: (a) A 1-dimensional ferromagnetic structure with $J > 0$. (b) antiferromagnetic structure with $J < 0$.

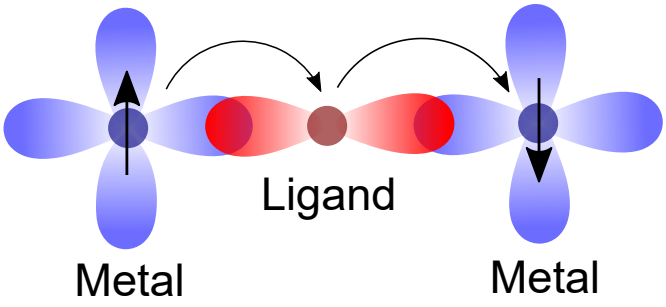


Figure 2.16: A schematic of superexchange between metal ions through a ligand. If the angle is 180°, antiferromagnetic interaction is favored. If the angle is 90°, ferromagnetic interaction is favored.

are different. Furthermore, there is an angular dependence to the exchange. If the angle of the superexchange is more towards 180°, then antiferromagnetism is favored. For an angle closer to 90°, then ferromagnetism is predicted [143]. However, when the exchange interactions compete, frustration sets in, and the conventional Goodneough-Kanamori rules are not enough. These competitions can lower the magnetic ordering temperature and promote exciting physics through the frustrated interaction. One of the settings where this appears is a honeycomb lattice.

A honeycomb lattice is a two-dimensional pattern of hexagons that resembles a honeycomb [Fig. 2.17(a)]. It is a common lattice structure found in various natural and synthetic materials, such as graphene, transition metal oxides, and magnetic materials. In recent years, honeycomb lattice has attracted considerable attention due to its unique electronic and magnetic properties. In particular, magnetic materials with honeycomb lattices exhibit interesting behavior, such as frustration [144–147], topological spin textures [148–153], and magnetic ordering [144, 154–156]. The frustration arises from the inability of magnetic moments to align in a single direction due to competing interactions [Fig. 2.17(b)], leading to a degenerate ground state. This frustration is particularly evident in antiferromagnetic honeycomb lattices, where neighboring spins tend to align in opposite directions [Fig. 2.17(c)]. Figure 2.18 summarizes the frustration of magnetic interaction in $Bi_3Mn_4O_{12}(NO_3)$, which has a honeycomb bilayer structure with $S = 3/2$ ground spin state [145]. The magnetic interactions include three intralayer interactions (J_1, J_2, and J_3) and four interlayer interactions (J_{c1}, J_{c2}, J_{c3} and J_{c4}) [Fig. 2.18(a,b)]. The compound is predicted to exhibit a disordered magnetic state because of the competition of interlayer interactions, J_{c1} and J_{c2} [157]. The neutron scattering verified the theoretical results by fitting the magnetic excitations [Fig. 2.18(c)].

One of the most famous examples of magnetic behavior in the honeycomb lattice

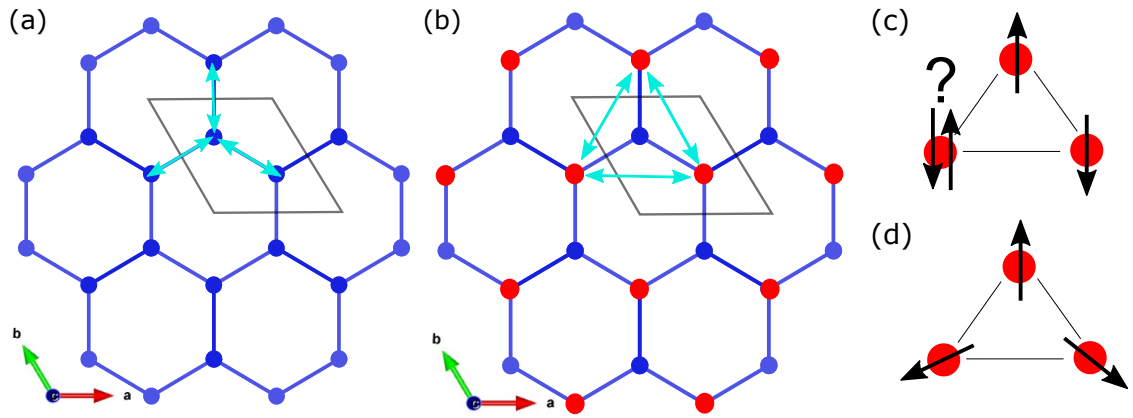


Figure 2.17: (a) A schematic of a honeycomb lattice with one type of atom is displayed. (b) A schematic of a honeycomb lattice with two distinct types of atoms is displayed. (c) A triangular interaction that leads to frustration. (d) One of the ways is to relieve the magnetic frustration, which leads to a noncollinear magnetic structure.

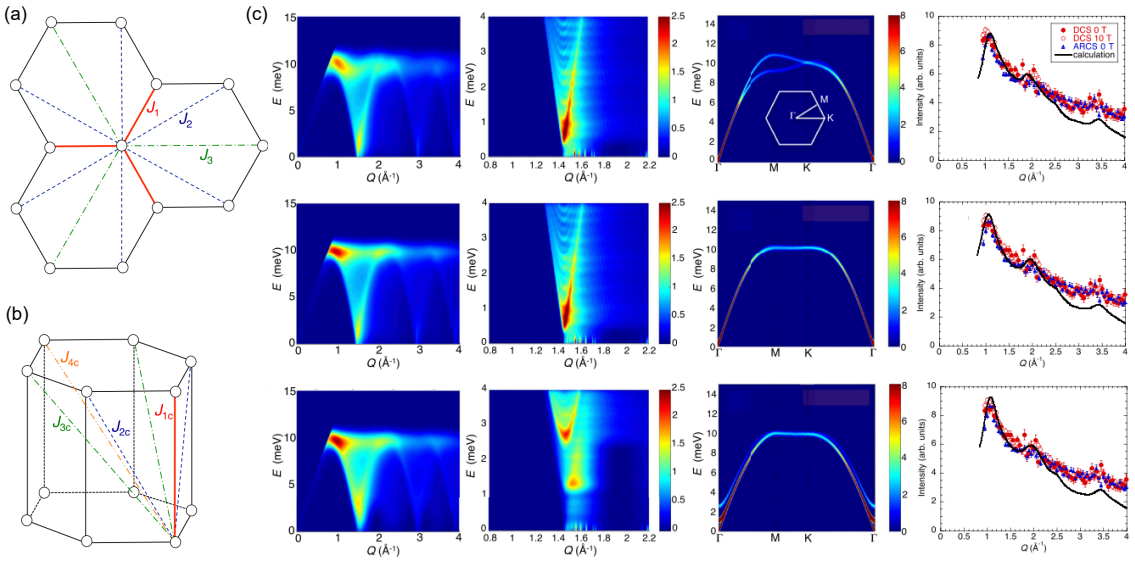


Figure 2.18: (a,b) A schematic of honeycomb bilayer structure and magnetic interactions in $Bi_3Mn_4O_{12}(NO_3)$ is displayed. (c) Calculated neutron scattering spectra with linear spin wave theory is displayed here. The magnetic field (10 T) is included perpendicular to the spin directions [145].

is the Kitaev model, proposed by Alexei Kitaev in 2006 [148]. The Kitaev model is a spin-1/2 model with interactions between nearest-neighbor spins, in which the interactions are anisotropic and depend on the orientation of the spins relative to the bonds connecting them as [158]:

$$\hat{\mathcal{H}} = \sum_{ij} K S_i^{\alpha} S_j^{\alpha} + \sum_{ij} K S_i^{\beta} S_j^{\beta} + \sum_{ij} K S_i^{\gamma} S_j^{\gamma}. \tag{2.21}$$

The Kitaev model exhibits a quantum spin liquid ground state, which is a highly entangled state with no long-range order, even at zero temperature. The quantum spin liquid state has potential applications in quantum computing, as it can be used to store and manipulate quantum information [159]. The topological spin textures in honeycomb lattices arise from the presence of topological defects, such as vortices and skyrmions [151–153]. These defects are characterized by a nontrivial topology, which results in a protected spin texture that cannot be easily destroyed. For example, skyrmions form due to the Dzyaloshinskii-Moriya interaction in ferromagnetic honeycomb lattices, which breaks the inversion symmetry and induces a chiral spin texture [160, 161]. The presence of these skyrmions can lead to novel spintronics applications, such as skyrmion-based memory devices [160]. In antiferromagnetic honeycomb lattices, the magnetic ordering can be described by a Kitaev model, which exhibits a topological phase transition between a trivial and a nontrivial phase [162] [Fig. 2.19]. This phase transition is related to the presence of Majorana fermions, which are quasiparticles that are their own antiparticles and have potential applications in quantum computing [163].

The effect of honeycomb lattice on magnetism has been studied in various materials, such as Na_2IrO_3 [165, 166] and α-$RuCl_3$ [167, 168], and $Na_2Co_2TeO_6$ [169, 170]. For example, Na_2IrO_3 is a spin-orbit-coupled Mott insulator that exhibits antiferromagnetic ordering with a honeycomb lattice structure (space group of $C2/m$) [Fig.

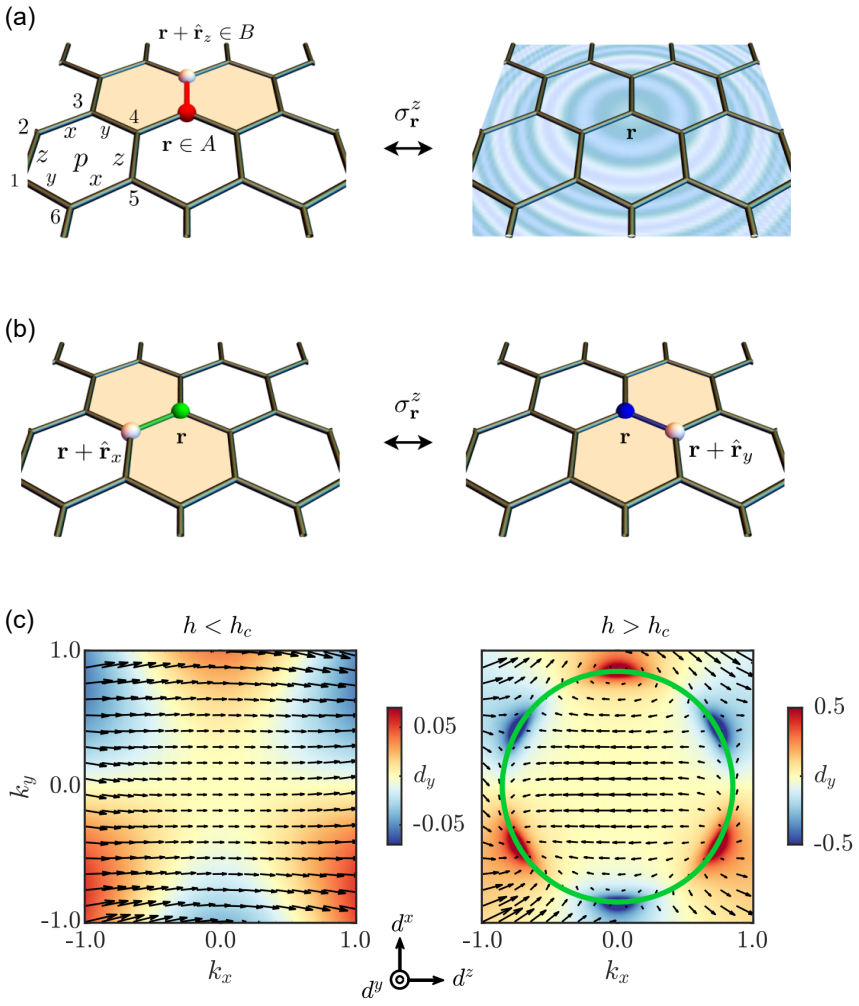


Figure 2.19: (a,b) Hybridization and hopping of 'flux-pair', respectively. (c) continuous topological phase transition is shown. The $h < h_c$ is topologically trivial, but the $h > h_c$ includes six merons [164].

2.20(a)] [165]. The Iridium has a pseudo spin of $S_{eff} = 1/2$. The magnetic transition temperature is $T_{\mathrm{N}} = 15$ K, which is smaller than the Weiss temperature $\Theta =$ -116. This indicates the frustration in the magnetic interaction [165]. The magnetic frustration index is defined as $f = \frac{|\Theta|}{T_{\mathrm{N}}}$ [171]. Using x-ray diffraction and inelastic neutron scattering, the magnetic order was determined to be a zig-zag structure [Fig. 2.20(b)] [166]. The signature of Kitaev interaction was revealed using resonant inelastic X-ray scattering [Fig. 2.20(c)] [172]. Another Kitaev candidate material is α-$RuCl_3$, which is a layered honeycomb lattice material (also $C2/m$ space group) [Fig. 2.20(d)] [167]. The crystal has a hexagonal face, which is a result of the crystal structure as shown in Fig. 2.20(e) [155]. Ru^{3+} has $J_{eff} = 1/2$ state, same as in the iridate materials. α-$RuCl_3$ exhibits antiferromagnetic ordering at low temperatures ($T_{\mathrm{N}} \approx 13$ K) [167]. The magnetic ordering in α-$RuCl_3$ is a zig-zag structure as a ground state, which is predicted within the framework of the Kitaev model [Fig. 2.20(f)]. Lastly, $Na_2Co_2TeO_6$ is another promising Kitaev candidate material. The compound also hosts a honeycomb lattice with Co^{2+} ion in the octahedral environment [Fig. 2.20(g)] [170]. The spin-orbit coupling splits the degenerate S = 3/2 states into S = 1/2 ground state. The magnetic structure in the ground state is argued to be either zig-zag or triple-Q state [169, 173]. With the absence of a linear magnetoelectric term and the structure distortion/phase transition, the zig-zag magnetic structure is likely [173]. With the application of the magnetic field, the spin-liquid phase is reported [169, 173].

2.7 Two-dimensional transition metal chalcogenides

The two-dimensional (2D) van der Waals crystals are under extremely high scientific interest for the fundamental understanding of the quantum nature of these materials as well as application purposes. The ability to exfoliate to a single layer

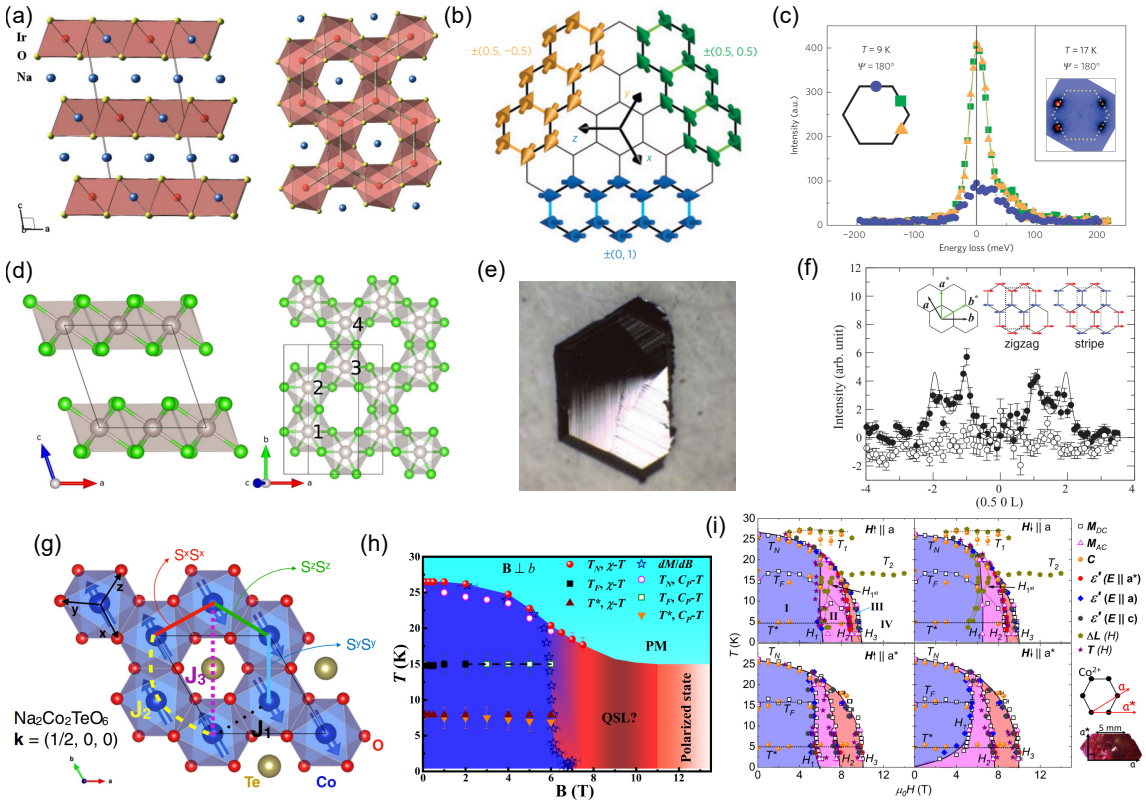


Figure 2.20: (a) A crystal structure of Na_2IrO_3, zig-zag magnetic structure, and evidence of the anisotropic bonds in RIXS measurement are displayed [165,166]. (b) A crystal structure of α-$RuCl_3$, a picture of physical crystal, and neutron scattering measurement are shown [167,168]. (c) A crystal structure of $Na_2Co_2TeO_6$ and two phase diagrams as a function of temperature and magnetic field are shown [169,170, 173].

improves mechanical, optical, electronic, and magnetic properties, enabling wearable technologies with thin, flexible, and nano-scale devices [174–177]. These materials are composed of metal atoms with a ligand arranged in a layered 2D lattice structure. The chalcogen atoms act as spacers between the metal atoms, allowing for the formation of strong intra-layer covalent bonds and weak inter-layer van der Waals interactions. This structure gives rise to their unique properties, such as tunable band gaps, high carrier mobility, and strong light-matter interactions [178–181].

One of the most studied 2D van der Waals crystals is molybdenum disulfide [Fig. 2.21(a)]. MoS_2 is a semiconductor with a direct bandgap [Fig. 2.21(b)], making it an excellent material for optoelectronic applications. It exhibits strong photoluminescence and excellent electrical properties [179, 182], including high carrier mobility and low contact resistance. The unique properties of MoS_2 have led to its use in a variety of applications, including photovoltaics, field-effect transistors, and sensors [179, 183–185]. Another 2D van der Waals chalcogenide that has received attention is tungsten diselenide (WSe_2). Like MoS_2, WSe_2 is a semiconductor with a direct bandgap. However, WSe_2 has a larger bandgap than MoS_2, making it useful for applications in the visible range of the electromagnetic spectrum. WSe_2 also exhibits high carrier mobility and excellent electrical properties, making it a promising material for optoelectronic devices [186, 187]. Other 2D van der Waals chalcogenides that have been studied include molybdenum diselenide ($MoSe_2$), tungsten disulfide (WS_2), and niobium diselenide ($NbSe_2$). These materials exhibit similar properties to MoS_2 and WSe_2, including direct bandgaps and high carrier mobility.

Strong light-matter interactions are one of the unique properties of 2D transition metal chalcogenides. The thinness of the materials allows for efficient light absorption and emission, making them ideal for optoelectronic applications [188]. Therefore, the electronic and optical properties can be tuned by controlling the number of layers

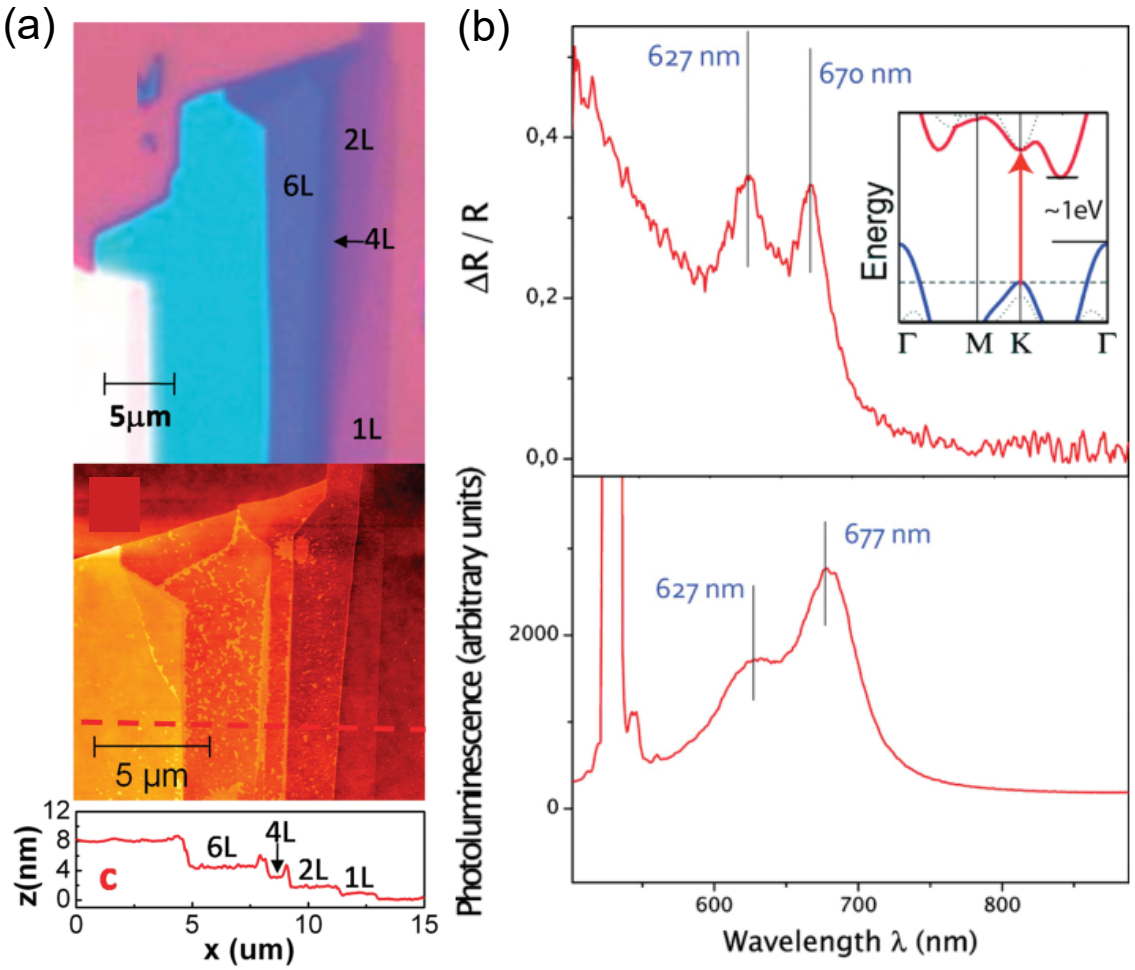


Figure 2.21: (a) Images of exfoliated MoS_2 flakes on Si substrate is displayed. The exfoliation was performed down to 1 layer. (b) Reflection and photoluminescence spectra of MoS_2 layers are shown. The absorption is at 1.85 and 1.98 eV [182].

and the composition of the material. Unlike graphene, which has a zero bandgap and therefore cannot be used for electronics [189–192], transition metal chalcogenides have a finite bandgap that can be tuned by controlling the number of layers and the composition of the material. For example, single-layer MoS_2 has a direct bandgap of 1.8 eV, which makes it suitable for optoelectronic applications, while bilayer MoS_2 has an indirect bandgap of 1.2 eV, which makes it suitable for field-effect transistors [193, 194].

2D transition metal chalcogenides also exhibit interesting magnetic properties. For example, MoS_2 has been shown to exhibit ferromagnetic behavior at the edges of the material, while the bulk material is diamagnetic [195]. This behavior is attributed to the presence of sulfur vacancies, which act as magnetic dopants. Furthermore, magnetism in these materials has allowed the concept of low-power ultra-compact 2D spintronic devices [125,196–199]. Experimental results of ferromagnetism in CrI_3 and $Cr_2Ge_2Te_6$ at the single layer have opened the doors for layer-dependent magnetism [200–203], followed by a family of 2D van der Waals magnetic crystals [204–208]. To give examples, Fig. 2.22(a-d) summarizes the electrical control with CrI_3 dual-gate device by applying a magnetic field, and Fig. 2.22(e,f) displays magnetic control with $Cr_2Ge_2Te_6$ with electrostatic gating.

Transition metal phosphorus trisulfides with chemical formula MPS_3 (M = Mn, Fe, Co, Ni, Zn, and Cd) are one of the magnetic family members of 2D van der Waals [Fig. 2.23(a,b)] [211]. Among them, $MnPS_3$ has an interesting prediction of ferrotoroidicity [212], although experimental results are absent so far [213]. Furthermore, the ease of exfoliation and tunability in external stimuli of $MnPS_3$ have attracted great attention. Examples include the tunability of electronic and magnetic properties [Fig. 2.23(c,d,e,f,g)] [214, 215], Dirac cones and topological magnetism at the monolayer limit [216], the layer-dependent structural and symmetry restora-

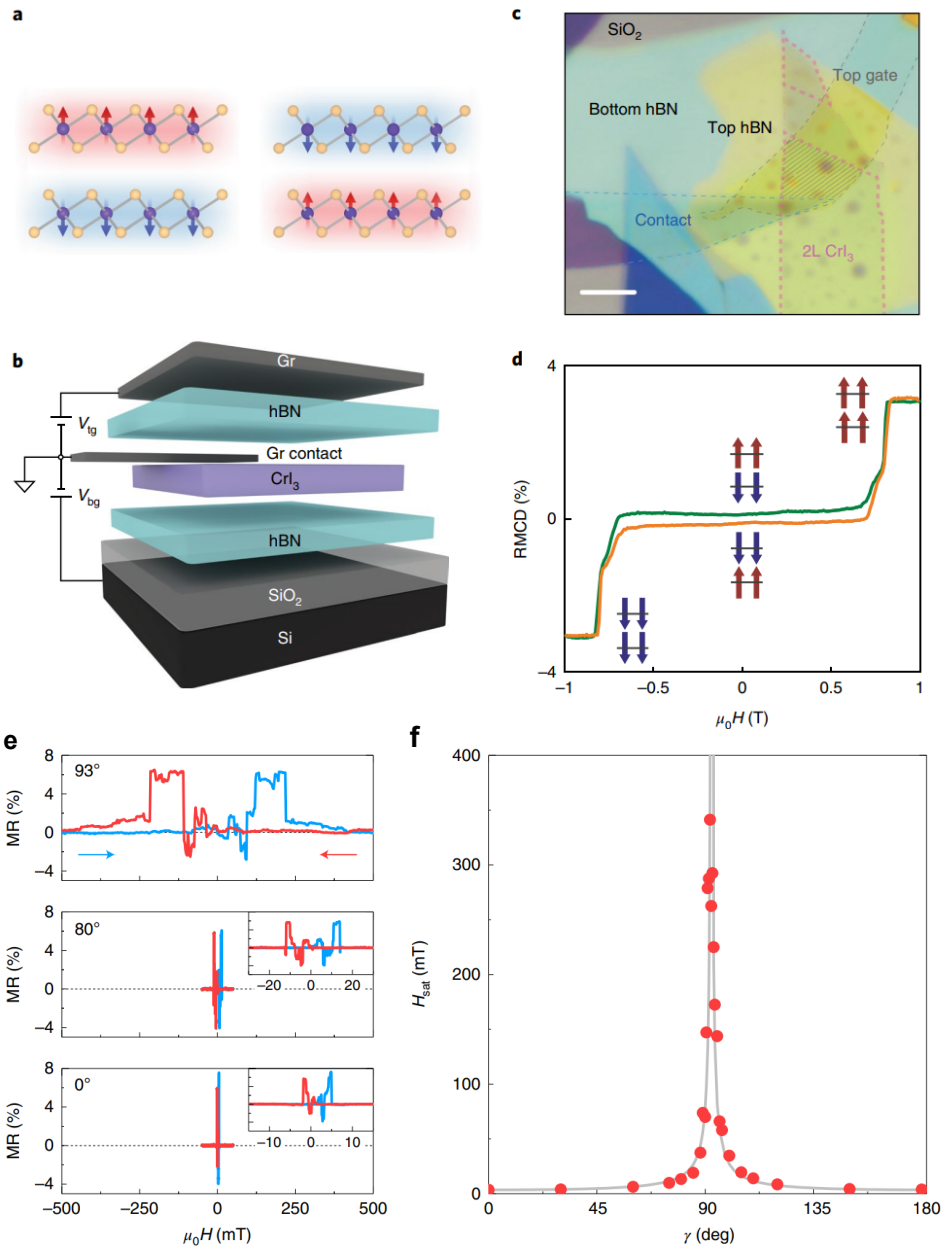


Figure 2.22: (a) A schematic of the CrI_3 crystal structure with magnetic ordering is shown. (b) A schematic of a CrI_3 dual-gated device is displayed. (c) the image of the dual-gated device is shown. (d) The reflectance magneto-circular dichroism (RMCD) signal as a function of the magnetic field is displayed for CrI_3. It starts as an antiferromagnetic state and transitions to a ferromagnetic state at around 0.75 T [202]. (e) Magnetoresistance signal as a function of the magnetic field and the angle is shown for $Cr_2Ge_2Te_6$. (f) A saturated field as a function of the angle γ in degrees is shown [203].

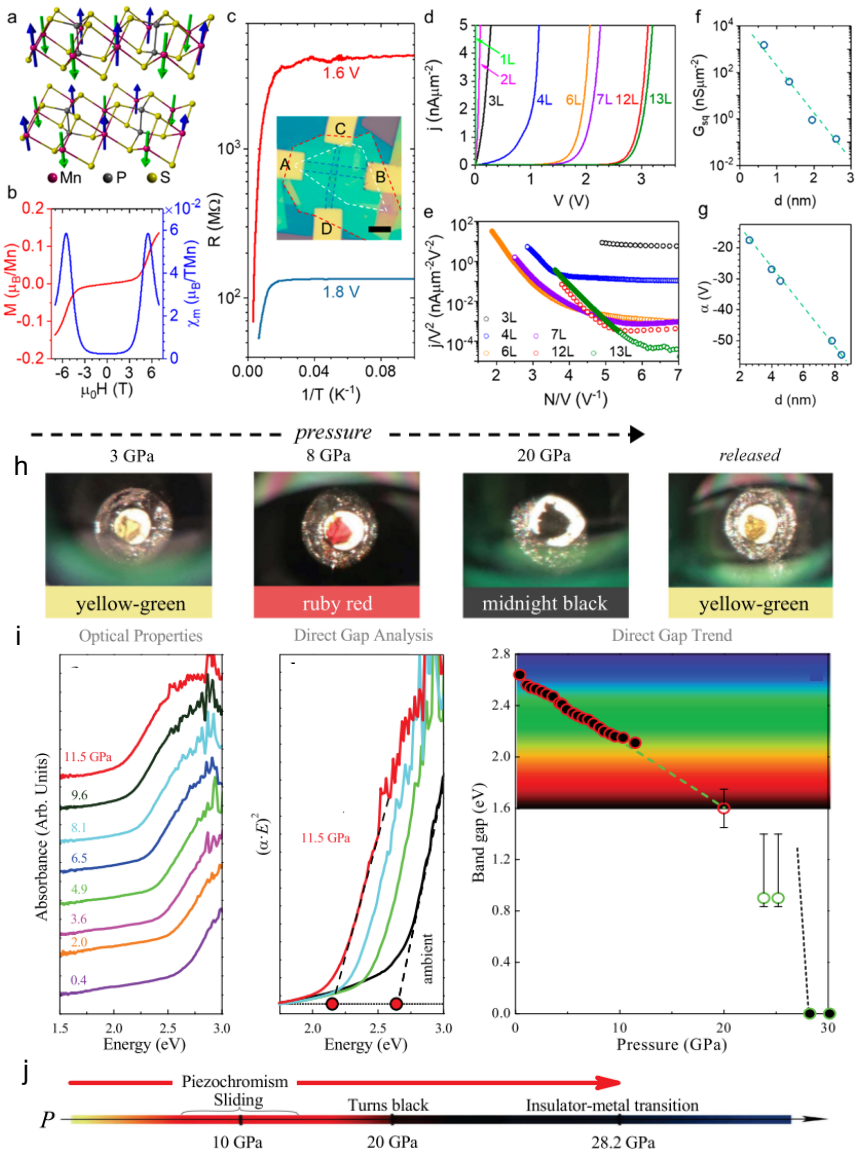


Figure 2.23: (a) Antiferromagnetic structure of $MnPS_3$. (b) Magnetization and magnetic susceptibility as a function of the magnetic field. (c) Resistance of a six-layer $MnPS_3$ device measured with 1.6 V (red) and 1.8 V (blue) applied bias. (d) Tunneling current density j at T = 1.5 K as a function of bias for different thicknesses of $MnPS_3$. (e) In the Fowler-Nordheim tunneling regime at high bias, $\ln(\frac{j}{V^2}$ is proportional to $\frac{N}{V}$. (f) The linear tunneling conductance decreases exponentially with $MnPS_3$ thickness. (g) the coefficient α decreases linearly with d [209]. (h) Pressure-induced color change of $MnPS_3$. (i) Absorption spectra and Tauc's plot as a function of pressure is displayed with band gap vs. pressure plot. (j) A schematic of pressure transitions [210].

tion with near-field infrared spectroscopy [217, 218], pressure-induced spin-crossover, insulator-metal, sliding, and superconducting transition with piezochromism [Fig. 2.23(h,i,j)] [210, 219, 220], linear magnetoelectricity at the ultrathin limit using the optical second harmonic generation [221], magnetism at the single monolayer [209], and ripple-induced symmetry crossover at the ultrathin limit [222]. On the other hand, $CrPS_4$ is a cousin of MPS_3 family with different stoichiometry and the absence of phosphorus-phosphorus dimer. However, $CrPS_4$ also displays similarly interesting properties, such as bulk antiferromagnetic to ferromagnetic state in the single-layer [214, 223], piezomagnetic response under strain [224], pressure-induced insulator-metal transition [225], structural stability down to the monolayer limit [226], the control of ferromagnetism with air-stability [227], and pressure-induced symmetry-breaking [228].

2.8 Materials of interest

2.8.1 $Fe_2Mo_3O_8$ and its analogs

$Fe_2Mo_3O_8$ is a polar magnet with giant magnetoelectric coupling, strong Dzyaloshinski-Moriya interactions, valence bond condensation (creating a cluster magnet), and the possibility of orbitally-selective transitions [28, 229–235]. Zinc substitution, first on the tetrahedral Fe site and then on the octahedral Fe site [31, 231], is of interest for magnetic properties as well [31, 230, 236, 237]. The structure of $Fe_2Mo_3O_8$ consists of corner-shared tetrahedral and octahedral sites separated by layers of Mo trimers [Fig. 2.24(a,b)] [229, 238, 239]. The FeO_4 tetrahedron is significantly elongated and distorted, and the FeO_6 octahedron is trigonally distorted as well, leading to a C_{3v} point group on both tetrahedral and octahedral Fe sites. As a result, $Fe_2Mo_3O_8$ has no inversion symmetry. The system has a 61 K magnetic ordering transition to a collinear

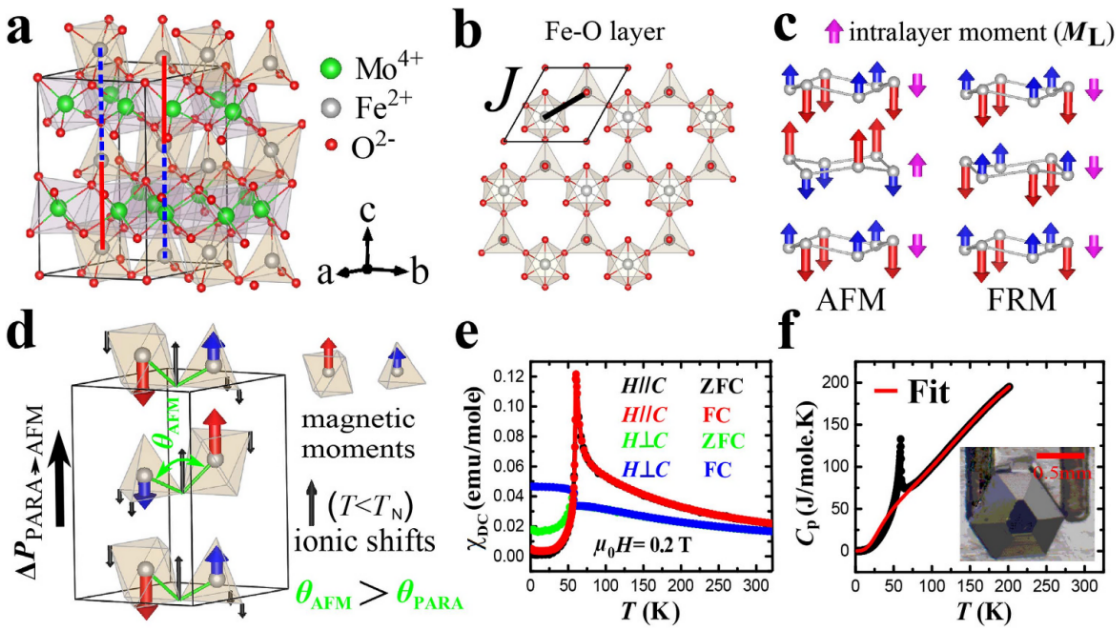


Figure 2.24: (a) Crystal structure of $Fe_2Mo_3O_8$. (b) A top view of the Fe-O layer, where the honeycomb lattice can be seen. The line represents the largest Fe-Fe exchange interaction J. (c) A schematic of antiferromagnetic (AFM) state and ferrimagnetic (FRM) state is displayed for $Fe_2Mo_3O_8$. (d) The change in polarization is along the c-axis due to the oxygen shift. (e) Magnetic susceptibility reveals $T_N \approx 61$ K. (f) Heat capacity also displays a phase transition at around 61 K with a picture of the crystal in the inset [28].

antiferromagnetic state with a concomitant structural distortion [Fig. 2.24(c,d,e,f)] [28, 29, 240–242]. Antiferromagnetic antiphase domain boundaries have been imaged in this state [117]. $Fe_2Mo_3O_8$ also displays a 5 T transition to the ferrimagnetic state with an extremely large magnetoelectric coefficient [28, 231]. $Ni_2Mo_3O_8$ also hosts robust magnetoelectric coupling with a field-tunable coupling mechanism [243]. Spectroscopic highlights in $Fe_2Mo_3O_8$ include (i) nonreciprocal directional dichroism [64], phonon trends across T_N [29, 242], and a variety of magnetic excitations in the terahertz range [244], (ii) Mössbauer to confirm the 2+ charge on the iron site [240, 241], and (iii) studies of charge transfer via time-dependent optical Kerr effects [245] complemented by first principles electronic structure calculations [31, 242, 246].

2.8.2 Ni_3TeO_6

The crystal structure of Ni_3TeO_6 is both polar and chiral as expected for an $R3$ space group [247]. Chains of distorted NiO_6 and TeO_6 octahedra lie along the c direction, and the three different Ni centers are distinguished by their local environments [248]. In this work, we denote the threefold axis of Ni_3TeO_6 as the 'chiral axis' of the compound [108, 248]. Although Ni_3TeO_6 hosts interlocking ferroelectric and chiral domain patterns [Fig. 2.26(a,b)] [248, 249], crystals can be polished to reveal a single chiral domain [Fig. 2.26(l)] [250]. Below $T_N = 53$ K, the system displays a collinear antiferromagnetic ground state [Fig. 2.25]. For $\mathbf{H}\|c$, there is a spin-flop transition at 9 T leading to a conical spin and a metamagnetic transition at 52 T - both of which are accompanied by magnetoelastic effects [Fig. 2.25 and Fig. 2.26(k)] [62, 251–253]. There are no magnetically-driven phase transitions when field is applied perpendicular to the c-axis [252]. The optical properties of Ni_3TeO_6 consist of several different color bands comprised of on-site Ni^{2+} d-to-d excitations along with a charge gap near 2.6 eV [68]. These features are sensitive to spin-

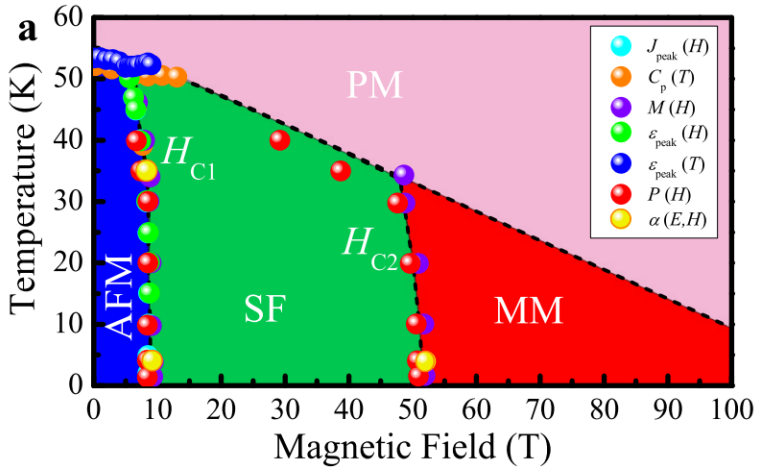


Figure 2.25: (a) A phase diagram of Ni_3TeO_6 is shown as a function of temperature and magnetic field. The T_N is at 53 K where the antiferromagnetic (AFM) ground state is displayed. At around 9 T, the spin-flop transition is observed and the meta-magnetic state is achieved at above 50 T. The saturation field is extrapolated to be above 100 T. [250].

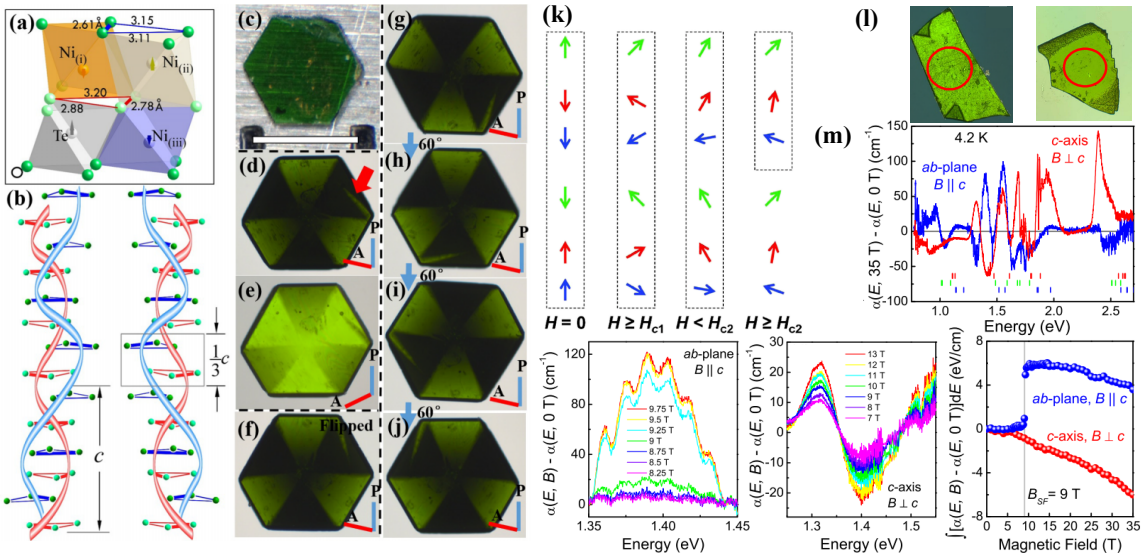


Figure 2.26: (a) The basic building block of Ni_3TeO_6 is displayed, which corresponds to one-third of one unit cell. We denoted the shortest bonds in red and blue triangles as bold lines. (b) Two different ferri-chiral states are shown as red and blue colors. (c) An optical microscope image of a 100 μm-thick single crystal of Ni_3TeO_6 is shown with the scale bar equals 1 mm. (d-j) The chiral domains of a Ni_3TeO_6 crystal are visible in transmission polarized optical microscope images are shown. Blue and red bars represent the angles of a polarizer and an analyzer, respectively [248]. (k) Magnetic structure and magnetic phase transitions are shown [252]. (l) Polished single crystal of Ni_3TeO_6 is shown, which has only one chiral domain [250]. (m) Spectroscopic properties of Ni_3TeO_6 as a function of the magnetic field. [68].

flop and metamagnetic transitions [Fig. 2.26(m)], and because spin-orbit coupling endows the excitations with magnetoelectric character, these phases support nonreciprocal directional dichroism [250]. Here, the excited Ni state (with a hole in the t_{2g} orbital) provides spin-orbit coupling on the order of 40 meV and assures that the matrix elements containing polarization and magnetization are non-zero [250]. Significantly, the broad band nonreciprocal directional dichroism in the magnetochiral configuration of Ni_3TeO_6 can be modeled using a quantitative first-principles-derived formalism [250].

2.8.3 $Co_4B_2O_9$ (B = Nb, Ta)

The $Co_4B_2O_9$ (B = Nb, Ta) system is quasi-two dimensional with a $P\bar{3}c1$ space group [Fig. 2.27(a)] [254]. This corundum-type structure is derived from Cr_2O_3 where four Cr sites are occupied by the magnetic Co^{2+} ions and two nonmagnetic Nb^{5+} or Ta^{5+} ions reside in the B sites. The octahedrally-coordinated Co^{2+} centers are trigonally distorted and both edge- and face-sharing. The B ions also occupy trigonally distorted octahedral sites in the buckled layer. Both systems order antiferromagnetically at T_N = 27 and 20 K for $Co_4Nb_2O_9$ and the Ta analog, respectively [Fig. 2.27(b)] [255, 256]. Originally thought to host collinear ab-plane spin structure with a small moment along c [254, 257], more recent work establishes a noncollinear spin arrangement - even sporting a different magnetic space group [258–260]. A number of teams report magnetostriction across T_N - presumably within the same space group [Fig. 2.27(c,d,e)] [261–263]. Under a magnetic field, these materials reveal a spin-flop transition (at 0.3 T for $H \parallel ab$) [255, 256, 261], large magnetoelectric coupling [261,262,264,265], magnetodielectric behavior [266], and a symmetry reduction with asymmetric distortion [Fig. 2.27(f)] [263]. The magnetoelectric coupling is approximately $\alpha_{[110]} = 20$ ps/m for both compounds [261,262,264,265]. Interestingly,

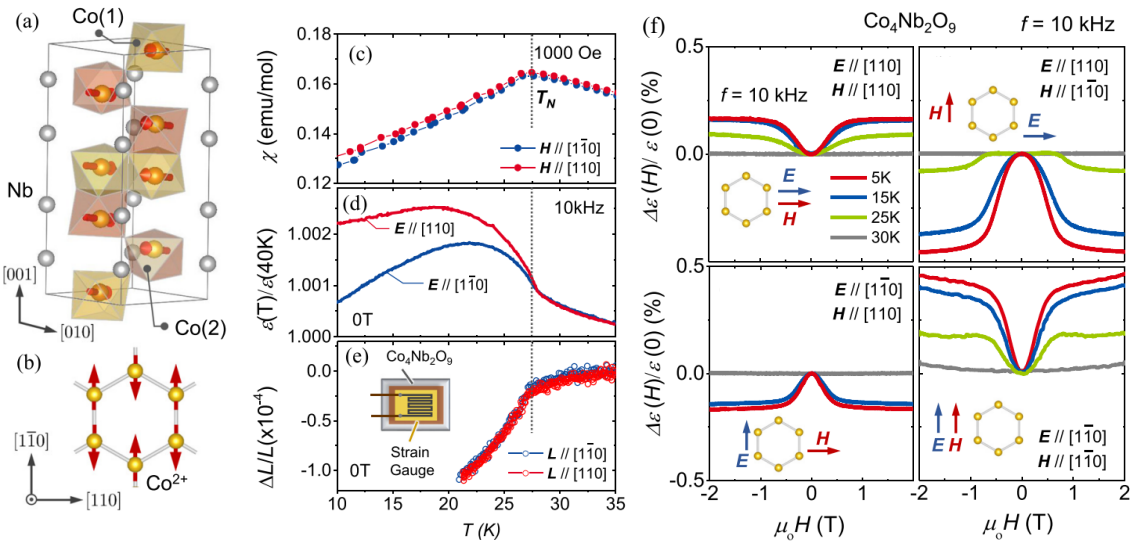


Figure 2.27: (a) A crystal structure of $Co_4Nb_2O_9$. (b) Magnetic structure in a honeycomb lattice in $Co_4Nb_2O_9$. (c,d,e) susceptibility, permittivity, and strain measurements reveal a magnetic ordering transition at around 27 K. (f) permittivity as a function of the magnetic field. Spin-flop transitions are revealed and anisotropic behavior is displayed as the directions of the magnetic field change [263].

this interaction is nonlinear [267, 268]. Despite evidence for magnetostriction across T_N [257, 262, 263, 269] and proposals that cast spin-phonon coupling as the underlying mechanistic driver for these effects [258, 261, 264, 269], the fundamental excitations of the lattice and their changes across the magnetic ordering transitions are under-explored with only one recent Raman study of polycrystalline $Co_4Nb_2O_9$ that identifies two low-frequency modes at 132 and 178 cm^{-1} that are sensitive to the magnetic ordering transition [266]. The absence of lattice dynamics calculations in that study unfortunately prevents additional analysis. $Co_4Nb_2O_9$ and the Ta analog are also ideal platforms for unraveling structure-property relations - not just across property trends but in higher level coupling processes as well [270].

2.8.4 $MnPS_3$ and $CrPS_4$

$MnPS_3$ has a $C2/m$ space group [271], forming Mn^{2+} honeycomb lattice in the ab-plane [Fig. 2.28(a,b)]. The Mn^{2+} ion with $S = \frac{5}{2}$ ground spin state is in the trigonally distorted octahedral environment surrounded by S atoms, which connects to other octahedrons by edge-sharing. The layer thickness is $\approx$3.22 $\mathring{A}$ separated by the van der Waals gap of $\approx$3.27 $\mathring{A}$ [Fig. 2.28(a,b)]. For $CrPS_4$, there is a controversy over the $C2$ vs. $C2/m$ space group [272–274], which we will discuss later. Regardless, Cr^{3+} ions create a rectangular lattice without the P-P dimer [Fig. 2.28(c,d)] [226, 228]. Each Cr^{3+} (S = 3/2) ion is also coordinated octahedrally by S atoms with a slight distortion. The layer thickness of $CrPS_4$ is slightly bigger than $MnPS_3$ with 3.69 $\mathring{A}$, but a smaller separation of 2.46 $\mathring{A}$ van der Waals gap is exhibited [Fig. 2.28(c,d)]. $MnPS_3$ undergoes T_N transitions from a paramagnetic state to Heisenberg-type collinear antiferromagnetic state at 78 K [274–276], whereas $CrPS_4$ has $T_N = 36$ K and $T' \approx 35$ K that is similar to a spin-reorientation [277]. A recent report of $MnPS_3$ suggests another magnetic transition from Heisenberg to XY system at around 38 K [278].

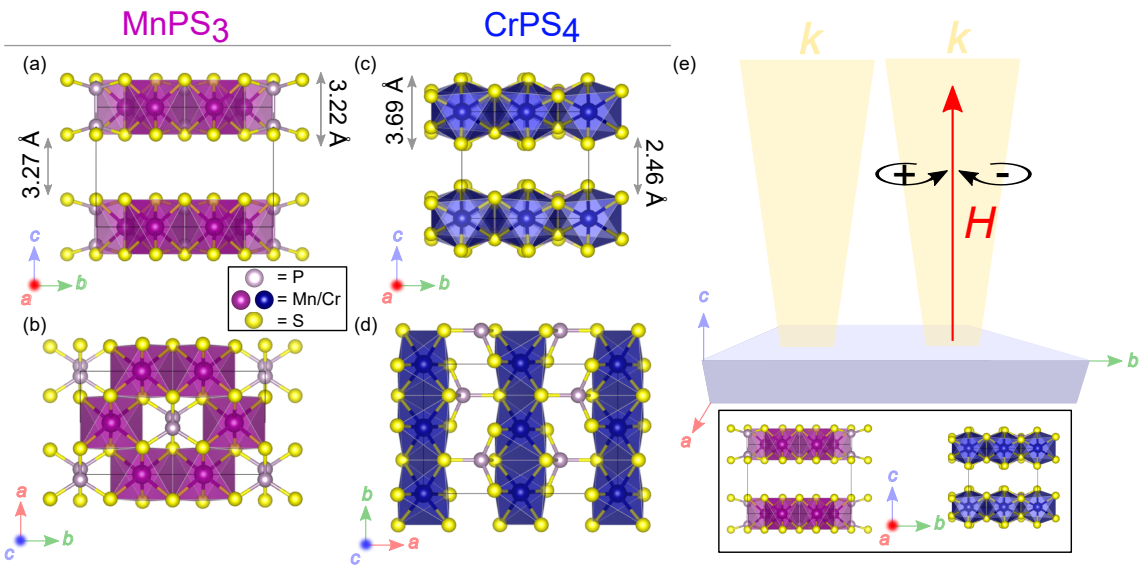


Figure 2.28: (a) The crystal structure of $MnPS_3$ in the a-axis view is displayed. The sheet thickness and size of the van der Waals gap are indicated as 3.22 and 3.27 $\mathring{A}$. (b) the c-axis view shows a clear hexagonal structure in the ab-plane. (c) The crystal structure of $CrPS_4$ with the sheet thickness of 3.69 $\mathring{A}$ and van der Waals gap of 2.46 $\mathring{A}$. (d) Unlike $MnPS_3$, $CrPS_4$ has a rectangular structure. (e) The experimental diagram is shown, displaying two light propagation, k, to differentiate the unpolarized and circularly-polarized measurements for optical spectroscopy and magnetic circular dichroism. H is the magnetic field. The bottom slab is the sample as indicated with the crystal structure.

With the magnetic field along $\parallel$ c-axis, Both $MnPS_3$ and $CrPS_4$ undergoes spin-flop transition at $\approx$5 and $\approx$1 T [209, 279, 280]. Spectroscopic studies of $MnPS_3$ include characterization and temperature dependence of d-to-d excitations and the band gap [281–283], exciton-magnon structure [284], a large exciton binding energy, [285] magnetic dynamics using ultrafast optical spectroscopy [286], vibrational spectra as a function of layer number [217, 218], piezochromism as a function of temperature and pressure [210], and Raman-active phonon modes as a function of temperature that reveals magnetoelastic coupling by spin-phonon coupling with 120, 155, and 160 cm^{-1} phonon modes [287–290], For $CrPS_4$, absorption and photoluminescence spectroscopy as a function of layers [225,291,292], infrared- and Raman-active phonon modes under pressure [228], polarized Raman-active phonon modes [293], and single-layer phonon modes using near-field [226]. However, the nature of the band gap and the local excitations in $CrPS_4$ has been misunderstood and mischaracterized.

Chapter 3

Spectroscopic methods

3.1 Optical theory

Light-matter interactions are determined by the optical properties of a material. Since electromagnetic wave has electric and magnetic field vectors, they can interact with the electronic and magnetic structure of solids. Therefore, we analyze and interpret the optical properties to understand the interactions among spin, orbital, lattice, and charge dynamics in a solid. Experimentally, optical properties can be determined from the reflectance R(ω) and transmittance T(ω) measurements, which are frequency dependent. From those measurements, we can extract various optical constants including absorption coefficient $\alpha(\omega)$, dielectric function $\epsilon_1(\omega)$, optical conductivity $\sigma(\omega)$, plasma frequency ω_p, oscillator strength S, and relaxation time $\tau(\omega)$ by using Kramers-Kronig analysis [294,295]. Furthermore, external stimuli such as magnetic field are combined with spectroscopic methods to drive quantum phase transitions, which will be discussed as well.

3.1.1 Maxwell's Equations

Maxwell's equations of electromagnetic waves lead to the understanding of light-matter interactions. By using these four equations, we can start to describe the optical properties of matter [294, 296].

$$\begin{aligned} \nabla \cdot \mathbf{D} &= \rho^{ext} \\ \nabla \cdot \mathbf{B} &= 0 \\ \nabla \times \mathbf{E} &= -\frac{\partial \mathbf{B}}{\partial t} \\ \nabla \times \mathbf{H} &= -\frac{\partial \mathbf{D}}{\partial t} + \mathbf{J}^{cond} + \mathbf{J}^{ext}. \end{aligned} \tag{3.1}$$

Here, $\mathbf{D}$ and $\mathbf{B}$ are the displacement field and magnetic induction, $\mathbf{E}$ and $\mathbf{H}$ are the electric and magnetic field, ρ^{ext} is the charge density induced by the external force, $\mathbf{J}^{cond}$ and $\mathbf{J}^{ext}$ are the current densities arising from the conduction electron and induced by an external force.

By assuming an isotropic media, we can obtain a linear response for $\mathbf{D}$, $\mathbf{B}$, and $\mathbf{J}^{cond}$ by these relations:

$$\begin{aligned} \mathbf{D} &= \epsilon \mathbf{E} \\ \mathbf{B} &= \mu \mathbf{H} \\ \mathbf{J}^{cond} &= \sigma \mathbf{E}, \end{aligned} \tag{3.2}$$

where ϵ is the dielectric function, μ is the magnetic permeability, and σ is the optical conductivity. Furthermore, polarization and magnetization are also linear functions:

$$\begin{aligned} \mathbf{P} &= \chi_e \mathbf{E} \\ \mathbf{M} &= \chi_m \mathbf{H}, \end{aligned} \tag{3.3}$$

where $\mathbf{P}$ is the polarization, $\mathbf{M}$ is the magnetization, χ_e is the electric susceptibility, and χ_m is the magnetic susceptibility. We can now solve these equations for a plane

wave without any external forces ($\rho^{ext} = 0$), we can arrive at a wave equation for a plane wave propagating in an energy-absorbing medium:

$$\nabla^2 \mathbf{E} = \frac{\epsilon}{c^2} \frac{\partial^2 \mathbf{E}}{\partial t^2}. \tag{3.4}$$

We describe the light with the complex wave vector with a single plane:

$$\mathbf{E} = \mathbf{E_0} e^{[i(\mathbf{k}\cdot\mathbf{r} - \omega t)]}, \tag{3.5}$$

where $\mathbf{k}$ is the wave vector and ω is the frequency. Substituting Eqn. 3.4 into Eqn. 3.5, we arrive at the following relation:

$$k^2 = \frac{\omega^2}{c^2} \epsilon(\omega). \tag{3.6}$$

We can express k by the complex refractive index $N = \sqrt{\epsilon(\omega)}$:

$$k = \frac{N\omega}{c}. \tag{3.7}$$

The complex refractive index is now defined as:

$$N(\omega) = n + ik. \tag{3.8}$$

Here, n and k are the refractive index and the extinction coefficient, respectively. We can also define the complex dielectric function:

$$\epsilon(\omega) = \epsilon_1 + i\epsilon_2. \tag{3.9}$$

More relationships from complex refractive index and dielectric function can be made

here:

$$\epsilon_1 = n^2 + k^2$$
$$\epsilon_2 = 2nk. \tag{3.10}$$

We can now begin to use these relationships to find the absorption coefficient α. Rewriting Eq. 3.5 yields:

$$E(x,t) = E_0 e^{i[(N\omega/c)x - \omega t]} = E_0 e^{-(2\pi k/\lambda_\omega)x} e^{i(kx-\omega t)}. \tag{3.11}$$

Here, the expression $2\pi k/\lambda_\omega$ describes the attenuation of the field, and λ_ω is the wavelength of light in a vacuum. $e^{-(2\pi k/\lambda_\omega)x}$ describes the attenuation of wave amplitude with distance. We can use Beer's law since the intensity is proportional to the square of the electric field:

$$I(x) = EE* = I_0 e^{-\alpha x}, \tag{3.12}$$

which α and the k relates as:

$$\alpha = \frac{2\omega k}{c} = \frac{4\pi k}{\lambda_\omega}. \tag{3.13}$$

Furthermore, α can be related to the imaginary part of the dielectric function as:

$$\alpha = \frac{\omega \epsilon_2}{cn}. \tag{3.14}$$

For a medium with a finite conductivity, the dielectric function is expressed as:

$$\epsilon(\omega) = 1 + \frac{i\sigma(\omega)}{\omega \epsilon_0}. \tag{3.15}$$

and for the absorption:

$$\alpha(\omega) = \frac{\sigma_1(\omega)}{n\epsilon_0 c}. \tag{3.16}$$

This is an important relationship because high conductivity means high absorption and low conductivity results in low absorption. We summarize the relationship between the various response functions of $\epsilon(\omega)$, $\sigma(\omega)$, and $N(\omega)$ in Table 3.1 [296, 297].

3.1.2 Beer's law

For transmittance measurements, we must use Beer's law to convert transmittance spectra as a function of frequency to an absorption coefficient. For a sample thickness $d < \delta = \frac{c}{\omega k}$, where δ is the penetration depth, the absorption coefficient can be directly determined from transmittance. This is one of the simplest and well-known relations.

By controlling the optical density, the Beer-Lambert law can be used:

$$I = I_0 e^{-\alpha d}, \tag{3.17}$$

with I and I_0 being the intensities of transmitted and incident beams, respectively. α is the absorption coefficient and d is the sample thickness. We know that the transmittance is $T = \frac{I}{I_0}$ and the absorbance is $A = -ln\frac{I}{I_0} = \alpha d$. By rearranging them, we arrive at the absorption coefficient directly from the thickness d and transmittance as a function of frequency $T(\omega)$ [298]:

$$\alpha(\omega) = -\frac{1}{d} ln(T\omega). \tag{3.18}$$

The limitation of Beer's law requires minimal or negligible reflectance, which is not

Table 3.1: Relationships between the various response functions $\epsilon(\omega)$, $\sigma(\omega)$, and $N(\omega)$

Dielectric constant $\epsilon(\omega)$	Conductivity $\sigma(\omega)$	Refractive index $N(\omega)$
$\epsilon = \epsilon_1 + i\epsilon_2$ $\sigma_1 = \frac{\omega\epsilon_2}{4\pi}$ $\sigma_2 = (1-\epsilon_1)\frac{\omega}{4\pi}$ $n = (\frac{1}{2}((\epsilon_1^2+\epsilon_2^2)^{1/2}+\epsilon_1))^{1/2}$ $k = (\frac{1}{2}((\epsilon_1^2+\epsilon_2^2)^{1/2}-\epsilon_1))^{1/2}$	$\epsilon_1 = 1 - \frac{4\pi\sigma_2}{\omega}$ $\epsilon_2 = \frac{4\pi\sigma_1}{\omega}$ $\sigma = \sigma_1 + i\sigma_2$ $n = (\frac{1}{2}(((1-\frac{4\pi\sigma_2}{\omega})^2+(\frac{4\pi\sigma_1}{\omega})^2)^{1/2}+$ $(1-\frac{4\pi\sigma_2}{\omega})))^{1/2}$ $n = (\frac{1}{2}(((1-\frac{4\pi\sigma_2}{\omega})^2+(\frac{4\pi\sigma_1}{\omega})^2)^{1/2}-$ $(1-\frac{4\pi\sigma_2}{\omega})))^{1/2}$	$\epsilon_1 = n^2 - k^2$ $\epsilon_2 = 2nk$ $\sigma_1 = \frac{nk\omega}{2\pi}$ $\sigma_2 = (1-n^2+k^2)\frac{\omega}{4\pi}$ $N = n + ik$

always the case. Otherwise, a correction is needed:

$$T = \frac{(1-R)^2 e^{-\alpha d}}{1 - R^2 e^{-2\alpha d}} \tag{3.19}$$

where R is the reflectance at the sample surface [299, 300]. The relationship comes from the Glover-Tinkham analysis, which accounts for both transmittance and reflectance [296, 301].

3.1.3 Kramers-Kronig analysis and sum rules

Transmittance experiments are used frequently since it is overall alignment is more forgiving. Furthermore, it is an easier way to get absorption directly from transmittance with the knowledge of sample thickness. However, the materials of interest do not always transmit light. Also, polishing a sample is not an easy skill to acquire. In these cases, reflectance measurements are used. Optical properties can be determined by measuring the reflectivity at normal incidence and dispersion relations. The reflectivity r and the power reflectance $R(\omega)$ are given by:

$$\begin{aligned} r &= \sqrt{R} e^{i\phi} \\ R(\omega) = rr^* &= \frac{(n-1)^2 + k^2}{(n+1)^2 + k^2}. \end{aligned} \tag{3.20}$$

The power reflectance $R(\omega)$ and phase-dispersion shift on reflectance $\phi(\omega)$ are related by Kramers-Kronig transformation [296]:

$$\phi(\omega) = \frac{\omega}{\pi} \int_0^\infty \frac{lnR(\omega) - lnR(\omega')}{\omega'^2 - \omega^2} d\omega'. \tag{3.21}$$

By combining Eq. 3.20 and 3.21, the refractive index n and the extinction coefficient k can be determined by $R(\omega)$ and $\phi(\omega)$ as:

$$\begin{aligned} n(\omega) &= \frac{1 - R(\omega)}{1 + R(\omega) - 2\sqrt{R(\omega)}cos\phi(\omega)} \\ k(\omega) &= \frac{2\sqrt{R(\omega)sin\phi(\omega)}}{1 + R(\omega) - 2\sqrt{R(\omega)}cos\phi(\omega)}. \end{aligned} \tag{3.22}$$

The real part of the dielectric function and optical conductivity can be determined as listed in Table 3.1:

$$\begin{aligned} \epsilon_1 &= n^2 - k^2 \\ \epsilon_2 &= 2nk. \end{aligned} \tag{3.23}$$

Our tools include measurements from far-infrared to ultraviolet frequency range, beyond which proper extrapolations should be used. There are four different models to consider: (i) a Hagen-Rubens relation ($R(\omega) = 1-(2\omega/\pi\sigma_0)^{1/2}$ is used for metallic materials; or as a constant for semiconductors/insulators in the low-frequency range, (ii) The two-fluid model ($R(\omega) = 1 - (2\omega/\pi\sigma_0)^2$ (iii) Marginal Fermi Liquid model ($R(\omega) = 1 - (2\omega/\pi\sigma_0)$ and (iv) Superconducting model ($R(\omega) = 1 - (2\omega/\pi\sigma_0)^4$. We note that the only difference between these models is the power index of ω. For the high frequency extrapolation, the equation is modeled as $R \sim \omega^{-\alpha}$, where α varies from 0 to 4 and does not have to be an integer. The $\alpha(\omega)$ can be determined by comparing the absorption and calculated optical conductivity.

Together with physical arguments about the behavior of the response in certain limits, the Kramers-Kronig relation can also be used to derive sum rules. That is:

$$\int_0^\infty \omega' Im(\frac{-1}{\epsilon(\omega')}d\omega' = \frac{1}{2}\pi\omega_p^2, \tag{3.24}$$

where ω_p is the plasma frequency. A partial sum rule [296] is also useful in quantifying

the change of absorption spectra:

$$f \equiv \frac{2c}{N_e \pi \omega_p^2} \int_{\omega_1}^{\omega_2} n\alpha(\omega, B) d\omega. \tag{3.25}$$

Here, f is the oscillator strength, N_e is the number of electrons per magnetic ion site, n is the refractive index, ω_p is the plasma frequency $\sim \sqrt{\frac{e^2\rho}{m\epsilon_0}}$, e and m are the charge and mass of an electron, ϵ_0 is the vacuum dielectric constant, ρ is the density of magnetic ion sites, c is the speed of light, and ω_1 and ω_2 are the frequency limits of integration.

3.1.4 Drude and Lorentz models

Generally, there are two basic models to consider that fit the descriptions of materials: the Drude and the Lorentz models. The former describes metals, quantitatively characterizing the free carrier response of metallic materials, whereas the latter quantifies localized excitations, which applies to semiconductors and insulators.

As a result, there are three parts to the dielectric function:

$$\epsilon = \epsilon_{free} + \epsilon_{bound} + \epsilon_{\infty}. \tag{3.26}$$

Here, ϵ_{free} is the contribution from free electrons (or holes), and ϵ_{bound} is the contribution from bound or localized carriers. For metallic compounds, ϵ_{free} dominates the optical response at relatively low frequencies, which screens the contributions from ϵ_{bound} due to the large free carrier density. Above the plasma frequency, bound carriers start to populate and begin to dominate the optical response of a material.

We begin with the Drude model and the description of metals first. There are four assumptions for the Drude model: (i) electron-electron and electron-metallic ion

collisions are neglected. The scattering due to electron-electron collisions is also not considered. (ii) Only the collision between electrons and ion cores is considered. (iii) There is a mean free time where an electron travels a certain amount of distance before the collision. This is the relaxation time τ, an average time before its next collision. $1/\tau$ is the probability per unit of time. (iv) After the collision, an electron emerges with a velocity with a random direction and with a speed appropriate to the local temperature.

With those assumptions, we can begin to describe the picture of the metal. Each metal ion consists of the nucleus and the core electrons. They are immobile. Valence electrons are weakly bounded to the metal ions. They generate the free electron gas, which is delocalized. They are also called conduction electrons.

The equation of motion of the Drude model can be written as:

$$m\frac{d^2r}{dt^2} + m\gamma\frac{dr}{dt} = -eE_{loc}. \tag{3.27}$$

Here, m is the effective mass of the free carriers, γ is the damping constant ($= 1/\tau$), e is the charge of an electron, and E_{loc} is the local electric field acting on the electron.

By assuming the homogeneous electric field is acting on the conduction electron, we can derive the dielectric function by combining Eqn. 3.27 and Maxwell's equation as:

$$\epsilon(\omega) = \epsilon_c - \frac{4\pi ne^2}{m(\omega^2 + i\omega/\tau)}, \tag{3.28}$$

where $\epsilon_c \approx 1$ when the polarization of the ion core is not considered. Then, the real and imaginary part of the dielectric function is derived:

$$\begin{aligned} \epsilon_1 &= \epsilon_c - \frac{\omega_p^2}{\omega^2 + 1/\tau^2} \\ \epsilon_2 &= \frac{\omega_p^2}{\omega\tau(\omega^2 + 1/\tau^2)}. \end{aligned} \tag{3.29}$$

Here, $\omega_p = \sqrt{\frac{4\pi ne^2}{m}}$ is the plasma frequency.

Using the relations listed in Table. 3.1, we can obtain expressions for optical conductivity:

$$\begin{aligned} \sigma_1 &= \frac{ne^2\tau}{m(1+\omega^2\tau^2)} = \frac{\sigma_{dc}}{1+\omega^2\tau^2} \\ \sigma_2 &= \omega\tau\frac{ne^2\tau}{m(1+\omega^2\tau^2)} = \omega\tau\frac{\sigma_{dc}}{1+\omega^2\tau^2}, \end{aligned} \tag{3.30}$$

where $\sigma_{dc} = \frac{ne^2\tau}{m}$ is the dc conductivity of the material. The relaxation time can be approximated by $\rho_{DC} \sim 1/\sigma_{DC}$.

Unlike metallic compounds, semiconductors and insulators have localized excitation. The Lorentz model treats the bound electrons similar to a harmonic oscillator or a mass-spring system. The electrons vibrate in an electromagnetic field. The equation of motion becomes:

$$m\frac{d^2r}{dt^2} + m\gamma\frac{dr}{dt} + m\omega_0^2 r = -eE_{loc}, \tag{3.31}$$

where $m\omega_0^2 r$ is the additional term that describes the binding energy between the bound electrons and the nucleus. Compared to metals, the electric field will cause an internal polarization in the medium because of the separation between positive and negative charges. The total electric field acting on an electron is:

$$E_{loc} = E_{ext} + E_{neighbor} + E_{int}. \tag{3.32}$$

Here, E_{ext} and E_{int} are the external and internal electric fields, respectively. $E_{neighbor}$ is the electric field due to the neighboring dipoles. Therefore, the total electric field is the sum of all the fields. The solution to Eq. 3.31 is:

$$r(\omega) = \frac{1}{m}\frac{-eE_{loc}}{(\omega_0^2 - \omega^2) + i\gamma\omega}. \tag{3.33}$$

From this, the induced dipole moment μ is related to r through this equation:

$$\mu(\omega) = \frac{e^2 E_{loc}}{m[(\omega_0^2 - \omega^2) + i\gamma\omega]}. \tag{3.34}$$

Since $\mu(\omega) = \alpha(\omega)E(\omega)$, the polarization per unit volume is given by:

$$P(\omega) = N\alpha(\omega)E(\omega) = \epsilon_0\chi(\omega)E(\omega). \tag{3.35}$$

The susceptibility $\chi(\omega)$, from the prior equation, is then:

$$\chi(\omega) = (\frac{Ne^2}{\epsilon_0 m})\frac{1}{\omega_0^2 - \omega^2 + i\Gamma\omega}. \tag{3.36}$$

where $(4\pi Ne^2/m)$ is the plasma frequency squared (ω_p^2). The dielectric function can then be written as:

$$\epsilon(\omega) = 1 + \frac{\omega_p^2}{\omega_0^2 - \omega^2 + i\Gamma\omega}. \tag{3.37}$$

where ω_p equals:

$$\omega_p == \sqrt{\frac{Ne^2}{\epsilon_0 m}}. \tag{3.38}$$

From this dielectric function, many optical parameters can be calculated, such as absorption $(\alpha(\omega))$, optical conductivity $(\sigma(\omega))$, refractive index $(n(\omega))$, and so on.

For this work, several projects call for the use of both the Drude and Lorentz models. These two models are extremely useful because we can use them to fit the experimental spectra to obtain the relaxation time, plasma frequency, *dc* conductivity, effective mass, and carrier densities of different materials. For example, the Drude model can give the number of free carriers in a system. By comparing the fit parameters for various doping concentrations, magnetic fields, or temperatures, trends can be observed. In this case, we are able to analyze how the material and spe-

cific excitations can be sensitive to different phase transitions. Figure 3.1(a) displays reflectance spectra of Fe_xTaS_2 (x = 0, 1/3, 1/4). By using Kramer-Kronig analysis, optical conductivity, σ_1, is obtained from reflectance data [Fig. 3.1(b)]. By using the Drude-Lorentz fit of the optical conductivity, two Drude functions are revealed for the Fe layer and TaS_2 sheet [Fig. 3.1(c)]. The oscillator strength of Fe Drude is smaller and the plasma frequency is much lower compared to TaS_2. Furthermore, the signature of chirality is captured in the complex free-carrier response emanating from Ta and Fe bands [302].

3.1.5 Band gap analyses

The band gap is defined as an energy difference between the top of the valence band and the bottom of the conduction band as shown in Fig. 3.2(a). Microscopically, a charge transfer excitation defines the band gap energy. In oxides, it is usually a transition between an oxygen $2p$ orbital to a metal $3d$ orbital. Also, there are two fundamentally different band gaps, direct and indirect band gaps. A direct gap is when the electron travels from the valence band to the conduction band with Δk = 0 [Fig. 3.2(b)]. An indirect gap is the same except $\Delta k \neq 0$ [Fig. 3.2(c)]. This change in k-momentum is caused by a phonon. In optical analysis, a Tauc plot can be calculated, and a gap energy equation can be written to include both of these terms:

$$\alpha(E) = A(E - E_g^{direct})^{0.5} + B(E - E_g^{indirect} \mp E_{phonon})^2. \tag{3.39}$$

where A and B are parameters, E_g are the direct and indirect gaps, and the phonon energy is E_{phonon}. Plots of $(\alpha E)^2$ and $(\alpha E)^{0.5}$ can extract a direct or indirect gap, respectively, with line segments that are linear in each graph [303–307]. Figure 3.3 shows a few examples of Si, Ge, ZnO, and TiO_2 and a way to extract the gap energy [308–310]. A linear region is extrapolated linearly to extract the gap energy.

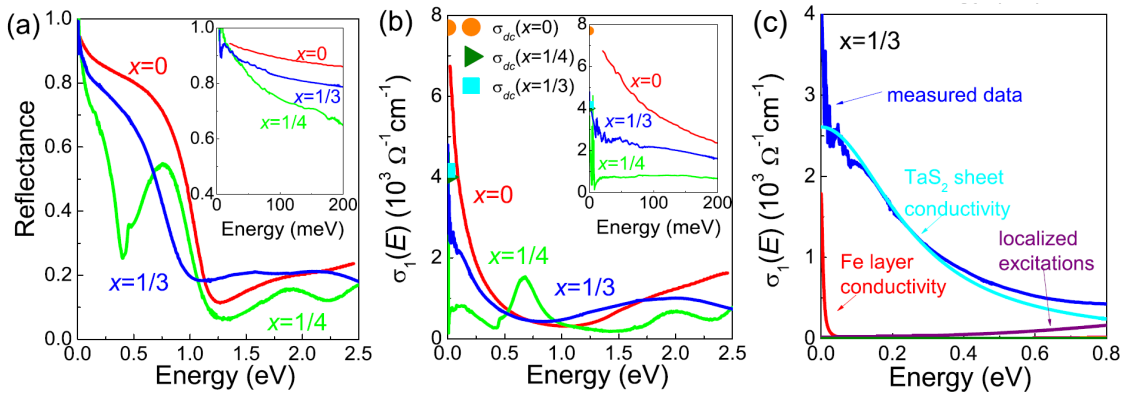


Figure 3.1: (a) Reflectance spectra of Fe_xTaS_2 is displayed with x = 0, 1/3, and 1/4. (b) σ_1 is shown by using Kramer-Kronig analysis on the reflectance data. (c) Using TaS_2 as a reference to isolate Fe layer conductivity [302].

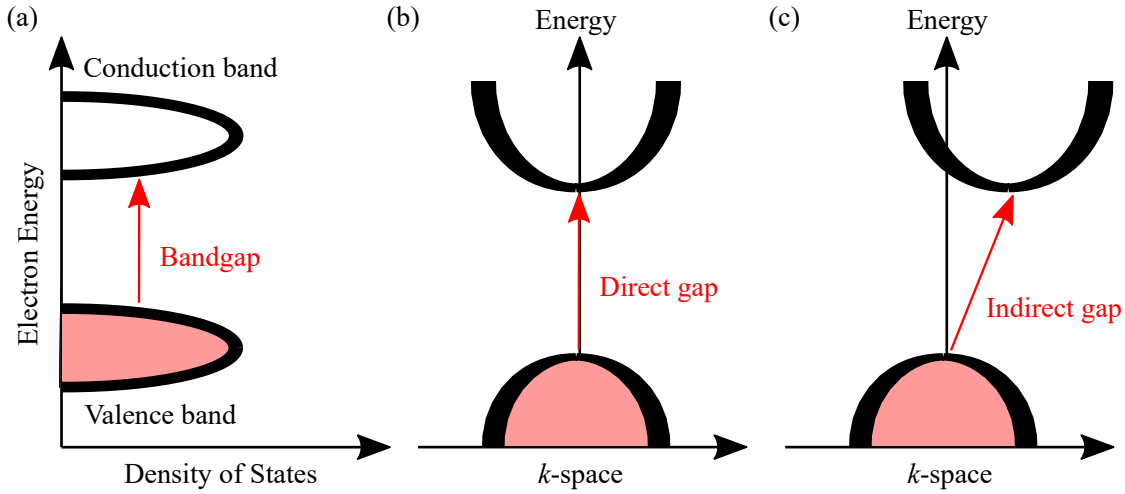


Figure 3.2: Energy diagram of the band gap defined by the energy difference between the top of the valence band to the bottom of the conduction band.

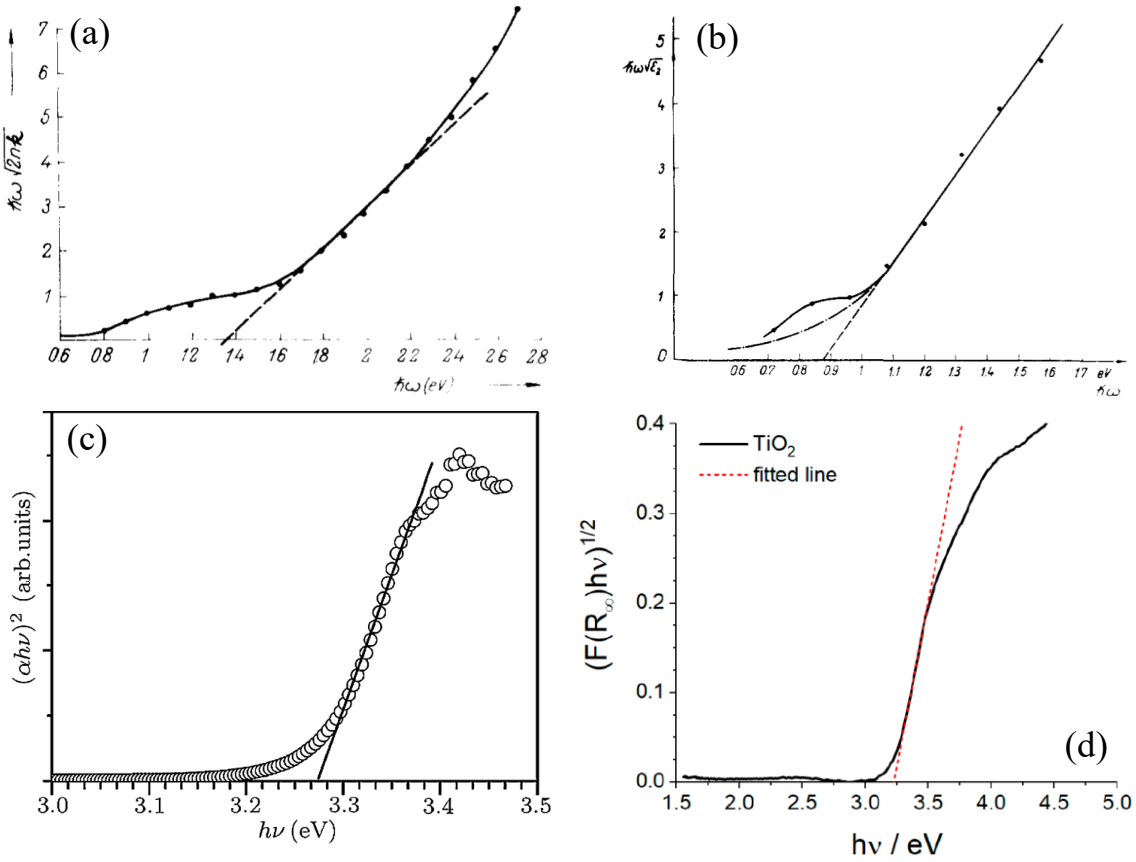


Figure 3.3: Examples of the extraction of band gaps in Si, Ge, ZnO, and TiO_2 using Tauc plot. A linear region in the graph is extrapolated linearly to obtain the gap energy.

Using the Tauc plot to track the gap energy as a function of temperature, physics can be captured. For semiconductors, there are a few different models describing the temperature behavior of the gap energy. Varshini model is a semi-empirical model expressed as:

$$E_g = E_0 - \alpha T^2/(T+\beta), \tag{3.40}$$

where α and β are the fitting parameters, which β is supposedly be related to the Debye temperature [311,312]. Then, there is an improved version of Varshini's model, O'Donnell's model, which is expressed as:

$$E_g(T) = E_g(0) - S\langle\hbar\omega\rangle[coth(\langle\hbar\omega\rangle/2kT) - 1]. \tag{3.41}$$

Here, $E_g(0)$ is the band gap at zero temperature, S is a dimensionless coupling constant, and $\langle\hbar\omega\rangle$ is an average phonon energy. S, in this case, is a notation directly related to vibronic coupling [313]. Another model is the Bose-Einstein model, which considers electron interaction within crystals and relates Debye temperature to the energy shift with temperature. It is described as:

$$E_g(T) = E_g(0) - \frac{2\alpha_B}{exp(\frac{\Theta_E}{T}) - 1}, \tag{3.42}$$

where α_B is the parameter related to the strength of exciton-phonon interactions within the crystal and Θ_E is the Einstein characteristic temperature. Debye temperature, Θ_D, can be determined by $\Theta_D = \frac{4}{3}\Theta_E$.

Not only determine the physical properties using the models to fit but phase transitions can also be observed by tracking the gap energy as a function of temperature if there is a structural distortion or spin-charge coupling in the system. Figure 3.4 displays band gap energies as a function of temperature for $Fe_2Mo_3O_8$ and its analogs [[314]]. Using Tauc's plot to determine the band gap energy as a function

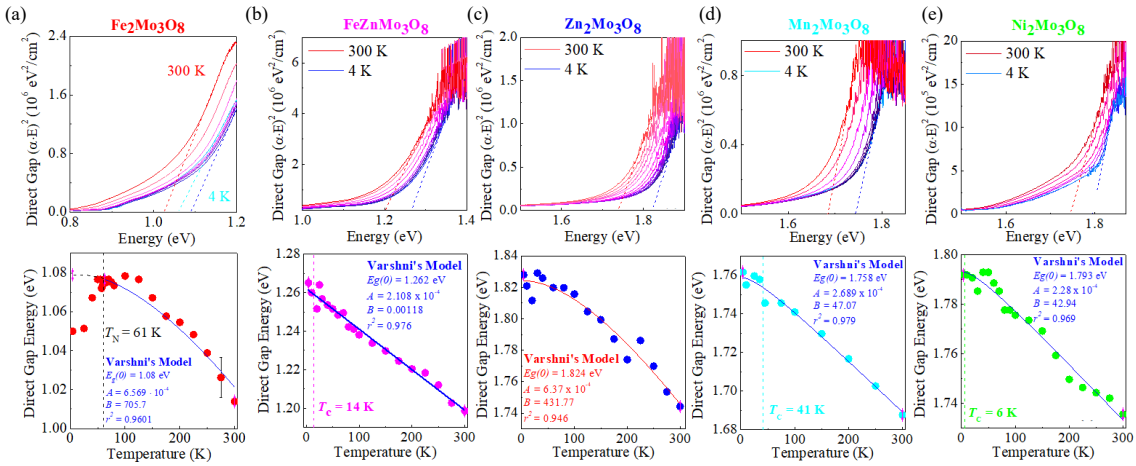


Figure 3.4: Band gap energies as a function of temperature for $Fe_2Mo_3O_8$ and its analogs are shown using Varshini's model. (a) The abrupt change across the T_N signifies spin-charge coupling in the system. (b-e) Normal temperature trends are shown [314].

of temperature, the Varshini model is used to fit the trends. For $Fe_2Mo_3O_8$, we observe an abrupt change across T_N, which signifies spin-charge coupling.

We note that there are other models such as Pässler model and improved models upon Varshini's. However, we only use Varshini and O'Donnell models to capture the physics.

3.1.6 Polarization and crystal anisotropy

Light is a transverse wave where the oscillation is in the plane perpendicular to the propagation direction, $\vec{k}$. We can polarize the light, inducing the directionality of the oscillation with respect to chosen coordinates (xyz or abc) in order to probe anisotropy or chirality. There are three types: i) linear, ii) circular, and iii) elliptical as shown in Fig. 3.5. These classifications can be made by the differences in the phase between the E_x or E_y. Let $E_x = E_{0x}e^{i(kz-\omega t)}$ and $E_y = E_{0y}e^{i(kz-\omega t+\phi)}$, where ϕ is the phase. If the phase difference is an integer n of π, linear polarization is achieved [Fig. 3.5(a)]. For $\frac{n\pi}{2}$, right- or left-circularly polarized light is produced [Fig. 3.5(b)]. If the $\Delta\phi$ = constant instead of $n\pi$ or $\frac{n\pi}{2}$, then the elliptical polarization is attained [Fig. 3.5(c)]. Table. 3.2 summarizes these.

Polarized light is immensely useful for anisotropic materials because the physical properties of the samples are now directional dependent. The electronic, magnetic, and vibrational properties are strongly associated with crystal symmetries. Light-matter interactions can be described by Eq. 3.2 for isotropic materials, which are highly symmetric. For anisotropic materials, the dielectric constant becomes a tensor. The relationship between the electric displacement D and the electric field E can be written as:

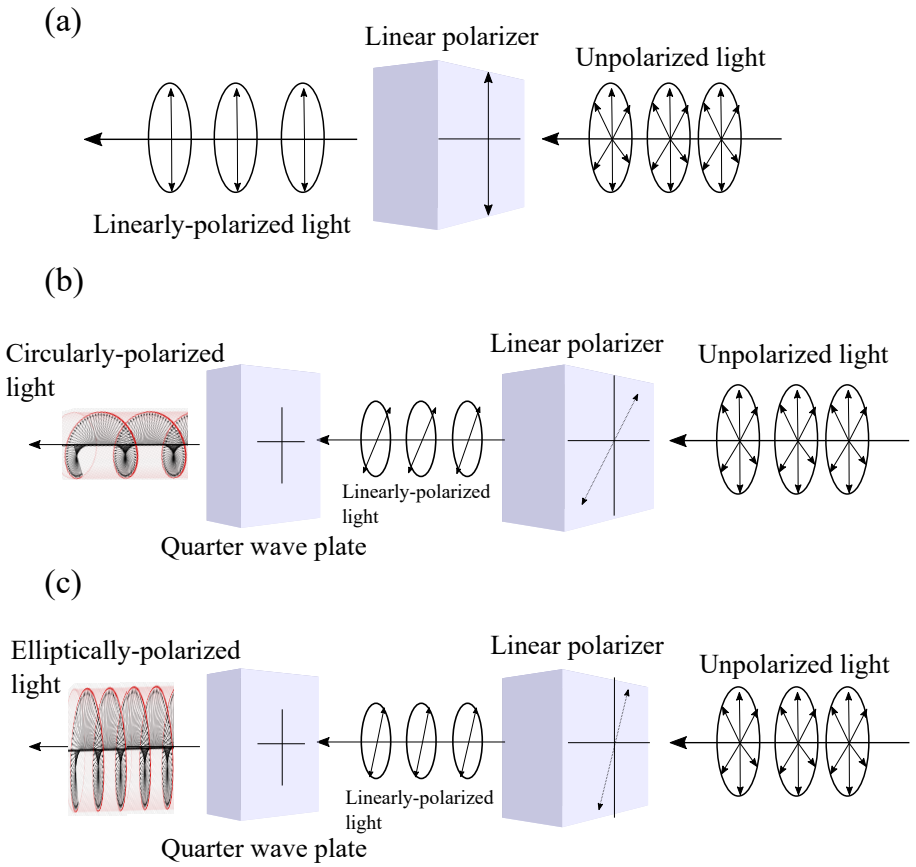


Figure 3.5: Schematic diagram of the representation of the linear, circular, and elliptical polarization. (a) Linear polarization can be achieved by using a linear polarizer. (b,c) For circular and elliptical polarization, a quarter wave plate is used with a linear polarizer.

Table 3.2: Conditions for differently polarized light

Phase difference $\Delta\phi$	**Types of polarization**
ϕ, E_x, and E_y are randomly varying on a timescale that is much shorter than that needed for observation	unpolarized light
$\Delta\phi = n\pi$, (n = 0, 1, 2...)	linear polarization
$\Delta\phi = \frac{n\pi}{2}$, ($n = \pm$ 1, 3, 5)	left or right circular polarization
$\Delta\phi$ = arbitrary but constant, (exclude $n\pi$ and $\frac{n\pi}{2}$)	elliptical polarization

$$
\begin{aligned}
D_x &= \epsilon_{xx}E_x + \epsilon_{xy}E_y + \epsilon_{xz}E_z \\
D_y &= \epsilon_{yx}E_x + \epsilon_{yy}E_y + \epsilon_{yz}E_z \\
D_z &= \epsilon_{zx}E_x + \epsilon_{zy}E_y + \epsilon_{zz}E_z.
\end{aligned} \tag{3.43}
$$

As written in the equation, $\epsilon_{xx,xy,...}$ are the dielectric tensor, which is now directionally dependent. With polarized light, anisotropies can be measured.

3.1.7 Magnetic circular dichroism

Magnetic circular dichroism (MCD) is an absorption difference technique between the left- and right-circularly polarized light under an external magnetic field. The origin of the MCD signal is due to the electromagnetic interaction of the external field with the electronic charge within the sample. We note that natural circular dichroism is different than MCD, which is caused by the difference in the speed of light between left- and right-circularly polarized light in a chiral material, whereas natural circular dichroism is an intrinsic effect for all magnetic materials. The MCD intensity can be expressed as:

$$
\Delta\alpha = \alpha_+ - \alpha_- = \Delta\epsilon_M c l \mathbf{B}, \tag{3.44}
$$

where $\Delta\alpha$ is the absorption difference between the right- and left-circularly polarized light, and $\alpha_\pm$ represents the absorption coefficient of the right- or left-circularly polarized light, respectively. $\Delta\epsilon_M$ is the difference of the molar attenuation coefficient, c is the speed of light, l is the penetration depth, and $\mathbf{B}$ is the magnetic induction.

It is well established that magnetic circular dichroism originates from Zeeman splitting in magnetic molecules:

$$
H_{Zeeman} = -g\mu_B \mathbf{J} \cdot \mathbf{B}. \tag{3.45}
$$

Here, μ_B is the Bohr magneton, **J** is the total electronic angular momentum, and g is the Landé g-factor. The general form of the MCD intensity can be qualitatively expressed as [315]:

$$I_{MCD} \sim [A(\frac{\partial f(E)}{\partial E}) + (B + \frac{C}{kT})f(E)]. \tag{3.46}$$

The A term describes the MCD signal from degenerate excited states whereas the C term originates from degenerate ground states. Notice that the C term is dependent on temperature because the population of electrons from the ground state depends on the thermal energy. The origin of the B term relates to the mixed excited states. The physics of those terms can be better understood from the following energy diagram. When the external magnetic field is applied, Zeeman splitting causes the ground and excited states to split into two different states [Fig. 3.6(a)]. The excitation energies induced by the right- and left-circularly polarized light is different. This is due to the different selection rules for the right and left circularly polarized light (Δm = +1 for rcp; Δm = -1 for lcp). Notice that the A term has a derivate shape whereas B and C terms do not [Fig. 3.6(b)].

We can extend this framework to solids. Figure 3.7 displays a schematic view of how bands split in a magnetic semiconductor. Since the angular momentum of the circularly polarized light can couple with the spin-angular momentum, the right and left circularly polarized light can probe the excitations in different spin channels. For a non-magnetic material [Fig. 3.7(a)], the excitation from the valence band to the conduction band has no spin-dependence, the corresponding MCD signal is zero in this case. For a magnetic semiconductor [Fig. 3.7(b)], the Zeeman interaction induces exchange splitting in the valence and conduction bands that depend upon the spin direction, forming a spin-polarized band structure which results in an absorption difference between the right and left circularly polarized light. The MCD

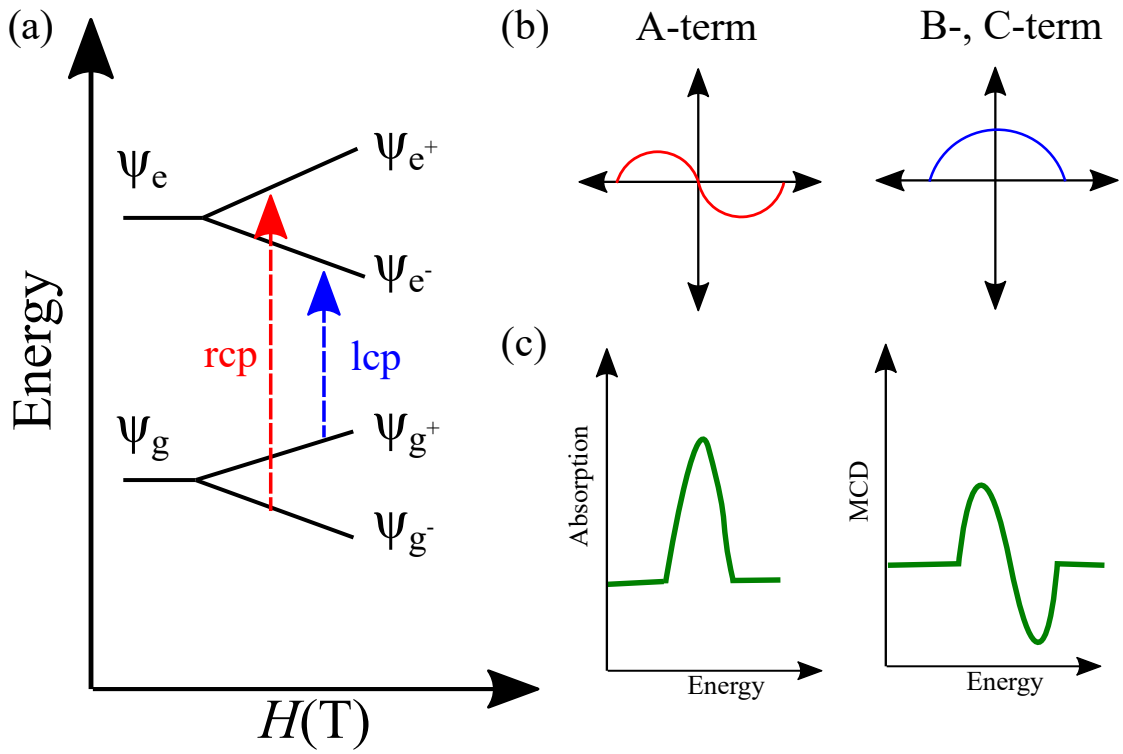


Figure 3.6: (a) Generic model of excitation with a selection of RCP and LCP for atomic/molecular transitions (b) Diagram of MCD response shows the derivative-like A-term response function and show the expected shape for B and C term response functions. (c) An example of a peak in the absorption spectrum and MCD spectrum. MCD exhibits a derivative feature as shown in Eqn. 3.48.

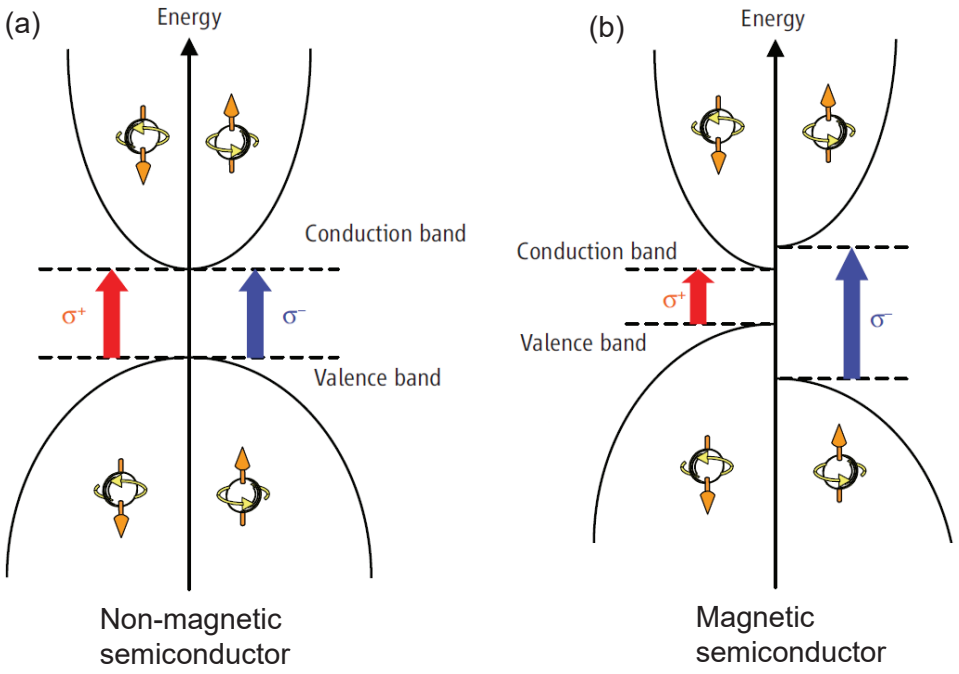


Figure 3.7: Schematic view of the density of states for (a) a non-magnetic and (b) a magnetic semiconductor [316].

signal is thus generated. Moreover, since the total magnetic moment in solids equals to the difference between the density of states in the spin-up and spin-down channel, the dichroic intensity is directly proportional to the magnetization.

There are other ways to see the connection between MCD and magnetization by describing the interaction between the circular polarized light and materials with the dielectric tensor. When the circularly polarized light interacts with materials, it will probe the off-diagonal components of the dielectric tensor as [317]:

$$\epsilon = \begin{vmatrix} \epsilon_{xx} & i\epsilon_{xy} & 0 \\ -i\epsilon_{xy} & \epsilon_{yy} & 0 \\ 0 & 0 & \epsilon_{zz} \end{vmatrix} \approx n^2 \begin{vmatrix} 1 & iQm_z & 0 \\ -iQm_z & 1 & 0 \\ 0 & 0 & 1 \end{vmatrix}, \epsilon_{\pm} = \epsilon_{xx} \pm \epsilon_{xy}. \tag{3.47}$$

Here, the $\pm$ sign represents the right or left circular polarization, respectively. Notice in the dielectric tensor, the off-diagonal component is linearly proportional to the magnetic moment projected on the z-direction. This equation shows how that the MCD signal is directly proportional to the magnetization.

The magnetic circular dichroism intensity can also correspond to the joint density of states, and even to specific bands. These relationships are expressed as [318–320]:

$$\Delta\alpha(E)_{MCD} = \vec{\mu}_i \cdot \vec{k} = |\vec{\mu}_i||\vec{k}| \cos\theta \approx \frac{(\alpha_+(E) - \alpha_-(E))d}{2} \approx \frac{\Delta E}{2} \frac{1}{\alpha(E)} \frac{d\alpha(E)}{dE}. \tag{3.48}$$

Here, $\Delta\alpha(E)_{MCD}$ is the absorption difference between right and left circularly polarized light $(\alpha_+(E) - \alpha_-(E))$, $d\alpha(E)/dE$ is the energy derivative of the linear absorption spectrum, d is the sample thickness, ΔE is the energy difference, $\vec{\mu}_i$ is the magnetic moment projected onto the light propagation direction $\vec{k}$, and θ is the angle

between the magnetic moment and the light propagation. The moment is proportional to the magnetic field, so it grows when the magnetic field increases. This means that the intensity of the $\alpha(E)_{MCD}$ will grow proportionally to the magnetic field as well. Equation 3.48 highlights the first-derivative relationship between linear absorption and magnetic circular dichroism. Any inflection point in the linear absorption spectra will be amplified in the dichroic response [Fig. 3.6(c)].

The dichroic response can be modeled using the calculated matrix elements of the optical conductivity tensor as [320, 321]:

$$\Delta\alpha_{MCD} \approx \frac{d\omega}{2c}\Im(\overleftrightarrow{n}_+ - \overleftrightarrow{n}_-) \approx \frac{2\pi d}{c}\Im[\frac{\overleftrightarrow{\sigma}_{xy}}{(1+\imath\frac{4\pi}{\omega}\overleftrightarrow{\sigma}_{xx})^{1/2}}]. \tag{3.49}$$

Here, $\overleftrightarrow{n}_\pm = (\overleftrightarrow{\epsilon}_{xx} \pm \overleftrightarrow{\epsilon}_{xy})^{1/2}$ is the refractive index of right or left circularly polarized (RCP or LCP) light arising from the dielectric function ϵ, d is the sample thickness, and c is the speed of light. In this case, we can have a direct comparison between the calculated and measured magnetic circular dichroism spectra.

3.2 Spectrometers

Spectroscopy is the study of light-matter interactions. Not only does it study how matter interacts with light, but it also looks at the frequency dependence of the interaction, yielding interesting physics inside of materials. The electromagnetic spectrum covers a wide energy range - from radio waves to ionizing waves. Depending on the wavelength of light, materials exhibit different physical properties, serving as an important tool for providing a microscopic understanding of spin, orbital, lattice, and charge interactions. In this work, we will focus on infrared through ultraviolet regions. Several different spectrometers were used in the analysis of each of the different regions. Each of these spectrometers has overlapping energy regions to

merge and obtain a full range (20 to 55,000 cm^{-1}). The following will lay out the spectrometers used in this work.

3.2.1 Fourier transform infrared spectroscopy

Before we discuss individual spectrometers, the Fourier transform technique should be mentioned to understand the ability to obtain a continuous spectrum in a wide energy range. The Fourier transform is widely integrated into infrared spectroscopy - Fourier transform infrared spectrometer (FTIR). The central part of the FTIR spectrometer is the interferometer, introducing an optical path difference between two beams of light and producing an interference pattern. The interferometer allows the production of a unique type of signal that has all of the infrared frequencies "encoded" into it, which is a method for measuring all of the infrared frequencies simultaneously rather than individually. A general understanding can be gained from the basic principles of a Michelson interferometer.

Figure 3.8 displays a schematic view of a Michelson interferometer. The light source of a choosing - in this case, an infrared beam - transmits incident light towards a beam splitter, splitting the incident beam into two equal parts. Different types of beam splitters are chosen based on the frequency range of the light source. One part of the beam is transmitted to a fixed mirror (M_1). The other part of the beam is reflected by the beam splitter and travels to a moving mirror (M_2). The returned beams reflected from the two mirrors (M_1 and M_2) are merged in the beam splitter. The recombined beam is then sent to the sample chamber. Signals are collected by the detector, and then a computer will perform the Fourier transformation to the raw signal. The moving mirror periodically modifies the optical path difference between the two arms of the beam, generating constructive or destructive interference patterns. Therefore, the given intensity of the signal is a function of the

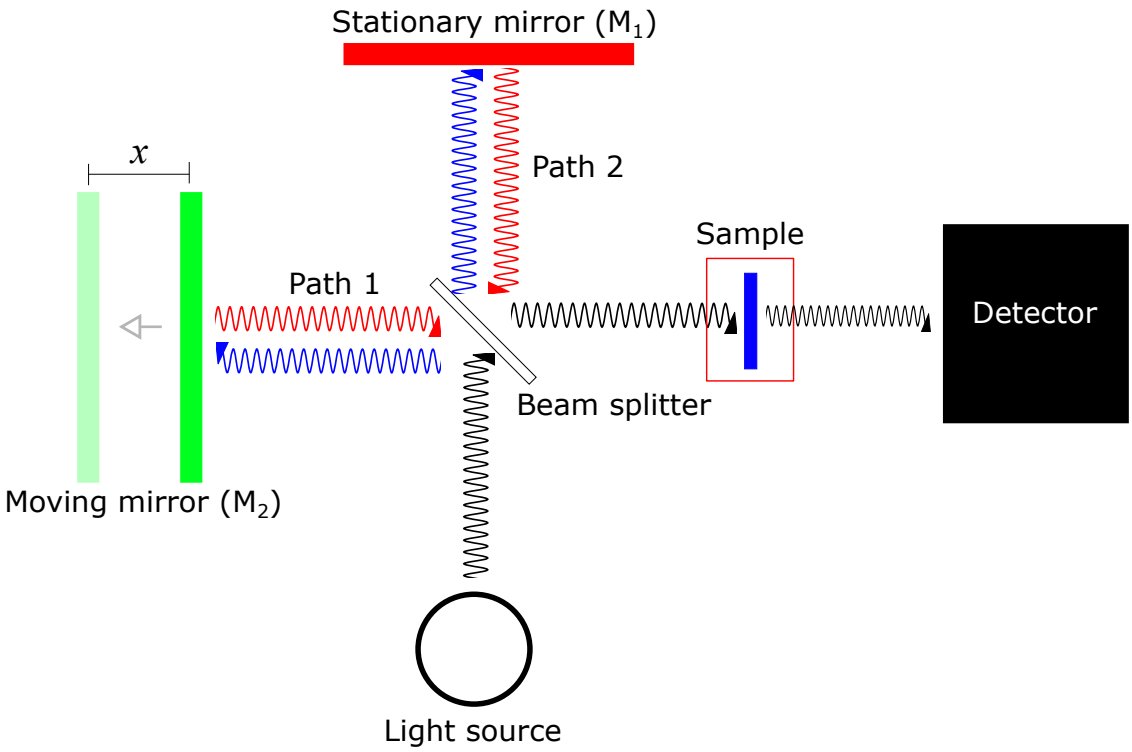


Figure 3.8: Schematic view of a Michelson interferometer in a Fourier transform infrared spectrometer setup.

moving displacement x, known as an interferogram [322]:

$$I(T) = \frac{I_0}{2}[1 + exp(-ln2x^2/\tau^2)cos(2\pi v_0 x)], \tag{3.50}$$

where $I_0 = |E_0|^2$, x is temporal delay, v_0 is the central frequency, and τ is the temporal duration [323].

If M_2 travels at a constant velocity, the relationship between the interferogram function $I(x)$ and the source intensity $S(\omega)$ is given by [Fig. 3.9]:

$$I(x) = \frac{1}{2}\int_0^\infty S(\omega)cos2\pi\omega dx, \tag{3.51}$$

where ω is the frequency in wavenumbers. $I(x)$ is the cosine Fourier transform of $B(\omega)$ and contains complete information about the spectrum [322]. This function describes the Fourier transformation of the raw signal, which converts the spatial displacement x to the frequency domain. This gives the single-beam infrared spectrum. The typical transmittance or reflectance spectrum is the ratio spectrum of the sample to reference.

3.2.2 Bruker IFS 113v Fourier transform infrared spectrometer

The majority of the far-infrared (21-700 cm^{-1}) and middle infrared (450-5000 cm^{-1}) work was obtained by using the Bruker IFS 113v Fourier Transform Infrared (FTIR) spectrometer. I employed both transmittance and reflectance measurements. Figure 3.10 displays a detailed design of the optical path inside the Bruker 113v spectrometer. The spectrometer contains four chambers – source, interferometer, sample, and detectors. The interferometer used here is Genzel-type, which is similar to the Michelson interferometer described in the prior section. The sample chamber

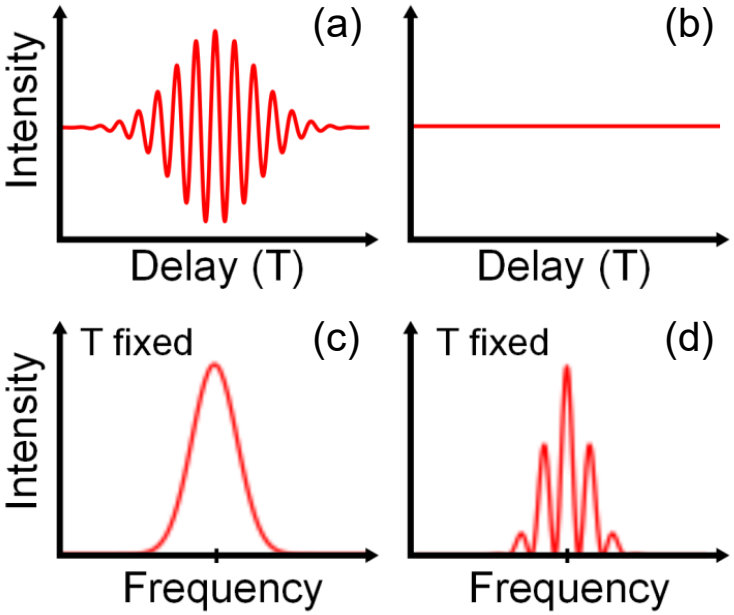


Figure 3.9: Typical interferogram is displayed here. (a,b) The intensity is measured as a function of a temporal delay (T) and (c,d) as a function of frequency [323].

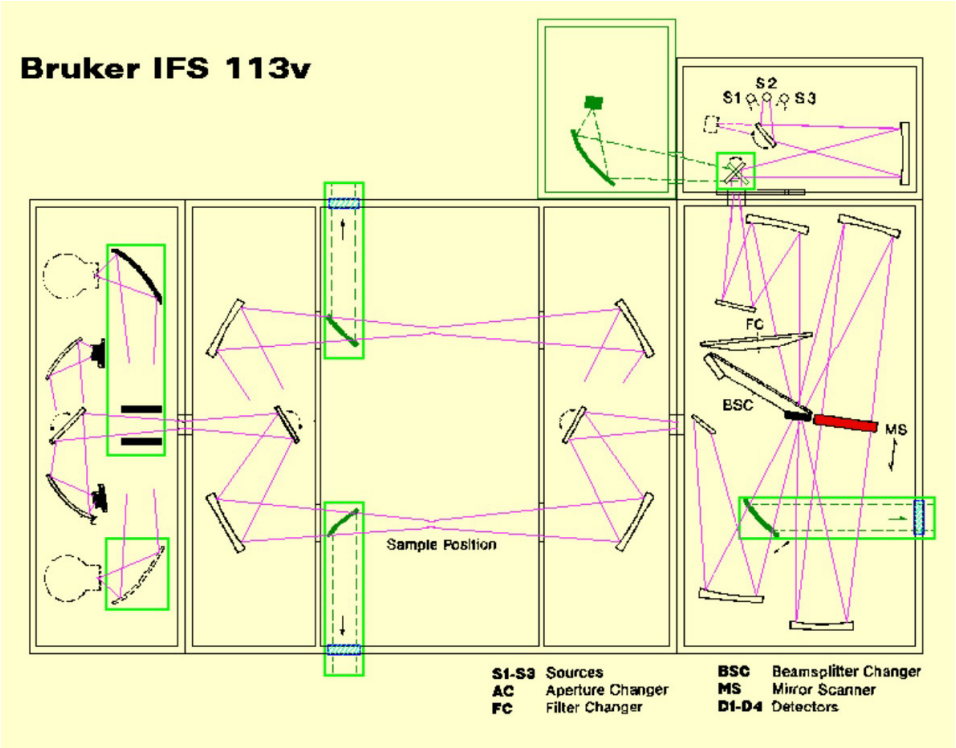


Figure 3.10: Schematic view of the Bruker IFS 113v FTIR spectrometer.

has front and back channels, which are optimized for transmittance or reflectance measurements, respectively. This system operates under a vacuum to reduce the background noise. The Si or B-doped Si bolometer, which is cooled with liquid helium, provides extra sensitivity. A schematic view of the beam path and optics is provided in Fig. 3.10.

In order to capture different energy regions most efficiently, the instrument uses a series of sources, detectors, and beam splitters for optimal resolution and signal. A list of combinations is shown in Table 3.3.

3.2.3 Bruker Equinox 55 Fourier Transform Infrared spectrometer with Bruker IR Scope II

For the middle infrared to visible range (600 - 17000 cm^{-1}), we use the Bruker Equinox 55 Fourier Transform Infrared spectrometer with the Bruker IR Scope II. This instrument is a combination of a spectrometer with a microscope attachment. Compared to the Bruker 113v, this instrument uses several different light sources, beam splitters, and detectors to provide a broader frequency range as well as a higher resolution and sensitivity for the measurements. In this case, we have the overlapped energy regions to compare the spectra from this instrument with the Bruker 113v, which allow us to double-check the accuracy and reliability of the shape and reflectance level of a spectrum. Furthermore, the Bruker IR Scope II is designed for accurate measurement of micro samples or small areas on larger samples by focusing with the microscope. The different types of sources, beam splitters, and detectors are listed in Table 3.4. The optical beam path of the spectrometer can be seen in Fig. 3.11.

Table 3.3: Bruker IFS 113v operating parameters

Range (cm^{-1})	Source	Beam splitter	Opt. Filter	Polarizer	Detector
10-50	Hg arc	Mylar 50 μ	Black PE	1	Si bolometer, DTGS
30-120	Hg arc	Mylar 23μ	Black PE	1	Si bolometer, DTGS
50-240	Hg arc	Mylar 12μ	Black PE	1	Si bolometer, DTGS
100-600	Hg arc	Mylar 3.5μ	Black PE	1	Si bolometer, DTGS
450-4000	Globar	KBr	open	2	B-doped Si bolometer, DTGS

Polarizer 1 = wire grid on oriented polyethylene (PE), Polarizer 2 = wire grid on AgBr

Table 3.4: Operating parameters of Bruker IRscope II

Range (cm^{-1})	Source	Beam splitter	Detector
600-7500 with middle-infrared polarizer	Globar	KBr	MCT
4000-12000 with near-infrared polarizer	Tungsten	Quartz	InSb
9000 -17000 with visible polarizer	Tungsten	Quartz	Si diode

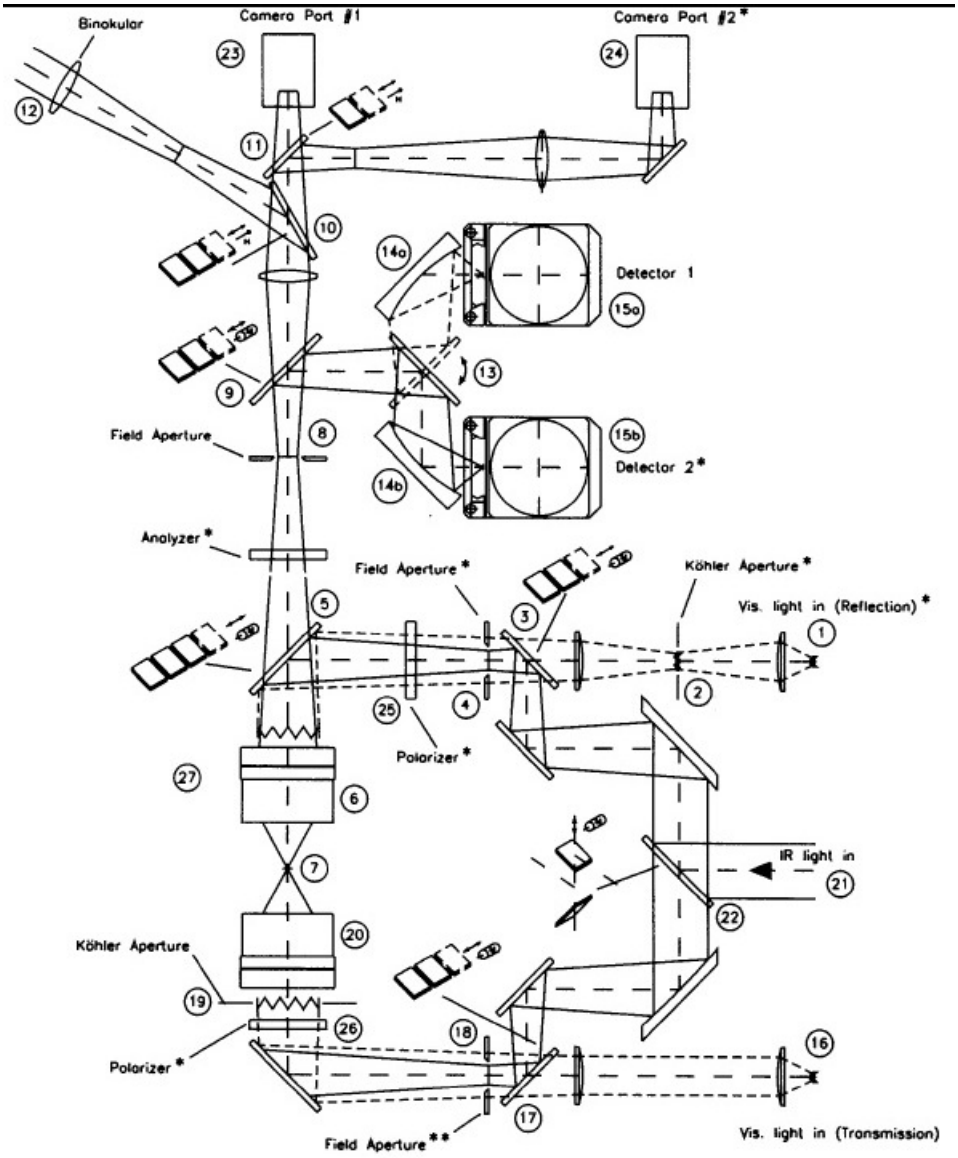


Figure 3.11: Optical path diagram of Bruker IRscope II. 1,16: a visible light source; 2,19: visible light aperture; 3,22: motorized switch mirror; 4,18: optional iris or knife edge aperture; 5,9,10,17: beam splitter changer; 6: objective lens; 7: Sample; 8: iris or knife edge aperture which defines the area of the sample analyzed; 12: binocular eyepiece; 13: two position detector selection mirror; 14: mirror routing to detector; 15: detector; 20: condenser; 21: IR beam (from spectrometer); 23,24: camera port; 25,26,27: polarizers.

3.2.4 Perkin Elmer λ-1050 grating spectrometer

Besides the Bruker 113v and the Bruker Equinox 55 FTIR spectrometers, we use a Perkin Elmer λ-1050 grating spectrometer to measure spectra in the near-infrared, visible, and ultraviolet regions (3000 - 52000 cm^{-1}). The Perkin-Elmer λ-1050 spectrometer features an all-reflecting, double-grating, double-beam optical system. The spectrometer is operated under nitrogen purging. The optical system is depicted schematically in Fig. 3.12.

Instead of using the interferometer, this instrument uses grating to get a specific wavelength of light. An optical grating can split and diffract light into several beams traveling in different directions. For chromatic light, the diffraction angle depends on the wavelength and the separation distance d between two successive grooves. This relation is known as the grating equation, given by:

$$dsin\theta = m\lambda, \tag{3.52}$$

where m is an integer and the order of diffraction, d is the groove spacing, λ is the diffracted wavelength, and θ is diffraction angle. A series of sources, polarizers, gratings, and detectors are used in order to achieve the optical data. All of them change automatically when different energy windows are measured. The detailed information is listed in Table 3.5.

Figure 3.12 displays the detailed optical path diagram for λ-1050. Source change is controlled by flipping mirror M1. The radiation of the source is reflected by mirror M2, and M3, and passes optical filter FW. Then, the beam is brought in the monochromator I through M4, slit SA, and M5. Depending on the desired wavelength range, the collimated radiation beam strikes either the 2400 lines/mm grating or the 1200 lines/mm grating.

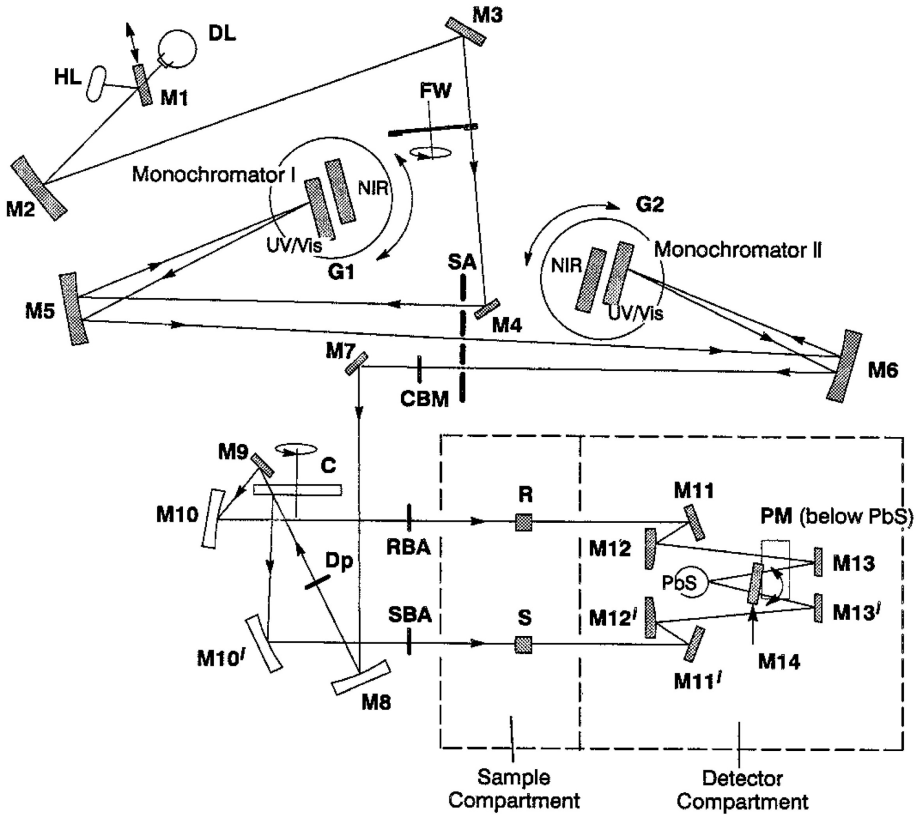


Figure 3.12: Optical layout of Perkin-Elmer λ-1050.

Table 3.5: λ-1050 operating parameters

Range (cm^{-1})	Source	Grating	Polarizer	Detector
3100-14250	Halogen Lamp	1200 lines/mm	Glan-Thompson prism	PbS
11240-31330	Halogen Lamp	1200 lines/mm	Glan-Thompson prism	Photomultiplier
31330-52000	Deuterium Lamp	2400 lines/mm	Glan-Taylor prism	Photomultiplier

The rotation position of the grating effectively selects a segment of the spectrum, reflecting this segment to mirror M5, go through the exit slit, and enter Monochromator II. The advantage of the double-monochromator is to maintain high spectral purity with an extremely low stray radiation content. The automatic grating change during monochromator slewing avoids the time-consuming re-alignment of the optics pathway due to the monochromator change.

The double beam is achieved via the chopper assembly C. As the chopper rotates, a mirror segment, a window segment, and two dark segments are brought alternately into the radiation beam. When a window segment enters the beam, radiation passes through to mirror M9 and is then reflected via mirror M10 to create the reference beam (R). When a mirror segment enters the beam, the radiation is reflected via mirror M10' to form the sample beam (S). When a dark segment is in the beam path, no radiation reaches the detector, permitting the detector to create the dark signal (D). Then, the measured spectrum is expressed as:

$$spectrum = (S - D)/(R - D). \tag{3.53}$$

Note that for reflectance measurements, we use an aluminum mirror as the reference. The spectra signature of the aluminum mirror is corrected by renormalization.

3.3 Spectroscopy under extreme conditions

Quantum materials can display interesting properties as long as the thermal fluctuation is eliminated. Therefore, low temperature is necessary to reveal quantum-related properties. Furthermore, quantum phase transitions can be driven using external stimuli such as a high magnetic field or pressure. Spectroscopy under these extreme conditions provides evidence for new states of matter, a microscopic un-

derstanding of how physical properties change through phase transitions, broken symmetries, or spin-orbital-charge-lattice interactions. In this dissertation, we measure the absorption spectra of different materials to study the optical properties of materials under variable temperatures and high magnetic fields.

3.3.1 Variable temperature spectroscopy

The low temperature measurements are carried out using an open-flow cryostat. The variable temperature experiments with the Bruker IFS 113v and Perkin-Elmer λ-1050 are performed in combination with an APD LT-3-110 Heli-Tran cryostat system with dual temperature sensors and a Lakeshore Model 330 temperature controller. Measurements with the Bruker Equinox 55 are made with Oxford Instruments Microstats He.

Figure 3.13 displays the complete setup of the system for variable temperature measurements, which includes a helium dewar, a helium gas tank, a transfer line, an open flow cryostat, a temperature controller, a vacuum pump, and a flowmeter. The helium dewar is connected to the helium gas tank in order to build pressure inside the dewar. This allows for the flow of helium to start. The transfer line is connected to the dewar and the open flow cryostat for the helium to travel from the dewar and to the sample. The transfer line and the open flow cryostat are connected to the flowmeter to control the amount of helium flowing into the system. A heater is attached to the cryostat to control the temperature. The sample chamber is under a vacuum in order to avoid ice forming as the temperature decreases. A turbo pump station is thus connected to the vacuum pump-out port. We note that the sample is mounted on the sample holder at the end of the cryostat and that it is important to place crycon grease between the cold stage of the cryostat and the sample holder to improve thermal contact. Since the transfer line and the outside of the cryostat

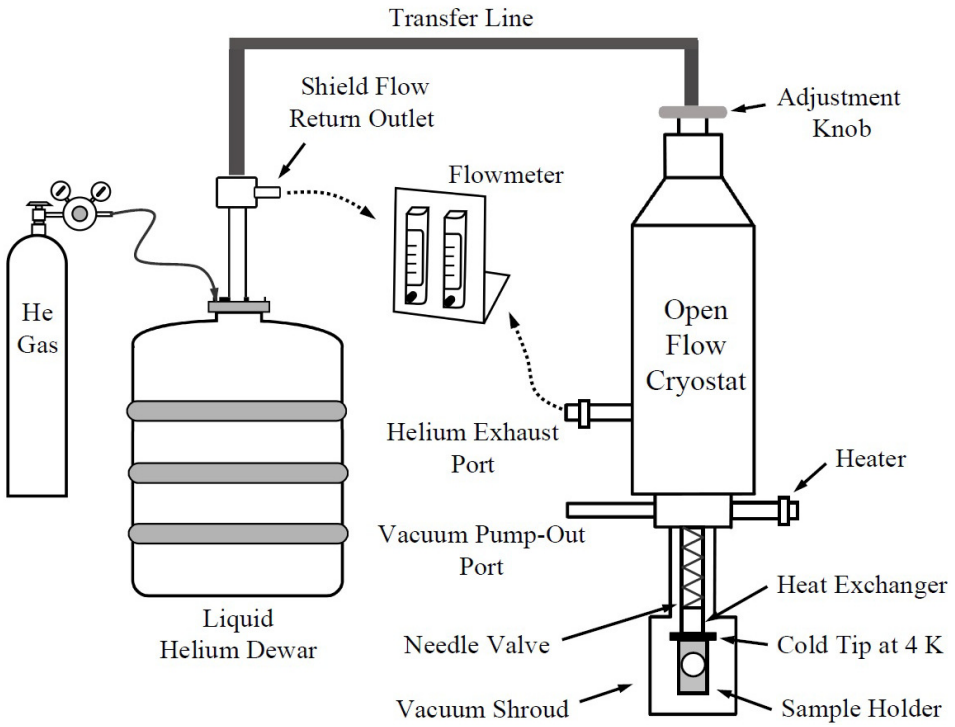


Figure 3.13: Set-up of LT-3-110 Heli-Tran liquid transfer line and cryostat .

are at room temperature, the system undergoes precooling before the liquid helium will begin flowing, which takes 20-25 minutes. The lowest temperature is ∼4 K. After cooling the sample, the liquid helium evaporates, and the gas is distributed in two ways: through the helium exhaust port on the side of the cryostat, and back through the transfer line with exit at the shield outlet port. The additional shield/return flow helps to keep the transfer line cold. The base of the cryostat is also equipped with another heater to prevent ice buildup and vacuum seal freezing. Cooling rates can be regulated in several different ways: (i) changing and maintaining pressure in the supply dewar, (ii) adjusting the flowmeter (attached to the helium exhaust port and the shield gas outlet), and (iii) adjusting the knob that controls the position of the needle valve at the end of the transfer line. Samples are mounted with GE varnish, rubber cement, and silver paste. The sample is then mounted on the heat exchanger/sample holder, under vacuum, and optical access is achieved through appropriate windows (depending on the frequency range). Two different thermal sensors are available. One is embedded in the tip of the cold stage and the other is mounted onto the sample holder.

3.3.2 High magnetic field spectroscopy

A great opportunity for spectroscopic measurements under high magnetic fields can be found at the National High Magnetic Field Laboratory. There are several types of magnets, including superconducting, resistive, hybrid, and pulsed magnets [Fig. 3.14]. These magnets and the facilities at the National High Magnetic Field Laboratory allow the possibility of measuring and investigating the spectroscopic response in very high magnetic fields. We use pulsed magnets from Fig. 3.14. However, we will also discuss resistive magnets even though the experiments did not turn out well and were not published. For more information, visit the National High

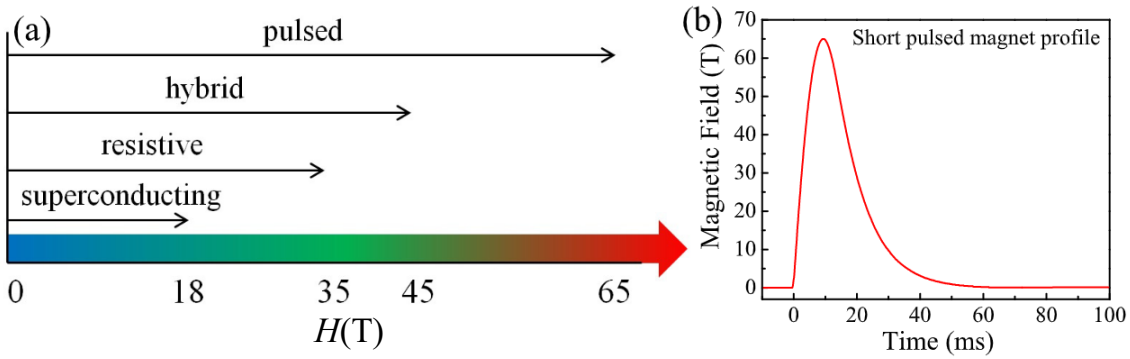


Figure 3.14: (a) A schematic energy scale of various magnets (superconducting, resistive, hybrid, and pulsed magnets) at National High Magnetic Field Laboratory. (b) Magnetic field profile of the short pulsed magnet at National High Magnetic Field Laboratory-Los Alamos National Laboratory. We note that split helix magnet is resistive, but only goes up to 25 T.

Magnetic Field Laboratory website at *http://www.nhmfl.gov*.

For high magnetic field spectroscopic experiments, it is important to notice several different things. First, the sample here is mounted on an optical probe inside a vacuum jacket. The vacuum jacket is then slightly filled with He exchange gas in order to achieve the base temperature. The jacket and probe with the sample are then immersed in a helium bath for the 4 K measurements. In optical measurements, the temperature can vary or reach up to around 100 K. In infrared measurements, the experiments must be done at 4 K as the detector (bolometer) must be used at the lowest temperatures. Another important issue is that the sample placement, probe, and vacuum jacket must be measured to be placed directly in the center of the magnetic field.

For magneto-optical experiments, a pulsed-field magnet was used in Los Alamos, NM. Magneto-optical spectroscopy was performed in the Faraday geometry at cryogenic temperatures (4.0 K) in a capacitor-driven 65 T pulsed magnet at the National High Magnetic Field Laboratory in Los Alamos, New Mexico. Our focus was on the 0.75 - 2.6 eV range with $\approx$ 2.4 meV resolution. Broadband light from a tungsten lamp was coupled to optical fibers and focused onto the sample for transmittance experiments. A collection fiber brought the light from the top of the probe to the grating spectrometer, where both charge-coupled device and InGaAs detectors were employed as appropriate. We designed a Voigt probe in order to measure toroidal geometry for nonreciprocal directional dichroism [Fig. 3.15]. Since Faraday geometry has a light propagation direction parallel to the magnetic field, the easiest way to achieve Voigt geometry is by reflecting the light with prisms in order to have a light propagation direction perpendicular to the magnetic field. Polyetheretherketone material is mainly used to make the end piece since it is nonmagnetic and extremely rigid. Those requirements are a must in a pulsed magnetic field in order to avoid

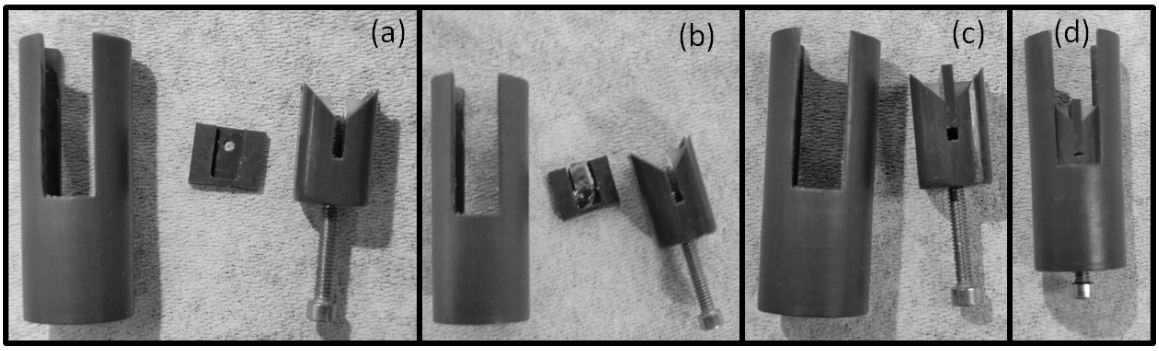


Figure 3.15: A Voigt geometry sample holder, made of nonmagnetic PEEK (polyetheretherketone) material. It consists of three pieces: a mountable sample slide, a prism holder to reflect the light onto the sample and back into the detector, and a piece to hold everything together and attach at the end of the magneto-optics probe. (a)-(d) shows the process of mounting the sample to attaching it to the probe for the Voigt geometry.

heating, vibrating, and breaking.

3.3.3 Magnetic circular dichroism setup at the National High Magnetic Field Laboratory

The magnetic circular dichroism experiments were performed at National High Magnetic Field Laboratory using the 25 T split helix magnet [324]. Figure 3.16 (a) displays a cutaway design of the split helix magnet cryostat. This magnet consists of two resistive coils with four wide optical ports. These ports are used to shine a light on the sample from the horizontal plane, giving access to more intricate and complicated measurements. High currents are applied in the resist coils to generate a magnetic field up to 25 T along the vertical direction. The direction of electric current can be switched in order to switch the magnetic field direction in the + or - z direction.

Figure 3.16 (b) shows the sample mounting probe for the transmission mode of the MCD experiment. The sample is mounted in a spherical sample holder with GE varnish. Since we used the Faraday geometry for the MCD experiment, the bottom part of the probe consists of a silver mirror and a converging lens. The silver mirror is used to reflect the light by 90 degrees so that the light is propagating along the vertical direction, which is parallel or antiparallel to the direction of the magnetic field. Since the reflection will change the phase of the left and right circularly polarized light by an equal amount, using the silver mirror will not affect the MCD signal. The sample holder is fixed at the back focal point of the converging lens to maximize the light power density.

Figure 3.16 (c) displays a complete setup for the magnetic circular dichroism experiment. A series of optical components are used to optimize the MCD signal. We used a 240 W Xe lamp as a light source and a 0.25 m monochromator. An optical

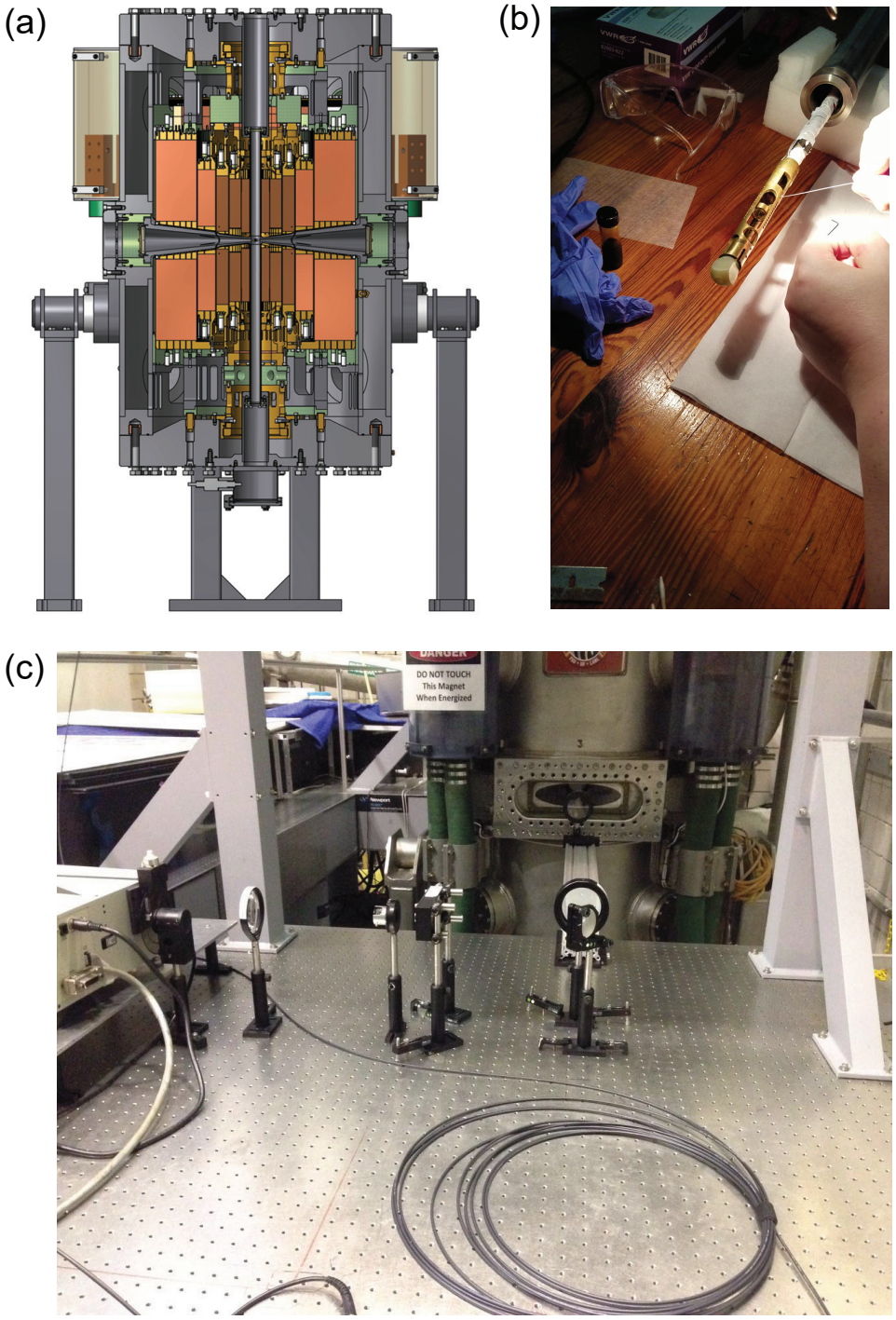


Figure 3.16: (a) Detailed structure of the 25 T split helix magnet in the NHMFL. Images are available at: https://nationalmaglab.org/about/around-the-lab/meet-the-magnets/meet-the-split-helix-magnet. (b) Sample mounting probe of the magnetic circular dichroism experiment. (c) MCD experimental setup at the NHMFL.

chopper is employed to increase the signal-to-noise ratio at a constant frequency, followed by a linear polarizer that is set to 45 degrees. A photoelastic modulator is placed after the linear polarizer to convert the linearly polarized light into right or left circular polarized light periodically at a constant time interval $\delta(t) = \lambda/4 \sin(\omega t)$. Several lenses are used to increase power density. We did not need to keep the phase information, so an optical fiber is used to collect the light and route it to the detector. The detector has the best sensitivity within the range of 0.8 and 2.8 eV (also depends on the sample). All signals were separated by lock-in amplifiers. The evacuated probe is in the liquid helium environment. A heater is built inside the probe to control the temperature.

3.4 Project-specific details: Sample growth, measurements, and complementary calculations

3.4.1 Band-Mott mixing hybridizes the gap in $Fe_2Mo_3O_8$

3.4.1.1 Single crystals growth

High quality single crystals of $Fe_2Mo_3O_8$, the Zn-substituted analogs $FeZnMo_3O_8$, and $Zn_2Mo_3O_8$, as well as $Mn_2Mo_3O_8$ and $Ni_2Mo_3O_8$, were grown by chemical vapor transport as discussed previously [28] by our collaborators, X. Xu, B. Gao, and S.-W. Cheong. Special care was taken to assure the stoichiometry of $FeZnMo_3O_8$. Crystals were polished to control optical density and expose the hexagonal face.

3.4.1.2 Optical measurements

A Bruker 55 Fourier transform infrared spectrometer equipped with a microscope attachment was used to measure transmittance over the 0.41 - 2.0 eV energy range.

Absorption was calculated as $\alpha(E) = -\frac{1}{d}\ln(\mathcal{T}(E))$, where $\mathcal{T}(E)$ is the transmittance, and d is the thickness. Performing these measurements in transmittance rather than reflectance avoids light leakage problems [29, 314]. The temperature was controlled by an open flow cryostat between 4 to 300 K.

3.4.1.3 Complementary electronic structures calculations

For theoretical calculations, G. L. Pascut, D. Vanderbilt, and K. Haule used the density functional theory (DFT) as implemented in WIEN2k [325] and a charge-self-consistent dynamical mean field theory (DMFT) as implemented in the eDMFT code [326, 327]. At the DFT level, the generalized gradient approximation Perdew-Burke-Ernzerhof (GGA-PBE) functional [328] is used, with RKmax = 7.0 and 312 k-points in the irreducible part of the 1^{st} Brillouin zone. At the eDMFT level, the fully rotationally invariant Coulomb interaction, a nominal double-counting scheme [329] is used, with the d-orbital occupations for double counting corrections for Mn, Fe, Co and Ni set to be 5, 6, 7, and 8, respectively. The temperature is fixed at 500 K. To define the DMFT projector, quasi-atomic orbitals were used by projecting bands in a large hybridization window (-10 to +10 eV) with respect to the Fermi level, in which partially screened Coulomb interactions have values of U = 10 eV and J_H = 1 eV in Mn, Fe, Co, and Ni ions. Additional detail is available in Ref. [314].

3.4.2 Nonreciprocal directional dichroism at telecom wavelengths

3.4.2.1 Crystal growth and orientation

High quality single crystals of Ni_3TeO_6 were grown by chemical vapor transport methods as described previously [251] by J. J. Yang and S.-W. Cheong at Rutgers University. The crystals were polished to expose either the ab-plane or the c-axis and

to control optical density. After polishing, the sample thicknesses were on the order of 30 μm. Optical microscope images and optical rotation data confirm that the crystals have a single chiral domain [250] as shown in Fig. 3.17. This is important in order to have a net magnetic moment. Otherwise, multiple domains can cancel the magnetic moment and eliminate the nonreciprocal effect. The crystals were coated with transparent epoxy to stabilize the structure during the field pulses.

3.4.2.2 Optical spectroscopy

Polarized optical transmittance was measured by M. Yokosuk as a function of energy and temperature using a series of spectrometers as described previously (0.78 - 2.5 eV; 4.2 -300 K) [62]. Absorption was calculated as $\alpha(E) = \frac{1}{d}\ln(T(E))$, where d is the sample thickness and $T(E)$ is the measured transmittance.

3.4.2.3 Magneto-optical spectroscopy

Magneto-optical work was performed in the toroidal geometry in a capacitor-driven 65 T pulsed magnet at the National High Magnetic Field Laboratory in Los Alamos, NM with our collaborators, M. Goryca and S. A. Crooker. We employed the standard transmission probe fitted with a specially-designed Voigt end-piece for this work. Figure 3.18 shows three different configurations to achieve nonreciprocal directional dichroism in Ni_3TeO_6. These measurements covered the 0.75 - 2.6 eV range with a 2.4 meV resolution and were carried out at 4 K. Broadband light from a tungsten lamp was coupled to optical fibers and focused onto the sample for transmittance experiments. A collection fiber brought the light from the top of the probe to the grating spectrometer, where both CCD and InGaAs detectors were employed as appropriate. The spectra were taken in four different measurement configurations: ($\pm\mathbf{k}$, $\pm\mathbf{H}$). Each run was carried out sequentially and consistently,

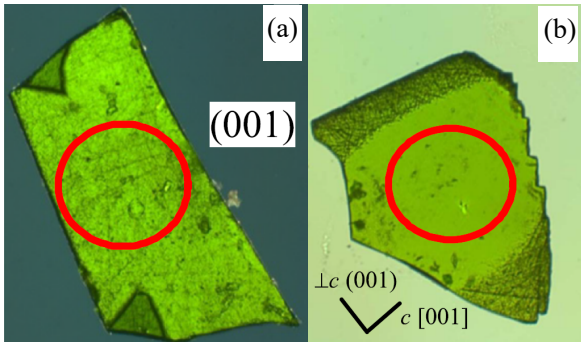


Figure 3.17: The image shows polished Ni_3TeO_6 crystal with single domain in *ab*-plane (a) and *c*-axis (b) [250].

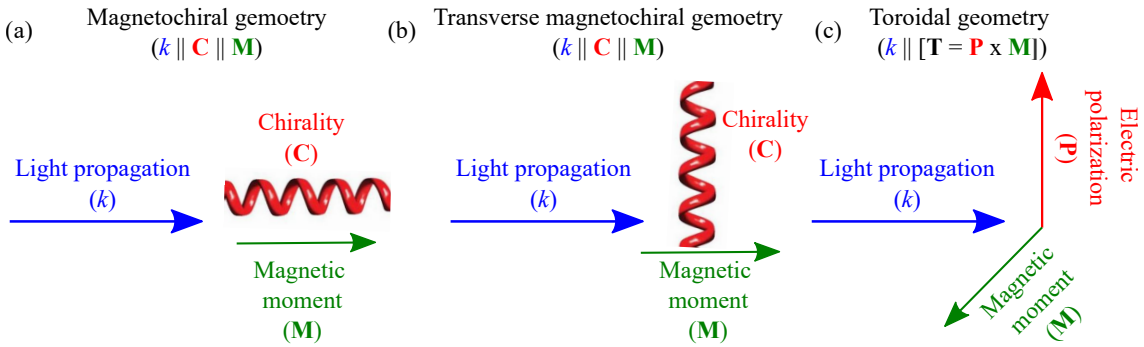


Figure 3.18: Schematics display three geometries in Ni_3TeO_6 to observe nonreciprocal directional dichroism. (a) Magnetochiral geometry consists of light propagation (k) parallel to chirality (**C**) and magnetic moment (**M**). (b) Transverse magnetochiral geometry has k parallel to **M**, but **C** is perpendicular. (c) Toroidal geometry (**T**) is composed of electric polarization (**P**) perpendicular to **M**. The light propagation direction is orthogonal to both.

starting with one **k** direction (and pulsing to obtain both ±**H**) and then switching to the other **k** direction by swapping the fibers (again pulsing both up and down). We calculated the absorption differences as: $\Delta\alpha = \alpha(\mathbf{H} = \pm\ 60\ \text{T})$ - $\alpha(\mathbf{H} = 0\ \text{T})$. As an example, nonreciprocal directional dichroism is calculated as: $\Delta\alpha_{\text{NDD}}(+\mathbf{k}, \pm\ \mathbf{H}) = \Delta\alpha(+\mathbf{k}, +\mathbf{H})$ - $\Delta\alpha(+\mathbf{k}, -\mathbf{H})$. Nonreciprocity can also be defined in terms of counter-propagating beams as $\Delta\alpha_{NDD}(\pm\mathbf{k}, +\mathbf{H})$. Traditional smoothing techniques were employed in the CCD detector regime.

3.4.2.4 Modeling the optical diode effect

H.-S. Kim, K. Haule, and D. Vanderbilt found magnetic configurations under the external **H**-field by optimizing total energies of a magnetic exchange hamiltonian derived from previous first-principles electronic structure calculations [252]. Distortions in the crystal structure induced by the external **H**-field were simulated by enforcing magnetic configurations obtained from the model optimization above during the first-principles density functional theory (DFT) calculations and structural relaxations, which were performed via the Vienna *ab-initio* Simulation Package (VASP) [330,331]. For VASP structural relaxations, a 500 eV of plane-wave energy cutoff, a $5 \times 5 \times 5$ Γ-centered **k**-point sampling, and a simplified rotationally-invariant DFT+U_{eff} formalism ($U_{\text{eff}} = 4$ eV) [332] on top of PBEsol exchange-correlation functional [333] were employed. After structural relaxations, WIEN2K full-potential DFT code [334] was used to compute electric dipole matrix elements and crystal fields in terms of the non-interacting band basis, which were then projected onto Ni^{2+} atomic multiplet states via exact diagonalization (ED) routine included in the Embedded DMFT Functional (EDMFTF) code [335]. Details on WIEN2K, ED calculations, computations of electric and magnetic dipole matrix elements, and estimations of magneto-electric response tensors are presented in our paper [250].

3.4.3 Spin-phonon interactions, frustration, and magnetoelectric coupling in $Co_4Nb_2O_9$ and the Ta analog

3.4.3.1 Single crystals growth

C. Kim, D. G. Oh, N. Lee, S. Choi, and S.-W. Cheong grew high quality single crystals of $Co_4Nb_2O_9$ and $Co_4Ta_2O_9$ by flux techniques as described previously [260, 268]. The sample dimensions were approximately $10 \times 5 \times 1$ mm^3 for $Co_4Nb_2O_9$ and $1 \times 1 \times 1$ mm^3 for the Ta analog. In each case, we employed the shiny *ab*-plane of the crystals directly and polished the sides to expose optically-flat surfaces for *c*-polarized work.

3.4.3.2 Reflectance spectroscopy and Kramers-Kronig analysis

Near normal reflectance measurements were carried out over a wide frequency range (between 25 and 55,000 cm^{-1}) using a series of spectrometers and polarizers to obtain the *ab*-plane and *c*-axes response. A Kramers-Kronig analysis was used to obtain the optical constants [296]. The low-frequency limit was extrapolated as a constant (appropriate for a semiconductor), and the high-frequency limit was extrapolated as $\omega^{-1.75}$. The infrared absorption, $\alpha(\omega)$, and the real part of the optical conductivity, $\sigma_1(\omega)$, are of primary interest in this work. Open-flow cryostats were employed for temperature control between 300 and 7 K.

3.4.3.3 Lattice dynamics calculations

The theoretical phonon frequencies were calculated using the VASP code by J. Kim [336, 337]. The pseudopotentials are of the projector-augmented-wave type as implemented in VASP [338, 339], with valence configurations $3d^74s^2$ for Co, $2s^2sp^4$ for O, $4d^34p^65s^2$ for Nb, and $5d^36s^2$ for Ta. The exchange-correlation functional is described by the Perdew-Burke-Ernzerhof type generalized gradient approximation [340], with Du-

darev type Hubbard U correction [332] on Co $3d$ orbits by 3 eV. The plane-wave cut-off energy is set to 400 eV. The Brillouin zone sampling grid is $12 \times 12 \times 4$ including the Γ point. Spin-orbit coupling was not taken into account. The structural coordinates were relaxed within a force threshold of 1.0 meV/Å. To obtain the Γ point phonon frequencies, the dynamical matrix was calculated with the primitive hexagonal cell by using density-functional-perturbation theory [341] and was processed with the PHONOPY code [342]. The oscillator strength and dielectric function were calculated by combining Born effective charge tensors and high-frequency dielectric constant from the electron response [343,344]. The dielectric function was also converted to reflectance for comparison with our measurements assuming normal incidence and reflection.

3.4.4 Spin-lattice coupling in $MnPS_3$ and giant magnetic circular dichroic signal in $CrPS_4$

3.4.4.1 Crystal Growth

High quality single crystals of $MnPS_3$ and $CrPS_4$ were prepared via chemical vapor transport as described previously by V. Hagland. [291, 345] Samples were exfoliated to control the optical density and reveal various exciations for spectroscopy measurements.

3.4.4.2 Optical spectroscopy

The ab-plane of $MnPS_3$ and $CrPS_4$ single crystals as well as the blank substrate were measured in transmittance using a λ-900 grating spectrometer covering the energy range from 1.4 to 6 eV. The linear absorption spectrum is calculated from measured transmittance as $\alpha(E) = \frac{1}{d}\ln(T(E))$, where $T(E)$ is the measured transmittance as a function of energy E and d is the sample thickness. An openflow cryostat were used to control temperature (4.2–300 K).

3.4.4.3 Magnetic circular dichroism spectroscopy

We measured the dichroic response of $MnPS_3$ and $CrPS_4$ from 1.4 to 3 eV. This is the energy window where the local d-to-d excitations and charge-transfer gap are. These experiments were performed at the National High Magnetic Field Laboratory using the 25 T split helix magnet [324] in Faraday geometry along with a 240 W Xe lamp and a 0.25 m monochromator. We measured the difference in transmittance between left- and right-circularly polarized (LCP and RCP) light at various magnetic fields, and converted the result to absorbance difference, as discussed in detail below. Thus, the dichroic spectrum is the difference in absorption between LCP and RCP. A chopper was employed to increase the signal to noise ratio at a constant frequency, followed by a linear polarizer that was set to 45°. A photoelastic modulator was placed after the linear polarizer to convert the linearly polarized light into left or right circular polarized light periodically at a constant time interval $\delta(t) = \lambda/4 \sin(\omega t)$. We did not need to keep the phase information, so an optical fiber was used to collect the light and route it to the detector. All signals were separated by lock-in amplifiers. The field sequence was chosen based upon the needed resolution, always within the +25 T → 0- T → 25 T → 0+ T → +25 T run pattern. The positive or negative sign of the magnetic field corresponds to the magnetic field direction and is parallel or antiparallel to the light propagation direction, respectively. The 0- and 0+ are both zero-field data; the sign denotes the sweep direction. Moreover, a training loop with this pattern was performed before each data collection run. The phase of the lockin was set at full field. Magnetic circular dichroism spectra were taken at several different temperatures - from ∼10 to 160 K for $MnPS_3$ and ∼11 to 100 K for $CrPS_4$.

Magnetization measurements Minsung Lee and Eleni Kyriazi performed High-field magnetization at the National High Magnetic Field Lab in Los Alamos. The pulsed-field magnetisation experiments used a 1.5 mm bore, 1.5 mm long, 1000- and 500-turn coil susceptometer, constructed from 50-gauge, high-purity copper wire. When a sample is within the coil, the signal is $V \propto (dM/dt)$, where M is the magnetization and t is time. Numerical integration is used to evaluate M. Samples were mounted within a 1.3 mm

diameter ampoule that can be moved in and out of the coil. The net M of the sample is obtained by subtracting the empty-coil data from those measured under identical conditions with the sample present. In order to maximize the sample signal, we used compensating coils to totally subtract the background out as $V_{total} = V_{1500coils} + \alpha V_{compensation} + V_{sample}$, where α can be manipulated to be equal to $V_{1500coils}$.

Chapter 4

Band-Mott mixing hybridizes the gap in $Fe_2Mo_3O_8$

In order to place the charge excitations on a firm foundation, we measured the optical properties of the $A_2Mo_3O_8$ family of materials (where A = Fe, Ni, Mn, Zn) and compared our findings with complementary electronic structure calculations. We show that the 1.7 eV gap in $Zn_2Mo_3O_8$ is determined by the charge excitations of the Mo trimer. Replacing Zn on the octahedral site with Fe yields $FeZnMo_3O_8$. This system has a substantially reduced and renormalized gap determined by Fe-O hybridized bands appears due to the periodic lattice potential. Further substitution yields $Fe_2Mo_3O_8$ which has both trigonally-distorted octahedral and tetrahedral sites occupied by Fe atoms, and the gap is further reduced to 1.0 eV. Here, the charge gap is more complex to describe because it has mixed band and Mott features. In other words, some orbitals hybridize strongly with oxygen and form very narrow bands whereas other orbitals exhibit real space localization and are Mott insulating. Mixed band and Mott gaps are commonly called orbitally- or site-selective Mott states [346–351]. What distinguishes $Fe_2Mo_3O_8$ from other orbitally-selective Mott systems is the narrow many-body resonance emanating from the edge of the flat valence band. The Kondo effect is, of course, normally studied in metals. In this work, we show that the Kondo effect can also appear in mixed metal semiconductors. In addition, the gap

in $Fe_2Mo_3O_8$ is sensitive to magnetic ordering at 61 K due to the heavily mixed character of the charge excitations. Moreover, the d-to-d excitations on the distorted octahedral Fe site are vibronically activated, and spin-orbit related features ride on top of the distorted tetrahedral on-site excitations below the magnetic ordering transition. We discuss these findings in terms of band-Mott mixing in 3- and 4d-containing quantum cluster magnets.

4.1 Optical response of $Fe_2Mo_3O_8$ and the A-substituted analogs (A = Zn, Mn, Ni)

Figure 4.1(c-e) summarizes the optical properties of the (Fe,Zn)Mo_3O_8 family of materials. The absorption spectrum of the parent compound, $Zn_2Mo_3O_8$, is low and flat in the near infrared, rising on approach to the O $2p \rightarrow$ Mo $3d$ charge transfer excitation. The direct band gap is 1.75 eV. Because Zn^{2+} has a d^{10} configuration, there are no d-to-d on-site excitations. $Zn_2Mo_3O_8$, therefore, provides an opportunity to study how the Mo trimer interacts with oxygen in isolation. At the same time, it is an important scaffold upon which additional complexity can be built.

Sequential A-site substitution of Fe, first into the distorted octahedral site in $FeZnMo_3O_8$, here denoted as Fe(O), and then into the distorted tetrahedral site in $Fe_2Mo_3O_8$, henceforth Fe(T), lowers the charge gap significantly [Fig. 4.1(f)]. We find direct gaps of 1.2 and 1.0 eV for $FeZnMo_3O_8$ and $Fe_2Mo_3O_8$, respectively. The gap values were determined from Tauc plots of $(\alpha \cdot E)^2$ vs. energy [352].

Figure 4.1(d) displays the absorption of $FeZnMo_3O_8$. The charge excitations across the gap consist of mixed O $2p$ + Mo $3d$ + Fe(O) $3d$ transitions. The lowest energy excitation across this gap comes from Fe(O) hybridizing with Mo-O trimers. The 1.2 eV gap is substantially lower in energy than the fundamental Mo-O band gap, which theoretically remains roughly equal to that in $Zn_2Mo_3O_8$. As Fe^{2+} populates the octahedral site in $FeZnMo_3O_8$, an on-site d-to-d transition arises near 0.95 eV. It overlaps strongly with the leading edge of the charge transfer band and is activated by vibronic coupling [Fig. 4.2(c,f)]

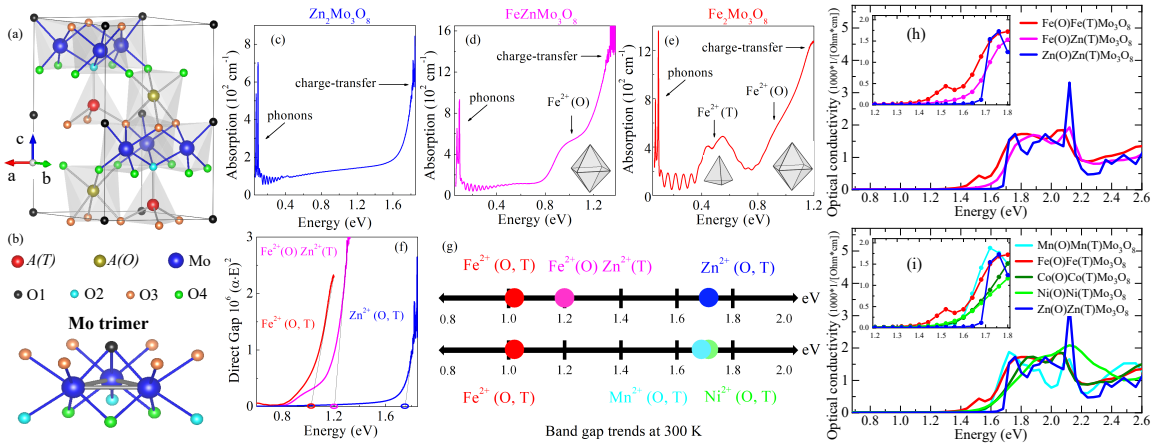


Figure 4.1: (a) Crystal structure of the $A_2Mo_3O_8$ compounds where A = Mn, Fe, Co, Ni, Zn. A(T) and A(O) represent ions in trigonally-distorted tetrahedral and octahedral environments, respectively. (b) Schematic view of the Mo trimer. (c-e) Absorption spectra of $Zn_2Mo_3O_8$, $FeZnMo_3O_8$, and $Fe_2Mo_3O_8$ measured at room temperature. (f) A Tauc plot reveals the direct band gap of $Zn_2Mo_3O_8$ and the Fe substituted analogs. (g) Band gap schematic showing the impact of two different types of T and O-site substitution. The upper and lower trend lines correspond to the $(Fe,Zn)_2Mo_3O_8$ series and the $A_2Mo_3O_8$ (A = Fe, Mn, Ni) materials, respectively. (h,i) Calculated optical conductivity of the $A_2Mo_3O_8$ materials.

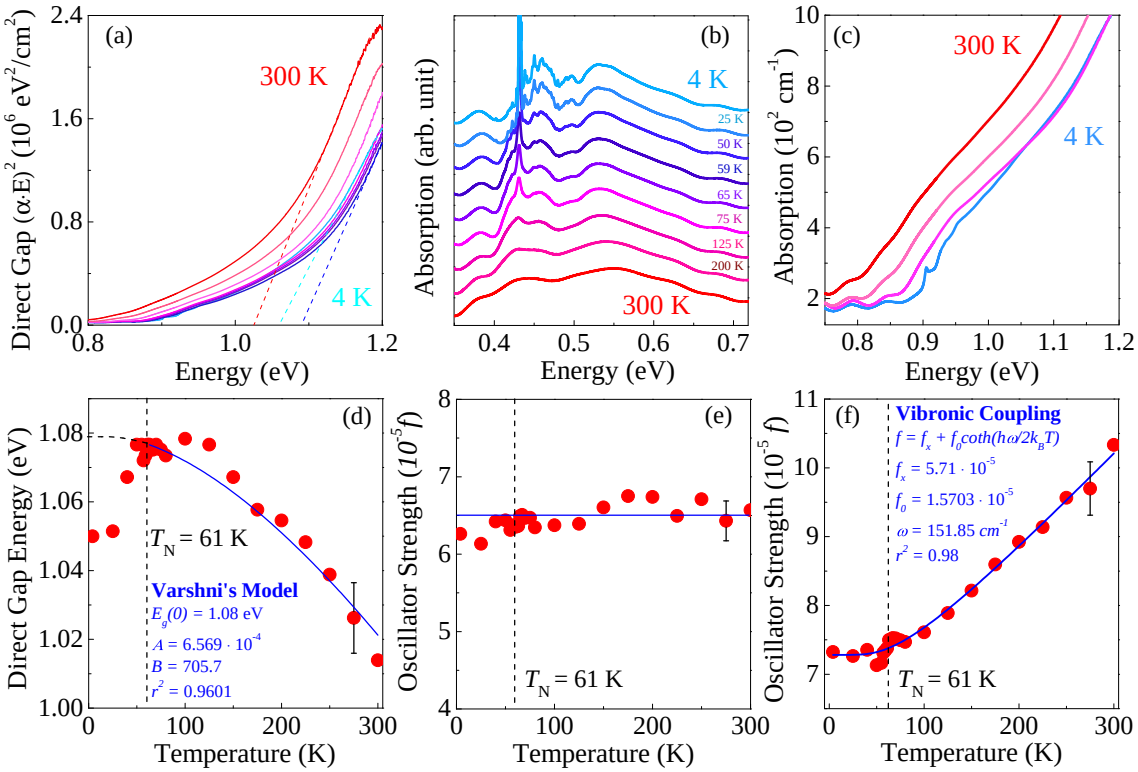


Figure 4.2: (a, d) Tauc plot of $(\alpha \cdot E)^2$ vs. energy for $Fe_2Mo_3O_8$ and a plot of band gap vs. temperature with a fit to the Varshni model. (b, e) Close-up view of the Fe^{2+} d-to-d on-site excitation on the tetrahedral site showing the fine structure that develops due to spin-orbit coupling below the 61 K magnetic ordering transition. (c, f) Close-up view of the Fe^{2+} d-to-d on-site excitation on the octahedral site and oscillator strength vs. temperature along with a fit to a modified vibronic coupling model [353–355].

[353–355]. Notice that absorption is low and flat near 0.5 eV - a sign of crystal quality and stoichiometry. Once the Fe(T) site is populated as well (as in $Fe_2Mo_3O_8$), the gap is reduced further, and two different types of d-to-d on-site excitations are identified inside the charge gap. As shown in Fig. 4.1(e), Fe on the trigonally-distorted tetrahedral site contributes additional atomic-like excitations centered at 0.5 eV. While oscillator strength is fully conserved as a function of temperature [Fig. 4.2(e)], a great deal of fine structure due to spin-orbit coupling rides on top of the band below the 61 K magnetic ordering transition [Fig. 4.2(b)]. A similar response develops in Fe^{2+}:ZnSe [356]. The full sequence of gap values is shown schematically in Fig. 4.1(g).

To test the influence of A-site substitution on the band gap and strength of the metal to MoO-trimer hybridization, we measured the optical properties of the Mn and Ni analogs of $Fe_2Mo_3O_8$ [Fig. 4.3]. $Mn_2Mo_3O_8$ and $Ni_2Mo_3O_8$ have charge gaps of 1.65 and 1.7 eV, respectively - very similar to that of the Zn end member. This result is attributable to $3d$ orbital filling and character. The Mn system has a half-filled d-manifold, which corresponds to a high spin Mott state with a large gap. The d^8 configuration in the Ni analog also has two holes and is thus in the large gap Mott insulating state. As a result, there is little mixing between the metal center and Mo-O trimer, hence these transition metals do not play an active role in determining the low-energy excitations across the gap. We mention in passing that the Mn and Ni compounds have on-site d-to-d excitations as well [Fig. 4.3].

On the other hand, $Fe_2Mo_3O_8$ has both Mott-type and band-insulating orbitals, which strongly hybridize with the Mo trimer. These interactions enable the Fe centers to control the low-energy physics as discussed below. Moreover, we find that the band gap of $Fe_2Mo_3O_8$ is sensitive to the 61 K magnetic ordering transition and the associated structural distortion [Fig. 4.2(a,d)]. This is different from the other $A_2Mo_3O_8$ compounds, where the temperature dependence of the band gaps are in excellent overall agreement with the Varshni model [311, 312] implying no (or extremely subtle) structural aspects to the magnetic ordering transitions. That the band gap decreases across T_N is due to the coupling of charge, structure, and magnetism and the flat bands emanating from the

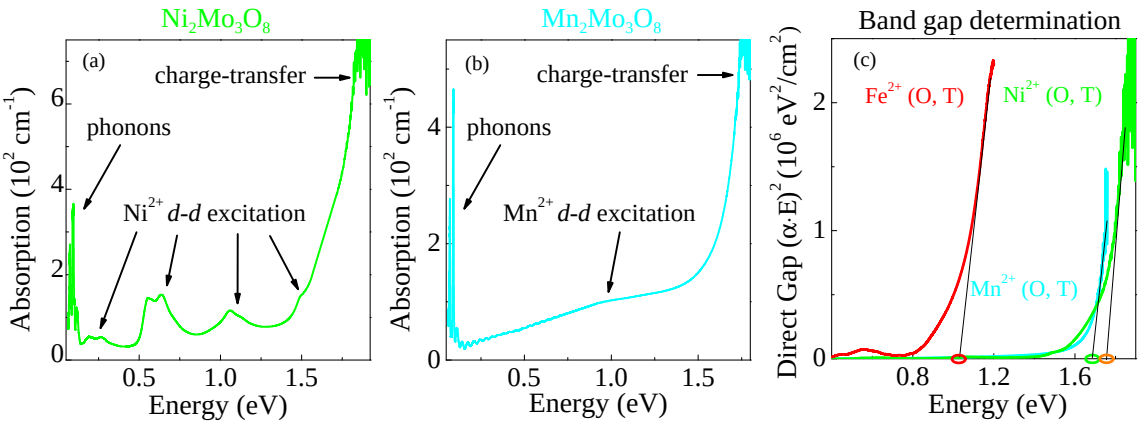


Figure 4.3: (a,b) Absorption spectra of $Ni_2Mo_3O_8$ and $Mn_2Mo_3O_8$ single crystals in the *ab*-plane at room temperature. (c) A Tauc plot is used to extract the direct band gap of these materials.

trigonally-distorted tetrahedral Fe site.

4.2 Strong hybridization, resonance, and interaction with the Mo trimer

Figure 4.1(h) displays the theoretical optical conductivity of $Zn_2Mo_3O_8$, $FeZnMo_3O_8$ and $Fe_2Mo_3O_8$ computed using a combination of Density Functional Theory and embedded Dynamical Mean Field Theory (DFT + eDFMT) methods [326, 327]. Here, we find the same trend of decreasing charge gap with Fe substitution. In $Zn_2Mo_3O_8$, the size of the optical gap is $\approx$1.7 eV which decreases to approximately 1.5 and 1.4 eV in $FeZnMo_3O_8$ and $Fe_2Mo_3O_8$, respectively. Figure 4.1(i) compares the theoretical optical conductivity of the Mn, Ni, and Co analogs. We find that the predicted gap is larger in all of these compounds (near 1.55 eV) as compared to $Fe_2Mo_3O_8$. The edge of the gap is very smooth and temperature smeared. This is quite different from $Fe_2Mo_3O_8$ where the gap is smaller with an additional peak at the onset.

To better understand what determines the low energy excitations and character of the gap in this class of compounds, we calculated the local density of states for the full set of $A_2Mo_3O_8$ materials [Fig. 4.4]. While the optical gap in general is different than the gap of the single-particle excitations measured by the local density of states, the two are very similar in these compounds. This is because the band gap is direct in $Zn_2Mo_3O_8$, and the hybridized bands in the Fe-containing compounds are extremely narrow. Hence momentum-conserving excitations have essentially the same gap size as finite momentum single-particle excitations. The insets show that the position of the conduction band in $FeZnMo_3O_8$ and $Fe_2Mo_3O_8$ decreases slightly as compared to $Zn_2Mo_3O_8$, although the change is small. Most of the action is in the valence bands, where the FeZn band edge moves considerably upward. In $Fe_2Mo_3O_8$, a very narrow many-body excitation forms at the onset of the gap. This is the origin of the first peak in the optical conductivity [Fig. 4.1(h,i)] and the reason that the gap is drawn strongly downward in this system.

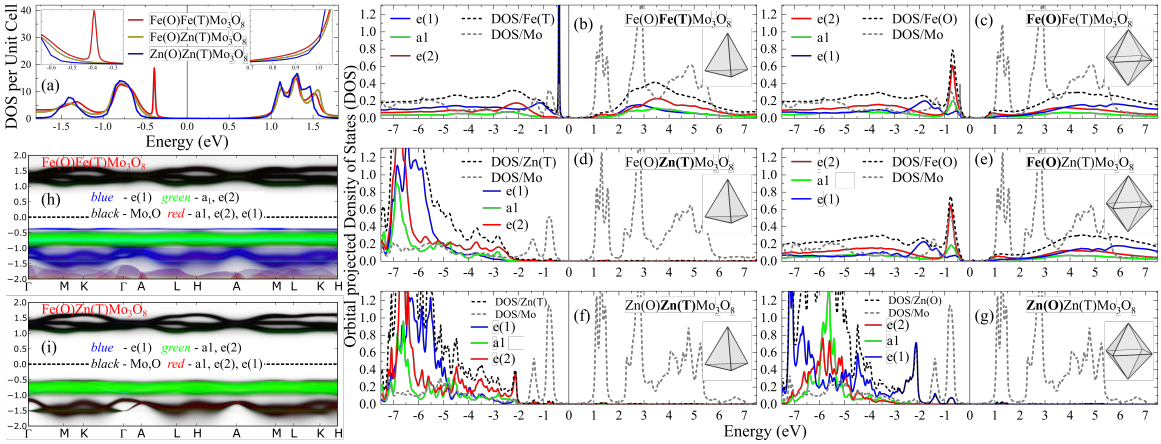


Figure 4.4: The density of states (DOS) for $A_2Mo_3O_8$ (A = Fe and Zn): (a) total DOS; (b-g) atom- and orbital-projected DOS. The (T) and (O) symbols refer to trigonally-distorted tetrahedral and octahedral environments. The vertical solid lines are placed at zero chemical potential. The schematic insets of gray tetrahedra/octahedra are guides to the eye pointing the reader to the electronic states of the transition metal ions in the corresponding environment. (h, i) Orbital projected spectral functions for $Fe_2Mo_3O_8$ and $FeZnMo_3O_8$ (blue - $e(1)$ tetrahedra; green - a_1 and $e(2)$ octahedra; red - a_1, $e(2)$ tetrahedra and $e(1)$ octahedra).

Figure 4.4(b-g) displays the projected density of states (DOS) per transition metal center and per orbital in the distorted tetrahedral (T) and octahedral (O) environments. The local point group symmetry around each iron center is C_{3v}. Therefore, the e and t_2 levels at the distorted tetrahedral site break into $e(1)$, a_1, and $e(2)$ orbitals. Similarly symmetry at the trigonally-distorted Fe octahedral site breaks t_{2g} and e_g into $e(2)$, a_1, and $e(1)$ states. These energy levels are shown in Fig. 4.5, and the symmetry breaking is diagrammed in Fig. 4.6.

Getting back to Figure 4.4(b-g), we notice that the Mo states (dotted grey line) are very similar across this entire family of materials. The low-energy excitations are, however, not on the Mo site when Fe is present. Figure 4.4(b) reveals that the sharp many-body resonance near $-0.4\,\mathrm{eV}$ emanates primarily from the Fe center in the trigonally-distorted tetrahedral environment, $e(1)$. Panel (c) shows that a broader, but still reasonably sharp excitation around $-0.8\,\mathrm{eV}$ arises from the doubly-degenerate $e(2)$ state on the distorted octahedral site. Since both of these fairly sharp excitations come from band formation via hybridization, the Mo partial density of states also has a small peak at the same energy [Figs. 4.7 and 4.8]. This demonstrates the quasi-particle nature of these peaks, which are Kondo-like and come from local spin screening on the aforementioned $e(1)$ and $e(2)$ distorted tetrahedral and octahedral orbitals, respectively.

What is exciting about this finding is that screening and many body Kondo peak formation [357, 358] are normally expected in a metal - not an insulator. The possibility of a Kondo resonance in a semiconductor like $Fe_2Mo_3O_8$ is potentially quite interesting, opening the door to a deeper exploration of the Kondo effect in a significantly wider variety of materials. While broader peaks like that at $-0.8\,\mathrm{eV}$ are not uncommon in transition metal compounds and appear for example in monoxides [359, 360], the very narrow resonance emanating from the $e(1)$ orbitals on the distorted tetrahedral site is unique to $Fe_2Mo_3O_8$. We assign it as an analog of the Zhang-Rice singlet in cuprates, [361, 362] arising due to the screening of the spin 1/2 hole on the trigonally-distorted tetrahedral Fe $e(1)$ sites in the Mott insulating state. This characteristic peak appears with very well-defined energy.

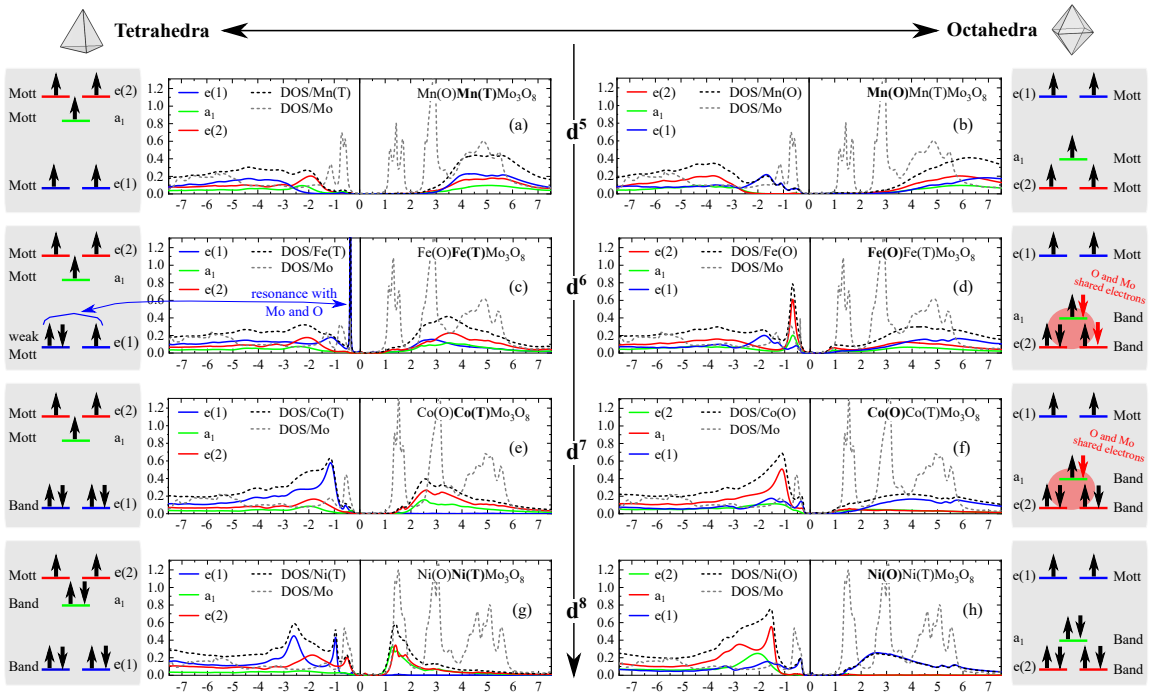


Figure 4.5: Atom- and orbital-projected density of states (DOS) together with a schematic view of the orbital occupation and character for $A_2Mo_3O_8$ (A = Mn, Fe, Co, and Zn). Each panel shows a schematic view of the orbital occupation (left side) and DOS (right side). Panels (a, c, e, g) refer to ions in trigonally-distorted tetrahedral environments (A(T)), whereas panels (b, d, f, h) refer to ions in trigonally-distorted octahedral environments (A(O)).

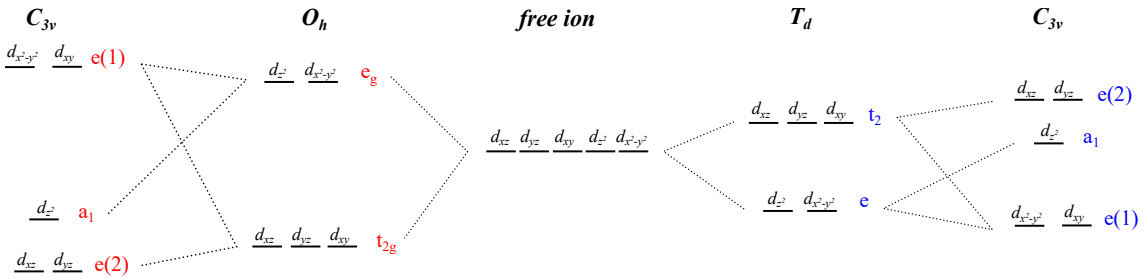


Figure 4.6: Diagram of d-orbital splitting from free ion states to octahedral + tetrahedral symmetries to C_{3v} local symmetry for the distorted octahedral and tetrahedral sites in $Fe_2Mo_3O_8$. States of e and a_1 symmetry are revealed in both the trigonally-distorted octahedra and tetrahedra. For clarity, we label the degenerate $d_{x^2-y^2}$ and d_{xy} set of orbitals as $e(1)$ whereas the doubly degenerate d_{xz} and d_{yz} set are labeled as $e(2)$. The d_{z^2} orbital always transforms as a_1. Note that the order of the e symmetry orbitals is swapped on the distorted octahedral and tetrahedral sites, and the a_1 symmetry orbital is always associated with the $e(2)$ pair.

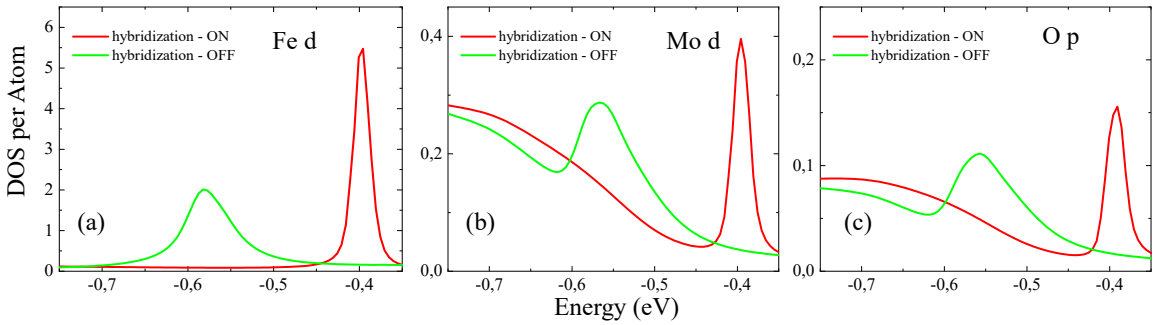


Figure 4.7: Atom projected density of states for $Fe_2Mo_3O_8$, computed using the self-consistent hybridization (red curve labeled "hybridization-ON") and the manually reduced hybridization in the energy region of the Kondo-like peak (green curve labeled "hybridization-OFF"), as explained in the text. Panels (a), (b), and (c) show the atom projected density of states for Fe d, Mo d, and one of the inequivalent O p atoms in the unit cell.

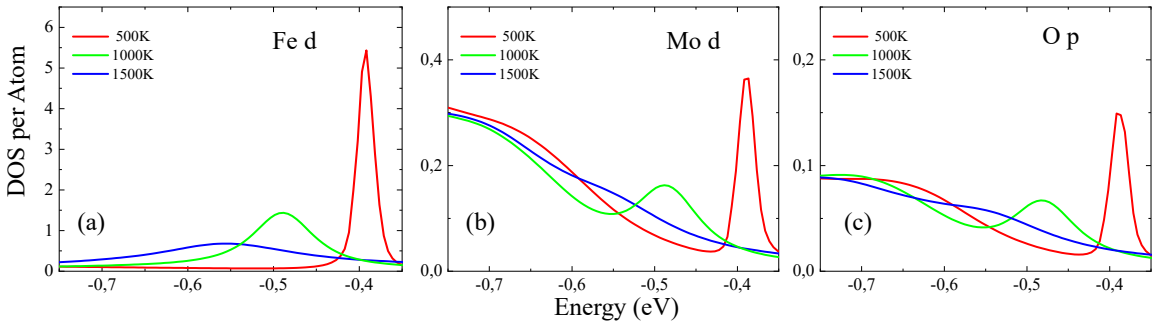


Figure 4.8: Temperature-dependent atom projected density of states for $Fe_2Mo_3O_8$. Panels (a), (b), and (c) show the atom projected density of states for Fe d, Mo d, and one of the inequivalent O p atoms in the unit cell.

It also mixes strongly with the Mo-O trimers [Fig. 4.9].

In order to test these predictions, we compare the theoretical optical conductivity [Fig. 4.1(h)] to the measured absorption spectrum of $Fe_2Mo_3O_8$ [Fig. 4.1(f)]. Overall, the calculated optical conductivity and the measured absorption spectrum are very consistent - although the features are not as well-defined as we might prefer. As a reminder, the spectral functions are very flat on the valence edge due to Fe occupation on the distorted tetrahedral site. This causes a sharp many-body resonance in the density of states [Fig 4.4(b)] which manifests as a small peak on the leading edge of the theoretical optical conductivity. The contribution from the distorted octahedral site is similar but less pronounced. Our calculations, therefore, predict that the many-body resonance on the valence band edge [Fig 4.4(b,c)] should lower the gap. This is exactly what we find. Obviously, this structure is strongly broadened in the experimental result, but the presence of these states causes the gap to be drawn noticeably downward in this system [Fig. 4.1(f)]. Similar reasoning applies to $FeZnMo_3O_8$, although only the distorted octahedral site is operative. Because the density of states are momentum-averaged, we also show the spectral functions [Fig. 4.4(h,i)].

4.3 Structure-property relations in the metal-substituted analogs

Figure 4.5 compares the density of states in $Fe_2Mo_3O_8$ with several other transition metal analogs which have orbital filling between d^5 and d^8 - namely the Mn, Co, and Ni analogs. We also show a schematic view of the orbital occupation for both the distorted tetrahedral and octahedral sites (left and right columns, respectively). The gap in each orbital can originate from the band structure due to the periodic potential (band gap) or from the Mott localization of electrons on a given A site, which we denote as a Mott gap. In principle, we can distinguish between the two because the single-particle spectral function is modified from the DFT bands by self-energy effects. We expect the spectral

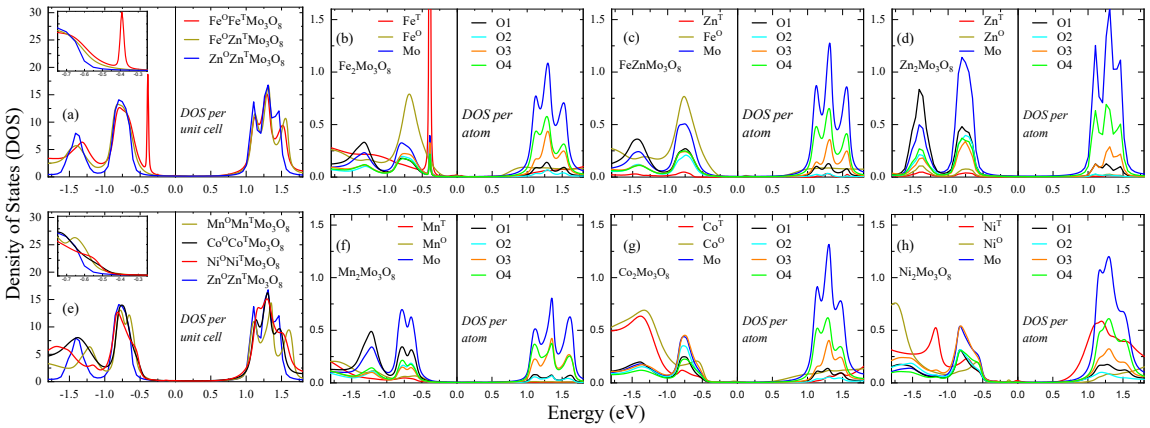


Figure 4.9: Density of states for the materials of interest in this work. Panels (a) and (e) show the density of states per unit cell. Panels (b-d) and (f-h) show the density of states per A, Mo, and O atoms. Only $Fe_2Mo_3O_8$ has a strong, sharp resonance near the Fermi energy.

function to be either zero or finite in the band gap case; it should diverge inside the gap for the Mott case [363–365]. Here, the electron state can no longer be described within the band picture.

The top panels of Fig. 4.5 show calculations for $Mn_2Mo_3O_8$ in which the electrons are in the high-spin d^5 configuration. The Mott gap opens in all orbitals on both tetrahedral and octahedra sites, and it is much larger than the band gap of the Mo-trimer. Consequently, the charge gap and low energy excitations in the Mn and Zn compounds are determined by the same Mo-trimer states. This is why they appear so similar.

$Fe_2Mo_3O_8$ is the most interesting of the series showing a complex interplay of band gaps, Mott gaps, and quasi-particle multiplets. The a_1 and $e(2)$ states on the distorted tetrahedra are Mott insulating with a large gap. As discussed above, the doubly degenerate $e(1)$ orbitals contain one hole, which is equally distributed among the two orbitals, and the Mott mechanism opens the gap - even though the self-energy pole is less strong and the gap smaller than in the a_1 and $e(2)$ states. Moreover, at the edge of the gap, strong hybridization, directly computable by the DMFT hybridization function, shows a very strong and narrow peak due to many body screening effects. With this mechanism, the spin-1/2 emanating from the $e(1)$ orbitals on the tetrahedral site are screened by the Mo-trimer electrons - a mechanism that is analogous to the Zhang-Rice state in cuprates [361]. Note that this is different from the sharp peak due to the valence band edge in transition metal monoxides [359, 360]. The latter appears in the antiferromagnetic state where all gaps are band-like in nature and spin states are split by a Zeeman field. As a consequence, many-body screening of spin is not possible. Here, spin preserves SU(2) symmetry, and the resonance screens the local spin on Fe. In addition, the narrow peak due to many body screening effects disappears in the antiferromagnetic ground state [Fig. 4.7]. The distorted octahedral site in the Fe d^6 state contains a combination of a Mott gap in the $e(1)$ states and a band gap in the a_1 and $e(2)$ states. This unusual combination is a so-called orbitally-selective Mott state [349,350]. Note that the sharp peak at the valence band edge appears as well, even though it is not as sharp as the resonance from the distorted tetrahedral

Fe $e(1)$ site. Its nature is different, as it appears in band-insulating a_1 and $e(2)$ orbitals similar to the valence band edge discussed in transition metal monoxides [359, 360]. Note that hybridization and band formation with oxygen and Mo electrons are needed to open the band gap in the octahedral Fe a_1 and $e(2)$ states. This is because the latter contains only four electrons in three nearly degenerate a_1 and $e(2)$ orbitals.

Next, we discuss the Co analog, which is in the d^7 configuration. In this case, the $e(1)$ orbitals on the tetrahedral site are fully filled, and the a_1 and $e(2)$ orbitals are in the high-spin Mott insulating state with a large gap - larger than the Mo-trimer gap. On the octahedral site, the $e(1)$ orbitals are Mott-insulating with a large gap, and the a_1 and $e(2)$ states are band-insulating in which Mo and oxygen provide one electron to form a covalent bond with the a_1 electrons. We note that no sharp low-energy peak is found at the valence band edge, although in principle such a peak is possible.

Figure 4.5(g,h) displays the partial density of states for the Ni analog with its d^8 configuration. In this case, the $e(1)$ and a_1 orbitals on the distorted tetrahedral site are fully filled, and the doubly-degenerate $e(2)$ state shows a Mott gap which is comparable to that of the Mo trimer. On the distorted octahedral site, the $e(2)$ and a_1 states are fully filled, and the $e(1)$ states are in the half-filled Mott insulating state. This Mott gap is again comparable to the Mo-trimer gap. Hence the reduction of the gap as compared to the Zn analog is minimal.

Chapter 5

Nonreciprocal directional dichroism at telecom wavelengths

5.1 Crystal structure, properties, and symmetry analysis

Figure 5.1 summarizes our overall approach and the symmetry conditions that are important in this work. We begin by calculating absorption difference spectra as $\Delta\alpha$ = $\alpha(\mathbf{H})$ - α(0 T) for the different measurement configurations. Nonreciprocity is determined from various differences in the $\Delta\alpha$ spectra, for instance $\Delta\alpha_{NDD}(+\mathbf{k}, \pm\mathbf{H}) = \Delta\alpha(+\mathbf{k}, +\mathbf{H})$ - $\Delta\alpha(+\mathbf{k}, -\mathbf{H})$ [Fig. 5.1(a)]. Notice that when both **k** and **H** are reversed, $\alpha_{NDD}(\pm\mathbf{k}, \pm\mathbf{H})$ = $\Delta\alpha(+\mathbf{k}, +\mathbf{H})$ - $\Delta\alpha(-\mathbf{k}, -\mathbf{H})$ vanishes [Fig. 5.1(b)]. Nonreciprocity can also be defined in terms of counter-propagating beams, $\Delta\alpha_{NDD}(\pm\mathbf{k}, +\mathbf{H})$, as shown in Fig. 5.2.

The top panels in Fig. 5.2 summarize the three different measurement configurations predicted within the framework of symmetry operational similarity [38,366]. In the toroidal configuration [Fig. 5.2(a)], electric polarization along c, combined with **H** perpendicular to c, breaks two-fold rotation, inversion, mirror, and time-reversal symmetries, so it has symmetry operational similarity with the wave vector of light **k** along the third direction.

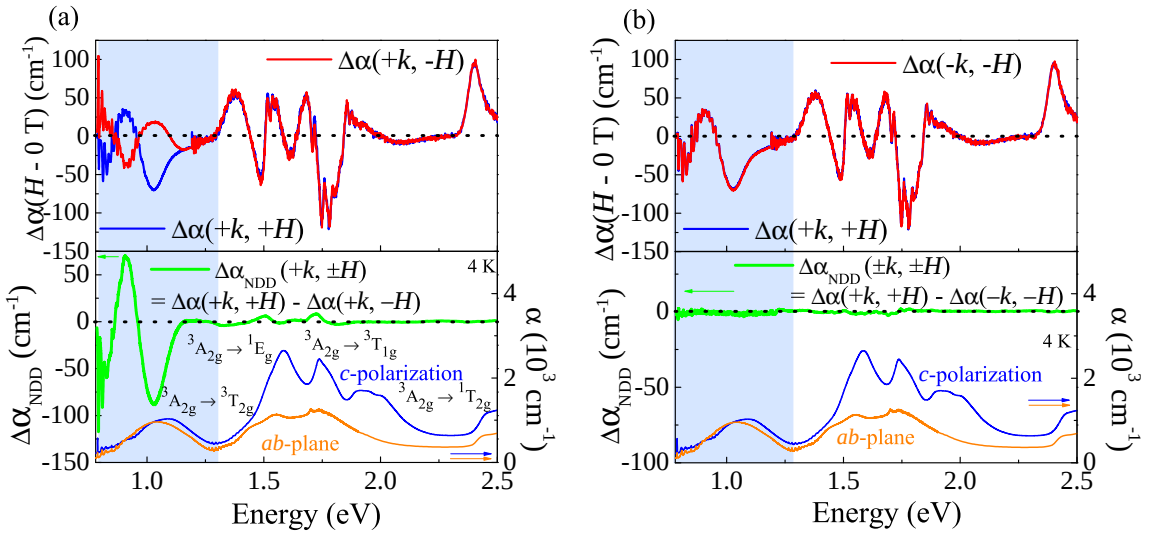


Figure 5.1: **Illustrating symmetry considerations for nonreciprocity in Ni_3TeO_6.** (a) Full field absorption difference spectra of Ni_3TeO_6 as a function of energy for the (+**k**, +**H**) and (+**k**, -**H**) configurations in the toroidal measurement geometry. For illustration purposes, we employ **H** = 60 T. Nonreciprocal directional dichroism is shown in green. Here, $\Delta\alpha_{NDD}$(+**k**, ±**H**) = $\Delta\alpha$(+**k**, +**H**) - $\Delta\alpha$(+**k**, -**H**). Experimentally, it is common to reverse the magnetic field direction as we have done here. Nonreciprocity can also be defined in terms of counter-propagating beams, $\Delta\alpha_{NDD}$(±**k**, +**H**), as shown in Fig. 2. (b) Full-field absorption difference spectra in the (+**k**, +**H**) and (-**k**, -**H**) configurations. Notice that they are the same. α_{NDD}(±**k**, ±**H**) = $\Delta\alpha$(+**k**, +**H**) - $\Delta\alpha$(-**k**, -**H**) (also shown in green) vanishes when both light propagation and magnetic field direction are switched simultaneously. The absolute absorption spectrum is shown at the bottom of each panel to provide context. Note that we used cubic term symbols here ($^3A_{2g}$, $^3T_{2g}$, ^1E_g, $^3T_{1g}$, $^1T_{2g}$) to denote Ni^{2+} atomic multiplets because the deviation from cubic symmetry by trigonal distortion at the Ni sites is small (≈0.1 eV in terms of crystal fields).

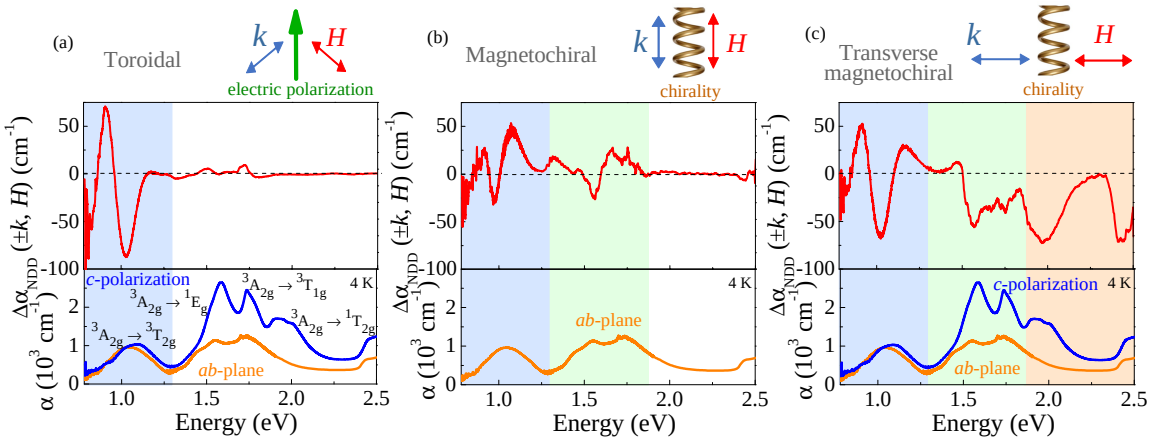


Figure 5.2: **Nonreciprocity of Ni_3TeO_6 in the three different measurement configurations.** Summary of the three different measurement configurations of interest in this work: (a) toroidal (**k** ⊥ **H** ⊥ polarization, (b) magnetochiral (**k** ∥ **H** ∥ chirality), and (c) transverse magnetochiral (**k** ∥ **H** ⊥ chirality). Nonreciprocal directional dichroism spectra of Ni_3TeO_6 at 60 T in the toroidal (d), magnetochiral (e), and transverse magnetochiral (f) configurations, respectively. These spectra were measured in the Voigt (d) and Faraday (e, f) geometries. The nonreciprocal responses in panels (b, c) are reproduced from Ref. 250. The linear absorption spectrum of Ni_3TeO_6 at 4.2 K is shown below each nonreciprocal panel for comparison. The polarization directions and on-site Ni *d*-to-*d* excitations are labeled.

Thus, light propagation parallel to the toroidal moment can exhibit nonreciprocal directional dichroism. The two other configurations of interest involve chirality (rather than electric polarization) which breaks inversion and mirror symmetries. The magnetochiral geometry is obtained when the light propagation direction and applied field are parallel to the chiral axis [Fig. 5.2(b)]. The transverse magnetochiral configuration, on the other hand, requires both the light propagation direction and magnetic field to be perpendicular to the chiral axis [Fig. 5.2(c)]. Note that we denote the C_3 axis in Ni_3TeO_6 as the chiral axis; previous studies have argued that nonreciprocity in chiral systems can be easily understood considering chirality as a vector-like quantity [108, 366].

5.2 Nonreciprocal effect in different measurement configurations

Figure 5.2 summarizes the nonreciprocal directional dichroism of Ni_3TeO_6 at the full field in the toroidal, magnetochiral, and transverse magnetochiral configurations. Overall, this behavior is a consequence of low symmetry, structural and magnetic chirality, and the presence of spin-orbit coupling, although the specific appearance of $\Delta\alpha_{\mathrm{NDD}}$ depends upon the measurement configuration as well. Focusing first on Ni_3TeO_6 in the toroidal geometry [Fig. 5.2(a)], we find a strong dichroic response in the vicinity of the 1.1 eV color band. This feature is assigned as a superposition of Ni^{2+} on-site d-to-d excitations ($^3A_{2g} \rightarrow {}^3T_{2g}$) emanating from the three different local environments of the Ni centers [68]. At 60 T, the largest field-induced changes are centered on the 1.1 eV color band and are on the order of 160 cm^{-1}. This corresponds to between zero and approximately 45% contrast, depending on the value of the absolute absorption. The dichroic contrast in the vicinity of the $^3A_{2g} \rightarrow {}^1E_g$ and $^3A_{2g} \rightarrow {}^3T_{1g}$ color bands is significantly smaller, and that at higher energy near the $^3A_g \rightarrow {}^1T_{2g}$ excitation is zero within our sensitivity. In the toroidal configuration, the overall size of $\Delta\alpha_{\mathrm{NDD}}$ and its energy distribution are quite different than what is observed in the magnetochiral and transverse magnetochiral geometries [250]. For instance, while

all configurations exhibit dichroic contrast near the 1.1 eV color band, that in the toroidal configuration is by far the largest.

Turning to nonreciprocal directional dichroism of Ni_3TeO_6 in the magnetochiral configuration [Fig. 5.2(b)], $\Delta\alpha_{\mathrm{NDD}}$ associated with the 1.1 and 1.65 eV color bands is on the order of ± 45 cm^{-1} at full field [250]. This is different than what we find in the toroidal configuration both in terms of size and shape. There is a lot more fine structure to $\Delta\alpha_{\mathrm{NDD}}$ in the magnetochiral configuration as well. Unlike the other two measurement configurations shown in Fig. 5.2, $\Delta\alpha_{\mathrm{NDD}}$ in the magnetochiral geometry appears only above the 9 T spin flop transition where spin canting introduces net magnetization [68, 251]. The nonreciprocal response of Ni_3TeO_6 is different yet again in the transverse magnetochiral configuration with dichroic contrast associated with all four types of d-to-d excitations in the absolute absorption spectrum [Fig. 5.2(c)]. This suggests that the color bands have magnetoelectric character in the chiral geometries as well. Differences in magnetoelectric coupling as it pertains to the various contrasts in toroidal, magnetochiral, and transverse magnetochiral geometries are discussed below.

5.3 Field dependence of the dichroic contrast in the toroidal geometry

Figure 5.3(a) displays nonreciprocal directional dichroism of Ni_3TeO_6 as a function of the magnetic field in the toroidal configuration. As discussed previously, the toroidal geometry involves placing the electric polarization direction mutually orthogonal to both the light propagation and magnetic field directions. In addition to large positive and negative lobes in the dichroic contrast, there is a great deal of fine structure below 0.9 eV. These features can be assigned to phonon sidebands as discussed below. Examination reveals that α_{NDD} appears at the lowest fields and grows systematically. This is because field-induced canting of Ni moments, which gives rise to net ferromagnetic moments and enables nonreciprocal behavior, can occur even at the smallest fields. That nonreciprocal directional

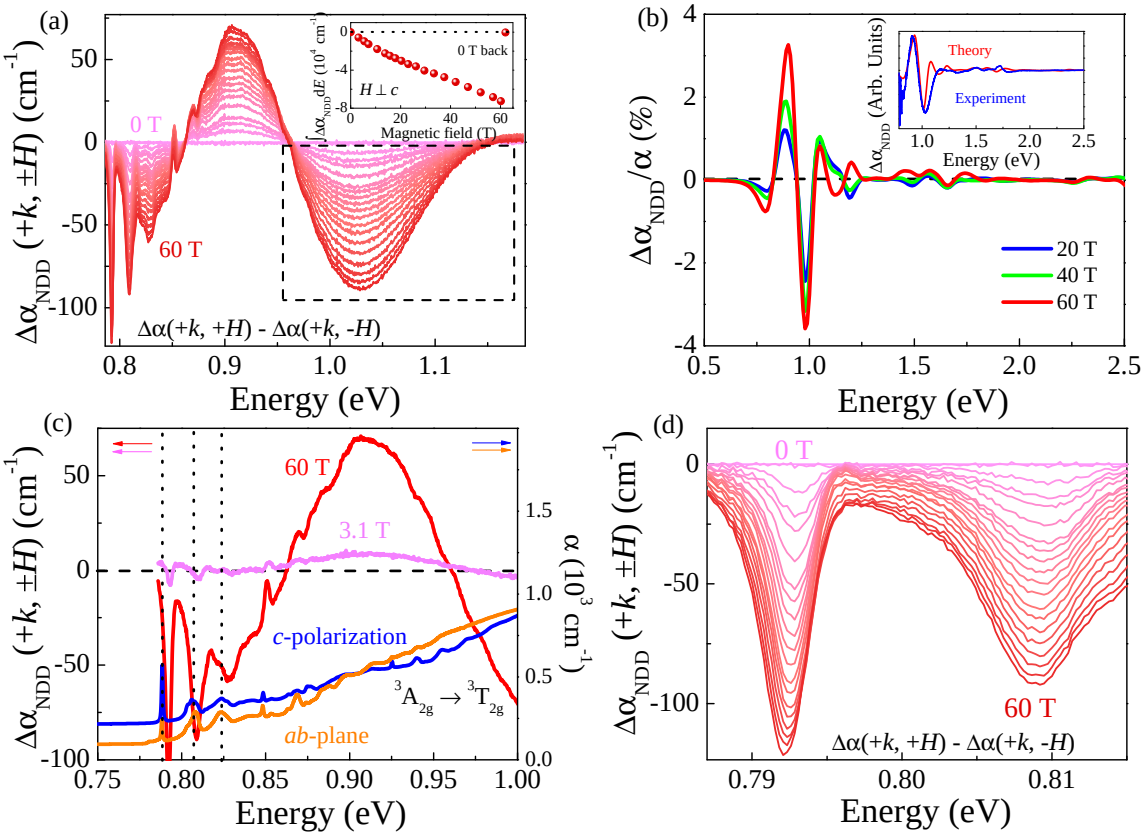


Figure 5.3: **Nonreciprocity in the toroidal geometry.** (a) Nonreciprocal directional dichroism of Ni_3TeO_6 in the toroidal configuration measured between 0 and 60 T at 4.0 K. The inset is the integration of the indicated feature in the dashed box over an appropriate energy window. No hysteresis is observed. (b) Simulated nonreciprocal directional dichroism of Ni_3TeO_6 in the toroidal configuration. The inset shows a comparison of the calculated and measured results at 60 T. The intensity is normalized to the maximum of $\Delta\alpha_{NDD}$. (c) Close-up view of $\Delta\alpha_{\mathrm{NDD}}$ at 3.1 and 60 T compared with the linear absorption spectrum. (d) Close-up view of $\Delta\alpha_{\mathrm{NDD}}$ as a function of field between 0 and 60 T. The complete list of magnetic fields in panels (a) and (d) is: 0, 3.1, 5.5, 7.2, 10.7, 13.8, 15.8, 17.9, 20.3, 23.1, 26.1, 29.6, 33.3, 37.5, 42.1, 47.0, 52.1, 57.1, 60.2 T.

dichroism can be seen at low fields is useful for a number of applications including optical isolators and rectifiers, high-fidelity holograms, and potentially in the telecom sector. In any case, we can quantify this trend by integrating α_{NDD} over an appropriate energy window and plotting the result as a function of the applied field [inset, Fig. 5.3(a)]. The shape reveals how the spins align in the direction of the applied field. The lack of sharp jumps or cusps is consistent with the absence of field-induced magnetic transitions for $\mathbf{H} \perp c$ [252]. No hysteresis is observed. In addition to switching the applied field direction, we investigated symmetry effects [108] in Ni_3TeO_6 by switching the light propagation direction [Fig. 5.4]. The results are identical. If both light propagation and the magnetic field directions are switched at the same time, nonreciprocal directional dichroism vanishes due to time-reversal symmetry [Fig. 5.1(b) and 5.5] [108].

Comparison between the experimental nonreciprocal directional dichroism in different geometries with the simulated versions provides insight into the nature of the contrast in different energy ranges. Figure 5.3(b) displays $\Delta\alpha_{\mathrm{NDD}}$ of Ni_3TeO_6 calculated by first-principles-based methods in the toroidal configuration [250]. The simulated spectrum compares reasonably well with the experimental result, except for the phonon sideband effects around 0.8 eV which are not included in the model, capturing the maximum near 0.9 eV, the minimum near 1.03 eV as well as the lack of contrast at higher energies. Note that our simulation is based upon a local ionic picture and includes only intra-Ni-ionic excitations [250], not the entire part of the structural (and magnetic) chirality of Ni_3TeO_6. The structural chirality of Ni_3TeO_6 manifests (i) at the local level with a chiral crystal-field environment at each Ni site as well as (ii) in the global arrangement of Ni sites. Our theory includes the former but not the latter. We refer to these as local and global chirality, respectively [367]. Based on the results from our ionic picture-based simulation that nicely capture the dichroic response near 1 eV, we speculate that excitations near 1 eV are relevant to the local chiral component, namely the formation of the Ni ionic toroidal moments perpendicular to the magnetic field and bulk electric polarization ($\mathbf{T} \equiv \mathbf{P} \times \mathbf{M}$), which are coupled with the propagation of light and induce nonreciprocal directional dichroism [108].

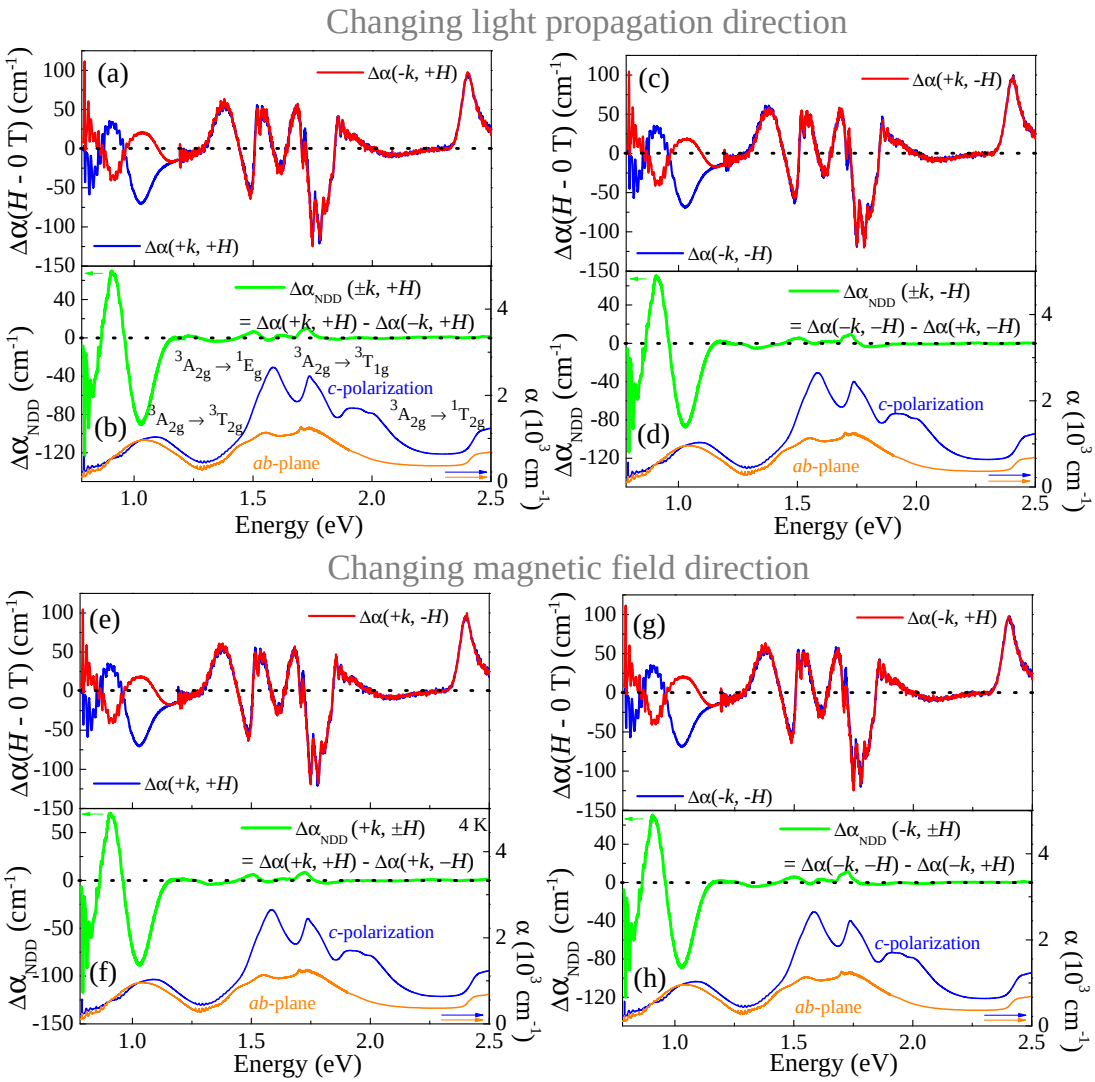


Figure 5.4: (a,c,e,g) Full-field absorption difference spectra as a function of energy for several different configurations as indicated. (b,d,f,h) Nonreciprocal directional dichroism is shown in green for four different configurations: $\Delta\alpha_{NDD}$(+**k**, ±**H**), $\Delta\alpha_{NDD}$(±**k**, +**H**), $\Delta\alpha_{NDD}$(-**k**, ±**H**), and $\Delta\alpha_{NDD}$(±**k**, -H), where for instance $\Delta\alpha_{NDD}$(±**k**, +**H**) = $\Delta\alpha$(+**k**, +**H**) - $\Delta\alpha$(-**k**, +**H**). These curves employ **H** = 60 T. The absolute absorption spectrum is included to provide context.

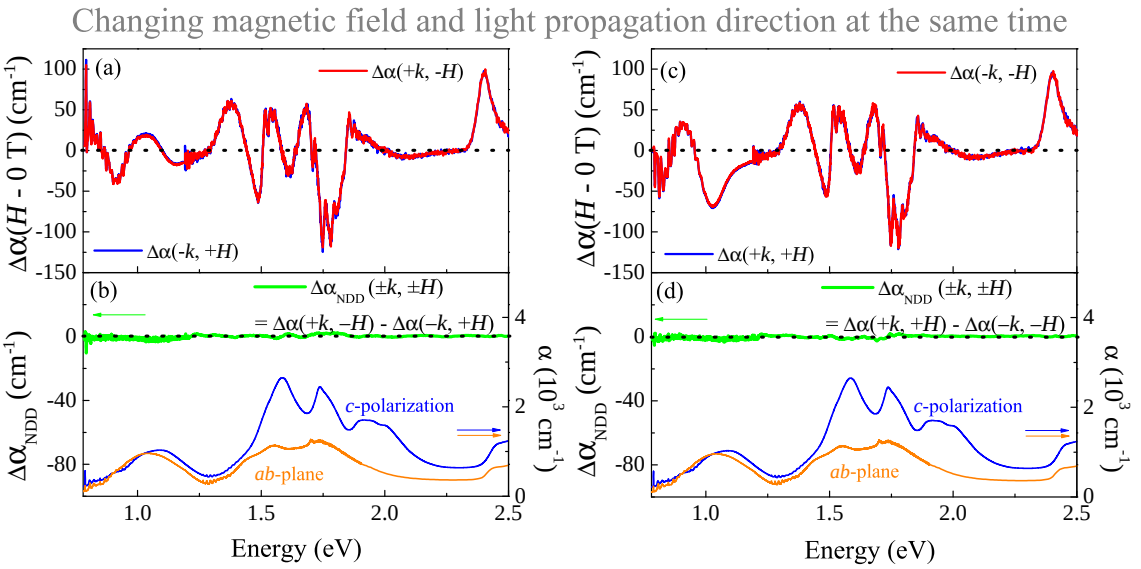


Figure 5.5: (a,c) Full-field absorption difference spectra in various configurations. Notice that they are the same. (b,d) α_{NDD} (shown in green) vanishes when both light propagation and magnetic field direction are switched simultaneously. This is because time-reversal symmetry is not broken when the direction of both **k** and **H** are changed together. A magnetic field of 60 T was employed here. The absolute absorption spectrum is shown at the bottom of each panel to provide context.

On the other hand, nonreciprocity at higher energies, which is sizable only in the magnetochiral and transverse magnetochiral cases [Fig. 5.2(b,c)], originates primarily from global chirality and is difficult to capture within our atomistic simulation framework. Since our simulated nonreciprocal directional dichroism is given as a sum of individual Ni atomic contributions, some aspects of global chirality originating from arrangements of Ni sites at different Wyckoff positions may partially cancel out to yield smaller responses compared to experimental results. Details are available in the Methods section.

Antiferromagnets traditionally offer foundational opportunities to investigate collective excitations that arise from charge-spin and charge-lattice coupling [368]. These features include excitons, zero phonon lines, phonon side bands, and magnon sidebands. They are commonly observed on the leading edge of the lowest energy *d*-to-*d* band in antiferromagnets like MnF_2 and α-Fe_2O_3 [369,370]. The absorption spectrum of Ni_3TeO_6 does not have a zero phonon line because it is in the strong coupling limit [371], but it does have a rich set of phonon sidebands on the leading edge of the $^3A_{2g} \rightarrow {}^3T_{2g}$ excitation [Fig. 5.3(c), Supplementary Fig. 6] [250]. These structures, often called 'phonon replicas', arise from vibronic coupling, the details of which are characterized by the Huang-Rys factor [313,371]. That the phonon progression on the leading edge of the Ni^{2+} *d*-to-*d* excitations matches features in $\Delta\alpha_{NDD}$ illustrates the physical connection and demonstrates that the phonon sidebands have magnetoelectric character. Nonreciprocal directional dichroism thus provides an opportunity to investigate how phonons activated in this manner are impacted by reversing the field and/or light propagation direction. At this time, there are only a handful of cases ($BiFeO_3$, few-layer CrI_3, and Cu_2OSeO_3) where phonons or phonon-derived properties such as thermal conductivity have been shown to host nonreciprocal effects [109, 372–374]. Nonreciprocal phonons obviously enable rectification of heat and sound [373] - a topic of sustained interest. A giant nonreciprocal response in the THz range has recently been reported in Ni_3TeO_6 [375], possibly originating from the effects mentioned above. Below, we demonstrate that the phonon sidebands in Ni_3TeO_6 not only display nonreciprocal directional dichroism [Fig. 5.3(d)] but that this contrast occurs along

with that related to the low-energy Ni^{2+} crystal field excitations across the telecom range.

5.4 Nonreciprocal directional dichroism at telecom wavelengths

We, therefore, return to the spectra in Fig. 5.3(c) which are even more intriguing when overlaid with useful telecom bands. The latter include the O-, E-, S-, C-, L-, and U-bands. Optical fiber communications typically operate in one of these windows. The C-band (1530 - 1565 nm) is perhaps the most familiar and employs drawn Er-glass fibers. While the optical properties of Er-glass fibers have been studied separately under electric and magnetic fields [376–380]. we are unaware of any attempt to explore rectification effects. Moreover, nonreciprocal directional dichroism has been revealed in a number of different energy regimes, it is rarely encountered in the near infrared [245, 381].

Figure 5.6 displays a close-up view of the nonreciprocal directional dichroism in Ni_3TeO_6 in the toroidal configuration plotted on a percentage basis and a wavelength scale. Examination reveals that $\Delta\alpha_{\mathrm{NDD}}$ has a near-perfect match to the full range of telecom wavelengths. The effects are strong, broad, and clearly evident at the full field (60 T) with a maximum contrast in the first phonon side band of approximately 45%. These features also appear even at the smallest fields (as shown by the spectrum at 3.1 T) because time-reversal is already broken. This, along with the fact that we are using unpolarized light, is an advantage for applications. Difference signals are already in regular use, and nonreciprocal effects can add an important layer of security. Ni_3TeO_6 hosts similar contrast in the magnetochiral and transverse magnetochiral configurations as well [Supplementary Fig. 7]. In addition to demonstrating that nonreciprocal directional dichroism can be positioned within useful telecom windows, this work opens the door to the development of high-efficiency / low-dissipation optical diodes and rectifiers from crystalline materials. We anticipate that linear or circular polarizers would amplify the size of this effect in Ni_3TeO_6, but the ability to achieve a polarization-independent signal is one of the beauties of

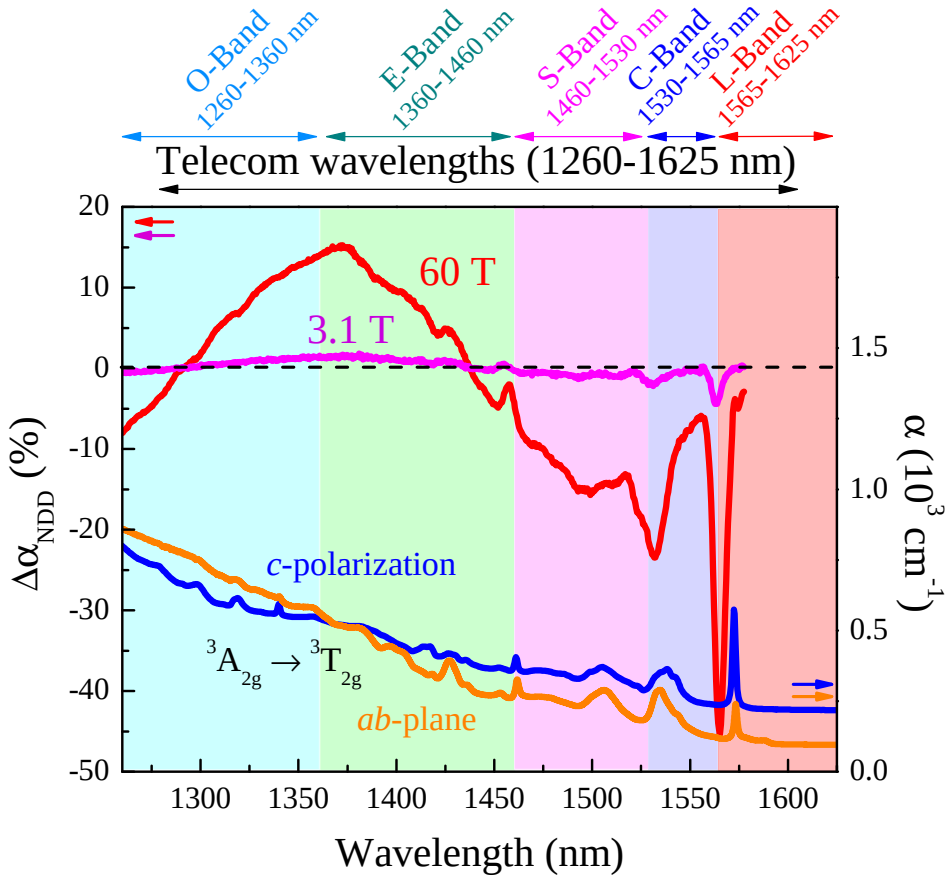


Figure 5.6: **Nonreciprocity at telecom wavelengths.** Close-up view of the nonreciprocal directional dichroism in Ni_3TeO_6 on a percentage basis as a function of wavelength in the toroidal configuration at 4.0 K. $\Delta\alpha_{NDD}$ is shown at 3.1 and 60 T. The absolute absorption spectrum is included for comparison. Various commercial telecom windows are summarized on the upper axes. The U-band (1625-1675 nm) is not shown.

magnetochiral materials.

5.5 Structure-property relations for photonics applications

Ni_3TeO_6 is a superb platform for fundamental studies of nonreciprocity because it hosts this peculiar property across a wide range of excitations and in three different measurement configurations. To our knowledge, there are no other nonreciprocal materials that have been studied in so many different geometries. In this work, we focus on the Ni^{2+} d-to-d excitations and associated phonon sidebands in the near infrared and optical range in the toroidal configuration, unraveling structure-property relationships via comparison with contrast in the magnetochiral and transverse magnetochiral geometries. We find that polarity allows the creation of Ni toroidal moments, which results in large contrast near the color band at 1.1 eV. The chiral geometries, on the other hand, yield smaller contrast over a much broader energy range. Our modeling of the size and shape of the spectral response supports this picture of the importance of polarity vs. chirality in the creation of large vs. broadband contrast. These findings enhance our ability to design and deliver complex materials properties on demand. At the same time, the discovery of nonreciprocal effects across the full telecom wavelength range presents a number of exciting opportunities. While tunability under a magnetic field is established in this work, the degree to which nonreciprocity can be controlled by other external stimuli or chemical substitution is unexplored. That said, the discovery of nonreciprocity in the telecom region is a significant conceptual advance that has the potential to jump-start the use of dichroic contrast in photonics applications - particularly in the area of high-efficiency optical diodes and rectifiers.

Chapter 6

Spin-phonon interactions, frustration, and magnetoelectric coupling in $Co_4Nb_2O_9$ and the Ta analog

6.1 Vibrational properties of B-site substituted materials

Figure 6.1(e, f) summarizes the infrared response of $Co_4Nb_2O_9$. A symmetry analysis reveals $7A_{2u} + 13E_u$ infrared-active modes and $6A_{1g} + 13E_g$ Raman-active modes. The doubly-degenerate E_u vibrational modes appear in the ab-plane whereas the singly-degenerate A_{2u} modes resonate along c. The Ta analog is isostructural with a $P\bar{3}c1$ space group and D_{3d} point group symmetry. As a result, the spectrum of $Co_4Ta_2O_9$ is quite similar to that of the Nb-containing compound [Figs. S1 and S2, Supplementary information]. Overall, the number of infrared-active modes and their peak positions are nearly identical

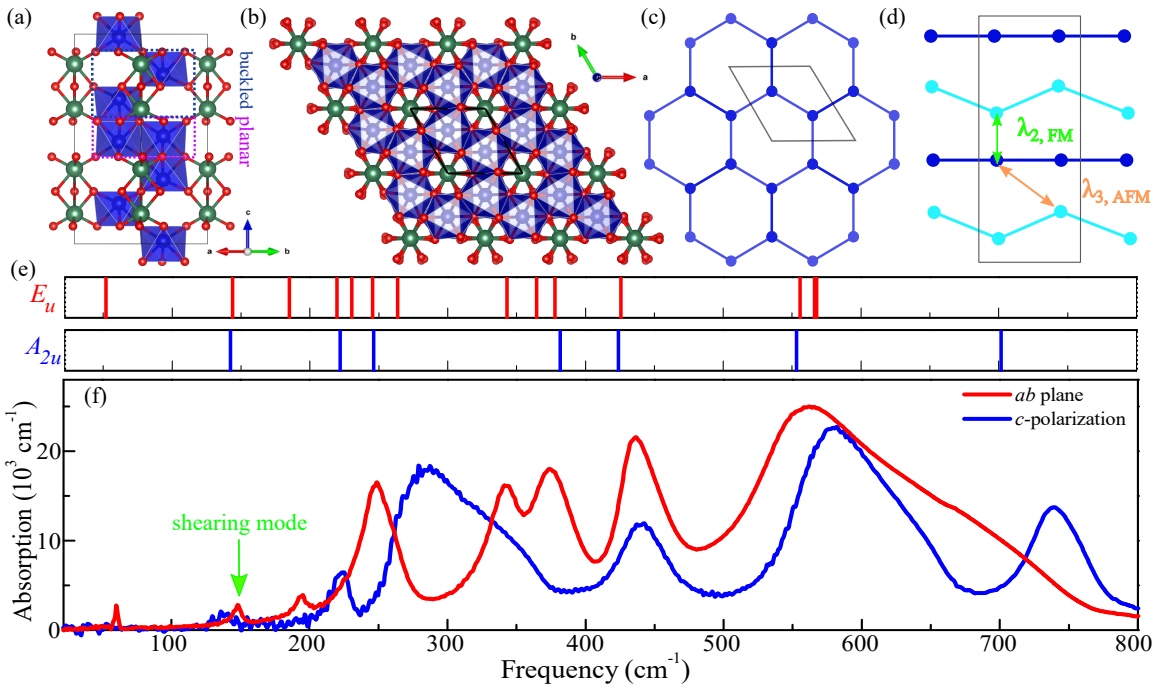


Figure 6.1: (a, b) Crystal structure of $Co_4Nb_2O_9$ with c-axis and ab-plane views [256,260,268]. Blue, red, and green represent Co, O, and Nb/Ta centers, respectively. The octahedra are drawn only for the magnetic ions. (c) A simplified view of the planar Co^{2+} layer (blue) reveals a honeycomb-like structure. Only the Co^{2+} ion is shown. (d) This schematic illustrates both the planar (blue) and buckled (cyan) layers. There are two relevant interlayer interactions, which are shown with different colors (λ_2 and λ_3). Again, only the Co^2 ions are displayed here. (e) Calculated phonon frequencies are summarized for the E_u and A_{2u} modes. (f) Polarized infrared absorption spectra of $Co_4Nb_2O_9$ at room temperature. The response of $Co_4Ta_2O_9$ is similar and shown in the Supplementary information. The mode assignments are identical.

in both $Co_4Nb_2O_9$ and $Co_4Ta_2O_9$. A summary and detailed comparison between the experimental and theoretical phonon frequencies, symmetries, and displacement patterns is available in Table S2, Supplementary information. The modes related to the heavy Nb and Ta centers appear at the lowest frequencies since $\omega \sim \sqrt{k/\mu}$. We also expect features involving Nb to resonate at slightly higher frequencies than those involving Ta due to simple mass effects. Here, ω is the frequency, k is the spring constant, and μ is the effective mass. We can test this supposition by examining the mode displacement patterns and realizing that the E_u modes at 60(58) cm^{-1} and the A_{2u} modes at 138(128) cm^{-1} reflect the presence of Nb vs. Ta, respectively. The E_u symmetry phonon near 150 cm^{-1} that involves shearing of the Co planes against each other will be important in our discussion as well. This structure is marked with a green arrow in Fig. 6.1(f). We also studied the temperature dependence of phonons in $Co_4Nb_2O_9$ and the Ta analog. The majority of features move systematically with decreasing temperature. The E_u symmetry shearing mode near 150 cm^{-1} is the exception.

6.2 Spin-phonon coupling in $Co_4B_2O_9$ (B = Nb, Ta)

Figure 6.2(a, c) displays a close-up view of the E_u symmetry vibrational mode near 150 cm^{-1} in both materials. These features harden with decreasing temperature in the paramagnetic phase and soften across T_N. The Nb compound hosts a sharp frequency shift across the magnetic ordering temperature whereas the Ta analog reveals a gradual transition with a sluggish frequency shift and noticeable precursor effect. As shown in Fig. 6.2(b, d), we fit frequency vs. temperature trends in the paramagnetic phase using a Boltzmann sigmoidal model to capture anharmonic effects:

$$\omega(T) = \frac{(\omega_l - \omega_h)}{(1 + e^{((T-T_i)/dT)})} + \omega_h. \tag{6.1}$$

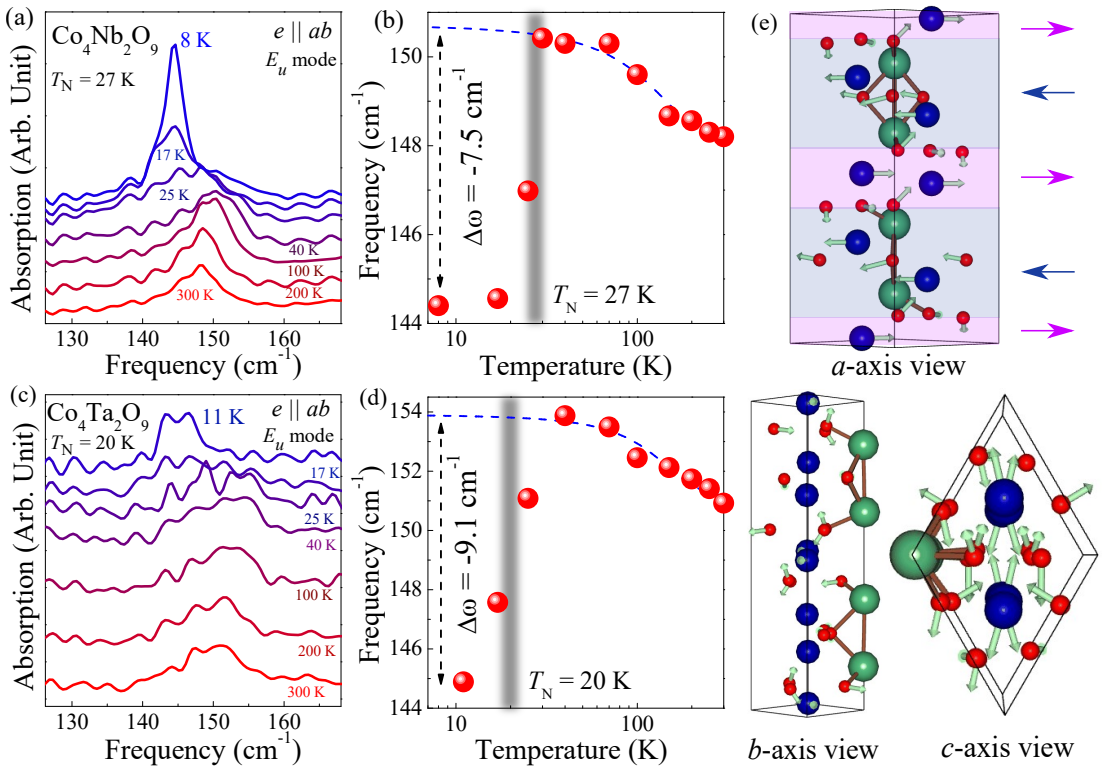


Figure 6.2: (a, b) Absorption spectrum of $Co_4Nb_2O_9$ as a function of temperature and peak position vs. temperature for the E_u symmetry shearing mode near 150 cm^{-1}. (c, d) Similar results for $Co_4Ta_2O_9$. The spectra in (a, c) are shifted for clarity, and the blue dashed lines in (b, d) are a simulated phonon response as discussed in the text. T_N is indicated by vertical gray lines. Phonon softening across T_N is readily apparent. (e) Calculated displacement pattern of the E_u symmetry phonon viewed along different directions. The shaded slabs in the top image indicate how the planar and buckled layers move against each other in a shearing motion.

Here, ω_h and ω_l are the phonon frequencies at high and low temperatures, respectively. T_i and dT are the inflection point and the width of the distribution. As demonstrated by the deviation from the model fit below the magnetic ordering transition, this phonon engages in strong spin-phonon coupling in both $Co_4Nb_2O_9$ and $Co_4Ta_2O_9$ [22, 60, 61].

In magnetic materials, it is well-known that phonon frequencies can be sensitive to the development of near-neighbor spin correlations [128, 130–132]. In such cases, the frequency is expressed as [134]:

$$\omega = \omega_o + \lambda\langle S_i \cdot S_j \rangle. \tag{6.2}$$

Here, ω_o is the unperturbed phonon frequency that is nicely revealed from the fit in Fig. 6.2(b, d) at base temperature, ω is the renormalized phonon frequency due to spin-phonon interactions, $\langle S_i \cdot S_j \rangle$ is the spin-spin correlation function, and λ is the spin-phonon coupling constant. Using Eqn. 6.2, our frequency vs. temperature trends, and the model fits of $\omega(T)$ shown in Fig. 6.2(b, d), we can extract frequency shifts across the magnetic ordering transitions and calculate spin-phonon coupling constants for $Co_4Nb_2O_9$ and $Co_4Ta_2O_9$.

The displacement pattern of the participating phonon is also key to our analysis. As a reminder, our calculations predict that the 150 cm^{-1} phonon mode is an out-of-phase E_u symmetry displacement involving the Co centers in which the planar and buckled layers vibrate against each other. The Nb and Ta centers do not participate very much in the motion. As a result, the relevant motion contains only one spin-containing center: Co^{2+} with $S = \frac{3}{2}$. With this insight and the fact that $\langle S_i \cdot S_j \rangle$ goes as S^2 in the low-temperature limit, we see that the spin-spin correlation function can be approximated as $\langle S_i \cdot S_j \rangle \sim S^2 = (\frac{3}{2})^2 = \frac{9}{4}$. $Co_4Nb_2O_9$ has a frequency shift ($\Delta\omega$) across T_N of -7.5 cm^{-1}. In other words, the mode softens across the magnetic ordering temperature. This means that the bond between layers gets weaker due to magnetism. We extract a spin-phonon coupling constant (λ) of -3.3 cm^{-1}. $Co_4Ta_2O_9$ has a larger frequency shift than $Co_4Nb_2O_9$. Using the same estimate for $\langle S_i \cdot S_j \rangle$ and $\Delta\omega$ = -9.1 cm^{-1}, we find λ = -4.0 cm^{-1}. This makes sense because Nb is a $4d$ element whereas Ta is $5d$, so the latter hosts more significant spin-orbit coupling.

We can extend this analysis to include additional effects. For instance, we can modify the spin-spin correlation function as $\langle S_i \cdot S_j \rangle \approx S^2 cos^2(\Theta)$ in order to capture the non-collinearity of the spin states reported in our systems [259,260]. This expression is a simple analog of Malus's rule for the polarization of light [382]. We use $\theta = 10.5°$ and $14°$ to obtain $\lambda = 3.4$ and 4.3 cm^{-1} for $Co_4Nb_2O_9$ and $Co_4Ta_2O_9$, respectively [259, 260]. Accounting for non-collinearity increases spin-phonon coupling constants in the $Co_4B_2O_9$ materials by about 10%. These values are an order of magnitude larger than what was extracted for the aforementioned Raman-active modes [266], so we see that coupling with odd- rather than even-symmetry vibrational modes is significantly more important.

We can also analyze the individual interactions between Co^{2+} sites. Here, it's important to recall that $Co_4Nb_2O_9$ and the Ta analog are composed of two different layers - akin to a superlattice consisting of planar graphene and buckled SiC [Fig. 6.1(c, d)]. Writing down the spin Hamiltonian for the planar layer, the buckled layer, and the interaction terms between layers in a pair-wise fashion, we obtain:

$$\hat{\mathcal{H}}_{spin} = \sum_{i,j} J_P S_i \cdot S_j + \sum_{i,j} J_B S_i \cdot S_j + \sum_{i,j} J_I S_i \cdot S_j. \tag{6.3}$$

Here, the J_P's are in-plane exchange interactions, the J_B's are those in the buckled layer, and the J_I's couple the two layers quantifying interlayer exchange interactions. The S_i's and S_j's are the spins. Interestingly, both $\partial^2 J_P / \partial u_m \partial u_n$ and $\partial^2 J_B / \partial u_m \partial u_n$ are zero because the motion of interest does not modulate these exchange interactions [Section 4, Supplementary Information]. In other words, the in-plane terms can be ignored because the distances and angles do not change as a result of the displacement. Here, the $u_{n,m}$'s are the displacements (or distances) between Co centers. Writing down the force constant ($k_{n,m}$), we find that:

$$k_{n,m} = \frac{\partial^2 \hat{\mathcal{H}}_{spin}}{\partial u_m \partial u_n} = \frac{\partial^2 J_I}{\partial u_m \partial u_n} \langle S_i \cdot S_j \rangle = \lambda_I \langle S_i \cdot S_j \rangle. \tag{6.4}$$

We, therefore, see that spin-phonon coupling in $Co_4Nb_2O_9$ and the Ta analog is entirely an

inter-plane effect and that it is the Co shearing mode shown in Fig. 6.2(e) that modulates the interlayer magnetic interactions. It turns out that there are two different types of inter-plane interactions in these systems, and by analyzing the bond angles and their tendencies toward parallel or anti-parallel alignment based upon Goodenough-Kanamori-Anderson rules [] along with the number of near neighbors, we can write:

$$\lambda_{Total}\langle S_i \cdot S_j\rangle = \lambda_I\langle S_i \cdot S_j\rangle = \lambda_{2,FM}\langle S_i \cdot S_j\rangle + 3\lambda_{3,AFM}\langle S_i \cdot S_j\rangle. \tag{6.5}$$

We immediately notice the competition between antiferromagnetic and ferromagnetic interactions in Eqn. 6.5 and Fig. 6.1(d), suggesting that $Co_4Nb_2O_9$ and $Co_4Ta_2O_9$ are frustrated. This competition reduces the overall size of the frequency shift across the magnetic ordering transition. It is also why the T_N's are so low. We suspect that the magnitude of $\lambda_{2,FM}$ is larger than that of $\lambda_{3,AFM}$'s, but there are more $\lambda_{3,AFM}$'s in the sum leading to a slight preference for an antiferromagnetic ground state. The findings are consistent with softer O–Co–O bond angles and temperature-dependent lattice constants [261, 266]. As we discuss below, magnetoelectric coupling in these materials is likely to emanate from inter-layer spin-phonon interactions.

6.3 Structure-property relations in this family of materials

Table 6.1 summarizes the properties of several representative transition metal oxides, 4- and 5*d*-containing systems, and 3*d*-5*d* hybrids. The entries are grouped by the electronic state. We immediately notice that some materials have multiple coupled modes and a tendency toward three-dimensional structure whereas others have only a single spin-phonon coupled mode along with a tendency toward layered or chain-like character.

Table 6.1: Spin-phonon coupling in $Co_4Nb_2O_9$ and $Co_4Ta_2O_9$ compared with that in a number of representative $3d$, $4d$, $5d$, and mixed oxides. An asterisk (*) indicates where information was available for us to estimate values.

Materials ($\mathbf{cm^{-1}}$)	**Sites**	**Electronic state**	ω_0 ($\mathbf{cm^{-1}}$)	$\Delta\omega$ ($\mathbf{cm^{-1}}$)	$\Delta\omega/\omega_0$ ($\mathbf{cm^{-1}}$)	λ ($\mathbf{cm^{-1}}$)	**Refs.**
$ZnCr_2O_4$	Cr^{3+}	$3d^3$	370	11	3%	6.2	130
$CdCr_2O_4$	Cr^{3+}	$3d^3$	365	9	2.5%	4	383
$SrMnO_3$	Mn^{4+}	$3d^3$	≈135	-	-	-	103
$Fe_{1-x}Cu_xCr_2S_4$	Fe^{3+}	$3d^5$	120 to 400	-	+3%,<1%	-	384
Fe_2TeO_6	Fe^{3+}	$3d^5$	300 to 800	<1 to 5*	<1 to 1.3%*	0.1 to 1.2	385
Sr_2CoO_4	Co^{4+}	$3d^5$	630 and 410	-	-	2 to 3.5	386
MnF_2	Mn^{2+}	$3d^5$	≈56 to 480.5	-	≈0.4 to 3.7%*	-0.4, -0.3, -0.3, 0.2	387
FeF_2	Fe^{2+}	$3d^6$	56 to 480.5	-	-	-0.4, -0.3, 0.5, 1.3	387
$\mathbf{Co_4Nb_2O_9}$	Co^{2+}	$3d^7$	144	-7.5	5%	-3.4	**This work**
$\mathbf{Co_4Ta_2O_9}$	Co^{2+}	$3d^7$	145	-9.1	6%	-4.3	**This work**
NiO	Ni^{2+}	$3d^8$	752.5, 1160	-12.5*	1.7%*, 2.7%*	-7.9, 14.7	388
Ni_3TeO_6	Ni^{2+}	$3d^8$	313, 597.3, 672	-0.4, 0.3, -3.7	<1%*	-0.4, 0.3, -3.7	62
$Y_2Ru_2O_7$	Ru^{4+}	$4d^4$	420.0, 492.0	-2 to 4*	<1%*	-6 to 9	133
$NaOsO_3$	Os^{5+}	$5d^3$	550 to 800	40	≈5.7%*	17.8*	104
$Cd_2Os_2O_7$	Os^{5+}	$5d^3$	100 to 800	-4.0 to 20*	<1 to 6%	-1.8 to 8.9 (with $S = 3/2$)*	104, 136
$Y_2Ir_2O_7$	Ir^{4+}	$5d^4$	420, 492	-9.7*	1.4%	-0.4 to 3.2 (with $J_{\text{eff}} = 1/2$)*	63
Sr_3NiIrO_6	Ir^{4+}	$5d^4$	133, 310, 534	-	-	2, 10, 5	22
Ba_2FeReO_6	Fe^{3+}/Re^{5+}	$3d^5/5d^2$	390 to 630	≈30	5.1%*	-	105
Sr_2CrReO_6	Cr^{3+}/Re^{5+}	$3d^3/5d^2$	600	≈25	4.9%*	-	105

As already discussed, the E_u symmetry Co^{2+} shearing mode near 150 cm^{-1} is the only feature to engage in spin-phonon coupling in the materials of interest here. We also see that the frequency shifts in Table 6.1 have both positive and negative signs. Among the materials with coupled modes that soften, $Co_4Nb_2O_9$ and the Ta analog host the largest relative frequency shift - even though competing antiferromagnetic and ferromagnetic interactions reduce the size of the overall shift. In certain cases, soft modes can trigger a transition.

The spin-phonon coupling constant, λ, is often challenging to define, and the procedure for doing so is inconsistent in the literature. We, therefore, find the relative frequency shifts to be the most reliable for comparison purposes. As pointed out in Ref. 136, the relative frequency shift of a phonon across a magnetic ordering transition $\Delta\omega/\omega_0$ is usually less than 1% for a transition metal oxide. $Co_4Nb_2O_9$ and the Ta analog are different with relative frequency shifts of 5 and 6%, respectively. These values are unusually large. In fact, the $\Delta\omega/\omega_0$'s that we find in $Co_4Nb_2O_9$ and $Co_4Ta_2O_9$ [Fig. 6.2(b, d)] are more comparable with the $5d$ oxides and $3d/5d$ hybrid systems shown in Table 6.1 where the relative frequency shifts correlate (in general) with the electronic shell and spin-orbit coupling.

The presence of a heavy element at the B site in $Co_4Nb_2O_9$ and $Co_4Ta_2O_9$ naturally raises questions about the spin Hamiltonian and whether additional terms such as anisotropy and Dzyaloshinskii-Moriya interactions contribute to spin-phonon coupling [63, 389]. Recent neutron scattering work also demonstrates that the excitation spectrum can not be reproduced without terms that give rise to spin noncollinearity [258, 259]. Focusing on $Co_4Nb_2O_9$, we see that the anisotropies $\geq$ J's $\geq$ Dzyaloshinskii-Moriya interaction [258, 259]. All of these terms are on the order of 1 meV. Of course, we are not interested in the absolute size of the anisotropy, exchange, or Dzyaloshinskii-Moriya interaction. Instead, we want to know how they are modulated by the phonon mode. In other words, we are interested in how these quantities *change* with the second derivative of the displacement.

If we modify Eqn. 6.4 to include these terms, the prefactors that contribute to spin-phonon coupling are $\partial^2 A/\partial u^2$ and $\partial^2 DM/\partial u^2$. Here A is the anisotropy, and DM is the

Dzyaloshinskii-Moriya interaction. The question is whether these contributions are large or small. Since A is an on-site term, we do not expect it to change very much with a vibration. Even if it does, we anticipate that shearing of the planar vs. buckled layers against each other will significantly diminish $\partial^2 A/\partial u^2$ due to their opposite motion. In other words, while $\partial^2 A/\partial u^2$ for the planar and buckled layers are not exactly equal, they have opposite signs due to the shearing motion of the layers which, when added together, significantly diminishes any impact of the overall anisotropy term. Therefore, we argue that in these unique circumstances $\partial^2 A/\partial u^2$ is small. On the other hand, the $\partial^2 DM/\partial u^2$ term multiplies a cross product between two sites, so it has the potential to contribute, although the fact that spin-orbit coupling and noncollinearity derive primarily from the B site suggests reduced importance because the displacement pattern involves shearing of the planar and buckled Co layers against each other rather than the motion of the B site. Another way to look at the issue is that the Dzyaloshinskii-Moriya interaction is in the Co-O-Co linkage of the buckled layers, and these bond lengths and angles do not change with the motion [258]. This again rules out contributions from the Dzyaloshinskii-Moriya interaction. In any case, including these additional terms has the disadvantage of obscuring one of the most interesting aspects of the simple Heisenberg analysis which is that spin-phonon coupling constants in $Co_4Nb_2O_9$ and the Ta analog are dominated by competing interlayer exchange interactions.

Hybridization models, shown to be important in Ba_2FeReO_6 and Sr_2CrReO_6 [105], are also worthy of consideration. Although there is hybridization in our systems [269], it does not involve Nb^{5+} or Ta^{5+} because these centers are associated with unfilled bands. As a result, hybridization mechanisms are probably not dominant here.

6.4 Revealing the origin of magnetoelectric coupling

Magnetoelectric coupling in the $Co_4B_2O_9$ (B = Nb, Ta) family of materials has been of sustained interest [257, 264, 264, 267, 268]. Suggested mechanisms include spin-phonon coupling [262, 263], domain and domain wall effects [264], Dzyaloshinskii-Moriya interactions through the spin-current model [258, 269], and critical spin fluctuations [261, 264]. With the direct observation of large frequency shifts across the magnetic ordering transitions, sizeable spin-phonon coupling constants, and microscopic analysis of the competing interlayer interactions, we are in a significantly better position to evaluate how magnetoelectric coupling might emerge from these candidate mechanisms. As established above, our analysis reveals that $Co_4Nb_2O_9$ and the Ta analog have strong spin-phonon interactions that involve competing interlayer exchange interactions modulated by the shearing motion of the Co layers. While there are Raman-active modes that are sensitive to the development of magnetic ordering [266], the infrared-active E_u symmetry shearing mode has a frequency shift that is an order of magnitude larger, indicating that odd-symmetry motion dominates spin-phonon coupling in this system. This type of exchange striction provides a very natural origin for magnetodielectric coupling [257, 262, 263, 269]. It is also the most likely origin of magnetoelectric coupling [257, 262, 263] given the fact that the Dzyaloshinskii-Moriya interaction operating through the spin-current model is significantly smaller and does not couple to the 150 cm^{-1} Co shearing mode. The change in dipole moment associated with magnetoelectric coupling [390] is consistent with the microscopic nature of this infrared-active mode.

Chapter 7

Summary and Outlook

In this dissertation, I present the spectroscopic investigation of magnetoelectric multiferroics containing heavy metal centers, revealing the consequences of the mixing of $3d$ transition metal with heavy metal centers and leading to exotic properties. While probing the phase transitions and fundamental excitations in these materials as a function of temperature, magnetic field, and chemical substitution, I reveal the microscopic mechanisms underlying hybridization, nonreciprocity, and coupling between spin, charge, orbital, and lattice degrees of freedom. These findings advance the understanding of the consequences of mixing transition metal and heavy metal centers in complex oxides.

$A_2Mo_3O_8$ (A = Fe, FeZn, Zn, Mn, Ni) provides an important platform to study quantum cluster magnets in heavy metal centers. To study the unusual hybridization, we measure the optical properties of $Fe_2Mo_3O_8$ and compare our findings with first principles electronic structure calculations. We find a 1.1 eV direct gap composed of heavily mixed charge-transfer excitations that is sensitive to magnetic ordering at 61 K, vibronic coupling that activates on-site d-to-d excitations on the distorted octahedral Fe site, and spin-orbit related features riding on top of the d-to-d excitation on the distorted tetrahedral Fe site below the magnetic ordering temperature. The Kondo effect is, of course, usually studied in metals. Here, we show that it can also appear in a semiconductor that has both Mott and band gaps. Similar to the metallic Kondo effect, the orbitals with Mott-like gaps

develop a many-body excitation near the valence edge. This draws the gap downward in energy (from 1.7 eV in $Zn_2Mo_3O_8 \rightarrow$ 1 eV in $Fe_2Mo_3O_8$) and screens the magnetic moment. This discovery opens the door to deeper exploration of the Kondo effect in semiconductors. $Fe_2Mo_3O_8$ is also a superb platform for unraveling structure-property relationships. What differentiates $Fe_2Mo_3O_8$ from the Zn, Mn, Co, and Ni members of this series is the band-Mott mixing, the Zhang-Rice resonance, and how the gap is hybridized. Taken together, these findings enhance our understanding of charge transfer in quantum cluster magnets and advance the use of this powerful scaffold in new types of charge storage devices.

Ni_3TeO_6 is a superb platform for fundamental studies of nonreciprocity because it hosts this peculiar property across a wide range of excitations and in three different measurement configurations. To our knowledge, there are no other nonreciprocal materials that have been studied in so many different geometries. In this work, we focus on the Ni^{2+} *d*-to-*d* excitations and associated phonon sidebands in the near infrared and optical range in the toroidal configuration, unraveling structure-property relationships via comparison with contrast in the magnetochiral and transverse magnetochiral geometries. We find that polarity allows the creation of Ni toroidal moments, which results in large contrast near the color band at 1.1 eV. The chiral geometries, on the other hand, yield smaller contrast over a much broader energy range. Our modeling of the size and shape of the spectral response supports this picture of the importance of polarity vs. chirality in the creation of large vs. broadband contrast. These findings enhance our ability to design and deliver complex materials properties on demand. At the same time, the discovery of nonreciprocal effects across the full telecom wavelength range presents a number of exciting opportunities. While tunability under magnetic field is established in this work, the degree to which nonreciprocity can be controlled by other external stimuli or chemical substitution is unexplored. That said, the discovery of nonreciprocity in the telecom region is a significant conceptual advance that has the potential to jump-start the use of dichroic contrast in photonics applications - particularly in the area of high-efficiency optical diodes and rectifiers.

$Co_4B_2O_9$ (B = Nb, Ta) is a quasi-two-dimensional mixed metal system with high magnetoelectric coupling strength, offering an excellent opportunity for structure-property relationships of heavy metal centers. To study the effects of 4- and 5d heavy metal centers, we measured the vibrational properties of $Co_4Nb_2O_9$ and the Ta analog and compared our findings with lattice dynamics calculations and a detailed model of spin-phonon coupling. Frequency vs. temperature trends for the Co^{2+} shearing mode near 150 cm^{-1} reveal significant shifts across the magnetic ordering temperature that are especially large in relative terms In addition to revealing one of the largest relative frequency shifts ever reported, these materials host a Co shearing mode that couples only with the interlayer interactions due to unique symmetry conditions. Interestingly, these interlayer interactions are frustrated and consist of both antiferromagnetic and ferromagnetic terms. Given the sizable contribution of spin-phonon interactions in these systems, it is likely that magnetoelectric coupling is driven by this effect.

$MnPS_3$ and $CrPS_4$ are two-dimensional van der Waals magnets, which are promising materials for spintronics. However, the electronic structures of $MnPS_3$ and $CrPS_4$ are under-explored and inconsistent. Thus, we measured optical properties as a function of temperature using variable temperature optical spectroscopy. $MnPS_3$ exhibits spin-charge coupling in the d-to-d excitations as well as charge-transfer excitation, which is evident by the abrupt change across the T_N. We also lay a groundwork for the correct assignments for the on-site and charge-transfer excitations of $CrPS_4$ using $Dq/B = 2.72$ eV. Furthermore, the temperature dependence of the band gap in $MnPS_3$ and $CrPS_4$ shows high coupling strength and high average phonon energy, respectively. To further investigate the magnetic properties of $MnPS_3$ and $CrPS_4$, magnetic circular dichroism spectroscopy is used to probe both compounds as a function of magnetic field and temperature. Using an energy cut of $\Delta\alpha_{MCD}$, we reveal orbital-selective spin-flop transitions at $\sim$3T and $\sim$1 T for $MnPS_3$ and $CrPS_4$, respectively. Surprisingly, $CrPS_4$ displays an additional magnetic phase above the saturation field of 10 T. Furthermore, $CrPS_4$ exhibits a giant magnetic circular dichroism signal. Combining these results together, we lay the groundwork for the two-

dimensional van der Waals magnets and facilitate the progress in low-power ultra-compact two-dimensional spintronics.

These extensive findings shed light on the intricate relationships among spin, charge, orbital, and lattice degrees of freedom in multifunctional materials that contain heavy metal centers. By substitution of heavy metal centers, the spin-orbit coupling can be a tuning parameter. Furthermore, the application of external magnetic fields can also be used as an additional tuning parameter, which can drive quantum transitions and observe nonreciprocal directional dichroism by controlling symmetries. Overall, incorporating heavy metal centers motivate fundamental research on other mixed metal systems under extreme conditions.

Bibliography

[1] Spaldin, N. A. & Fiebig, M. The renaissance of magnetoelectric multiferroics. *Science* **309**, 391–392 (2005).

[2] Yang, S. Y. *et al.* Above-bandgap voltages from ferroelectric photovoltaic devices. *Nature Nanotechnology* **5**, 143–147 (2010).

[3] Chatterjee, S., Bera, A. & Pal, A. J. *p–i–n* Heterojunctions with $BiFeO_3$ Perovskite Nanoparticles and *p*- and *n*-Type Oxides: Photovoltaic Properties. *ACS Applied Materials & Interfaces* **6**, 20479–20486 (2014).

[4] Biswas, P. P. *et al.* Photovoltaic and photo-capacitance effects in ferroelectric $BiFeO_3$ thin film. *Applied Physics Letters* **110**, 192906 (2017).

[5] Heron, J. T., Schlom, D. G. & Ramesh, R. Electric field control of magnetism using $BiFeO_3$-based heterostructures. *Applied Physics Reviews* **1**, 021303 (2014).

[6] Taniguchi, K., Abe, N., Takenobu, T., Iwasa, Y. & Arima, T. Ferroelectric polarization flop in a frustrated magnet $MnWO_4$ induced by a magnetic field. *Physical Review Letters* **97**, 097203 (2006).

[7] Yamasaki, Y. *et al.* Magnetic reversal of the ferroelectric polarization in a multiferroic spinel oxide. *Physical Review Letters* **96**, 207204 (2006).

[8] Park, S., Choi, Y. J., Zhang, C. L. & Cheong, S.-W. Ferroelectricity in an $S = 1/2$ chain cuprate. *Physical Review Letters* **98**, 057601 (2007).

[9] Dong, S., Xiang, H. & Dagotto, E. Magnetoelectricity in multiferroics: a theoretical perspective. *National Science Review* **6**, 629–641 (2019).

[10] Shao, Y. *et al.* Enhanced magnetoelectric effect by spin-orbit coupling in M-type hexaferrite. *Physical Review B* **106**, 144419 (2022).

[11] Kim, B. J. *et al.* Novel $J_{\text{eff}} = 1/2$ Mott state induced by relativistic spin-orbit coupling in Sr_2IrO_4. *Physical Review Letters* **101**, 076402 (2008).

[12] Streltsov, S. V. & Khomskii, D. I. Orbital physics in transition metal compounds: new trends. *Physics-Uspekhi* **60**, 1121–1146 (2017).

[13] Taylor, A. E. *et al.* Spin-orbit coupling controlled $J = 3/2$ electronic ground state in $5d^3$ oxides. *Physical Review Letters* **118**, 207202 (2017).

[14] Zwartsenberg, B. *et al.* Spin-orbit-controlled metal–insulator transition in Sr_2IrO_4. *Nature Physics* **16**, 290–294 (2020).

[15] Kim, H.-H. *et al.* Giant stress response of terahertz magnons in a spin-orbit Mott insulator. *Nature Communications* **13**, 6674 (2022).

[16] Varotto, S. *et al.* Direct visualization of Rashba-split bands and spin/orbital-charge interconversion at $KTaO_3$ interfaces. *Nature Communications* **13**, 6165 (2022).

[17] Morrow, R. *et al.* Independent ordering of two interpenetrating magnetic sublattices in the double perovskite Sr_2CoOsO_6. *Journal of the American Chemical Society.* **135**, 18824–18830 (2013).

[18] Yan, B. *et al.* Lattice-site-specific spin dynamics in double perovskite Sr_2CoOsO_6. *Physical Review Letters* **112**, 147202 (2014).

[19] Gu, J. *et al.* p-type $CuRhO_2$ as a self-healing photoelectrode for water reduction under visible light. *Journal of the American Chemical Society* **136**, 830–833 (2014).

[20] Ye, M. *et al.* Covalency-driven collapse of strong spin-orbit coupling in face-sharing iridium octahedra. *Physical Review B* **98**, 201105 (2018).

[21] Singleton, J. *et al.* Magnetic properties of Sr_3NiIrO_6 and Sr_3CoIrO_6: Magnetic hysteresis with coercive fields of up to 55 T. *Physical Review B* **94**, 224408 (2016).

[22] O'Neal, K. R. *et al.* Spin–lattice and electron–phonon coupling in $3d/5d$ hybrid Sr_3NiIrO_6. *npj Quantum Materials* **4**, 48 (2019).

[23] Bordács, S. *et al.* Magnetic-order-induced crystal symmetry lowering in ACr_2O_4 ferrimagnetic spinels. *Physical Review Letters* **103**, 077205 (2009).

[24] Kant, C. *et al.* Optical phonons, spin correlations, and spin-phonon coupling in the frustrated pyrochlore magnets $CdCr_2O_4$ and $ZnCr_2O_4$. *Physical Review B* **80**, 214417 (2009).

[25] Wysocki, A. L. & Birol, T. Magnetically induced phonon splitting in ACr_2O_4 spinels from first principles. *Physical Review B* **93**, 134425 (2016).

[26] Liang, T. *et al.* Heat capacity peak at the quantum critical point of the transverse Ising magnet $CoNb_2O_6$. *Nature Communications* **6**, 7611 (2015).

[27] Datta, R., Pradhan, S. K., Masanta, S., Majumdar, S. & De, S. K. Short range spin-spin correlation, spin-phonon coupling and isostructural phase transition in hetero-tri-spin $3d$-$5d$-$4f$ double perovskite Sm_2CoIrO_6. *Journal of Solid State Chemistry.* **314**, 123391 (2022).

[28] Wang, Y. *et al.* Unveiling hidden ferrimagnetism and giant magnetoelectricity in polar magnet $Fe_2Mo_3O_8$. *Scientific Reports* **5**, 12268 (2015).

[29] Stanislavchuk, T. N. *et al.* Spectroscopic and first principle DFT+eDMFT study of complex structural, electronic, and vibrational properties of $M_2Mo_3O_8$ (M = Fe, Mn) polar magnets. *Physical Review B* **102**, 115139 (2020).

[30] Scheie, A. *PyCrystalField*: software for calculation, analysis and fitting of crystal electric field Hamiltonians. *Journal of Applied Crystallography* **54**, 356–362 (2021).

[31] Streltsov, S. V., Huang, D.-J., Solovyev, I. V. & Khomskii, D. I. Ordering of Fe and Zn ions and the magnetic properties of $FeZnMo_3O_8$. *JETP Letters* **109**, 786–789 (2019).

[32] Matsumoto, M. & Koga, M. Symmetry analysis of magnetoelectric effects in honeycomb antiferromagnet $Co_4Nb_2O_9$. *Journal of the Physical Society of Japan.* **88**, 094704 (2019).

[33] Vargesson, N. Thalidomide-induced teratogenesis: History and mechanisms. *Birth Defects Research Part C: Embryo Today: Reviews* **105**, 140–156 (2015).

[34] Katsura, H., Nagaosa, N. & Balatsky, A. V. Spin current and magnetoelectric effect in noncollinear magnets. *Physical Review Letters* **95**, 057205 (2005).

[35] Johnson, R. D. *et al.* $Cu_3Nb_2O_8$: a multiferroic with chiral coupling to the crystal structure. *Physical Review Letters* **107**, 137205 (2011).

[36] Johnson, R. D. *et al.* Giant improper ferroelectricity in the ferroaxial magnet $CaMn_7O_{12}$. *Physical Review Letters* **108**, 067201 (2012).

[37] Cheong, S.-W. & Xu, X. Magnetic chirality. *npj Quantum Materials* **7**, 40 (2022).

[38] Cheong, S.-W. SOS: symmetry-operational similarity. *npj Quantum Materials* **4**, 53 (2019).

[39] Viirok, J. *et al.* Directional dichroism in the paramagnetic state of multiferroics: A case study of infrared light absorption in $Sr_2CoSi_2O_7$ at high temperatures. *Physical Review B* **99**, 014410 (2019).

[40] Kuwahara, H. *et al.* Striction-coupled magnetoresistance in perovskite-type manganese oxides. *Science* **272**, 80–82 (1996).

[41] Tokura, Y., Kawasaki, M. & Nagaosa, N. Emergent functions of quantum materials. *Nature Physics* **13**, 1056–1068 (2017).

[42] Nakano, M. *et al.* Infrared-sensitive electrochromic device based on VO_2. *Applied Physics Letters* **103**, 153503 (2013).

[43] Nakano, M. *et al.* Collective bulk carrier delocalization driven by electrostatic surface charge accumulation. *Nature* **487**, 459–462 (2012).

[44] Fiebig, M., Miyano, K., Tomioka, Y. & Tokura, Y. Visualization of the Local Insulator-Metal Transition in $Pr_{0.7}Ca_{0.3}MnO_3$. *Science* **280**, 1925–1928 (1998).

[45] Obeysekera, D., Gamage, K., Gao, Y., Cheong, S.-w. & Yang, J. The magneto-transport properties of $Cr_{1/3}TaS_2$ with chiral magnetic solitons. *Advanced Electronic Materials* **7**, 2100424 (2021).

[46] Seki, S. *et al.* Propagation dynamics of spin excitations along skyrmion strings. *Nature Communications* **11**, 256 (2020).

[47] Rowley, S. E. *et al.* Ferroelectric quantum criticality. *Nature Physics* **10**, 367–372 (2014).

[48] Rivadulla, F. *et al.* Effect of Mn-site doping on the magnetotransport properties of the colossal magnetoresistance compound $La_{2/3}Ca_{1/3}Mn_{1-x}A_xO_3$ ($A = \mathrm{Co}, \mathrm{Cr}$; *xlt*; 0.1). *Physical Review B* **62**, 5678–5684 (2000).

[49] Takahashi, H. *et al.* Superconductivity at 43 K in an iron-based layered compound $LaO_{1-x}F_xFeAs$. *Nature* **453**, 376–378 (2008).

[50] Lahneman, D. J. *et al.* Insulator-to-metal transition in ultrathin rutile $VO_2/TiO_2(001)$. *npj Quantum Materials* **7**, 72 (2022).

[51] Moriya, T. & Miyadai, T. Evidence for the helical spin structure due to antisymmetric exchange interaction in $Cr_{1/3}NbS_2$. *Solid State Communications* **42**, 209–212 (1982).

[52] Qian, F. *et al.* New magnetic phase of the chiral skyrmion material Cu_2OSeO_3. *Science Advances* **4**, eaat7323 (2018).

[53] Deng, L. *et al.* Room-temperature skyrmion phase in bulk Cu_2OSeO_3 under high pressures. *Proceedings of the National Academy of Sciences* **117**, 8783–8787 (2020).

[54] Qian, F. *et al.* New magnetic phase of the chiral skyrmion material Cu_2OSeO_3. *Science Advances* **4** (2018).

[55] Tanner, D. B. *Optical effects in solids* (University of Florida, lecture notes, 2019).

[56] Skomski, R., Manchanda, P. & Kashyap, A. *Anisotropy and Crystal Field*, 103–185 (Springer International Publishing, Cham, 2021).

[57] Ashcroft, N. W. & Mermin, N. D. Solid state physics. *Saunders College* (1976).

[58] Brinzari, T. V. *et al.* Quantum critical transition amplifies magnetoelastic coupling in $Mn[N(CN)_2]_2$. *Physical Review Letters* **237202**, 1–5 (2013).

[59] Chen, P. *et al.* Size-dependent infrared phonon modes and ferroelectric phase transition in $BiFeO_3$. *Nano Letters* **10**, 4526–4532 (2010).

[60] Fan, S. *et al.* Excitations of intercalated metal monolayers in transition metal dichalcogenides. *Nano Lett.* **21**, 99–106 (2021).

[61] Hughey, K. D. *et al.* Phonon mode links ferroicities in multiferroic $[(CH_3)_2NH_2]Mn(HCOO)_3$. *Physical Review B* **96**, 180305 (2017).

[62] Yokosuk, M. O. *et al.* Tracking the continuous spin-flop transition in Ni_3TeO_6 by infrared spectroscopy. *Physical Review B* **92**, 144305 (2015).

[63] Son, J. *et al.* Unconventional spin-phonon coupling via the Dzyaloshinskii–Moriya interaction. *npj Quantum Mater.* **4**, 17 (2019).

[64] Yu, S. *et al.* High-temperature terahertz optical diode effect without magnetic order in polar $FeZnMo_3O_8$. *Physical Review Letters* **120**, 037601 (2018).

[65] Hutchings, M. Point-charge calculations of energy levels of magnetic ions in crystalline electric fields. vol. 16 of *Solid State Physics*, 227–273 (Academic Press, 1964).

[66] Stevens, K. W. H. Matrix elements and operator equivalents connected with the magnetic properties of rare earth ions. *Proceedings of the Physical Society. Section A* **65**, 209 (1952).

[67] Bauer, E. & Rotter, M. Magnetism of complex metallic alloys: Crystalline electric field effects. *ChemInform* **41** (2010).

[68] Yokosuk, M. O. *et al.* Magnetoelectric coupling through the spin flop transition in Ni_3TeO_6. *Physical Review Letters* **117**, 147402 (2016).

[69] Radwanski, R. J. & Ropka, Z. Nio - from first principles. *arXiv* (2006).

[70] Xu, X. S. *et al.* Optical properties and magnetochromism in multiferroic $BiFeO_3$. *Physical Review B* **79**, 134425 (2009).

[71] Chen, P., Lee, N., Mcgill, S., Cheong, S. & Musfeldt, J. L. Magnetic-field-induced color change in α-Fe_2O_3 single crystals. *Physical Review B* **85**, 1–5 (2012).

[72] Russell, P. G., McClure, D. S. & Stout, J. W. Zeeman splitting of narrow lines in crystalline MnF_2, FeF_2, and CoF_2. Evidence for spin-wave excitations. *Physical Review Letters* **16**, 176–178 (1966).

[73] Eremenko, V. V., Litvinenko, Y. G. & Myatlik, V. I. Magnetic field attenuation of light absorption by antiferromagnetic $FeCO_3$. *Journal of Experimental and Theoretical Physics Letters* **12** (1970).

[74] Eremenko, V. V. & Petrov, E. G. Light absorption in antiferromagnets. *Advances in Physics* **26**, 31–78 (1977).

[75] Spaldin, N. A. & Ramesh, R. Advances in magnetoelectric multiferroics. *Nature Materials* **18**, 203–212 (2019).

[76] Parkin, S. S. P., Hayashi, M. & Thomas, L. Magnetic domain-wall racetrack memory. *Science* **320**, 190–194 (2008).

[77] Eerenstein, W., Mathur, N. D. & Scott, J. F. Multiferroic and magnetoelectric materials. *Nature* **442**, 759–765 (2006).

[78] Hill, N. A. Why are there so few magnetic ferroelectrics? *The Journal of Physical Chemistry B* **104**, 6694–6709 (2000).

[79] Rondinelli, J. M., Eidelson, A. S. & Spaldin, N. A. Non-d^0 Mn-driven ferroelectricity in antiferromagnetic $BaMnO_3$. *Phys. Rev. B* **79**, 205119 (2009).

[80] Bersuker, I. B. Journal of physics: Conference series **428** (2013).

[81] Kubel, F. & Schmid, H. Structure of a ferroelectric and ferroelastic monodomain crystal of the perovskite $BiFeO_3$. *Acta Crystallographica Section B Structural Science* **46**, 698–702 (1990).

[82] Wang, J. *et al.* Epitaxial $BiFeO_3$ multiferroic thin film heterostructures. *Science* **299**, 1719–1722 (2003).

[83] $BiFeO_3$ ($FeBiO_3$ rt) Crystal Structure: Datasheet from "PAULING FILE Multinaries Edition – 2012" in SpringerMaterials (https://materials.springer.com/isp/crystallographic/docs/sd_1102250). Copyright 2016 Springer-Verlag Berlin Heidelberg & Material Phases Data System (MPDS), Switzerland & National Institute for Materials Science (NIMS), Japan.

[84] $TbMnO_3$ Crystal Structure: Datasheet from "PAULING FILE Multinaries Edition – 2012" in SpringerMaterials (https://materials.springer.com/isp/crystallographic/docs/sd_1714336). Copyright 2016 Springer-Verlag Berlin Heidelberg & Material Phases Data System (MPDS), Switzerland & National Institute for Materials Science (NIMS), Japan.

[85] Fiebig, M., Lottermoser, T., Meier, D. & Trassin, M. The evolution of multiferroics. *Nature Reviews Materials* **1**, 16046 (2016).

[86] Ederer, C. & Spaldin, N. A. Origin of ferroelectricity in the multiferroic barium fluorides BaMF$_4$: A first principles study. *Physical Review B* **74**, 024102 (2006).

[87] Ahn, S.-J., Kim, J., Shin, N. & Koo, Y.-M. The covalent bonding interaction in the ferroelectric $LuMnO_3$. *Journal of Applied Physics* **110**, 084112 (2011).

[88] Eibschütz, M., Guggenheim, H., Wemple, S., Camlibel, I. & DiDomenico, M. Ferroelectricity in $BaM^{2+}F_4$. *Physics Letters A* **29**, 409–410 (1969).

[89] Fennie, C. J. & Rabe, K. M. Ferroelectric transition in $YMnO_3$ from first principles. *Physical Review B* **72**, 100103 (2005).

[90] de Groot, J. *et al.* Charge order in $LuFe_2\mathbf{O}_4$: an unlikely route to ferroelectricity. *Physical Review Letters* **108**, 187601 (2012).

[91] Angst, M. *et al.* Charge order in $LuFe_2\mathbf{O}_4$: Antiferroelectric ground state and coupling to magnetism. *Physical Review Letters* **101**, 227601 (2008).

[92] Fan, S. *et al.* Site-specific spectroscopic measurement of spin and charge in $(LuFeO_3)_m/(LuFe_2O_4)_1$ multiferroic superlattices. *Nature Communications* **11**, 5582 (2020).

[93] Senn, M. S., Wright, J. P. & Attfield, J. P. Charge order and three-site distortions in the Verwey structure of magnetite. *Nature* **481**, 173–176 (2012).

[94] Newnham, R. E., Kramer, J. J., Schulze, W. A. & Cross, L. E. Magnetoferroelectricity in Cr_2BeO_4. *Journal of Applied Physics* **49**, 6088–6091 (1978).

[95] Sharma, G., Saha, J., Kaushik, S., Siruguri, V. & Patnaik, S. Improper ferroelectricity in helicoidal antiferromagnet $Cu_3Nb_2O_8$. *Solid State Communications* **203**, 54–57 (2015).

[96] Kimura, T. *et al.* Magnetic control of ferroelectric polarization. *Nature* **426**, 55–58 (2003).

[97] Tokura, Y., Seki, S. & Nagaosa, N. Multiferroics of spin origin. *Reports on Progress in Physics* **77**, 076501 (2014).

[98] Murakawa, H., Onose, Y., Miyahara, S., Furukawa, N. & Tokura, Y. Ferroelectricity induced by spin-dependent metal-ligand hybridization in $Ba_2CoGe_2O_7$. *Physical Review Letters* **105**, 137202 (2010).

[99] Arima, T. Ferroelectricity induced by proper-screw type magnetic order. *Journal of the Physical Society of Japan* **76**, 073702 (2007).

[100] Hughey, K. D. *et al.* High-field magnetoelectric and spin-phonon coupling in multiferroic $(NH_4)_2[FeCl_5{\cdot}(H_2O)]$. *Inorganic Chemistry* **61**, 3434–3442 (2022).

[101] Kato, H. *et al.* Metallic ordered double-perovskite Sr_2CrReO_6 with maximal Curie temperature of 635 K. *Applied Physics Letters* **81**, 328–330 (2002).

[102] Philipp, J. B. *et al.* Structural and doping effects in the half-metallic double perovskite A_2CrWO_6 (A =Sr, Ba, and Ca). *Physical Review B* **68**, 144431 (2003).

[103] Kamba, S. *et al.* Strong spin-phonon coupling in infrared and Raman spectra of $SrMnO_3$. *Physical Review B* **89**, 064308 (2014).

[104] Calder, S. *et al.* Enhanced spin-phonon-electronic coupling in a $5d$ oxide. *Nature Communication* **6**, 8916 (2015).

[105] García-Flores, A. F. *et al.* Spin-electron-phonon excitation in Re-based half-metallic double perovskites. *Physical Review Letters* **108**, 177202 (2012).

[106] Rikken, G. L. J. A., Strohm, C. & Wyder, P. Observation of magnetoelectric directional anisotropy. *Physical Review Letters* **89**, 133005 (2002).

[107] Kézsmárki, I. *et al.* One-way transparency of four-coloured spin-wave excitations in multiferroic materials. *Nature Communications* **5**, 3203 (2014).

[108] Hlinka, J. Eight types of symmetrically distinct vectorlike physical quantities. *Physical Review Letters* **113**, 165502 (2014).

[109] Lee, J. H., Kézsmáki, I. & Fishman, R. S. First-principles approach to the dynamic magnetoelectric couplings for the non-reciprocal directional dichroism in $BiFeO_3$. *New Journal of Physics* **18**, 043025 (2016).

[110] Bordács, S. *et al.* Unidirectional terahertz light absorption in the pyroelectric ferrimagnet $CaBaCo_4O_7$. *Physical Review B* **92**, 214441 (2015).

[111] Kézsmárki, I. *et al.* Enhanced directional dichroism of terahertz light in resonance with magnetic excitations of the multiferroic $Ba_2CoGe_2O_7$ oxide compound. *Physical Review Letters* **106**, 057403 (2011).

[112] Jung, J. H. *et al.* Optical magnetoelectric effect in the polar $GaFeO_3$ ferrimagnet. *Physical Review Letters* **93**, 037403 (2004).

[113] Saito, M., Ishikawa, K., Taniguchi, K. & Arima, T. Magnetic control of crystal chirality and the existence of a large magneto-optical dichroism effect in CuB_2O_4. *Physical Review Letters* **101**, 117402 (2008).

[114] Zhao, T. *et al.* Electrical control of antiferromagnetic domains in multiferroic $BiFeO_3$ films at room temperature. *Nature Materials* **5**, 823–829 (2006).

[115] Johnson, R. D. *et al.* X-ray imaging and multiferroic coupling of cycloidal magnetic domains in ferroelectric monodomain $BiFeO_3$. *Physical Review Letters* **110**, 217206 (2013).

[116] García-Fernández, M. *et al.* Antiferromagnetic domain structure in bilayer manganite. *Physical Review B* **88**, 075134 (2013).

[117] Kim, M. G. *et al.* Imaging antiferromagnetic antiphase domain boundaries using magnetic Bragg diffraction phase contrast. *Nature Communications* **9**, 5013 (2018).

[118] Kim, M. G. *et al.* Real-space observation of fluctuating antiferromagnetic domains. *Science Advances* **8**, eabj9493 (2022).

[119] Kimura, K., Katsuyoshi, T., Sawada, Y., Kimura, S. & Kimura, T. Imaging switchable magnetoelectric quadrupole domains via nonreciprocal linear dichroism. *Communications Materials* **1**, 39 (2020).

[120] Poojitha, B. *et al.* Effect of phonon anharmonicity on ferroelectricity in $Eu_xBa_{1-x}TiO_3$. *Physical Review Materials* **3**, 024412 (2019).

[121] Moya, X. & Mathur, N. D. Turn your phonon. *Nature Materials* **16**, 784–785 (2017).

[122] Calero, C., Chudnovsky, E. M. & Garanin, D. A. Field dependence of the electron spin relaxation in quantum dots. *Physical Review Letters* **95**, 166603 (2005).

[123] Bibes, M. & Barthélémy, A. Towards a magnetoelectric memory. *Nature Materials* **7**, 425–426 (2008).

[124] Lee, J. H. *et al.* A strong ferroelectric ferromagnet created by means of spin–lattice coupling. *Nature* **466**, 954–958 (2010).

[125] Jungwirth, T., Marti, X., Wadley, P. & Wunderlich, J. Antiferromagnetic spintronics. *Nature Nanotechnology* **11**, 231–241 (2016).

[126] Němec, P., Fiebig, M., Kampfrath, T. & Kimel, A. V. Antiferromagnetic opto-spintronics. *Nature Physics* **14**, 229–241 (2018).

[127] McQuarrie, D. A. *Quantum Chemistry* (University Science Books, 2008), second edn.

[128] Granado, E. *et al.* Magnetic ordering effects in the Raman spectra of $La_{1-x}Mn_{1-x}O_3$. *Physical Review B* **60**, 11879–11882 (1999).

[129] Pal, A. *et al.* Spin-induced strongly correlated magnetodielectricity, magnetostriction effect, and spin-phonon coupling in helical magnet $Fe_3(PO_4)O_3$. *Physical Review B* **106**, 094404 (2022).

[130] Sushkov, A. B., Tchernyshyov, O., II, W. R., Cheong, S. W. & Drew, H. D. Probing spin correlations with phonons in the strongly frustrated magnet $ZnCr_2O_4$. *Physical Review Letters* **94**, 137202 (2005).

[131] Fennie, C. J. & Rabe, K. M. Magnetically induced phonon anisotropy in $ZnCr_2O_4$ from first principles. *Physical Review Letters* **96**, 205505 (2006).

[132] Birol, T. & Fennie, C. J. Origin of giant spin-lattice coupling and the suppression of ferroelectricity in $EuTiO_3$ from first principles. *Physical Review B* **88**, 094103 (2013).

[133] Lee, J. S. *et al.* Strong spin-phonon coupling in the geometrically frustrated pyrochlore $Y_2Ru_2O_7$. *Physical Review B* **69**, 214428 (2004).

[134] Baltensperger, W. Influence of magnetic order on conduction electrons and phonons in magnetic semiconductors. *Journal of Applied Physics* **41**, 1052–1054 (1970).

[135] Poojitha, B., Rathore, A., Kumar, A. & Saha, S. Signatures of magnetostriction and spin-phonon coupling in magnetoelectric hexagonal $15R-BaMnO_3$. *Physical Review B* **102**, 134436 (2020).

[136] Sohn, C. H. *et al.* Strong spin-phonon coupling mediated by single ion anisotropy in the all-in–all-out pyrochlore magnet $Cd_2Os_2O_7$. *Physical Review Letters* **118**, 117201 (2017).

[137] Wooten, F. *Optical Properties of Solids* (Elsevier, 1972).

[138] Sun, Q. C. *et al.* Spectroscopic determination of phonon lifetimes in Rhenium-doped MoS_2 nanoparticles. *Nano Letters* **13**, 2803–2808 (2013).

[139] Ising, E. Beitrag zur Theorie des Ferromagnetismus. *Zeitschrift für Physik* **31**, 253–258 (1925).

[140] Heisenberg, W. *Über* den anschaulichen Inhalt der quantentheoretischen Kinematik und Mechanik. *Zeitschrift für Physik* **43**, 172–198 (1927).

[141] Mermin, N. D. & Wagner, H. Absence of ferromagnetism or antiferromagnetism in one- or two-dimensional isotropic Heisenberg models. *Physical Review Letters* **17**, 1133–1136 (1966).

[142] Blundell, S. *Magnetism in Condensed Matter* (Oxford University Press Inc., New York, 2001).

[143] Goodenough, J. B. *Magnetism and the Chemical Bond* (Interscience Publishers, New York - London, 1963).

[144] Balents, L. Spin liquids in frustrated magnets. *Nature* **464**, 199–208 (2010).

[145] Matsuda, M. *et al.* Frustrated magnetic interactions in an $S = 3/2$ bilayer honeycomb lattice compound $Bi_3Mn_4O_{12}(NO_3)$. *Physical Review B* **100**, 134430 (2019).

[146] Singh, Y. & Gegenwart, P. Antiferromagnetic Mott insulating state in single crystals of the honeycomb lattice material Na_2IrO_3. *Physical Review B* **82**, 064412 (2010).

[147] Kitagawa, K. *et al.* A spin-orbital-entangled quantum liquid on a honeycomb lattice. *Nature* **554**, 341–345 (2018).

[148] Kitaev, A. Anyons in an exactly solved model and beyond. *Annals of Physics* **321**, 2–111 (2006).

[149] Jiang, H. C., Wang, Z. & Balents, L. Identifying topological order by entanglement entropy. *Nature Physics* **8**, 902–905 (2011).

[150] He, J., Zong, Y.-H., Kou, S.-P., Liang, Y. & Feng, S. Topological spin density waves in the hubbard model on a honeycomb lattice. *Physical Review B* **84**, 035127 (2011).

[151] Göbel, B., Mook, A., Henk, J. & Mertig, I. Antiferromagnetic skyrmion crystals: Generation, topological hall, and topological spin hall effect. *Physical Review B* **96**, 060406 (2017).

[152] Li, Z.-X., Cao, Y., Wang, X. & Yan, P. Symmetry-protected zero modes in metamaterials based on topological spin texture. *Physical Review Applied* **13**, 064058 (2020).

[153] Yu, X. Magnetic imaging of various topological spin textures and their dynamics. *Journal of Magnetism and Magnetic Materials* **539**, 168332 (2021).

[154] Viciu, L. *et al.* Structure and basic magnetic properties of the honeycomb lattice compounds $Na_2Co_2TeO_6$ and $Na_3Co_2SbO_6$. *Journal of Solid State Chemistry* **180**, 1060–1067 (2007).

[155] Sears, J. A. *et al.* Magnetic order in α-$RuCl_3$: A honeycomb-lattice quantum magnet with strong spin-orbit coupling. *Physical Review B* **91**, 144420 (2015).

[156] Asai, S. *et al.* Magnetic ordering of the buckled honeycomb lattice antiferromagnet Ba_2NiTeO_6. *Physical Review B* **93**, 024412 (2016).

[157] Alaei, M., Mosadeq, H., Sarsari, I. A. & Shahbazi, F. Origin of magnetic frustration in $Bi_3Mn_4O_{12}(NO_3)$. *Physical Review B* **96**, 140404 (2017).

[158] Lee, P. A. The kitaev model. *Annual Review of Condensed Matter Physics* **10**, 193–214 (2019).

[159] Broholm, C. *et al.* Quantum spin liquids. *Science* **367**, eaay0668 (2020).

[160] Fert, A., Reyren, N. & Cros, V. Magnetic skyrmions: advances in physics and potential applications. *Nature Reviews Materials* **2**, 1–15 (2017).

[161] Rohart, S. & Thiaville, A. Skyrmion confinement in ultrathin film nanostructures in the presence of dzyaloshinskii-moriya interaction. *Physical Review B* **88**, 184422 (2013).

[162] Jackeli, G. & Khaliullin, G. Mott insulators in the strong spin-orbit coupling limit: from Heisenberg to a quantum compass and Kitaev models. *Physical Review Letters* **102**, 017205 (2009).

[163] Aguado, R. & Kouwenhoven, L. P. Majorana qubits for topological quantum computing. *Physics Today* **73**, 44–50 (2020).

[164] Zhang, S.-S., Halász, G. B. & Batista, C. D. Theory of the Kitaev model in a [111] magnetic field. *Nature Communications* **13**, 399 (2022).

[165] Singh, Y. & Gegenwart, P. Antiferromagnetic Mott insulating state in single crystals of the honeycomb lattice material Na_2IrO_3. *Physical Review B* **82**, 064412 (2010).

[166] Choi, S. K. *et al.* Spin waves and revised crystal structure of honeycomb Iridate Na_2IrO_3. *Physical Review Letters* **108**, 127204 (2012).

[167] Johnson, R. D. *et al.* Monoclinic crystal structure of $\alpha - RuCl_3$ and the zigzag antiferromagnetic ground state. *Physical Review B* **92**, 235119 (2015).

[168] Sears, J. A. *et al.* Magnetic order in $\alpha - RuCl_3$: A honeycomb-lattice quantum magnet with strong spin-orbit coupling. *Physical Review B* **91**, 144420 (2015).

[169] Lin, G. *et al.* Field-induced quantum spin disordered state in spin-1/2 honeycomb magnet $Na_2Co_2TeO_6$. *Nature Communications* **12**, 5559 (2021).

[170] Songvilay, M. *et al.* Kitaev interactions in the Co honeycomb antiferromagnets $Na_3Co_2SbO_6$ and $Na_2Co_2TeO_6$. *Physical Review B* **102**, 224429 (2020).

[171] Balents, L. Spin liquids in frustrated magnets. *Nature* **464**, 199–208 (2010).

[172] Hwan Chun, S. *et al.* Direct evidence for dominant bond-directional interactions in a honeycomb lattice iridate Na_2IrO_3. *Nature Physics* **11**, 462–466 (2015).

[173] Zhang, S. *et al.* Electronic and magnetic phase diagrams of Kitaev quantum spin liquid candidate $Na_2Co_2TeO_6$ (2022). URL `https://arxiv.org/abs/2212.03849`.

[174] Zhang, Y., Tan, Y. W., Stormer, H. L. & Kim, P. Experimental observation of the quantum hall effect and berry's phase in graphene. *Nature* **438**, 201–204 (2005).

[175] Wang, Q. H., Kalantar-Zadeh, K., Kis, A., Coleman, J. N. & Strano, M. S. Electronics and optoelectronics of two-dimensional transition metal dichalcogenides. *Nature Nanotechnology* **7**, 699–712 (2012).

[176] Ovchinnikov, D., Allain, A., Huang, Y. S., Dumcenco, D. & Kis, A. Electrical transport properties of single-layer WS_2. *ACS Nano* **8**, 8174–8181 (2014).

[177] Akinwande, D., Petrone, N. & Hone, J. Two-dimensional flexible nanoelectronics. *Nature Communications* **5**, 5678 (2014).

[178] Zhang, Y., Tan, Y.-W., Stormer, H. L. & Kim, P. Experimental observation of the quantum Hall effect and Berry's phase in graphene. *Nature* **438**, 201–204 (2005).

[179] Mak, K. F., Lee, C., Hone, J., Shan, J. & Heinz, T. F. Atomically thin MoS_2: a new direct-gap semiconductor. *Physical Review Letters* **105**, 136805 (2010).

[180] Li, L. *et al.* Black phosphorus field-effect transistors. *Nature Nanotechnology* **9**, 372–377 (2014).

[181] Novoselov, K. S., Mishchenko, A., Carvalho, A. & Neto, A. H. C. 2d materials and van der waals heterostructures. *Science* **353**, aac9439 (2016).

[182] Splendiani, A. *et al.* Emerging photoluminescence in monolayer MoS_2. *Nano Letters* **10**, 1271–1275 (2010).

[183] Radisavljevic, B., Radenovic, A., Brivio, J., Giacometti, V. & Kis, A. Single-layer MoS_2 transistors. *Nature Nanotechnology* **6**, 147–150 (2011).

[184] Chhowalla, M. *et al.* The chemistry of two-dimensional layered transition metal dichalcogenide nanosheets. *Nature Chemistry* **5**, 263–275 (2013).

[185] Koppens, F. H. L. *et al.* Photodetectors based on graphene, other two-dimensional materials and hybrid systems. *Nature Nanotechnology* **9**, 780–793 (2014).

[186] Fang, H. *et al.* High-performance single layered WSe_2 *p*-FETs with chemically doped contacts. *Nano Letters* **12**, 3788–3792 (2012).

[187] Jones, A. M. *et al.* Optical generation of excitonic valley coherence in monolayer WSe_2. *Nature Nanotechnology* **8**, 634–638 (2013).

[188] Gong, C. *et al.* Band alignment of two-dimensional transition metal dichalcogenides: application in tunnel field effect transistors. *Applied Physics Letters* **103**, 053513 (2013).

[189] Katsnelson, M. I. Graphene: carbon in two dimensions. *Materials Today* **11**, 34–41 (2008).

[190] Yang, L., Park, C. H., Son, Y. W., Cohen, M. L. & Louie, S. G. Quasiparticle energies and band gaps in graphene nanoribbons. *Physical Review Letters* **99**, 186801 (2007).

[191] Novoselov, K. S. *et al.* Electric field effect in atomically thin carbon films. *Science* **306**, 666–669 (2004).

[192] Sarma, S. D., Adam, S., Hwang, E. & Rossi, E. Electronic transport in two-dimensional graphene. *Reviews of modern physics* **83**, 407 (2011).

[193] Cao, T. *et al.* Valley-selective circular dichroism of monolayer molybdenum disulphide. *Nature Communications* **6**, 1–7 (2015).

[194] Steinhoff, A. *et al.* Efficient excitonic photoluminescence in direct and indirect band gap monolayer MoS_2. *Nano Letters* **15**, 6841–6847 (2015).

[195] Zhang, J. *et al.* Magnetic molybdenum disulfide nanosheet films. *Nano Letters* **7**, 2370–2376 (2007).

[196] Zibouche, N., Kuc, A., Musfeldt, J. & Heine, T. Transition-metal dichalcogenides for spintronic applications. *Annalen der Physik* **526**, 395–401 (2014).

[197] Casto, L. D. *et al.* Strong spin-lattice coupling in $CrSiTe_3$. *APL Materials* **3**, 041515 (2015).

[198] Lin, X., Yang, W., Wang, K. L. & Zhao, W. Two-dimensional spintronics for low-power electronics. *Nature Electronics* **2**, 274–283 (2019).

[199] Sierra, J. F., Fabian, J., Kawakami, R. K., Roche, S. & Valenzuela, S. O. Van der Waals heterostructures for spintronics and opto-spintronics. *Nature Nanotechnology* **16**, 856–868 (2021).

[200] Huang, B. *et al.* Layer-dependent ferromagnetism in a van der Waals crystal down to the monolayer limit. *Nature* **546**, 270–273 (2017).

[201] Gong, C. *et al.* Discovery of intrinsic ferromagnetism in two-dimensional van der Waals crystals. *Nature* **546**, 265–269 (2017).

[202] Huang, B. *et al.* Electrical control of 2D magnetism in bilayer CrI_3. *Nature Nanotechnology* **13**, 544–548 (2018).

[203] Verzhbitskiy, I. A. *et al.* Controlling the magnetic anisotropy in $Cr_2Ge_2Te_6$ by electrostatic gating. *Nature Electronics* **3**, 460–465 (2020).

[204] Banerjee, A. *et al.* Neutron scattering in the proximate quantum spin liquid α-$RuCl_3$. *Science* **356**, 1055–1059 (2017).

[205] Ashton, M. *et al.* Two-dimensional intrinsic half-metals with large spin gaps. *Nano Letters* **17**, 5251–5257 (2017).

[206] Sun, Q. & Kioussis, N. Prediction of manganese trihalides as two-dimensional dirac half-metals. *Physical Review B* **97**, 094408 (2018).

[207] Fei, Z. *et al.* Two-dimensional itinerant ferromagnetism in atomically thin Fe_3GeTe_2. *Nature Materials* **17**, 778–782 (2018).

[208] Bonilla, M. *et al.* Strong room-temperature ferromagnetism in VSe_2 monolayers on van der Waals substrates. *Nature Nanotechnology* **13**, 289–293 (2018).

[209] Long, G. *et al.* Persistence of magnetism in atomically thin $MnPS_3$ crystals. *Nano Letters* **20**, 2452–2459 (2020).

[210] Harms, N. C. *et al.* Piezochromism in the magnetic chalcogenide $MnPS_3$. *npj Quantum Materials* **5**, 56 (2020).

[211] Wang, F. *et al.* New frontiers on van der waals layered metal phosphorous trichalcogenides. *Advanced Functional Materials* **28**, 1802151 (2018).

[212] Ressouche, E. *et al.* Magnetoelectric $MnPS_3$ as a candidate for ferrotoroidicity. *Physical Review B* **82**, 100408 (2010).

[213] Wildes, A. R., Okamoto, S. & Xiao, D. Search for nonreciprocal magnons in $MnPS_3$. *Physical Review B* **103**, 024424 (2021).

[214] Sivadas, N., Daniels, M. W., Swendsen, R. H., Okamoto, S. & Xiao, D. Magnetic ground state of semiconducting transition-metal trichalcogenide monolayers. *Physical Review B* **91**, 235425 (2015).

[215] Chittari, B. L. *et al.* Electronic and magnetic properties of single-layer MPX_3 metal phosphorous trichalcogenides. *Physical Review B* **94**, 184428 (2016).

[216] Sugita, Y., Miyake, T. & Motome, Y. Multiple Dirac cones and topological magnetism in honeycomb-monolayer transition metal trichalcogenides. *Physical Review B* **97**, 035125 (2018).

[217] Neal, S. N. *et al.* Near-field infrared spectroscopy of monolayer $MnPS_3$. *Physical Review B* **100**, 075428 (2019).

[218] Neal, S. N. *et al.* Symmetry crossover in layered MPS_3 complexes ($M = \mathrm{Mn}, \mathrm{Fe}, \mathrm{Ni}$) via near-field infrared spectroscopy. *Physical Review B* **102**, 085408 (2020).

[219] Wang, Y. *et al.* Pressure-driven cooperative spin-crossover, large-volume collapse, and semiconductor-to-metal transition in manganese(ii) honeycomb lattices. *Journal of the American Chemical Society* **138**, 15751–15757 (2016).

[220] Kim, H.-S., Haule, K. & Vanderbilt, D. Mott metal-insulator transitions in pressurized layered trichalcogenides. *Physical Review Letters* **123**, 236401 (2019).

[221] Chu, H. *et al.* Linear magnetoelectric phase in ultrathin $MnPS_3$ probed by optical second harmonic generation. *Physical Review Letters* **124**, 027601 (2020).

[222] Wang, Z. *et al.* Real-space observation of ripple-induced symmetry crossover in ultrathin $MnPS_3$. *ACS Nano* **17**, 1916–1924 (2023).

[223] Zhuang, H. L. & Zhou, J. Density functional theory study of bulk and single-layer magnetic semiconductor $CrPS_4$. *Physical Review B* **94**, 195307 (2016).

[224] Joe, M. *et al.* A comprehensive study of piezomagnetic response in $CrPS_4$ monolayer: mechanical, electronic properties and magnetic ordering under strains. *Journal of Physics: Condensed Matter* **29**, 405801 (2017).

[225] Susilo, R. A. *et al.* Band gap crossover and insulator–metal transition in the compressed layered $CrPS_4$. *npj Quantum Materials* **5**, 58 (2020).

[226] Neal, S. N. *et al.* Exploring few and single layer $CrPS_4$ with near-field infrared spectroscopy. *2D Materials* **8**, 035020 (2021).

[227] Son, J. *et al.* Air-stable and layer-dependent ferromagnetism in atomically thin van der Waals $CrPS_4$. *ACS Nano* **15**, 16904–16912 (2021).

[228] Harms, N. C. *et al.* Metal site substitution and role of the dimer on symmetry breaking in $FePS_3$ and $CrPS_4$ under pressure. *ACS Applied Electronic Materials* **4**, 3246–3255 (2022).

[229] Sheckelton, J. P., Neilson, J. R., Soltan, D. G. & McQueen, T. M. Possible valence-bond condensation in the frustrated cluster magnet $LiZn_2Mo_3O_8$. *Nature Materials* **11**, 493–496 (2012).

[230] Mourigal, M. *et al.* Molecular quantum magnetism in $LiZn_2Mo_3O_8$. *Physical Review Letters* **112**, 027202 (2014).

[231] Kurumaji, T., Ishiwata, S. & Tokura, Y. Doping-tunable ferrimagnetic phase with large linear magnetoelectric effect in a polar magnet $Fe_2Mo_3O_8$. *Physical Review X* **5**, 031034 (2015).

[232] Li, Y., Gao, G. & Yao, K. Dzyaloshinskii-Moriya interaction of polar magnet $Fe_2Mo_3O_8$ and its multiferroicity. *Europhysics Letters* **118**, 37001 (2017).

[233] Chen, H. Magnetically driven orbital-selective insulator–metal transition in double perovskite oxides. *npj Quantum Materials* **3**, 57 (2018).

[234] Solovyev, I. V. & Streltsov, S. V. Microscopic toy model for magnetoelectric effect in polar $Fe_2Mo_3O_8$. *Physical Review Materials* **3**, 114402 (2019).

[235] Nikolaev, S. A., Solovyev, I. V. & Streltsov, S. V. Quantum spin liquid and cluster Mott insulator phases in the Mo_3O_8 magnets. *npj Quantum Materials* **6**, 25 (2021).

[236] Nakayama, S., Nakamura, R., Akaki, M., Akahoshi, D. & Kuwahara, H. Ferromagnetic behavior of $(Fe_{1-y}Zn_y)_2Mo_3O_8$ ($0 \leq y \leq 1$) induced by nonmagnetic Zn substitution. *Journal of the Physical Society of Japan* **80**, 104706 (2011).

[237] Inosov, D. Quantum magnetism in minerals. *Advances in Physics* **67**, 149–252 (2018).

[238] McCarroll, W. H., Katz, L. & Ward, R. Some ternary oxides of tetravalent Molybdenum. *Journal of the American Chemical Society* **79**, 5410–5414 (1957).

[239] Ansell, G. B. & Katz, L. A refinement of the crystal structure of zinc molybdenum(IV) oxide, $Zn_2Mo_3O_8$. *Acta Crystallographica* **21**, 482–485 (1966).

[240] Varret, F., Czeskleba, H., Hartmann-Boutron, F. & Imbert, P. Étude par effet Mössbauer de l'ion Fe^{2+} en symétrie trigonale dans les composés du type (Fe, M)$_2Mo_3O_8$ (M = Mg, Zn, Mn, Co, Ni) et propriétés magnétiques de (Fe, Zn)$_2Mo_3O_8$. *Journal de Physique* **33**, 549–564 (1972).

[241] Czeskleba, H., Imbert, P. & Varret, F. Mössbauer study of $Fe_2Mo_3O_8$ and $FeZnMo_3O_8$. *AIP Conference Proceedings* **5**, 811–815 (1972).

[242] Reschke, S. *et al.* Structure, phonons, and orbital degrees of freedom in $Fe_2Mo_3O_8$. *Physical Review B* **102**, 094307 (2020).

[243] Tang, Y. S. *et al.* Metamagnetic transitions and magnetoelectricity in the spin-1 honeycomb antiferromagnet $Ni_2Mo_3O_8$. *Physical Review B* **103**, 014112 (2021).

[244] Csizi, B. *et al.* Magnetic and vibronic terahertz excitations in Zn-doped $Fe_2Mo_3O_8$. *Physical Review B* **102**, 174407 (2020).

[245] Sheu, Y. M. *et al.* Picosecond creation of switchable optomagnets from a polar antiferromagnet with giant photoinduced Kerr rotations. *Physical Review X* **9**, 031038 (2019).

[246] Biswas, A. *et al.* Cubic–quartic optical solitons in Kerr and power law media. *Optik* **144**, 357 – 362 (2017).

[247] Živković, I., Prša, K., Zaharko, O. & Berger, H. Ni_3TeO_6 — a collinear antiferromagnet with ferromagnetic honeycomb planes. *Journal of Physics: Condensed Matter* **22**, 056002 (2010).

[248] Wang, X., Huang, F.-T., Yang, J., Oh, Y. S. & Cheong, S.-W. Interlocked chiral/polar domain walls and large optical rotation in Ni_3TeO_6. *APL Materials* **3**, 076105 (2015).

[249] Ye, M. & Vanderbilt, D. Domain walls and ferroelectric reversal in corundum derivatives. *Physical Review B* **95**, 014105 (2017).

[250] Yokosuk, M. O. *et al.* Nonreciprocal directional dichroism of a chiral magnet in the visible range. *npj Quantum Materials* **5**, 20 (2020).

[251] Oh, Y. S. *et al.* Non-hysteretic colossal magnetoelectricity in a collinear antiferromagnet. *Nature Communications* **5**, 3201 (2014).

[252] Kim, J. W. *et al.* Successive magnetic-field-induced transitions and colossal magnetoelectric effect in Ni_3TeO_6. *Physical Review Letters* **115**, 137201 (2015).

[253] Lass, J. *et al.* Field-induced magnetic incommensurability in multiferroic Ni_3TeO_6. *Physical Review B* **101**, 054415 (2020).

[254] Bertaut, E., Corliss, L., Forrat, F., Aleonard, R. & Pauthenet, R. Etude de niobates et tantalates de metaux de transition bivalents. *Journal of Physics and Chemistry of Solids* **21**, 234–251 (1961).

[255] Kolodiazhnyi, T., Sakurai, H. & Vittayakorn, N. Spin-flop driven magneto-dielectric effect in $Co_4Nb_2O_9$. *Applied Physics Letters* **99**, 132906 (2011).

[256] Cao, Y. *et al.* High-quality single crystal growth and spin flop of multiferroic $Co_4Nb_2O_9$. *Journal of Crystal Growth* **420**, 90–93 (2015).

[257] Khanh, N. D. *et al.* Magnetoelectric coupling in the honeycomb antiferromagnet $Co_4Nb_2O_9$. *Physical Review B* **93**, 075117 (2016).

[258] Deng, G. *et al.* Spin dynamics and magnetoelectric coupling mechanism of $Co_4Nb_2O_9$. *Physical Review B* **97**, 085154 (2018).

[259] Ding, L. *et al.* Noncollinear magnetic structure and magnetoelectric coupling in buckled honeycomb $Co_4Nb_2O_9$: A single-crystal neutron diffraction study. *Physical Review B* **102**, 174443 (2020).

[260] Choi, S. *et al.* Noncollinear antiferromagnetic order in the buckled honeycomb lattice of magnetoelectric $Co_4Ta_2O_9$. *Physical Review B* **102**, 214404 (2020).

[261] Yin, L. H. *et al.* Colossal magnetodielectric effect and spin flop in magnetoelectric $Co_4Nb_2O_9$ crystal. *Applied Physics Letters* **109**, 032905 (2016).

[262] Xie, Y. M., Lin, C. S., Zhang, H. & Cheng, W. D. Magnetodielectric and magnetoelastic coupling in $Co_4Nb_2O_9$ below Néel temperature. *AIP Advances* **6**, 045006 (2016).

[263] Khanh, N. D. *et al.* Anisotropic magnetodielectric coupling in antiferromagnet $Co_4Nb_2O_9$. *Applied Physics Letters* **114**, 102905 (2019).

[264] Fang, Y. *et al.* Magnetic-field-induced dielectric anomaly and electric polarization in $Co_4Ta_2O_9$. *Journal of the American Ceramic Society* **98**, 2005–2007 (2015).

[265] Fang, Y. *et al.* Large magnetoelectric coupling in $Co_4Nb_2O_9$. *Scientific Reports* **4**, 3860 (2015).

[266] Yadav, S. *et al.* Temperature-dependent structural, dielectric, and Raman spectroscopy studies on magnetoelectric $Co_4Nb_2O_9$. *The Journal of Physical Chemistry C* **126**, 14986–14994 (2022).

[267] Cao, Y. *et al.* Nonlinear magnetoelectric effect in paraelectric state of $Co_4Nb_2O_9$ single crystal. *Scientific Reports* **7**, 14079 (2017).

[268] Lee, N. *et al.* Highly nonlinear magnetoelectric effect in buckled-honeycomb antiferromagnetic $Co_4Ta_2O_9$. *Scientific Reports* **10**, 12362 (2020).

[269] Solovyev, I. V. & Kolodiazhnyi, T. V. Origin of magnetoelectric effect in $Co_4Nb_2O_9$ and $Co_4Ta_2O_9$: The lessons learned from the comparison of first-principles-based theoretical models and experimental data. *Physical Review B* **94**, 094427 (2016).

[270] Chakarawet, K. *et al.* Effect of spin–orbit coupling on phonon-mediated magnetic relaxation in a series of zero-valent vanadium, niobium, and tantalum Isocyanide Complexes. *Inorganic Chemistry* **60**, 18553–18560 (2021).

[271] Ouvrard, G., Brec, R. & Rouxel, J. Structural determination of some MPS_3 layered phases (M = Mn, Fe, Co, Ni and Cd). *Materials Research Bulletin* **20**, 1181–1189 (1985).

[272] Toffoli, P., Khodadad, P. & Rodier, N. L'orthothiophosphate de chrome. *Acta Crystallographica Section B Structural Crystallography and Crystal Chemistry* **33**, 285–287 (1977).

[273] Diehl, R. & Carpentier, C. D. The crystal structure of chromium thiophosphate, $CrPS_4$. *Acta Crystallographica Section B Structural Crystallography and Crystal Chemistry* **33**, 1399–1404 (1977).

[274] Joy, P. A. & Vasudevan, S. Magnetism in the layered transition-metal thiophosphates MPS_3 (M=Mn, Fe, and Ni). *Physical Review B* **46**, 5425–5433 (1992).

[275] Okuda, K. *et al.* Magnetic properties of layered compound $MnPS_3$. *Journal of the Physical Society of Japan* **55**, 4456–4463 (1986).

[276] Šiškins, M. *et al.* Magnetic and electronic phase transitions probed by nanomechanical resonators. *Nature Communications* **11**, 2698 (2020).

[277] Bud'ko, S. L., Gati, E., Slade, T. J. & Canfield, P. C. Magnetic order in the van der Waals antiferromagnet $CrPS_4$: Anisotropic H-T phase diagrams and effects of pressure. *Physical Review B* **103**, 224407 (2021).

[278] Chaudhuri, S., Kuo, C. N., Chen, Y. S., Lue, C. S. & Lin, J. G. Low-temperature magnetic order rearrangement in the layered van der Waals compound $MnPS_4$. *Physical Review B* **106**, 094416 (2022).

[279] Goossens, D. J., Wildes, A. R., Ritter, C. & Hicks, T. J. Ordering and the nature of the spin flop phase transition in $MnPS_3$. *Journal of Physics: Condensed Matter* **12**, 1845–1854 (2000).

[280] Bud'ko, S. L., Gati, E., Slade, T. J. & Canfield, P. C. Magnetic order in the van der Waals antiferromagnet $CrPS_4$: Anisotropic $H-T$ phase diagrams and effects of pressure. *Physical Review B* **103**, 224407 (2021).

[281] Boerio-Goates, J., Lifshitz, E. & Francis, A. H. Electronic spectroscopy of nearly octahedrally coordinated manganese in manganese phosphide sulfide ($MnPS_3$) and cadmium phosphide sulfide ($CdPS_3$) lattices. *Inorganic Chemistry* **20**, 3019–3023 (1981).

[282] Grasso, V., Neri, F., Perillo, P., Silipigni, L. & Piacentini, M. Optical-absorption spectra of crystal-field transitions in $MnPS_3$ at low temperatures. *Physical Review B* **44**, 11060–11066 (1991).

[283] Piryatinskaya, V. G., Kachur, I. S., Slavin, V. V., Yeremenko, A. V. & Vysochanskii, Y. M. Temperature behavior of the fundamental optical absorption band in quasi-two-dimensional crystalline $MnPS_3$. *Low Temperature Physics* **38**, 870–873 (2012).

[284] Gnatchenko, S. L., Kachur, I. S., Piryatinskaya, V. G., Vysochanskii, Y. M. & Gurzan, M. I. Exciton-magnon structure of the optical absorption spectrum of antiferromagnetic $MnPS_3$. *Low Temperature Physics* **37**, 144–148 (2011).

[285] Birowska, M., Faria Junior, P. E., Fabian, J. & Kunstmann, J. Large exciton binding energies in $MnPS_3$ as a case study of a van der Waals layered magnet. *Physical Review B* **103**, L121108 (2021).

[286] Matthiesen, M. *et al.* Controlling magnetism with light in a zero orbital angular momentum antiferromagnet. *Physical Review Letters* **130**, 076702 (2023).

[287] Sun, Y.-J., Tan, Q.-H., Liu, X.-L., Gao, Y.-F. & Zhang, J. Probing the magnetic ordering of antiferromagnetic $MnPS_3$ by Raman spectroscopy. *The Journal of Physical Chemistry Letters* **10**, 3087–3093 (2019).

[288] Kim, K. *et al.* Antiferromagnetic ordering in van der Waals 2D magnetic material $MnPS_3$ probed by Raman spectroscopy. *2D Materials* **6**, 041001 (2019).

[289] Vaclavkova, D. *et al.* Magnetoelastic interaction in the two-dimensional magnetic material $MnPS_3$ studied by first principles calculations and Raman experiments. *2D Materials* **7**, 035030 (2020).

[290] Lim, S. Y., Kim, K., Lee, S., Park, J.-G. & Cheong, H. Thickness dependence of antiferromagnetic phase transition in Heisenberg-type $MnPS_3$. *Current Applied Physics* **21**, 1–5 (2021).

[291] Lee, J., Wang, Z., Xie, H., Mak, K. F. & Shan, J. Valley magnetoelectricity in single-layer MoS_2. *Nature Materials.* **16**, 887–891 (2017).

[292] Gu, P. *et al.* Photoluminescent quantum interference in a van der waals magnet preserved by symmetry breaking. *ACS Nano* **14**, 1003–1010 (2020).

[293] Kim, S., Lee, J., Lee, C. & Ryu, S. Polarized Raman spectra and complex Raman tensors of antiferromagnetic semiconductor $CrPS_4$. *The Journal of Physical Chemistry C* **125**, 2691–2698 (2021).

[294] Scott, J. F. Soft-mode spectroscopy: Experimental studies of structural phase transitions. *Reviews of Modern Physics* **46**, 83–128 (1974).

[295] Whangbo, M.-H., Koo, H.-J. & Dai, D. Spin exchange interactions and magnetic structures of extended magnetic solids with localized spins: theoretical descriptions on formal, quantitative and qualitative levels. *Journal of Solid State Chemistry* **176**, 417–481 (2003).

[296] Wooten, F. *Optical Properties of Solids* (1972).

[297] Kuzmany, H. *Solid-State Spectroscopy* (Springer, Berlin, 2009), second edn.

[298] Ferraro, J. R., Nakamoto, K. & Brown, C. W. *Introductory Raman Spectroscopy* (Academic Press, San Diego, 2003), second edn.

[299] Mielenz, K. D. Physical parameters in high-accuracy spectrophotometry. *Journal of Research of the National Bureau of Standards* **76A**, 455–467 (1972).

[300] Mielenz, K. D. & Mavrodineanu, R. Reflection correction for high accuracy transmittance measurements on filter glasses. *Journal of Research of the National Bureau of Standards* **77A**, 699–703 (1973).

[301] Tinkham, M. Far infrared absorption in ordered magnetic systems. In *Far-Infrared Properties of Solids*, 196–222 (Springer US, Boston, MA, 1970).

[302] Fan, S. *et al.* Electronic chirality in the metallic ferromagnet $Fe_{1/3}TaS_2$. *Physical Review B* **96**, 205119 (2017).

[303] Tauc, J. Optical properties and electronic structure of amorphous Ge and Si. *Materials Research Bulletin* **3**, 37–46 (1968).

[304] Kimiagar, S. & Abrinaei, F. Effect of temperature on the structural , linear , and nonlinear optical properties of MgO-doped graphene oxide nanocomposites. *Nanophotonics* (2017).

[305] Meinert, M. & Reiss, G. Electronic structure and optical band gap determination of $NiFe_2O_4$. *Journal of Physics: Condensed Matter* **26**, 1–4 (2014).

[306] Ghobadi, N. Band gap determination using absorption spectrum fitting procedure. *International Nano Letters* **3**, 1–4 (2013).

[307] Zhu, T., Ong, W. L., Zhu, L. & Ho, G. W. TiO_2 fibers supported β-FeOOH nanostructures as efficient visible light photocatalyst and room temperature sensor. *Nature Publishing Group* **5**, 1–15 (2015).

[308] Tauc, J. Optical properties and electronic structure of amorphous Ge and Si. *Materials Research Bulletin* **3**, 37–46 (1968).

[309] Viezbicke, B. D., Patel, S., Davis, B. E. & Birnie III, D. P. Evaluation of the Tauc method for optical absorption edge determination: ZnO thin films as a model system. *physica status solidi (b)* **252**, 1700–1710 (2015).

[310] Makula, P., Pacia, M. & Macyk, W. How to correctly determine the band gap energy of modified semiconductor photocatalysts based on uv–vis spectra. *The Journal of Physical Chemistry Letters* **9**, 6814–6817 (2018).

[311] Sarswat, P. K. & Free, M. L. A study of energy band gap versus temperature for Cu_2ZnSnS_4 thin films. *Physica B: Condensed Matter* **407**, 108–111 (2012).

[312] O'Donnell, K. P. & Chen, X. Temperature dependence of semiconductor band gaps. *Applied Physics Letters* **58**, 2924–2926 (1991).

[313] Huang, K. & Rhys, A. Theory of light absorption and non-radiative transitions in F-centres. *Proceedings of the Royal Society of London. Series A, Mathematical and Physical Sciences* **204**, 406–423 (1950).

[314] Park, K. *et al.* Band-Mott mixing hybridizes the gap in $Fe_2Mo_3O_8$. *Physical Review B* **104**, 195143 (2021).

[315] Mason, W. R. A practical guide to magnetic circular dichroism spectroscopy (2006).

[316] Ando, K. Seeking room-temperature ferromagnetic semiconductors. *Science* **312**, 1883–1885 (2006).

[317] Holinsworth, B. S. *et al.* Magnetic field control of charge excitations in $CoFe_2O_4$. *APL Materials* **6**, 066110 (2018).

[318] Dobrowolska, M. & *et al*. Controlling the Curie temperature in (Ga,Mn)As through location of the Fermi level within the impurity band. *Nature Materials.* **11**, 444–449 (2012).

[319] Rice, W. D. & et al. Persistent optically induced magnetism in oxygen-deficient strontium titanate. *Nature Materials.* **13**, 481 (2014).

[320] Holinsworth, B. S. & *et al*. Magnetic field tunability of spin-polarized excitations in a high-temperature magnet. *Physical Review B* **96** (2017).

[321] Amft, M., Burkert, T., Sanyal, B. & Oppeneer, P. First-principles calculations of optical and magneto-optical properties of $Ga_{1-x}Mn_xAs$ and MnAs. *Physica B* **404**, 3782 (2009).

[322] Griffiths, P. R. & de Haseth, J. A. *Fourier transform infrared spectrometry* (Jon Wiley and Sons Inc, Hoboken, 2007), 2nd edn.

[323] Salazar-Serrano, L. J., Valencia, A. & Torres, J. P. Observation of spectral interference for any path difference in an interferometer. *Optics Letters* **39**, 4478–4481 (2014).

[324] Toth, J. & Bird, M. D. Fea-aided design for a working model of a split florida-helix. *Applied Superconductivity IEEE Transactions* **18**, 1051–8233 (2008).

[325] Blaha, P. *et al. WIEN2k: An Augmented Plane Wave Plus Local Orbitals Program for Calculating Crystal Properties* (Techn. Universitat, 2019).

[326] Haule, K. *DMFT code* (2007-2020). `http://hauleweb.rutgers.edu/tutorials/`.

[327] Haule, K. Structural predictions for correlated electron materials using the functional dynamical mean field theory approach. *Journal of the Physical Society of Japan* **87**, 041005 (2018).

[328] Perdew, J. P., Burke, K. & Ernzerhof, M. Generalized gradient approximation made simple. *Physical Review Letters* **77**, 3865–3868 (1996).

[329] Haule, K. Exact double counting in combining the dynamical mean field theory and the density functional theory. *Physical Review Letters* **115**, 196403 (2015).

[330] Kresse, G. & Hafner, J. *Ab initio* molecular dynamics for liquid metals. *Physical Review B* **47**, 558–561 (1993).

[331] Kresse, G. & Furthmüller, J. Efficient iterative schemes for *ab initio* total-energy calculations using a plane-wave basis set. *Physical Review B* **54**, 11169–11186 (1996).

[332] Dudarev, S. L., Botton, G. A., Savrasov, S. Y., Humphreys, C. J. & Sutton, A. P. Electron-energy-loss spectra and the structural stability of nickel oxide: An LSDA+U study. *Physical Review B* **57**, 1505–1509 (1998).

[333] Csonka, G. I. *et al.* Assessing the performance of recent density functionals for bulk solids. *Physical Review B* **79**, 155107 (2009).

[334] Blaha, P., Schwarz, K., Madsen, G. K. H., Kvasnicka, D. & Luitz, J. *WIEN2k, an augmented plane wave + local orbitals program for calculating crystal properties* (Karlheinz Schwarz, Techn. Universität Wien, Austria, 2001).

[335] Haule, K. Structural predictions for correlated electron materials using the functional dynamical mean field theory approach. *Journal of the Physical Society of Japan* **87**, 041005 (2018).

[336] Kresse, G. & Furthmüller, J. Efficient iterative schemes for ab initio total-energy calculations using a plane-wave basis set. *Physical Review B* **54**, 11169–11186 (1996).

[337] Kresse, G. & Furthmüller, J. Efficiency of ab-initio total energy calculations for metals and semiconductors using a plane-wave basis set. *Computational Materials Science* **6**, 15 – 50 (1996).

[338] Blöchl, P. E. Projector augmented-wave method. *Physical Review B* **50**, 17953–17979 (1994).

[339] Kresse, G. & Joubert, D. From ultrasoft pseudopotentials to the projector augmented-wave method. *Physical Review B* **59**, 1758–1775 (1999).

[340] Perdew, J. P., Burke, K. & Ernzerhof, M. Generalized gradient approximation made simple. *Physical Review Letters* **77**, 3865–3868 (1996).

[341] Gajdoš, M., Hummer, K., Kresse, G., Furthmüller, J. & Bechstedt, F. Linear optical properties in the projector-augmented wave methodology. *Physical Review B* **73**, 045112 (2006).

[342] Togo, A. & Tanaka, I. First principles phonon calculations in materials science. *Scripta Materialia* **108**, 1–5 (2015).

[343] Gonze, X. & Lee, C. Dynamical matrices, born effective charges, dielectric permittivity tensors, and interatomic force constants from density-functional perturbation theory. *Physical Review B* **55**, 10355–10368 (1997).

[344] Paudel, T. R. & Lambrecht, W. R. L. First-principles calculation of the zone center phonons in $ZnSiN_2$: Comparison with infrared data. *Physical Review B* **76**, 115205 (2007).

[345] Joy, P. A. & Vasudevan, S. The intercalation reaction of pyridine with manganese thiophosphate, $MnPS_3$. *Journal of the American Chemical Society* **114**, 7792–7801 (1992).

[346] Chen, Q. *et al.* Realization of the orbital-selective Mott state at the molecular level in $Ba_3LaRu_2O_9$. *Physical Review Materials* **4**, 064409 (2020).

[347] Pascut, G. L. & Haule, K. Role of orbital selectivity on crystal structures and electronic states in $BiMnO_3$ and $LaMnO_3$ perovskites. *Physical Review B* **107**, 045147 (2023).

[348] Lichtenstein, A. I., Katsnelson, M. I. & Kotliar, G. Finite-temperature magnetism of transition metals: An ab-initio dynamical mean-field theory. *Physical Review Letters* **87**, 067205 (2001).

[349] Anisimov, V., Nekrasov, I., Kondakov, D., Rice, T. & Sigrist, M. Orbital-selective Mott-insulator transition in $Ca_{2-x}Sr_xRuO_4$. *The European Physical Journal B* **25**, 191–201 (2002).

[350] de'Medici, L., Georges, A. & Biermann, S. Orbital-selective Mott transition in multiband systems: Slave-spin representation and dynamical mean-field theory. *Physical Review B* **72**, 205124 (2005).

[351] Haule, K. & Pascut, G. L. Mott transition and magnetism in rare earth nickelates and its fingerprint on the X-ray scattering. *Scientific Reports* **7**, 10375 (2017).

[352] Pankove, J. I. *Optical Processes in Semiconductors* (Dover Publications; 2nd Revised ed. edition, 2010).

[353] Ballhausen, C. *Introduction to Ligand Field Theory*. McGraw-Hill series in Advanced Chemistry (McGraw-Hill, 1962).

[354] Stoneham, A. *Theory of Defects in Solids: Electronic Structure of Defects in Insulators and Semiconductors*. Oxford Classic Texts in the Physical Sciences (Clarendon Press, 2001).

[355] O'Neal, K. R. *et al.* Vibronic coupling and band gap trends in $CuGeO_3$ nanorods. *Physical Review B* **96**, 1–6 (2017).

[356] Evans, J. W., Harris, T. R., Reddy, B. R., Schepler, K. L. & Berry, P. A. Optical spectroscopy and modeling of Fe^{2+} ions in zinc selenide. *Journal of Luminescence* **188**, 541–550 (2017).

[357] Yee, C.-H., Kotliar, G. & Haule, K. Valence fluctuations and quasiparticle multiplets in plutonium chalcogenides and pnictides. *Physical Review B* **81**, 035105 (2010).

[358] Hewson, A. C. *The Kondo Problem to Heavy Fermions* (Cambridge University Press, 1993).

[359] Mandal, S., Haule, K., Rabe, K. M. & Vanderbilt, D. Systematic beyond-DFT study of binary transition metal oxides. *npj Computational Materials* **5**, 115 (2019).

[360] Mandal, S., Haule, K., Rabe, K. M. & Vanderbilt, D. Influence of magnetic ordering on the spectral properties of binary transition metal oxides. *Physical Review B* **100**, 245109 (2019).

[361] Zhang, F. C. & Rice, T. M. Effective Hamiltonian for the superconducting Cu oxides. *Physical Review B* **37**, 3759–3761 (1988).

[362] Eskes, H. & Sawatzky, G. A. Tendency towards local spin compensation of holes in the high-T_c copper compounds. *Physical Review Letters* **61**, 1415–1418 (1988).

[363] Pavarini, E., Koch, E., Scalettar, R. & Martin, R. (eds.) *The Physics of Correlated Insulators, Metals, and Superconductors*, vol. 7 of *Schriften des Forschungszentrums Jülich Reihe Modeling and Simulation* (Forschungszentrum Jülich GmbH Zentralbibliothek, Verlag, Jülich, 2017).

[364] Demchenko, D. O., Joura, A. V. & Freericks, J. K. Effect of particle-hole asymmetry on the Mott-Hubbard metal-insulator transition. *Physical Review Letters* **92**, 216401 (2004).

[365] Kotliar, G. *et al.* Electronic structure calculations with dynamical mean-field theory. *Reviews of Modern Physics* **78**, 865–951 (2006).

[366] Cheong, S. W., Talbayev, D., Kiryukhin, V. & Saxena, A. Broken symmetries, non-reciprocity, and multiferroicity. *npj Quantum Mater.* **3**, 1–7 (2018).

[367] Zhou, X., Feng, W., Yang, X., Guo, G.-Y. & Yao, Y. Crystal chirality magneto-optical effects in collinear antiferromagnets. *Physical Review B* **104**, 024401 (2021).

[368] Sell, D. D., Greene, R. L. & White, R. M. Optical exciton-magnon absorption in MnF_2. *Physical Review* **158**, 489–510 (1967).

[369] Greene, R. L., Sell, D. D., Yen, W. M., Schawlow, A. L. & White, R. M. Observation of a spin-wave sideband in the optical spectrum of MnF_2. *Physical Review Letters* **15**, 656–659 (1965).

[370] Chen, P., Lee, N., McGill, S., Cheong, S.-W. & Musfeldt, J. L. Magnetic-field-induced color change in α-Fe_2O_3 single crystals. *Physical Review B* **85**, 174413 (2012).

[371] Henderson, B. & Imbusch, G. F. *Optical spectroscopy of inorganic solids* (Oxford [Oxfordshire]; Clarendon Press, 1989).

[372] Liu, Z. *et al.* Observation of nonreciprocal magnetophonon effect in nonencapsulated few-layered CrI_3. *Science Advances* **6**, eabc7628 (2020).

[373] Nomura, T. *et al.* Phonon magnetochiral effect. *Physical Review Letters* **122**, 145901 (2019).

[374] Fishman, R. S. *et al.* Spin-induced polarizations and nonreciprocal directional dichroism of the room-temperature multiferroic $BiFeO_3$. *Physical Review B* **92**, 094422 (2015).

[375] Langenbach, M. Giant directional dichroism in chiral Ni_3TeO_6 in THz spectroscopy in high magnetic fields (2019).

[376] Leung, F., Chiu, W. & Demokan, M. Fiber-optic current sensor developed for power system measurement. In *1991 International Conference on Advances in Power System Control, Operation and Management, APSCOM-91.*, 637–643 vol.2 (1991).

[377] Guan, B. & Wang, S. Fiber grating laser current sensor based on magnetic force. *IEEE Photonics Technology Letters* **22**, 230–232 (2010).

[378] Wen, F., Wu, B.-J., Li, C.-Z., Wu, S.-J. & Perumal, S. Magnetic field response of erbium-doped magneto-optic fiber Bragg grating. *Optical Engineering* **51**, 1 – 5 (2012).

[379] Nascimento, I. M., Baptista, J. M., Jorge, P. A. S., Cruz, J. L. & Andrés, M. V. Erbium doped optical fiber lasers for magnetic field sensing. In Kalinowski, H. J., Fabris, J. L. & Bock, W. J. (eds.) *24th International Conference on Optical Fibre Sensors*, vol. 9634, 765 – 768. International Society for Optics and Photonics (SPIE, 2015).

[380] Zhang, T., Zhang, J., Cheng, L., Li, Y. & Guan, B.-O. Magnetic field sensing through magnetic force using erbium-doped fiber laser. In *2017 Conference on Lasers and Electro-Optics Pacific Rim*, s1169 (Optical Society of America, 2017).

[381] Nakagawa, N. *et al.* Magneto-chiral dichroism of $CsCuCl_3$. *Physical Review B* **96**, 121102 (2017).

[382] Collett, E. *Field guide to polarization* (SPIE, 2005).

[383] Valdés-Aguilar, R., Sushkov, A. B., Choi, Y. J., Cheong, S.-W. & Drew, H. D. Spin-phonon coupling in frustrated magnet $CdCr_2O_4$. *Physical Review B* **77**, 092412 (2008).

[384] Rudolf, T. *et al.* Phonon anomalies and charge dynamics in $Fe_{1-x}Cu_xCr_2S_4$ single crystals. *Physical Review B* **72**, 014450 (2005).

[385] Pal, P. *et al.* Investigation of spin-phonon coupling and local magnetic properties in magnetoelectric Fe_2TeO_6. *Journal of Magnetism and Magnetic Materials* **540**, 168512 (2021).

[386] Pandey, P. K., Choudhary, R. J., Mishra, D. K., Sathe, V. G. & Phase, D. M. Signature of spin-phonon coupling in Sr_2CoO_4 thin film: A Raman spectroscopic study. *Applied Physics Letters* **102**, 142401 (2013).

[387] Lockwood, D. J. & Cottam, M. G. The spin-phonon interaction in FeF_2 and MnF_2 studied by Raman spectroscopy. *Journal of Applied Physics* **64**, 5876–5878 (1988).

[388] Aytan, E. *et al.* Spin-phonon coupling in antiferromagnetic nickel oxide. *Applied Physics Letters* **111**, 252402 (2017).

[389] Kim, T. *et al.* Spin-orbit coupling effects on spin-phonon coupling in $Cd_2Os_2O_7$. *Physical Review B* **102**, 201101 (2020).

[390] Spaldin, N. A. Analogy between the magnetic dipole moment at the surface of a magnetoelectric and the electric charge at the surface of a ferroelectric. *Journal of Experimental and Theoretical Physics* **132**, 493–505 (2021).

Vita

Kiman Park was born in the city of Incheon, South Korea. He came over to the United States in 2006, where he would live in Knoxville, Tennessee. He attended the University of Tennessee between 2014-2018, where he received his B.S. degree majoring in Chemistry. Kiman joined the chemistry department of the University of Tennessee in the fall of 2018 to pursue his Ph.D. degree under Dr. Janice Musfeldt. His research focuses on the spectroscopic investigation of complex oxides and the coupling they present between charge, magnetism, and the lattice. Kiman Park received a Doctor of Philosophy Degree in Chemistry from the University of Tennessee in the Spring of 2023.